THE UNIVERSITY OF HULL

Dune Dynamics under Unsteady Flows

being a Thesis submitted for the Degree of Doctor of Philosophy
in the University of Hull

by

Hao Hu, B.S

January 2019

Abstract

River bedforms keep translating and deforming perpetually during their migration. During flow field unsteadiness they also change in size and shape over time and in space. However, our knowledge of how bedforms adapt to changing flows remains inadequately understood. Therefore, how do dunes adapt to different changing flows (floods and tides), and how does the coupled sediment transport affect dune morphology and dynamics is urgent to be investigated.

Large-scale flume experiments were conducted to simulate dune dynamics during carefully controlled floods with various hydrographs, while field surveys were undertaken in both the middle reach, close to the backwater zone, and within the estuary of the Changjiang (Yangtze) River, in order to examine the combined effect of the flood and tide on dune evolution.

The result indicates that the sediment transport mechanisms dominate how dunes adapt to unsteady flows. The analysis of dune three-dimensionality reflects that the generation of the larger dunes is the main factor controlling sediment transport and thereby the bedform adaptation. Moreover, the processes of bedform adaptation to changing flows will be varying under different sediment transport mechanisms due to diverse sediment redistribution over and between dunes.

In the tidally influenced area where riverbed is composed of fine sediment, our result implies that clay content is a first-order control on bedform aspect ratio and the specific sediment composition of the riverbed, in some extent, affects the mechanism of sediment transport related to the exchange between suspended sediment and riverbed.

This work extends our knowledge on how dunes generate and develop under variable flows and has delineated how variations in transport stage can be coupled with the variation in the dominant sediment transport mechanisms. Moreover, these

developments will provide fundamental knowledge that is of significance for a wide variety of purposes, such as improving morphodynamic modelling over large spatio-temporal scales, environmental and engineering management, and more reliable flood predictions.

Acknowledgments

First, I want to express my deepest gratitude to my PhD supervisor, Prof. Daniel R. Parsons, for his support, guidance, patience, and encouragement throughout my PhD life.

Dan, thank you for offering me the opportunity to study and research in the United Kingdom. I thank you for your supporting my attendance at so many international conferences, expanding my horizons. I thank you that you always encouraged me to do what I want to do. I thank you that you are so nice that every time during our discussion, you told me you are expecting my 'but', rather than just 'yes'. I thank you…

Moreover, I am honoured to work in the UBED project team and thank you for involving me in the flume experimental work in the Deep. Thanks for giving me this chance to cooperate with the outstanding teammates including Annie Ockleford, Rich Hardy, Phil Ashworth, and Jim Best. And thanks to Brendan Murphy, Mike Dennet, Kim Rosewell, and Mark Anderson for their help in the laboratory work. Besides that, I would like to thank Dr. Steve Simmons, Dr. Leiping Ye, Dr. Xuxu WU and Dr. Chris Unsworth for their help with many aspects of my study.

I must thank the China Scholarship Council (CSC) and the University of Hull for offering a joint scholarship supporting my PhD study and living in the UK financially. Ross Jennings, Lucy Wright, Charlotte Stephenson, Dave Jordan, Laura-Beth Jordan, Jess Moloney, Rita Santos, Chloe Morris, Jazmin Scarlett etc., thanks for giving me so many wonderful memories! And also, my friends Jinlong Wang, Chao Jiang, Hualong Luan, Weiming Xie, Peng Yu, Qiang Fu, Heng Zhao, thanks for your support, Forever R.503.

Finally, I would like to express my deep gratitude to my family who have been always the greatest support and love during my study overseas in the UK. Particularly, I want to say thanks to my wife Yuan Yuan, who has been doing the utmost to support me in the past three years. At her best age, she unswervingly supported my decision to take this overseas PhD. Over three years, it was so difficult that we were 9000 Km apart. I am sorry I could do nothing for you when you got in that car accident, when you felt sick, and when you just need my company. But we did it, and I promise in the future life, nothing will separate us.

Contents

Figures

Tables

Nomenclature

Asy	asymmetry calculated via (Lups-Ldowns)/(Lups+Ldowns)
a	the major axis of the ellipse
b	the minor axis of the ellipse
b_i	radial aDcp beam velocity
C	echo intensity scale (dB per RSSI count)
C'	grain-related Chezy roughness coefficient
D_{50}	median grain size (m)
D_*	dimensionless particle parameter
D	the average elevation changes
D'	average elevation change
D_{lag}	bedform migration distance between consecutive bed profiles
d_w	designed water depth
$d1$	water depth of pre-condition
$d2$	water depth of post-condition
Fr	Froude number
f	a fitting parameter
F	deformation fraction
g	gravity acceleration (ms^{-2})
h	water depth
H	bedform height from both top to downstream trough (Htotr) and trough to the downstream top (Htrto)

H_{std}	the standard deviation of H
<*h*>	spatially averaged water depth
I_{dB}	echo intensity recorded in counts
$\langle I_{dB} \rangle$	water corrected backscatter
k_s'	the grain roughness, $3D_{90}$
L	bedform length calculated from both length between two subsequent crests and troughs
L_{Xmit}	transmit length
$Lups$	length of the stoss face, the upward length
$Ldowns$	length of the lee face, the downward length
L_{std}	the standard deviation of L
p	the porosity of the bed
Q	flow discharge
$Q1$	flow discharge of pre-condition
$Q2$	flow discharge of post-condition
q_T	sediment transport related to bedform translation
q_D	sediment transport related to bedform deformation
Q_{tot}	total bed material flux
$q^2/2$	turbulence kinetic energy
R	specific gravity
r	the range from the transducer to the middle of the bin
s	specific density
S	water slope
S_l	lee face slope angle (degrees) computed as Htotr/Ldowns
S_s	stoss face slope angle (degrees) computed as Htrto/Lups
t_e	the time of equilibrium period for each state

t_*	normalised time
Δt	the time difference between the two consecutive profiles
T	transport stage parameter
Te	temperature (°C)
u	x velocity in a right handed coordinate system
u'	the deviation of u
$\bar{u}$	mean streamwise flow velocity (m s^{-1})
$u1$	flow velocity of pre-condition
$u2$	flow velocity of post-condition
u_*	shear velocity (m/s)
u_f'	is the friction velocity, $u_f' = \sqrt{g}\frac{U}{C'}$; *U* is depth-averaged flow velocity;
$\overline{u'w'}$	Reynolds stress
$u(z)$	time-averaged current velocity at the height z above the bed
V_s	horizontal sediment velocity
$\langle V_b \rangle$	spatially averaged bedform migration rates
v_{bed}	apparent bedload speed
v_{DGPS}	boat speed computed via GPS
v_{BT}	the bottom tracking velocity
v	y velocity in a right handed coordinate system
w	z velocity in a right handed coordinate system
$\bar{w}$	mean crosswise flow velocity (m s^{-1})
W	flume width (m)
Δx	the length of the translated bed profiles
$\Pi(x)$	the elevation difference between the translated bed profiles
$x0$	the longitudinal distance of the ellipse

$y0$	the transverse distance of the ellipse
z	topography data along x and y direction
z_0	roughness length
z_*	water depth normalised height above the bed
α	sound absorption coefficient
β_b	the shape factor of bedforms
η	Bed elevation
κ	von Kármán constant
μ_d	the dynamic friction coefficient
υ	kinematic viscosity coefficient (m^2s^{-1})
θ	the angle of rotation of the ellipse
θ'	the grain-related Shield's parameter, $\theta' = \frac{u_f'^2}{(s-1)gD_{50}}$;
ρ_s	sediment density (kgm^{-3})
ρ_w	water density (kgm^{-3})
σ	the standard deviation for the random field
τ	shear stress
τ_*	dimensionless Shields stress
τ_0	total boundary shear stress
τ_{*cr}	critical threshold of bed-shear stress for sediment transport ($kgm^{-1}s^{-2}$)
w_s	settling velocity

CHAPTER 1

1. Introduction

1.1. Background

Alluvial river channels are self-formed systems, created by sediment transport and simultaneously shaped by sediment deposition [*Van Rijn*, 1993; *Church*, 2006; *Bridge*, 2009 ; *Yalin*, 2015]. The relationships between hydraulic and sedimentary processes control the modification and adjustment of the channel system across a wide range of temporal and spatial scales, ranging from the grain movement to channel migration and longer-term floodplain evolution [*Allen*, 2009; *Venditti*, 2013]. In sand-bedded alluvial channels, bedforms (ripples, dunes, and larger bar forms) are the ubiquitous bed roughness elements that dominate the river stage level, flow and sediment transport, subsequently, modify the channel dynamics [*Ashworth et al.*, 2000; *Wilbers*, 2004; *Best*, 2005a]. A wide variety of bedforms have been defined in response to the different flow strengths (Figure 1-1): in subcritical or tranquil flows (i.e. $Fr = U/\sqrt{gh} < 1$, where U is the mean flow velocity, g is gravity acceleration and h is the water depth), the bed starts at lower-stage plane bed and grows to ripples and dunes with the increase of the flow strength; but in supercritical flows, the bed develops to upper-stage plane, followed by the generation of antidunes when upstream breaking waves form [*Southard and Boguchwal*, 1990]. Therefore, the correlation between the flow and bedform morphology (i.e. phase diagram) is widely used to predict the bedform type and size under a certain flow condition [*Yalin*, 1972; *Van Rijn*, 1984b], although this method could be problematic when applied to large rivers with deeper water depth [*Rubin and McCulloch*, 1980; *Kostaschuk and Villard*, 1996; *Berg et al.*, 1998].

Moreover, the cross-strata (or cross-sets which are the groups of cross-strata formed by the same type of bedforms), formed by bedform migration and deposition, are a common sedimentary structure in sedimentary deposits and rock [*RL*, 1982; *Leclair*, 2002; *Reesink and Bridge*, 2007]. As different bedform types can leave behind different types of cross-strata, it is possible to determine paleo-flow conditions based on the preserved sedimentary structures [*Leclair and Bridge*, 2001; *Bridge*, 2009]. The accurate paleo-environmental analysis is critically dependent on the current understanding of how bedform dimensions and kinematics respond to the flow strength [*Venditti*, 2013]. Therefore, an understanding of how the processes of the flow over dunes lead to erosion, transport and deposition is essential to more complete interpretations, in order to decipher the sedimentary structure to reconstruct flow processes via the rock record [*Best*, 2005a].

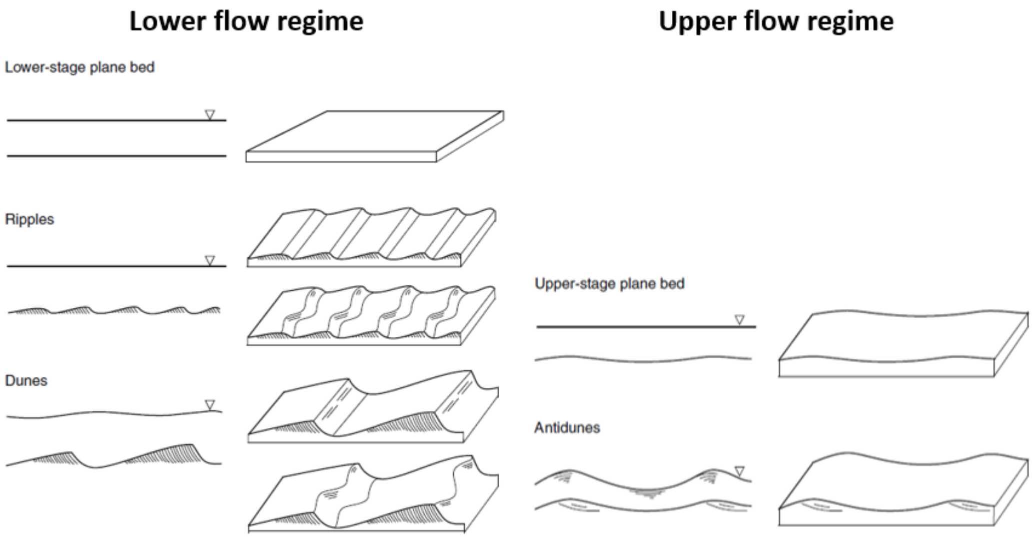

Figure 1-1. The typical sequence of bedforms in alluvial channels. Bed morphologies for each flow regime occur with increasing flow strength from top to bottom. After Venditti [2013].

The generation of the bedforms in the river bed leads to the increase of hydraulic roughness, as the bedform-related flow resistance (i.e form roughness) is much greater than grain-related roughness [*Van Rijn*, 1984b; *Wilbers*, 2004]. Form roughness is produced by the occurrence of flow separation in the lee of the bedform resulting in the energy dissipation [*McLean and Smith*, 1979; *Bennett and Best*, 1995; *McLean et al.*, 1999a], and it has been recognised as the dominant factor in controlling the water level [*Paarlberg et al.*, 2007; *Morvan et al.*, 2008; *Paarlberg et al.*, 2009; *Paarlberg et al.*, 2010]. Moreover, flow separation is dependent on both the size [*Balachandar et al.*, 2007; *Balachandar and Reddy*, 2011] and shape [*Paarlberg et al.*, 2007; *Kwoll et al.*, 2016; *Kwoll et al.*, 2017] of the bedform. In unsteady flows, the dune adjustment in response to the flow changes alters the hydraulic roughness and the subsequent river stage [*Wilbers*, 2004]. Thus, it is extremely important to predict dune dimensions during a flood and ensure the impact of bedform roughness and its change over time is incorporated in predictions in order to adequately protect property and people who live near the river banks [*Julien and Klaassen*, 1995; *Wilbers and Ten Brinke*, 2003].

Additionally, the generation of large dunes may obstruct the river navigation [*Engelund and Fredsoe*, 1982; *Paarlberg et al.*, 2010], and their migration has the potential to pose a threat to infrastructure [*Amsler et al.*, 1997]. Indeed, large dunes passing over submerged tunnel can lead to scour and tunnel exposure, threatening stability [*Amsler and Schreider*, 1999]. Furthermore, similar threats were observed for wind turbine bases and sub-aqueous cables [*Bolle et al.*, 2013] and local pier-scour [*Hong et al.*, 2016].

Therefore, completely understanding bedforms and bedform dynamics in rivers in changing flows is important for a wide range of interdisciplinary scientists including geomorphologists, sedimentologists, and hydraulic engineers to implement further research.

1.2. Rationale

It has long been highlighted that important feedbacks exist between the turbulent flow field, river bed morphology, and sediment transport [*Van Rijn*, 1993; *Leeder*, 2009; *Parsons and Best*, 2013], and that these feedbacks change in response to forcing mechanisms [*Naqshband et al.*, 2014c; *Naqshband et al.*, 2017]. Over the past century, a large number of scholars have conducted their research on bedforms (ripples, dunes, sandwaves and bars, which are the major roughness elements in rivers and estuaries) via sophisticated and quantitative laboratory methods [*Nelson and Smith*, 1989; *Bennett and Best*, 1995; *Maddux et al.*, 2003a; *Martin and Jerolmack*, 2013; *Schindler et al.*, 2015], field surveys [*Carling et al.*, 2000a; *Fredsøe*, 2005; *Kostaschuk et al.*, 2005; *Parsons et al.*, 2005; *Coleman and Nikora*, 2011; *Bradley et al.*, 2013; *Hendershot*, 2014] and numerical models [*Paarlberg et al.*, 2008; *Shimizu et al.*, 2009; *Nelson et al.*, 2010; *Nabi et al.*, 2013a; *Schmeeckle*, 2015]. However, almost all of these developed models assume the steady uniform flow conditions and determine a bed equilibrium using empirical or weakly non-linear formulations [*Van Rijn*, 1984b; *Kleinhans*, 2005a; *Edmonds and Slingerland*, 2010], while, in fact, all fluvial and estuarine circumstances display temporal variations in flow discharge and water level, creating a range of unsteadiness scales [*Martin and Jerolmack*, 2013; *Unsworth*, 2015]. Furthermore, our knowledge of the well-known bedform-flow unsteadiness hysteresis is currently only understood empirically [*Martin and Jerolmack*, 2013], but our ability to predict river behaviour is critically dependent on the accurate examination of flow resistance [*Wilbers*, 2004]. Thus, fundamental questions about the co-evolution of hydrodynamics and bedforms remain unsolved and there is no universal explanation for the development and response of bedforms to unsteady flows [*Best*, 2005a; *Venditti*, 2013].

Additionally, the formation of bedforms could cause dramatic changes in the bedload transport rate [*Gomez and Church*, 1989; *Gomez*, 1991], and can dominate the suspended sediment transport by bed-related macroturbulence [*Kostaschuk and Church*, 1993; *Kwoll et al.*, 2016; *Kwoll et al.*, 2017]. A systematic, quantitative investigation of flow and sediment dynamics during bedform adaptation to unsteady flows is thus needed to establish fully the criteria that are necessary to define temporal and spatial variability-response in bedform roughness and form drag.

The complex interactions between bedforms to flow field changes over time, including superimposition [*Venditti et al.*, 2005a; *Winter et al.*, 2008; *Reesink and Bridge*, 2011], splitting [*Gabel*, 1993; *Jerolmack and Mohrig*, 2005; *Warmink et al.*, 2014], amalgamation [*Reesink and Bridge*, 2007; *Reesink and Bridge*, 2009; *Best et al.*, 2013], and pass through [*Martin and Jerolmack*, 2013; *Warmink*, 2014] are well recognised during bedform migration and cause the various phase lags in response to the changing flows. However, exactly how?, by how much?, and critically, at what rate? Bedforms respond currently remains un-quantified [*Best*, 2005a; *Parsons and Best*, 2013]. Thus, the incorporation of these dynamically-evolving processes is key to better quantify the spatio-temporal evolution of roughness in response to changes in flow [*Parsons and Best*, 2013].

1.3. Aims and objectives

This study seeks to improve our basic understanding of the links between the flow and sediment dynamics and dune morphology under unsteady flows and to generate a quantitative understanding of the morphodynamical processes responsible for bedform adjustment to unsteady flows. This aim will be achieved via a comprehensive investigation that combines deployment of recently established state-of-the-art methods in both the laboratory and field. With flume experiments, it is easier to establish condition-controllable experiments to investigate the effect of different conditions on dune dynamics under unsteady flows. However, the effect of tides on dune dynamics is hard to be simulated in a flume experiment, therefore, field measurements were adopted here to investigate how would the tides influence dune dynamics. The combination of laboratory and field investigation gives us a whole view on dune dynamics from unidirectional fluvial rivers and bidirectional tidal areas. These developments will provide fundamental knowledge that is of significance for a wide variety of purposes, such as improving morphodynamic modelling over large spatio-temporal scales, environmental and engineering management, and more reliable flood predictions.

1.3.1. Flume experiments

The vast majority of research on dunes via flume experiments is based on fixed beds, which is easier to achieve and measure, but it ignores the movable bed effects, resulting in discrepancies between flume results and field observations [*Grant and Madsen*, 1982; *Naqshband*, 2014; *Naqshband et al.*, 2014b]. For example, the ratio of the bedload to suspended load discharge is known to vary as flow changes and has the potential to alter flow separation [Baas et al., 2009], subsequently influencing both the shape of the dune and flow structure near bed [*Naqshband et al.*, 2014b]. The principal aim of the present investigation is, therefore, to quantify the morphology, flow fields, concurrent sediment transport and topographic change over mobile beds under a range of unsteady flow conditions; and thus, identify the dynamic interactions between the flow, sediment transport, and the bed morphology in response to change.

Herein, the following set of research questions are addressed:

1) *What is the first-order factor in controlling dune size in different flow stages?*

Numerous researches have been done on building relationships between flow conditions and dune characteristics (e.g. [*Yalin*, 1964; *Allen*, 1982]), but latest research [*Bradley and Venditti*, 2017] has compiled all available published dune dimensions from a range of rivers and showed that dune size was poorly predicted by those pervasively adopted scaling relations [*Bradley and Venditti*, 2019]. The poor understanding of the factors influencing dune size and dune adaptation to certain flow conditions limits our ability on accurately predicting dune dimensions and shapes.

Increasing evidence [*Naqshband et al.*, 2014a; *Venditti et al.*, 2016; *Reesink et al.*, 2018] shows that dunes are inherently variable even under given stable flow conditions. Moreover, all fluvial and estuarine circumstances display temporal variations in flow discharge and water level, creating a range of unsteadiness scales [*Martin and Jerolmack,* 2013*; Unsworth,* 2015]. The dual variables undoubtedly further complicate our understanding on dune dimension prediction.

Recent research [*Reesink et al.*, 2018] shows that it is sediment transport and redistribution that ultimately drive the translation and deformation of dunes. This highlights that the understanding of sediment transport and redistribution under different flow stages is the key to improve the prediction of dune size and shape.

Therefore, the flume experiments were set up under different transport conditions at different flow depths to explore how dunes adapt to designed changing flows.

2) *What controls the differences of dune 3D texture?*

Current understanding of dune evolution on changing flows remains on two-dimensional (2D) pattern. However, *Venditti et al.* [2005a] suggested that all dune bedforms must eventually become three-dimensional, due to minor, transient excesses or deficiencies of sand being passed from one bedform to another. Very little attention has been given to the dynamics of pattern evolution [*Friedrich*, 2010], while non-uniform heights, lengths and spacings, and highly sinuous crestlines of 3D dunes have significant effect on sediment transport and evolution of the planimetric morphology of dunes [*Venditti*, 2013].

Translation and deformation are two basic types of manifestations of dune evolution and they reflect how sediment transport affects dune migration and deforamtion [McElroy and Mohrig, 2009]. The variable speed of translation and deformation along the crestlines leads to the merging and splitting of dunes [*Hendershot et al.*, 2018]. However, majority of the work on sediment transport associated with dune adaptation under changing flows has focused on the translational component [*Venditti et al., 2016; Hendershot et al.*, 2018], while few research [*Venditti et al.*, 2016] explored the effect of the deformation on dune evolution. Therefore, for further understanding dune adaptation under unsteady flows, it is key to investigate what controls the differences of dune 3D texture during their evolution.

3) *How do dunes initiate from a roughly flatbed under different flow conditions?*

The typical sequence of bedforms in alluvial channels, growing from flatbed to ripples and developing to anti-dunes with increasing flow strength under low flow regime [*Venditti*, 2003; *Best*, 2005]. When the flow strength near bed exceeds the threshold for forcing the bed material to move, bedforms generate. Linear stability analysis, involving analysis of both fluid and sediment over an infinitesimally small bed perturbation or defect, is the pervasive theory for the generation of bedforms [*Venditti et al.*, 2005b].

Most work of bedform initiation has been focused on flatbed without defects [*Williams and Kemp*, 1971; *Coleman and Melville*, 1996; *Coleman and Nikora*, 2011], while recent work has proved that defects play a significant role on bedform initiation [*Venditti et al.*, 2005b]. The bed surface in natural rivers and estuaries cannot be ideally flat, therefore, it is necessary to further understand how bedforms generate and develop under roughly flatbed, where defects, mounds or pits exist in the initial bed.

In fact, it is the movement of bed material resulting in the bedform generation and development, while flow strength is the factor driving the movement. Different intensities of flow strength lead to different manifestations of bed material movement: sliding, rolling, jumping or suspension (i.e. different particle step length) [*Paarlberg et al.*, 2007; *Paarlberg et al.*, 2008; *Duin et al.*, 2012], and they result in distinct development of bedforms [*Venditti*, 2003; *Van Rijn*, 2007]. However, current work [*Venditti*, 2003; *Venditti et al.*, 2005b; *Coleman and Nikora*, 2011] on bedform initiation has been concentrated on low flow strength, and few attention has been given on effect of different flow conditions on dune initiation.

In summary, investigation on bedform initiation from a roughly flatbed under different flow conditions is necessary to fully understand bedform initiation and development, and its result has significant implications for advancing numerical models.

4) *How do dunes adapt to changes in hydraulic condition?*
5) *How does sediment transport affect dune adaptation?*

In fluvial environments, a flood event with flash change in hydraulic condition are the important factor that dramatically changes flow and sediment-transport dynamics, thereby changes bed morphology (ef. bedforms), within a short period [*Julien and*

Klaassen, 1995; *Amsler et al.*, 1997; *Paarlberg et al.*, 2008]. The 'morphodynamic' feedback between the flow, sediment transport, and bedform morphology is controlling dune evolution.

Most work (e.g. [*Martin and Jerolmack*, 2013; *Warmink et al.*, 2014]) has revealed that dune growth or decay attributes to dune merging, cannibalization, split, while little is unknow about the precise mechanisms of dune adaptation related to the adaption of sediment transport to changes in hydraulic condition [*Reesink et al.*, 2018].

Furthermore, dune development and dynamics can affect infrastructure [Amsler and Schreider, 1999], the development of cross-strata [Reesink and Bridge, 2009; Reesink et al., 2015], and even leads to the extra water level increase during a flood [Reesink et al., 2018]. Thus, completely understanding bedforms and bedform dynamics in rivers under changing flows is important for a wide range of interdisciplinary scientists including geomorphologists, sedimentologists, and hydraulic engineers to implement further research.

1.3.2. Fieldwork survey

As dune dynamics in a tidal area can be affected by various factors across a range of temporal scales, such as changes in both flow strength and water level along with alterations in sediment supply across tides and seasons. The time scale is generally the significant issue for the simulation in flume experiments. Thus, the effective and common approach to investigate dune dynamics in tidally influenced areas is through direct field observation. With the development of advanced equipment, increasingly detailed and intensive measurements are accessible in the field. For example, the multibeam sonars (MBESs) provide the opportunity to collect high-resolution 3D bathymetry [*Parsons et al.*, 2005], and the acoustic Doppler current profiles (aDcps) allow us to rapidly and accurately characterise the spatio-temporal flow structure in various types of water bodies.

Hence, the field surveys reported herein, with the state-of-the-art instruments, will address these additional research questions:

6) *How do compound bedforms form and what controls the distribution of superimposed small dunes in a tidal area?*
7) *How does the hydraulic condition affect roughness and development of compound dunes?*

Compound bedforms are commonly found existing in both unidirectionally and bidirectionally fluvial environments [*Bartholdy et al.*, 2002; *Van Dijk and Kleinhans*, 2005; *Lefebvre et al.*, 2011; 2013]. In tidal influenced areas, the superimposed bedforms are recognized as tide driven forms, and their shapes could reverse by the changing of flow direction from ebb to flood tide. In contrast, the primary bedforms stay ebb-oriented throughout the tidal cycle. They are generally recognized to be equilibrium with the flow condition during the ebb tide, if their less slop is close to angle-of-repose [*Lefebvre et al.*, 2013]. However, in unidirectionally fluvial environments, the secondary bedforms are revealed to be induced by current flows, while the host large bedforms are the relicts of large dunes generated during the earlier freshet flows [*Carling et al.*, 2000b]. Little attention has been paid on compound bedforms within areas between tidal boundary and tidal current boundary where water level increases and decreases along with tides, but flow direction keeps ebb oriented [*Chen et al.*, 2012].

The bed roughness (i.e. flow resistance) is a fundamental parameter in the understanding and simulation of hydro- and sediment- dynamics in a river and coastal area in numerical models, such as flood predictors, and form roughness is related to the dimension, shape, and spacing of the bedforms [*Lefebvre et al.*, 2016; *Lefebvre and Winter*, 2016b]. Thus, understanding why and how the compound bedforms form is very important for the accurate estimation of bedform roughness. Moreover, compared with the primary dunes, the secondary bedforms paly a much more significant role on sediment transport and bed roughness, therefore, further understanding on characteristics of secondary bedforms is needed.

8) *How do low-angle dunes evolve in beds with clay contained within a tidal cycle?*

Growing evidence from field observations suggests that symmetrical dunes with smaller lee-side angles (i.e. low-angle dunes, LADs, generally less than 10° [Paarlberg et al., 2009]) are the prominent bedforms in tidally influenced, suspended sediment dominated, sand-bedded rivers and estuaries [Smith and McLean, 1977; Kostaschuk and Villard, 1996; Carling et al., 2000a; Best and Kostaschuk, 2002; Kwoll et al., 2016;

Lefebvre and Winter, 2016a]. Most of the existing research of dune morphodynamics has focused on non-cohesive bed conditions where median grain size D_{50} is larger than 150 µm [Field et al., 1981; Németh et al., 2006] and the classic bedform stability diagram proposed by Allen [1985] is established based on cohesionless sediments. However, recent studies have highlighted the effect of cohesive material, or ‘’sticky stuff’’ (mud, clay and microorganisms, i.e. cohesive bed) on bedform geometry and dynamics, indicating that present bedform phase diagrams and predictors are overly simplistic [Malarkey et al., 2015; Schindler et al., 2015; Baas et al., 2016; Parsons et al., 2016]. Previous research observed that various scales of dunes existed in beds with clay contained, for example, the Changjiang (Yangtze) Estuary [Cheng et al., 2001; Wu et al., 2009]. However, their studies have mainly focussed on classifying their geometric characteristics [Li et al., 2003; Cheng et al., 2004; Shuwei et al., 2017] or exploring how to predict bedload transport rate based on dune migration [Yang et al., 1999], while how these LADs evolve under this specific condition has been rarely studied. Thus, further understanding of bedform dynamics in large tidal environments composed of fine bed materials is needed to be enriched.

1.4. Research Approach

To meet the above-mentioned aims and address the research questions, a series of large flume experiments were conducted in a large recirculating flume and three field surveys were made in the Changjiang (Yangtze) estuary: two in the middle reach and one near the river mouth.

1.4.1. Flume experiments

Experiments were undertaken at the University of Hull's Total Environment Simulator (TES) flume/wave tank facility. Within the laboratory experiments, the development and dynamics of bedforms under a series of changing flows have been investigated. Flow changes were designed according to six different flow conditions (including two water depths and three flow velocities), called “basic states.” Based on these basic states, a total of 19 individual runs were conducted across the three different series of experiments: i) 6 “basic” runs (BAS) with constant flow conditions, each run for ~6 hours; ii) a suite of 5 “sudden change” runs (SUD) with rapid hydraulic condition changes between the basic states again run for ~6 hours; and, iii) 8 “flood wave” runs (FLD), with fast (F) and slow (S) hydraulic condition changes between the basic states and back to the initial condition (details for each experiment are provided in Appendix A). For the “flood wave” (FLD) series under gradual change, the time period of the rising limb for the fast and slow wave was set to 72 and 153 minutes, while that of the falling limb was set to 63 and 207 minutes, respectively. Both rising and falling limbs were divided into 16 equal time steps.

Twelve Ultrasonic Sensors (URSs) were mounted a rack orthogonal to the flow on a Stebon^{TM} 4.5 m robotic traverse and they were swept upstream and downstream automatically every 2.3 minutes to measure the bed elevation and dune morphology and its change over time. Water surface slope was measured along the channel at 2 Hz by 8 wave rods (HR Wallingford WG8 Twin-wire wave rod system), spaced 1 m apart along the channel. Five fixed Nortek ADVs were installed in order to measure flow velocities: one was installed in the upstream set at 40% of the water depth from the bed and the other four were installed in an instrument box within the test section. Finally, a three frequency Acoustic Backscatter Sensor (ABS) was installed in the instrument box to monitor suspended sediment transport. Full details of the experimental set-up are provided in Chapter 3 and 4.

1.4.2. Fieldwork study

A series of three field campaigns were conducted within the Changjiang (Yangtze) River and Estuary, to explore the impact of changing flow conditions on bedform response. Two surveys were conducted near the limit of the backwater zone, one during the wet season and one during the dry season. An additional field campaign was conducted within the estuary zone near the river mouth in order to explore the increasing influence of the tidal currents on bedform responses.

A Reson Seabat 7125 Multibeam Echo-Sounder (MBES) was employed to record three-dimensional (3D) bathymetry for the surveys in the middle reach of the Changjiang Estuary, while a single beam Inner Space 24 kHz Thermal Depth Recorder (449M) was used to record bathymetry in the river mouth surveys. The multibeam sonar system was configured for 512 beams operating in the equi-distance mode at the frequency of 400 kHz, and a 150° wide swath was obtained perpendicular to the vessel track. The maximum ping rate is 50 Hz (±1 Hz), and the highest theoretical depth resolution can reach 6 mm [*RESON*, 2007]. Heave, pitch and roll (representing navigation, orientation, and attitude data) were recorded using an Applanix POS MV V3 gyroscope inertial guidance system mounted inside the vessel and was set to the origin of the coordinates.

Simultaneously, a Teledyne RD Instruments 600 kHz Rio Grande Workhorse acoustic Doppler current profiler (aDcp) was used to quantify the 3D flow velocities throughout a vertical water column over each longitudinal survey section. Boat position were measured by using the Trimble real-time differential global positioning system (DGPS), tied to a local navigation beacon with sub-meter accuracy (typically ~0.3 m). Moreover, water samples through the water column were collected in order to calibrate suspended sediment concentration for aDcp backscatter intensity. Several riverbed samples were also collected by a grab sampler and were further analysed in the laboratory. Full details of the field surveys are provided in Chapter 5, 6, and 7.

1.5. Thesis structure

The main research questions will be answered in the following five chapters of the thesis:

Chapter 2 contains an extensive literature review concerning river dune dynamics, and flow field unsteadiness relevant to the present study.

Chapter 3 and **Chapter 4** concentrate on reporting bedform dynamics based on flume experiments in order to investigate dune development during floods. **Chapter 3** overviews all the data and describes how dunes adapt to changing flows on morphology across the suite of experiments. **Chapter 4** focuses on three specific experiments in more detail where detailed morphodynamics and sediment transport before, during and after flow wave passages are examined, and the impact of hysteresis effects are investigated.

Chapter 5, Chapter 6 and Chapter 7 focus on bedform dynamics based on fieldwork in the Changjiang (Yangtze) River. **Chapter 5** and **Chapter 6** report the results of two fieldwork seasons conducted in the middle reach of the Changjiang Estuary, near the backwater limit, where the tidal influence is relatively weak. The former chapter explores the bedform morphodynamics, while the latter presents the flow and sediment dynamics. **Chapter 7** describes the results of fieldwork conducted in the lower reach of the Changjiang Estuary near the river mouth, where the tidal influence is relatively stronger. This chapter specifically identifies low-angle dunes and their evolution within a tidal cycle.

Chapter 8 gives an overview and synthesis of the main findings derived from this work together with identifying future challenges. The original main research questions are explored, and it is shown how they have been addressed. Furthermore, recommendations about possible directions for future research are proposed.

CHAPTER 2

2. Literature Review

2.1. Roughness and flow resistance

2.1.1. Introduction

Surface roughness is created by the ubiquitous presence of bedforms in most alluvial systems, and consequently influences flow-form processes. As half of the earth's surface is drained by the world's largest rivers [Ashworth and Lewin, 2012], roughness related to flow resistance is crucial in predicting flood flows to longer-term system evolution. Figure 2-1 displays recognition of the distinction between three types of "roughnesses" and their definition which will be applied herein.

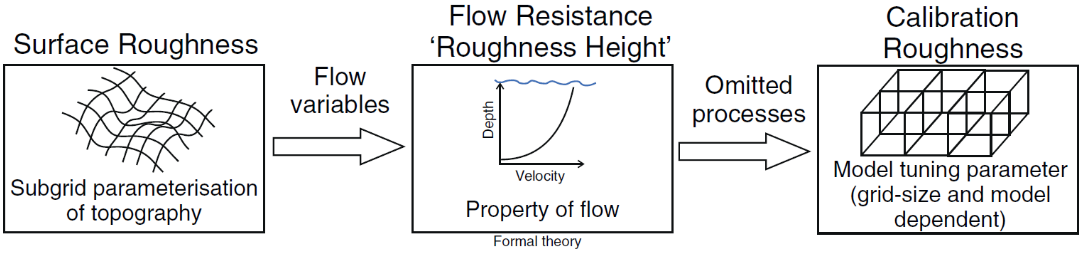

Figure 2-1. Definitions of roughness in Earth Science (from Smith [2014]).

The variation of river stage for a given discharge is related to the generation and development of roughness elements of underwater topography (ripples, dunes, and sandbars). The complicated hydrodynamics induced by roughness elements results in the generation and distribution of near-bed shear stresses and turbulence [*Best*, 2005a]. As a result, roughness governs functional relationships between hydrology and sediment transport [*Smith*, 2014].

The bed roughness (i.e. flow resistance) is a fundamental parameter in the understanding and simulation of hydro- and sediment- dynamics in a river and coastal area in numerical models, such as flood predictors (e.g. [*Morvan et al.*, 2008]). For a given boundary surface, the "energy losses" resulting in "flow resistance" is caused by the near bottom turbulence and the macro-flow structures within a prescribed channel reach [*Morvan et al.*, 2008]. According to the scales, flow resistance (i.e. boundary shear stress components) is traditionally divided into five distinct types associated with roughness elements: grain resistance (i.e. Nikuradse roughness related to the individual grain of the surface channel bed, representing skin drag), bedload resistance (sediment movement roughness which refers to momentum transfer in particle entrainment), bedform resistance (form roughness which attributes to bedforms such as ripples and dunes, representing form drag), bar resistance and bank and planform resistance (e.g. roughness associated with overall channel shape, bends and meanders) [*Dietrich and Whiting*, 1989; *Morvan et al.*, 2008]. As the grain scale roughness is usually very small in most natural flows, it is often neglected [*Kostaschuk et al.*, 2004]. Thus, at the sub-reach scale, form roughness is widely recognised as the main form of dissipative flow resistance [*Venditti*, 2013]. Grain roughness (k_{sg}), which is also called sand roughness, can be a dominant component of the bed roughness when stream beds consist of gravel or cobbles. As sand roughness is representative in its impact on the flow [*Van Rijn*, 1984a], the 50%, 84%, or 90% grain size (D_{50}, D_{84}, or D_{90}, respectively) is generally used as a representative diameter of the grains in calculation [*Kamphuis*, 1974; *Hey*, 1979; *Van Rijn*, 1984b]. The coefficients used to calculate roughness are various ($k_{sg} = nD_i$). *Van Rijn* [1982] concluded that k_{sg} is to be within the range of $1.25D_{35} < k_{sg} < 5.1D_{84}$, highly dependent on the characteristics of bed material and local bed condition [*Van Rijn*, 1984b], while in some other research, the differences between various bed materials can reach two orders of magnitude [*Clifford et al.*, 1992; *Wilcock*, 1996]. *Millar* [1999], however, found that there was no significant discrepancy between these various representative grain sizes, and attributed this to the presence of larger scale bedform roughness in gravel beds, such as clusters.

The common approach to studying flow resistance is to establish flume-scaled experiments, produce empirical formulas, and validate these with field data. Abundant research has been carried out to estimate bed roughness over bedforms through flume experiments, fieldwork, and numerical models [*Rauen et al.*, 2009; *Smith et al.*, 2011;

Guerrero and Lamberti, 2013; *Lefebvre et al.*, 2013a]. *Van Rijn* [1984b] presented a method to predict the effective hydraulic roughness of bedforms in sandy beds using approximately 1500 sets of field and flume data. Subsequently, *Yang et al.* [2005] investigated the mechanism of flow resistance over bedforms according to the published data (both flume and field). Both results show that the grain roughness is a function of the median diameter (D_{50}) of the bed material (sand beds), which is equal to 2 times.

A number of studies have been performed to estimate roughness over bedforms by fieldwork [*Dyer*, 1971; *Grant and Madsen*, 1982; *Chriss and Caldwell*, 1987; *Raudkivi*, 1988; *Williams*, 1995; *Villard and Kostaschuk*, 1998; *Best*, 2005a; *Lefebvre et al.*, 2011b; 2013a; *Venditti*, 2013], flume experiments [*Yang et al.*, 2005] and numerical models [*Rauen et al.*, 2009; *Smith et al.*, 2011; *Guerrero and Lamberti*, 2013; *Lefebvre et al.*, 2013a; *Lefebvre et al.*, 2014a; *Lefebvre et al.*, 2014b]. Form roughness creates form drag due to flow separation, resulting in the pressure differential, especially over the lee-sides of the topographic elements, having a steeper slope than stoss-sides. As form roughness related to the dimension, shape, and spacing of the bedforms [*Nelson et al.*, 1993; *Best*, 2005a; *Allen*, 2009], generally, we assume that the variation of bedforms with changing flow strength leads to the change of form roughness [*Lefebvre et al.*, 2011a; *Lefebvre et al.*, 2013a; *Lefebvre et al.*, 2013b; *Kwoll et al.*, 2014]. Furthermore, by making an analogy between grain and form roughness, form roughness may also be determined by bedforms that are higher, longer, or steeper than the median or mean bedform height, bedform length, or bedform steepness, respectively [*van der Mark et al.*, 2008], because their effect on flow structure is different [*Kwoll et al.*, 2016; *Lefebvre et al.*, 2016; *Lefebvre and Winter*, 2016b; *Kwoll et al.*, 2017].

The partition between grain and form drag is crucial to comprehend physically-based mechanisms, and some models are relatively sensitive to parameterization of form roughness [*Lane et al.*, 1999; *Lane et al.*, 2004; *Kean and Smith*, 2006; *Sandbach et al.*, 2012]. The presence of bedforms alters the local hydrodynamics, resulting in the production of an overall enhancement in the spatially-averaged bed shear stress [*Smith and McLean*, 1977].

Bedload transport is widely recognised to be highly sensitive to the ‘local’ skin friction [*Villaret et al.*, 2011], thus, whether the result of a model is satisfactory or not, highly depends on the accuracy of bed roughness calculated or input [*Davies and Robins*, 2017]. Moreover, recently, some scholars (e.g. [*Parsons et al.*, 2007; *Ashworth and Lewin*, 2012]) have observed that roughness elements, in the form of sand dunes, can have large effects on secondary circulation patterns in large rivers. Coherent, channel-scale, secondary flow cells have been recognised as important aspects of hydrodynamics within small channels, and supposed to be present in large rivers [*Parsons et al.*, 2007]. Such observations highlight that there still needs further research on the investigation of bed roughness effects, especially in large rivers and estuaries [*Parsons and Best*, 2013].

2.1.2. Approaches used to estimate roughness

Three classic methods for estimating roughness exist and are based on semi-empirical formulae [*Chezy*, 1768; *Weisbach*, 1845; *Manning et al.*, 1890], rather than derived from rigorous physics. They are traditional approaches to calculate reach-scale flow resistance with known water slope and some of their variables (e.g. *f* and *n*) which are adjusted to account for channel's energy losses [*Ferguson*, 2013]. However, water surface slope is often difficult to measure accurately, particularly in large rivers and estuaries, particularly under unsteady flow conditions [*Villard and Kostaschuk*, 1998; *Kostaschuk et al.*, 2004].

In contrast, "the Law of the Wall" is a physics-based approach to calculate resistance and the roughness height k_s is related to measurable properties of riverbeds [*Ferguson*, 2013]. In hydraulic fields, 'roughness height' is often regarded as a surrogate of 'flow resistance', especially, when bedforms highly influence the local flow patterns [*Smith and McLean*, 1977]. In this sense, however, k_s is a characteristic of the flow rather than of the surface, and the distinction between them is rare, and also hard to be made clear [*Smith*, 2014].

The von Kármán-Prandtl Law of the Wall (i.e. log-fit method [*You*, 2005], Equation 1-1) is a function of velocities through the water column. Until relatively recent, current meters, which need to be spaced at logarithmically increasing intervals above the bed, are utlised to collect velocity data in the filed [*Dyer*, 1971]. Based on these data, it was concluded that variation in the position of the array over the dune form could contribute to the change of roughness length [*Dyer*, 1971]. With the development of velocity measuring technology, continuous current speed profiles are now attainable [*Chriss and Caldwell*, 1987; *Kostaschuk and Villard*, 1996; *Lefebvre et al.*, 2011b] via acoustic Doppler current profilers (aDcps) for field investigation, and the time-averaged velocity profile is found to ideally display a logarithmic distribution above the bed [*Lefebvre et al.*, 2013a].

$$u(z) = \frac{u_*}{\kappa}\ln\left(\frac{z}{z_0}\right) = \frac{1}{\kappa}ln\left(\frac{30z}{k_s}\right) \qquad 2\text{-}1$$

where u is the time-averaged current velocity at the height z above the bed; u_* is shear velocity and z_0 (height z at where velocity is zero) is the roughness length, and κ is the von Kármán constant (0.41). According to experiments in pipes, z_0 equals to $0.11(\nu/u_*) + 0.03k_s$ [*Van Rijn*, 1984b], which was approximately $k_s/30$ (k_s = equivalent roughness height of Nikuradse) for rough flow [*Nikuradse*, 1950].

The “roughness height” and “roughness length” are commonly confusedly used in some literature. Here we define the momentum roughness length as z_0, as it is a length scale that characterizes the momentum loss, while roughness height as k_s.

The “Law of the Wall” allows an indirect estimation of hydraulic roughness through the roughness length, which defines the frictional force that the bed exerts on the flow [*Smith and McLean*, 1977]. One of the essential conditions required by the log-fit method is that the measured mean velocity profile must be logarithmic. However, such a condition is not always met in estuarine systems or large rivers. *You* [2005] developed a new method to estimate bed roughness from time series of mean velocities collected at only two levels near the bed. He concluded that this new method is more satisfactory in strong tidal currents, and also superior to the traditional log-fit method in terms of the number of current metres required and the accuracy of k_s estimated.

Another method widely used in computing roughness is directly from bedform dimensions (e.g. [*Van Rijn*, 1984b; *Bartholdy et al.*, 2010a; *Bartholdy et al.*, 2010b]). Bedform height (H) and wavelength (L) are convinced to be two main physical parameters used to estimate roughness length (z_0) or roughness height (k_s) from the aspect of bedforms’ characteristics (Table 2-1) and *Soulsby* [1997] generalised the universal expression:

$$z_0 = a_b \frac{H^2}{L} \tag{2-2}$$

The wide range of a_b in equation 2-2 may attribute to the lack of knowledge on the effect of other parameters on the roughness length, for example, the bedform shape [*Ganju and Sherwood*, 2010; *Kwoll et al.*, 2016; *Lefebvre et al.*, 2016].

These formulae are generally calibrated on equilibrium data of non-tidal rivers, but for an unsteady flow, the influence of change through time needs to be taken into account. Unlike rivers, bedform dimensions adapt to the changing discharge during floods and tides, the continuous variation in flow strength and direction results in the concomitant variation in roughness length [*Lefebvre et al.*, 2011b; *Lefebvre et al.*, 2013b].

Table 2-1. Some bedform roughness predictors (from Lefebvre et al. [2011b]).

Authors	Validity	Expression
Swart (1976)	Wave-formed ripples	$z_0 = 0.83 \frac{H^2}{L}$
Grant and Madsen (1982)	Wave-formed ripples under oscillatory flow or combined waves and currents	$z_0 = 0.92 \frac{H^2}{L}$
Nielsen (1992)	Roughness of rippled bed under waves	$z_0 = 0.27 \frac{H^2}{L}$
Soulsby (1997)	Generalization of previous equations	$z_0 = a_b \frac{H^2}{L}$ and $a_b = 1$
Van Rijn (1984)	Ripples, dunes and large dunes $0.01 < H/L < 0.2$	$z_0 = 0.04H (1 - e^{-25H/L})$
Bartholdy et al. (2010)	Dunes under currents	$z_0 = 0.019H$

2.1.3. Log-linear segments of velocity profiles

Velocity profiles consisting of two logarithmic-profile regions (lower and upper ones respectively) were firstly identified in the field by *Chriss and Caldwell* [1987], and they concluded that the stress estimated from the upper one presents the impact of bedform drag which is more than 4 times of the bed stress determined from the viscous sublayer. *Villard and Kostaschuk* [1998], however, concluded that the upper segment reflects the total stress of the flow.

In large rivers, dunes are generally superimposed by small-scale bedforms (ripples or mega-ripples), which could also impact the flow resistance [*Smith and McLean*, 1977; *Dalrymple and Rhodes*, 1995; *Villard and Kostaschuk*, 1998; *Lefebvre et al.*, 2011b;

2013a]. *Lefebvre et al.* [2013a] made a summary and displayed a schematization of a velocity profile over a bed with superimposed bedforms. The increase of velocity as described by the "Law of the Wall" is composed of several log-linear segments and each one relates to the friction induced by one scale of roughness, representing a hierarchy of boundary layers (Figure 2-2). Boundary layer characteristics can be calculated from the best-fit applied on the log-linear segments: the shear velocity is related to the slope of the best-fit line, and the roughness length to its y-intercept [*Lefebvre et al.*, 2013a].

When there exist several roughness elements, the total physical current-related form roughness height (k_{sbf}) of bedforms is calculated by quadratic summation [*Van Rijn*, 2007]:

$$k_{sbf} = \sqrt{{k_{sr}}^2 + {k_{smr}}^2 + {k_{sd}}^2} \qquad 2\text{-}3$$

where k_{sr} is ripple-related roughness, k_{smr} is mega-ripple-related roughness and k_{sd} is dune-related roughness. However, the total roughness combines k_{sbf} and k_{sg} linearly (Equation 1-4, *Villaret et al.* [2011]):

$$k_s = k_{sbf} + k_{sg} \qquad 2\text{-}4$$

This formula is still the most efficient for the lower alluvial regime (ripples and dunes, when *Fr* < 1) [*Huybrechts et al.*, 2011; *McCann et al.*, 2011; *Villaret et al.*, 2011].

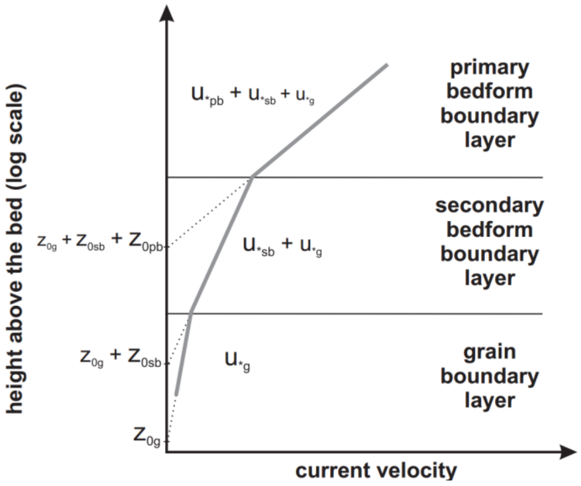

Figure 2-2. Schematisation of a velocity profile over a bed with compound bedforms. The velocity profile is made up of different boundary layers controlling the different log-linear segments (from Lefebvre et al. [2013a]).

2.1.4. Impact factors on form roughness

Flow resistance is highly related to the turbulence near the riverbed [*Morvan et al.*, 2008]. The topography of riverbed has a vital impact attributing to various behaviours of local turbulence. Thus, some research has compared the differences between two types of dunes: (1) symmetric bedforms (low-angle bedforms), which are approximately sinusoidal [*Kostaschuk and Villard*, 1996; *Best and Kostaschuk*, 2002]; (2) asymmetric bedforms (angle-of-repose bedforms), which are roughly wedge-shaped, with a higher angle in the lee side (nearly 30 degrees) than the stoss side.

Villard and Kostaschuk [1998] concluded that the lower segment on symmetric dunes reflects skin friction, but for asymmetric dunes, it is skin friction plus form roughness from the superimposed dunes. Besides, the corresponding characteristics of flow separation is another impact which also plays a crucial role in hydraulic roughness, flow structure and sediment transport, as turbulence, related to flow separation, generating above lee side, is responsible for the form shear stress which can represent a substantial part of total shear stress in rivers [*Best and Kostaschuk*, 2002; *Paarlberg et al.*, 2007; 2009; *Lefebvre et al.*, 2014b].

According to previous field investigations [*Smith and McLean*, 1977; *McLean and Smith*, 1979; *Kostaschuk and Villard*, 1996; *Roden*, 1998; *Kostaschuk and Villard*, 1999; *Carling et al.*, 2005; *Kostaschuk and Best*, 2005], 10° and 18° are the two main thresholds for lee-side angle (α): when $\alpha < 10°$, there is no flow separation occurred; when $\alpha > 18°$, permanent recirculating flow generates; when $10° < \alpha < 18°$, intermittent flow separation expects to be present. However, due to the limitation of equipment in detecting near bottom processes of hydrodynamics and sediment transport in the field [*Wilbers*, 2004], the exactly accurate thresholds should be further investigated in the future.

Lefebvre et al. [2014b] used the Delft3D model to investigate bedform hydraulic roughness over angle-of-repose bedforms under unidirectional flow condition. Form shear stress was found not to scale with the size of the flow separation zone but related to the product of the normalised extent of the wake region (extent of the wake region/extent of water body above the bedforms) and the average TKE within the wake region.

Additionally, some other scholars have investigated the relationships between roughness and some other aspects of the bed and flow field. *van der Mark et al.* [2008] designed a laboratory experiment concerning the impact of variability in bedform geometry on form roughness and made comparisons between form roughness and grain roughness, which was also done by *Petit* [1989]. *Tuijnder and Ribberink* [2009] investigated the bed roughness by controlling dune dimension and the exposure of the usually coarser immobile layer. *Rauen et al.* [2009] researched the bed roughness according to quantify the bedform development. As a result, the changes of the bed roughness, from the flatbed state to the final stage when ripples were developed, spanned two orders of magnitude, and this variation was independent of the flow and sediment transport conditions. *Smith et al.* [2011] used means of the SWAN model to investigate the significant loss of wave energy caused by the formation of bottom ripples and the grain size of the sediment. The improved model can be used to predict both the wave height and period. *Guerrero and Lamberti* [2013] combined aDcp and single-beam echo-sounder (SBES) to determine the river channel bed-roughness and argued the relationship between the roughness and the bedforms. Then, the logarithmic formula that connects the total Chezy parameter to the ratio of the water-depth to dune-amplitude was produced. Consequently, the numerical model MIKE21C was introduced to focus on generalizing the morphodynamic processes.

Most of these studies outlined above are conducted under or treated as steady and unidirectional flow conditions, except that *Grant and Madsen* [1982] established a model to predict the roughness in unsteady oscillatory flows over movable, non-cohesive beds. The roughness over mobile beds was showed to be a function of the boundary shear stress, rather than the constant geometric scale. The result of total roughness showed that when bedforms were present, they contributed to a remarkable portion of the boundary roughness.

However, very few research studies have focused on estimating quantitative variation of bed roughness influenced by bedforms in tidal conditions, as it is quite difficult to carry out the measurements in the field due to time limitations and varying flows and flume experiments, due to scaling tidal waves [*Williams*, 1995; *Lefebvre et al.*, 2011b; 2013a; *Lefebvre et al.*, 2014a; *Lefebvre et al.*, 2014b].

In tidal flow conditions, *Williams* [1995] presented that as the presence of asymmetry sand waves, it showed a smaller drag coefficient during the flood tides than that during the ebb tides. Variation of drag coefficient over sand waves during the whole tidal cycle was found to be little, which means asymmetry of bedforms has no detectable effect. Otherwise, he also concluded that separation of roughness related to bedform and skin friction was impossible with then measuring approaches.

Recently, with the improvement of the resolution of the instruments, *Lefebvre et al.* [2011b] quantified the hydraulic roughness of large compound bedforms in a tidally influenced area and investigated its relationship with bedform dimension. As a result, the velocity profiles showed different types. During the ebb phase, the velocity profiles displayed at least two boundary layers: a lower one related to the superimposed secondary bedforms and an upper one associated with the ebb-oriented primary bedforms. During the flood phase, the velocity profiles just showed one single log-linear fit associated with the secondary bedforms. Consequently, in order to improve the prediction of complex bedform roughness in tidal flows, a better estimation of the presence and shape of the flow separation zone over complex bedforms still needs to be determined [*Lefebvre et al.*, 2013a; *Lefebvre et al.*, 2014a; *Lefebvre et al.*, 2016].

Lefebvre et al. [2014a] used the Delft3D models to test the sensitivity of roughness length under tidal flow conditions. They concluded that the total roughness is an order of magnitude larger during the ebb than that during the flood, because of the variation of the flow direction in relation to the bedform asymmetry. During the ebb stage, roughness is significantly influenced by the ebb-oriented primary bedforms, because a flow separation zone (FSZ) and wake region develop over the steep lee side.

Additionally, most of the experimental research related to dunes focuses on flow structure and sediment transport above fixed beds [*Cellino and Graf*, 2000; *Best and Kostaschuk*, 2002; *Kleinhans*, 2004; *Best*, 2005a; *Venditti*, 2007; 2013]. It has the advantage that they allow detailed flow measurements without the complications of both a migrating and changing bedform and the difficulties of flow measurement in the presence of sediment transport over a fully mobile bed [*Best and Kostaschuk*, 2002]. However, due to the presence of a dense sediment layer close to the bed and migrating secondary bedforms over the stoss side of the dune toward the dune crest, the near-bed flow and sediment processes are significantly different from the near-bed flow and sediment dynamics measured over fixed dunes [*Naqshband et al.*, 2014c]. It means that the difference of the velocity profile above fixed dunes or mobile beds has a significant influence on roughness estimation and sediment transport, and whether the log-fit method is appropriate needs to be further investigated in circumstances with high suspension.

As shown above, the velocity profile is divided into several segments due to the presence of bedforms, and varies with the development of bedforms and the variation of flow in tidally influenced areas (estuaries and coasts). Moreover, the bed roughness has a close relationship with whether there exists the flow separation zone or the extent of the wake region. Therefore, the conventional approach used to estimate bed roughness (log-fit method) maybe not appropriate in numerical models which is generally a constant roughness parameter [*Davies and Robins*, 2017], especially in tidally-influenced areas, and the further better understanding of bed roughness above bedforms under tidal flow conditions is urgent to be resolved.

2.1.5. Application of roughness in models

In numerical models applied in both hydraulic engineering and geoscience investigations, roughness is a surrogate which is normally parameterised to present momentum and energy dissipation mechanisms that are hard to explicitly present in the simplified or discrete formulae or unable to be accounted in given model characteristics, such as mesh size, topography resolution, time scale [*Morvan et al.*, 2008; *Smith*, 2014]. So, it is not hard to comprehend that roughness in numerical models is used to denote the omitted physical processes, called “calibration parameter”, and generally, it has no physical significance [*Whatmore and Landström*, 2010].

Morvan et al. [2008] made a detailed review on roughness in the hydraulic application of numerical models. They concluded that the type and amount of physics that each model encompasses (lateral and vertical velocity, density, and turbulence) result in the variation of roughness, and friction factors are usually dramatically water depth and flow strength dependent.

For 1D models, the Manning roughness coefficient (n) is most commonly used, as it is less flow dependent (actually, it is mistakenly regarded), while others, such as Colebrook-White friction factor (f) and Chezy coefficient (C) are more dependent on the channel geometry and flow characteristics. However, all of them are subjective to be estimated. Moreover, 1D models focus more on reach and long time scale, so the roughness, called “lumped” parameter is generally a summation of all potential effects in a reach scale.

For 2D models, although they use the same coefficients like 1D models, the roughness models are different. The friction factors of 2D models related to shear stress are based on vertical water column, while that of 1D models are from the entire bed and bank. In addition, unlike 1D models, some 2D models do not contain turbulence influence, or you could explicitly add it through specific terms. All of the above indicates that 2D models should not directly use the friction factor from 1D model [*Morvan et al.*, 2008].

For 3D models, taking Navier-Stokes equations as an example, roughness is a much smaller term in this situation (Figure 2-3), as roughness is explicitly captured in the numerical mesh. As such a roughness term is applied to just capture the boundary condition and any scales of roughness not represented at the scale of the grid and below. Therefore, the impact of roughness is much more localized and limited. In different dimensional representations in open channel flow, the role and impact of the roughness value upon the solution are very different and this value does not represent the same physical effect [*Morvan et al.*, 2008]. As such, both the grid size and sample resolution are important for the accuracy of output results [*Saleh*, 1993; *Morvan et al.*, 2008; *Smith*, 2014]. *Smith* [2014] indicated that enhanced resolution of measuring data revealed roughness variability at increasingly fine scales [*Jiang et al.*, 2007; *Darby et al.*, 2010]. Therefore, it is necessary to make sure that the roughness parameter is consistent with its physical interpretation in terms of its size relative to the grid size, meaning that a coarser discretization scheme or a model with a lower grid size will attribute more momentum loss mechanisms to its calibrated roughness term [*Morvan et al.*, 2008].

Increased computing power has dramatically shortened the time needed to simulate flow and morphodynamics within higher-dimension models, enabling us to investigate mechanisms operating at finer scales, including turbulence using models such as large eddy simulation [*Nabi et al.*, 2012; *Nabi et al.*, 2013b; *Nabi et al.*, 2013c; *Hardy et al.*, 2014] and direct numerical simulation [*Shimizu and Schmeeckle*, 2001; *Shun-ichiro et al.*, 2003; *Bhaganagar and Hsu*, 2009]. Nevertheless, for large-scale simulations (typical of a large river with a scale of 10^3 km, 10^3 m, and 10^1 m for lengths, widths, and depths, respectively), they are still time-consuming. Therefore, in this sense, the parameterised roughness term is necessary to represent subgrid scale impacts, including the effects of bedforms [*Paarlberg et al.*, 2007; 2009; *Sandbach et al.*, 2012]. *Sandbach et al.* [2012] reported that future work should aim to assess whether or not empirical or semi-physical generalisations can be developed and developing improved modelling of the additional parameters is needed to upscale roughness lengths in 3D CFD simulations. This is likely extremely important for bedforms, particularly those where unsteadiness is important, such as that found in tidally influenced areas, as both the flow conditions and the bed topography change constantly.

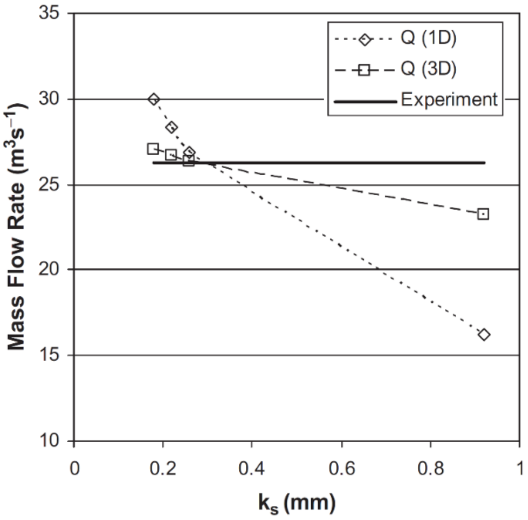

Figure 2-3. Variation of the mass flow rate in 1D and 3D for Kenneth Yuen's experiment 16 [Yuen, 1989] compared to the measured value. The 1D case is computed from Manning's equation using $n = k_s^{1/6}\left[\frac{(R/k_s)^{1/6}}{18log(11R/k_s)}\right]$ *for conversion purposes, where R=Hydraulic roughness (from Morvan et al. [2008]).*

2.2. Flow structure

2.2.1. Introduction

There have been extensive studies being carried out in both the field and laboratory to investigate flow field over dunes [*McLean and Smith*, 1979; *Nelson and Smith*, 1989; *Mendoza and Wen Shen*, 1990; *Lyn*, 1993; *Nelson et al.*, 1993; *Bennett and Best*, 1995; *McLean et al.*, 1999b; *Venditti and Bennett*, 2000; *Maddux et al.*, 2003a; *Maddux et al.*, 2003b; *Fernandez et al.*, 2006; *Wren et al.*, 2007; *Coleman and Nikora*, 2011; *Bradley et al.*, 2013; *Venditti*, 2013]. Bed shear stress is often used in these studies as an index of the fluid force and is used to estimate sediment mobilization and transport in theoretical and empirical treatments. The "Law of the Wall", near-bed Reynolds shear stress and turbulent kinetic energy method are most appropriate for sub-reach scale studies and this approach has been used extensively to understand the interactions of roughness with the flow [*Biron et al.*, 2004].

The "Law of the Wall" method provides spatial patterns of roughness height and shear stress, but the flow must conform to a logarithmic velocity profile [*Smith and McLean*, 1977; *Lefebvre et al.*, 2011b]. An alternative approach is based on calculating the near-bed Reynolds shear stress directly and thus measure turbulent shear stress near the bed. This is often only possible with 2D velocities [*Stacey et al.*, 1999; *Biron et al.*, 2004] and thus limitations apply. Calculating in 3D and determining the turbulent kinetic energy directly has also been developed and applied. This method uses 3D velocities, without estimating roughness height, and can provide the best estimate of shear stress when bedforms exist, particularly as it takes the upwelling and downwelling fluctuation attributing to bedforms into account [*Pope et al.*, 2006].

Macro turbulence induced by dunes is generally formed and observed in large rivers [*Best*, 2005b; *Kwoll*, 2013] and this event is highly related to sediment transport. Thus, understanding of flow structure over large dunes would be vast important to predict sediment transport and subsequently dune adaptation.

2.2.2. Flow structure over dunes under steady and unidirectional flows

Under unidirectional flows, asymmetric bedforms tend to be out-of-phase with the variations in the local water surface slope (Figure 2-4). Significant differences have been observed for symmetric bedforms, found with upper stage beds (*Fr* > 1), which are typically in-phase with the water surface [*Cheel*, 2005]. Increasing research and observations have recently highlighted that low-angle dunes are the most common bedforms found in tidally influenced areas, with beds consisting of fine particle size under lower flow regime conditions [*Kostaschuk and Villard*, 1996; *Kostaschuk and Villard*, 1999; *Best and Kostaschuk*, 2002; *Best et al.*, 2004; *Best*, 2005a; *Bradley et al.*, 2013; *Venditti*, 2013; *Hendershot*, 2014; *Hendershot et al.*, 2016]. There is no evidence yet to confirm whether the symmetric bedforms existing in lower flow regimes are in-phase or out-of-phase with the local water surface slopes.

2.2.2.1. Flow structure over fixed 2D dunes

Angle-of-repose dunes

The majority of previous research has focused on the asymmetric dunes, with angle-of-repose lee-side, which are the most common bedforms in a steady, uniform and unidirectional flow state in a laboratory or commonly observed in rivers [*Best*, 2005a; *Venditti*, 2013].

Figure 2-4a displays a typical schematic diagram of flow structure over an asymmetrical, angle-of-repose dune, and five major regions can be recognised: (1) flow separation zone with recirculating flow generates at the crest, expanding to 4-6 bedform-height long downstream the crest, and finishes at the reattachment point; (2) a shear layer and turbulent wake originate at the crest; (3) expanding flow zone; (4) a internal boundary layer grows from the attachment point; (5) the maximum velocity generally over the crest, and the flow there influences sediment supply to lee-side [*Best*, 2005a].

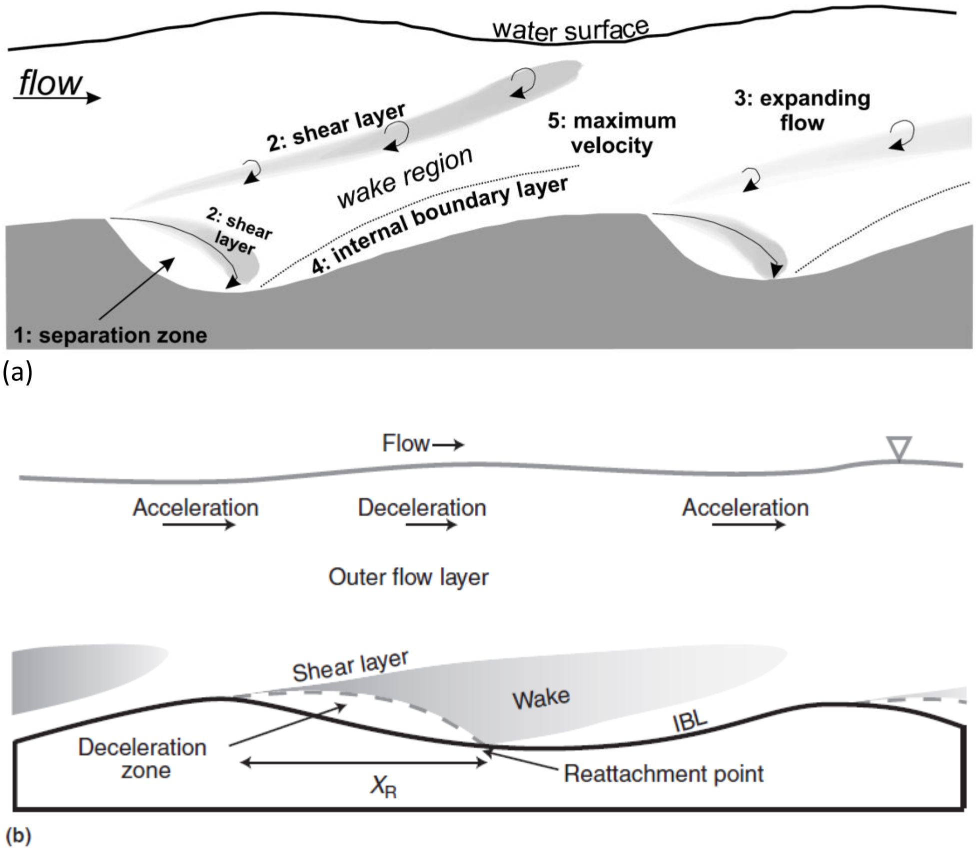

Figure 2-4. Schematic diagram of the principal regions of flow (a) over asymmetrical, angle-of-repose dunes (from Best [2005a]); (b) over symmetrical, low-angle dunes (from Venditti [2013]).

Macroturbulence (i.e. “kolks” or “boils”) generates flow structures that influence water surface and can dominate the time-dependent flow structure over dunes, but its origin has not been explicitly identified [*Kwoll et al.*, 2016; *Kwoll et al.*, 2017]. *Yalin* [2015] ascribed this to the boundary-layer bursting process, while *Bennett and Best* [1995] and *Venditti and Bennett* [2000] to Kelvin-Helmholtz instabilities formed along the shear layer. Moreover, *Nezu* [1993] attributed this to shear-layer destabilization coupled with the ejection of slow-moving fluid from the recirculation bubble, whereas *Müller and Gyr* [1986] to vortex shedding and amalgamation [*Venditti*, 2013].

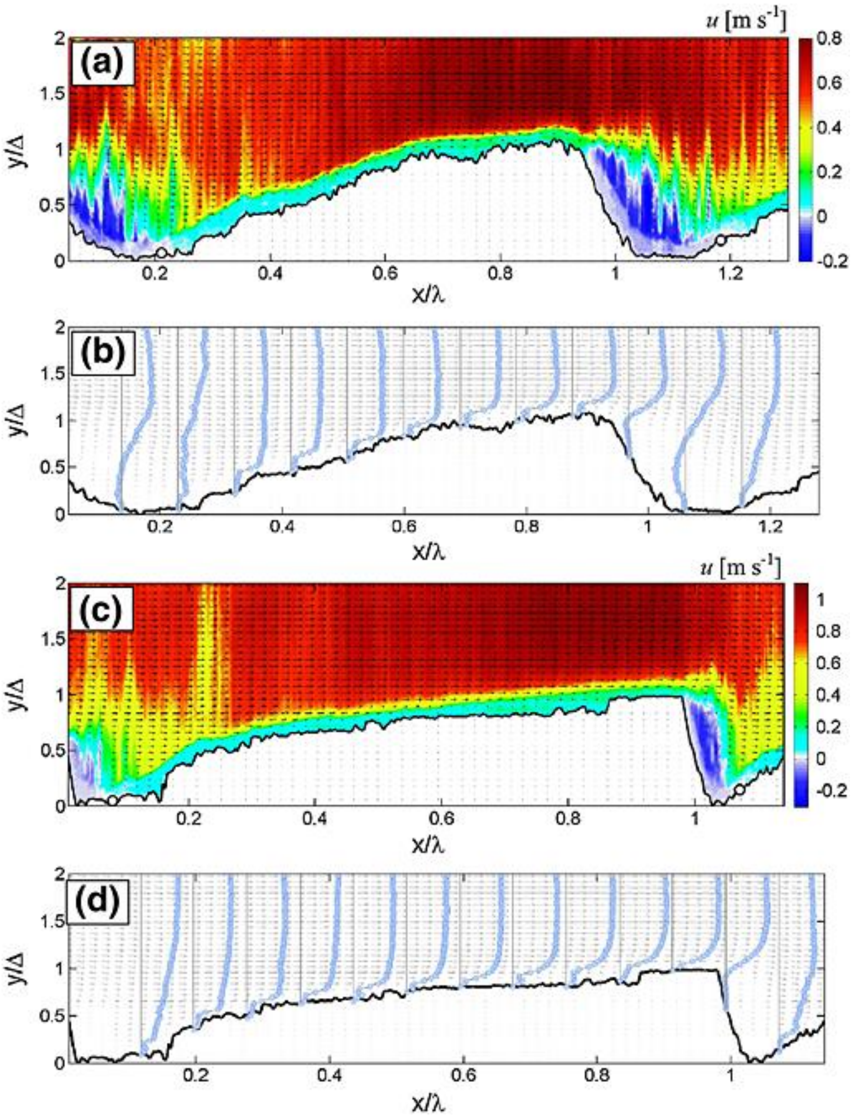

Figure 2-5. Contour maps and selected profiles of the mean streamwise flow velocity $\overline{u}$ *(m s*$^{-1}$*) for (a, b) EXP1 with a dune length of 2.25 m and (c, d) EXP2 with a dune length of 4.35 m. The arrows represent the mean velocity vector field V (*$\overline{u}$*,* $\overline{w}$*) and the solid line shows the dune profile with open circles indicating the flow reattachment point. Flow direction is from left to right. Vertical, solid lines along the dune bed indicate the location of the velocity profiles origin with negative velocities to the left and positive velocity to the right of this line. The distance between two vertical lines scales with* $\overline{u}$ *= 1.25 m s*$^{-1}$ *(from Naqshband et al. [2014c]).*

Low-angle dunes (LADs)

There is growing evidence from field observations to suggest that more symmetrical dunes with smaller lee-side angles (i.e. low-angle dunes) are the prominent bedforms in tidally influenced and suspended sediment dominated sand-bedded rivers and estuaries [*Smith and McLean*, 1977; *Kostaschuk and Villard*, 1996; *Carling et al.*, 2000a; *Carling et al.*, 2000b; *Best and Kostaschuk*, 2002; *Bradley et al.*, 2013; *Hendershot et al.*, 2016]. The biggest difference between flows over asymmetric and symmetric dunes is that, instead of the separation zone, a well-defined region of decelerated flow is present over the lee of symmetrical, low-angle dunes (Figure 2-4b).

The structure of the turbulent flow, which is related to energy dissipation over bedforms, controls the flow resistance [*Best*, 2005a; *Kwoll et al.*, 2016; *Lefebvre et al.*, 2016; *Kwoll et al.*, 2017]. Therefore, asymmetric dunes with permanent flow separation are thought to have a higher flow resistance than symmetric dunes with no or intermittent flow separation occurring in the lee [*Lefebvre et al.*, 2013a; *Kwoll et al.*, 2016].

2.2.2.2. Flow structure over mobile 2D dunes

The majority of research on dunes has focused on bedload dominated conditions, which means they ignored the influence of suspended sediment [*Simoes*, 2010; *Naqshband*, 2014]. Additionally, research on dune dynamics via flume experiments has largely been based on fixed beds, which is easier to achieve and measure, but ignores movable bed effects, resulting in a discrepancy between the flume results and field observations [*Grant and Madsen*, 1982; *Naqshband*, 2014; *Naqshband et al.*, 2014c]. The ratio of bedload to suspended load discharge could change bedform migration rate and the typical grain size deposited on dune lee sides [*Naqshband et al.*, 2014c] or have the potential to alter flow separation [Baas et al., 2009], subsequently influencing both the shape of dune and the flow structure near bottom [*Naqshband et al.*, 2014c]. Moreover, it has been recognised that greater flow velocities during floods bring or suspend greater amounts of suspended sediment load [Jordan, 1965; Nittrouer et al., 2008; Ramirez and Allison, 2013]. The rate of bedform adaption can thus be strongly controlled by the amount of sediment suspended [*Kostaschuk et al.*, 2009; *Bradley et al.*, 2013].

Figure 2-5 displays the flow structure over angle-of-repose bedforms with mobile beds. The results confirm well with those of *Best* [2005a] in that the flow separation zone, flow acceleration, deceleration, internal boundary layer and outer shear layer were observed. They observed that the existence of secondary bedforms and showed a flow recirculation area over their lee-sides, attributing this to the effects on the near bottom flow and sediment dynamics. Therefore, the presence of the secondary, superimposed bedforms, which may alter sediment transport delivered to the dune crest, is another important factor in controlling sediment transport patterns [*Reesink and Bridge*, 2007]. Secondary bedforms tend to grow in size during floods, at least during the initial rising stage, increasing bed roughness through modification and interactions of coherent flow fields over bedforms of various scales [*Fernandez et al.*, 2006], producing greater amount of suspended sediment and altering the flow structure near bottom, especially in the interval boundary layer along the primary dunes' stoss. As a result, this adds more difficulties in predicting bedform morphology during floods [*Julien and Klaassen*, 1995; *Yen and Lee*, 1995; *Amsler et al.*, 1997; *Carling et al.*, 2000a; *Carling et al.*, 2000b; *Unsworth*, 2015]. However, if suspended sediment concentration is high, the majority of the finer sediments can be removed by the flood flows, which can alter the form of the bed and alter the formation of bedforms during changes in flow stage and under new hydraulic conditions [*Kostaschuk et al.*, 2009].

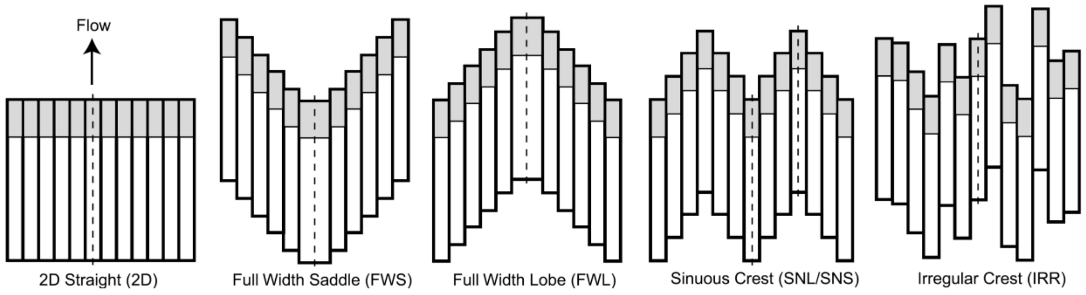

Figure 2-6. Dune morphologies tested. Grey areas are in the lee of the dune crest on each plank. Lines down the centre (and along the right lobe of the sinuous crest) indicate where the velocity profiles were taken from Venditti [2007].

2.2.2.3. Flow structure over 3D dunes

Venditti et al. [2005b] suggested that all dune bedforms must eventually become three-dimensional, due to minor, transient excesses or deficiencies of sand being passed from one bedform to another. Furthermore, based on detailed flume experiments of fixed beds, the three-dimensionality of dunes could impact the form drag, compared with that two-dimensional (2D) dunes in similar flow conditions [*Maddux et al.*, 2003a; *Maddux* *et al.*, 2003b; *Venditti*, 2003; 2007]. Maddux et al. [2003b] quantified the differences of the flows between crest line and node line, while *Venditti* [2007] investigated the flow field over four types of three-dimensional (3D) dune morphologies (full-width saddles, full-width lobes, sinuous crests, and irregularly shaped crests, see Figure 2-6).

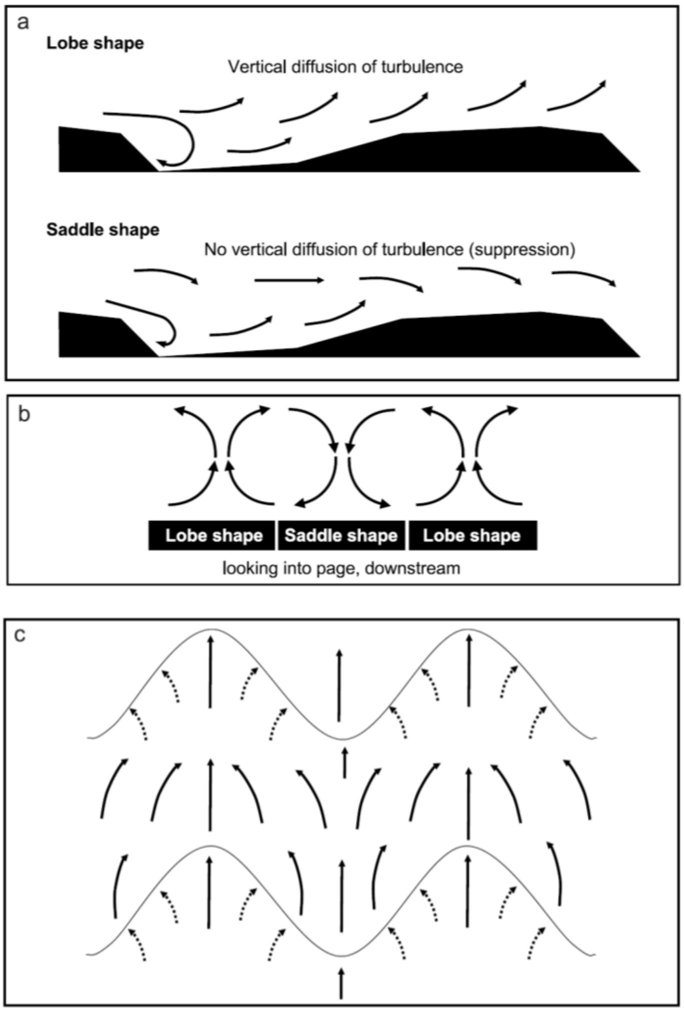

Figure 2-7. Divergence and convergence of mean flow over lobe and saddle crest lines in the (a) x-z plane, (b) y-z plane (averaged over one dune length), and (c) x-y plane (near the bed). The dashed arrows in Figure 12c indicate patterns observed in experiments by Allen [1968], and the solid arrows are consistent with the present experiments (from Venditti [2007]).

Maddux et al. [2003b] concluded that friction coefficients of the three-dimensional dunes were higher, but the turbulence was weaker compared with those of two-dimensional dunes under similar conditions. In contrast, *Venditti* [2007] reported that the accurate shape of crest lines also has a dominant impact on flow resistance and turbulence that lobe-shaped dunes enhanced both the turbulence and flow resistance, while saddle-shape dunes diminished both of them (Figure 2-7). Additionally, *Parsons et al.* [2007] firstly presented the evidence of the impact of three-dimensionality on the flow, based on field data obtained from a large river. They concluded that dunes' three-dimensionality is connected to the morphology of the upstream dune, with changes in crestline curvature and crestline bifurcations/junctions significantly influencing the downstream dune form. Moreover, dunes with lobe- or saddle-shaped crest lines were found to have larger, more structured regions of vertical velocity with smaller separation zones than more 2-D straight-crested dunes. The gaps between their results are exactly the proof of the lack of our knowledge on this aspect, and the influence of three-dimensionality on flow structure is thus perhaps one of the key issues that require urgent research to advance our understanding of bedform dynamics at a wide range of spatial scales [*Best*, 2005a; *Parsons and Best*, 2013].

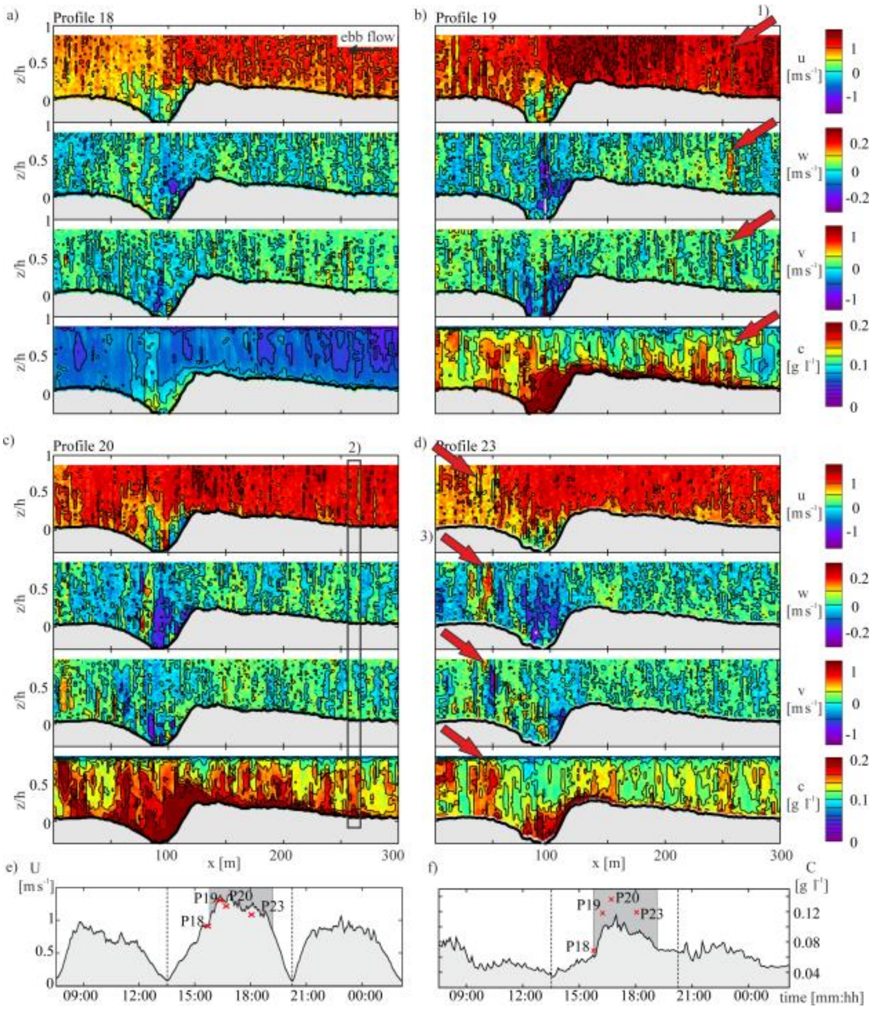

Figure 2-8. (a–d) Selected ship transects collected during the ebb tide. Shown is the streamwise (u) [m s^{-1}], vertical (w) [m s^{-1}], and crosswise (v) [m s^{-1}] velocity and SSC (c) [g L^{-1}]. (e) Depth-averaged current velocity (U) [m s^{-1}] from TRBM aDcp, average <U> [m s^{-1}] of selected transects is indicated by the red cross. (f) Depth-averaged SSC (C) [g L^{-1}] from TRBM aDcp, average <C> [g L^{-1}] of selected transects is indicated by the red cross. Arrows + rectangle show coupled flow and sediment suspension structures, demonstrating (1) their occurrence along the bedform stoss-side, (2) an example of the crosswise rotational pattern associated with structures, and (3) structures originating downstream of the flow deceleration/reversal zone (from Kwoll et al. [2014]).

2.2.3. Flow structure over dunes under unsteady flows

Majority of the research on hydrodynamics and sediment transport over bedforms is based on steady uniform flows in controlled flume experiments. However, all fluvial and estuarine environments exhibit temporal variations in flow discharge, which creates unsteady changes in the flow field. Furthermore, presently, research on dunes under unsteady flow conditions [*Raudkivi*, 1966; *Raudkivi and Witte*, 1990; *Dalrymple and Rhodes*, 1995; *Julien and Klaassen*, 1995; *Yen and Lee*, 1995; *Carling et al.*, 2000a; *Carling et al.*, 2000b; *Hendershot*, 2014] has focused on dune geometry evolution, while few studies have also investigated the changes in flow structure over dunes, especially in tidally influenced areas [*Smith and McLean*, 1977; *Grant and Madsen*, 1982; *Kostaschuk and Best*, 2005; *Lefebvre et al.*, 2011b; 2013a; *Lefebvre et al.*, 2014a; *Lefebvre et al.*, 2014b]. Although the advanced equipment available for field observations has increasingly developed over recent decades, there are inherent limitations for the simultaneous measurement of both flow dynamics and sediment transport, especially in the near-bed region, which forbids our understanding [*Naqshband et al.*, 2014c].

Based on feedback between morphology and hydrodynamics, we divide unsteady flow into two main types: (1) floods with dramatic variation of river discharge and water level, resulting in rapid evolution of bedforms, such as shape, type and dimension, and consequently flow structure changes; (2) tides with smooth variation, resulting in relatively slow transformation of bedforms, but different flow directions during different tidal stages. Therefore, the variation of flow structure during a flood is mainly subject to morphologic alteration, while that within a tide attributes to both flow strength and direction changes.

Angle-of-repose dunes

Kwoll et al. [2014] investigated tide-dependent variations of both hydrodynamics and sediment transport over ebb-oriented, asymmetric bedforms in the Danish Knudedyb inlet, and analysed the differences of flow structure over dunes between the flood and ebb tides. During the ebb tides (i.e. the flow direction and bedform orientation are aligned), flow separation was found to be present in the lee-side, and regular water-depth-scale coherent flow structures of upward-directed temporally-decelerated flow dominated the flow field, which occurred repeatedly downstream of the bedform trough toward the crest (Figure 2-8). In contrast, during the flood tides (i.e. the flow direction and bedform orientation are opposed, Figure 2-9), flow separation was not observed, and the developed secondary bedforms resulted in a smaller scale of coherent flow structures in their stosses. The temporally steep hydraulic stoss-side suppressed the near-bed sediment to transport to a longer distance [*Kwoll et al.*, 2014].

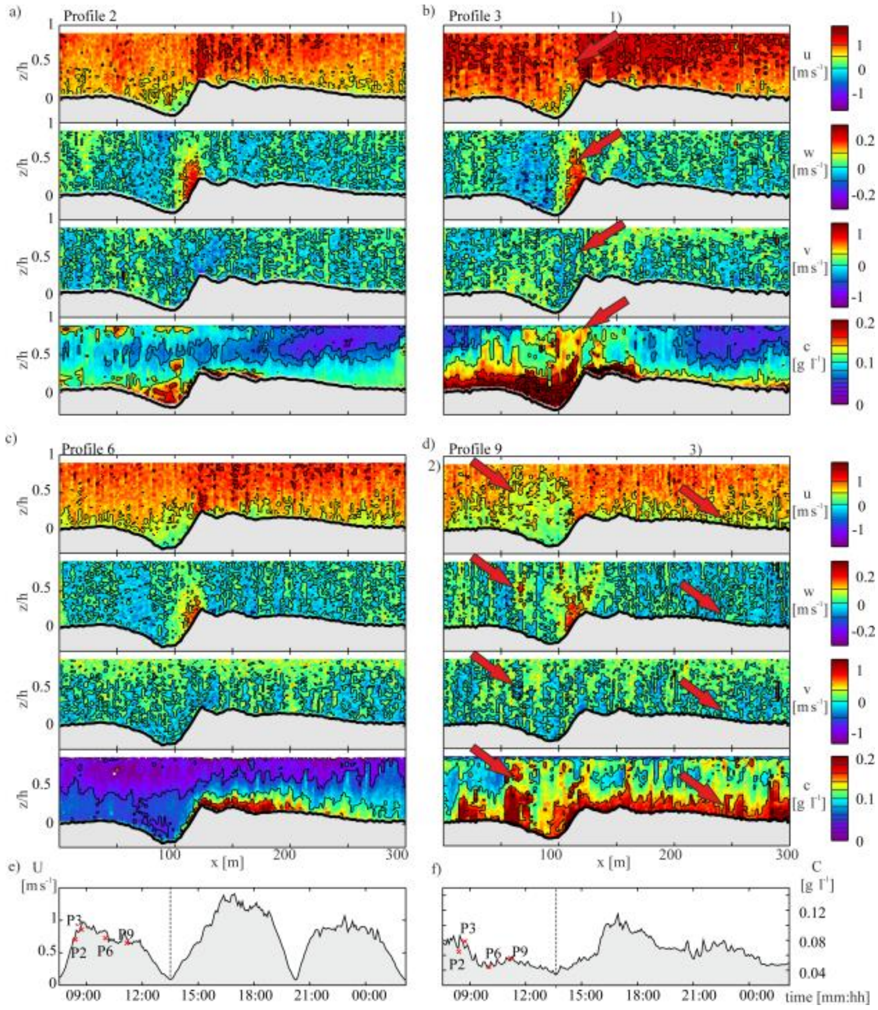

Figure 2-9. (a–d) Selected ship transects collected during the flood tide. Shown is the streamwise (u) [m s^{-1}], vertical (w) [m s^{-1}], and crosswise (v) [m s^{-1}] velocity and SSC (c) [g L^{-1}]. (e) Depth-averaged current velocity (U) [m s^{-1}] from TRBM aDcp, average <U> [m s^{-1}] of selected transects is indicated by the red cross. (f) Depth-averaged SCC (C) [g L^{-1}] from TRBM aDcp, average <C> [g L^{-1}] of selected transects is indicated by the red cross. Arrows show (1) areas of high SSC associated with the upward-directed flow at the primary bedform crest, (2) suspension structures occurring above the trough under accelerating flow, and (3) small-scale suspension structures on the bedform stoss (from Kwoll et al. [2014]).

In *Kwoll et al.* [2014], the secondary bedforms affect near bed flow patterns during the floods tide more strongly, compared with that during the ebbs. In contrast, *Lefebvre et al.* [2011b] working in similar conditions, made an opposed conclusion. During the flood phase, the velocity profiles displayed a single log-linear relationship with distances above the bed, whereas, during the ebb phase, they presented at least two boundary layers, as the influence of superimposed secondary bedforms impacted the velocities.

Additionally, the changes of flow direction affect the generation of flow separation zone (FSZ), which has a significant impact on flow structure, which is confirmed by *Lefebvre et al.* [2013b]. The shape of the FSZ is not affected by the variation of current velocities or water levels, but the changes in the bed morphology are influenced [*Unsworth*, 2015].

Low-angle dunes (LADs)

Figure 2-10 displays five typical flow patterns over low-angle dunes under different stages of a tidal cycle in the field. The results reveal the detailed temporal development between flow and morphology in the tidally-influenced area [*Bradley et al.*, 2013]. Both the upper falling (Figure 2-10a) and rising tides (Figure 2-10e), with weak flow strengths, displayed no coherent patterns over the dunes, while the lower falling (Figure 2-10b), rising (Figure 2-10c) and low tide (Figure 2-10d) which have higher flow strength showed apparent evidence of topographical forcing, indicating that the fluid accelerated over the stoss and decelerated in the trough, due to flow expansion [*Bradley et al.*, 2013].

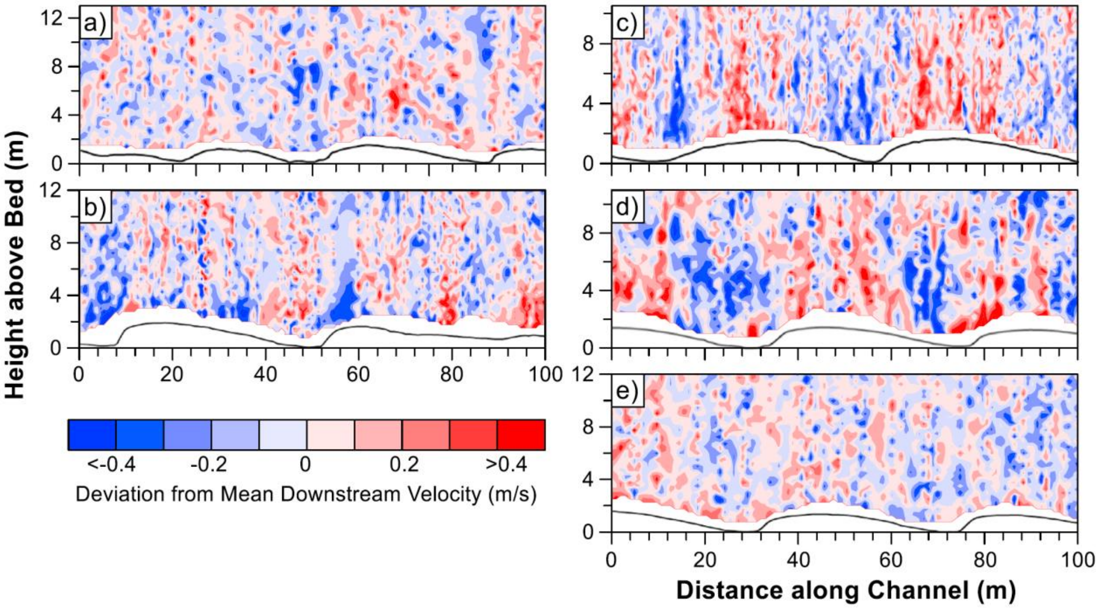

Figure 2-10. Deviation in downstream velocity from the mean (u'_x) for (a) Upper Falling Tide (Transect B), (b) Lower Falling Tide (Transect F), (c) Low Tide (Transect H), (d) Lower Rising Tide (Transect I), and (e) Upper Rising Tide (Transect J). High Tide is not included because there was an alongstream velocity gradient that dominated the signal. River flow is right to left. Vertical exaggeration is 3x (from Bradley et al. [2013]).

2.3. Hysteresis effect

2.3.1. Introduction

Bedforms persistently adjust to local flow conditions which, in most natural systems, are non-uniform and unsteady, with prominent variations in both flow magnitudes (floods) and directions (tidally influenced areas). These changes driving hysteresis effects in flow resistance [*Simons and Richardson*, 1961; *Raudkivi and Witte*, 1990; *Julien et al.*, 2002; *Paarlberg et al.*, 2010; *Sandbach et al.*, 2012; *Hardy et al.*, 2014], sediment transport rates [*Naqshband et al.*, 2014c] and morphodynamic adjustments [*Gabel*, 1993; *Julien et al.*, 2002; *Martin and Jerolmack*, 2013] are commonly investigated. It is proved that hysteresis effect is one of the most import factors that affect precise prediction and simulation of dune evolution under unsteady flows. Thus, understanding the mechanism of hysteresis is needed for numerical modelling, especially for long-term and large area numerical simulation.

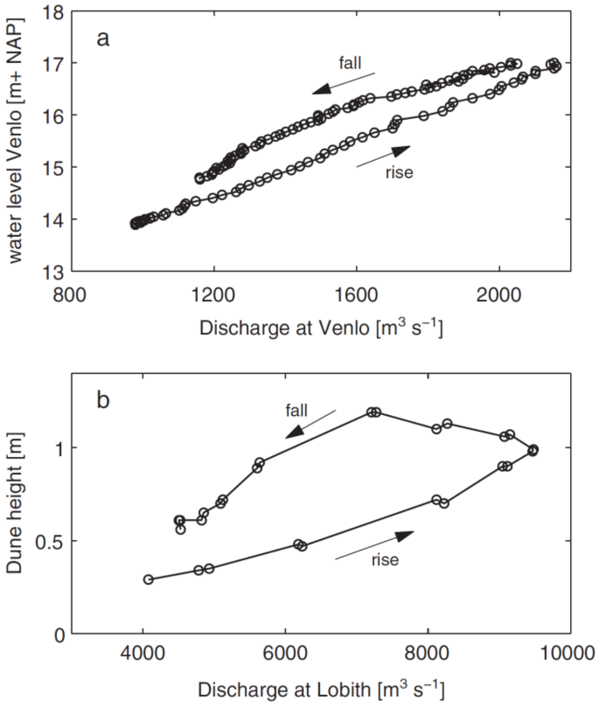

Figure 2-11. (a) hysteresis in water level in the river Meuse at Venlo during February 2002 flood (Termes [2004]); (b) Hysteresis effect in dune height in the river Rhine near the Pannerdensche Kop during the 1998 flood (Wilbers and Ten Brinke [2003]) (from Paarlberg et al. [2010]).

2.3.2. Floods

Figure 2-11*a* shows a clear example of a hysteresis effect in dune geometry revealed in the water levels and dune height (Figure 2-11b) for a given discharge altering during the passage of a flood. In the hysteresis of stage-discharge curve proposed by *Simons and Richardson* [1961] (Figure 2-12), clear interactions were presented that at the same discharge, the flow depth is found to be different in falling and rising stages, resulting in a loop of the stage-discharge curve that resembles a hysteresis curve.

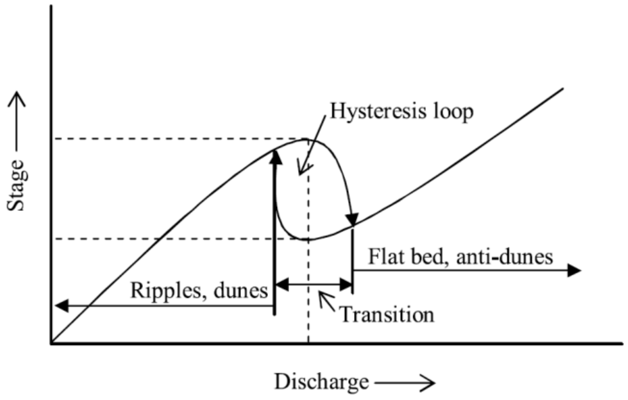

Figure 2-12. Hysteresis of the stage-discharge curve (form Shimizu et al. [2009]).

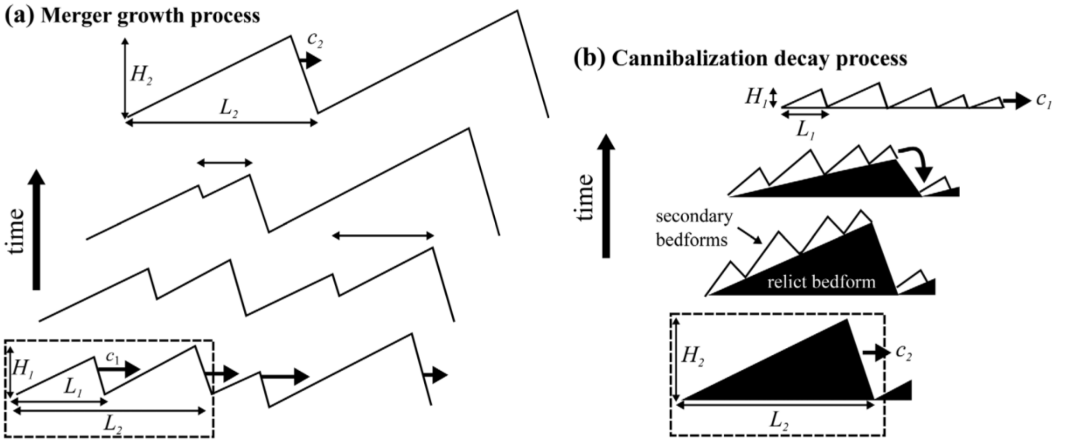

Figure 2-13. Conceptualization of bedform growth and decay processes. (a) For the growth process, differences among celerities cause bedforms to collide and merge into larger features until a new equilibrium is reached. (b) For the decay process, secondary bedforms (white) migrating across the larger relict flood peak bedform (black) erode the relict crest and the relict trough. H1, L1, and c1 refer to low flow mean equilibrium bedform quantities, while H2, L2, and c2 are for high flow. Dashed boxes outline reconstitution volumes V1 for merger growth and V2 for cannibalization decay (from Martin and Jerolmack [2013]).

Paarlberg et al. [2010] attributed hysteresis effects in bed response to (i) accelerations and decelerations during the passage of a flood wave (i.e. the Jones formula, see e.g. *Perumal et al.* [2004]) and (ii) dunes forming on the bed during the passage of a flood wave. *Martin and Jerolmack* [2013] (Figure 2-13 and Figure 2-14) concluded a detailed comprehension for the second point that, the merging processes create larger bedforms for the rising limb of a flood wave, and the cannibalisation processes for the falling leg. They investigated the differences in the rate of change in hydraulic and bedform state and found that full flood flow can be produced without hysteresis if the rise to peak flow is at the same rate as bedform adaption.

Additionally, *Reesink et al.* [2013] reported on the important role of water surface slope on the morphodynamic adjustment of dunes. Water-surface slope and bed shear stress commonly increase during the arrival of a flood wave, followed by a decline in absolute flow depth during falling stage (Figure 2-15). They also concluded that the separation of water surface slope and depth supports a separation of 'true hysteresis' of different bedform growth and decay processes [*Martin and Jerolmack*, 2013], 'rate-dependent hysteresis' related to the time needed for bedform adaptation to reach an equilibrium form [*McElroy and Mohrig*, 2007; *Paarlberg et al.*, 2010], and 'natural variability' in dune geometries [*Rubin and McCulloch*, 1980; *Parsons et al.*, 2005]. However, they found that superimposed bedforms developed on the stoss of primary dunes during the rising limb of water depth, rather than in decreasing stage, which is not consisted with the results of other research (e.g. [*Martin and Jerolmack*, 2013]), that dunes decay by cannibalisation. They attributed this to disequilibrium between dune geometry and the flow over the stoss-side, and bed morphology was the most sensitive impact on changes in water depth. Therefore, fuller understanding of the causes for, and constraints on, dune adaptation to changing flows requires robust quantification of the flow field over out-of-equilibrium dunes and how sediment transport processes alter in response.

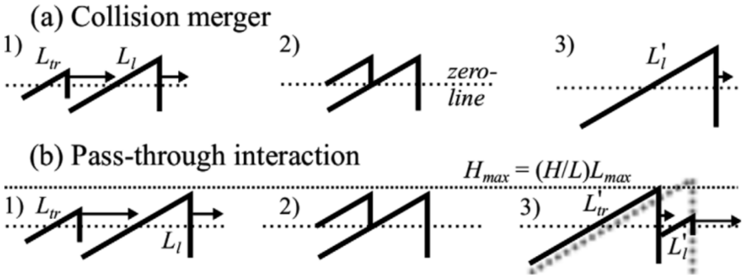

Figure 2-14. Diagram describing interactions in the bed-form merger growth model. Bedforms are treated as right angle triangles with constant steepness, H=L, which move with celerities inversely proportional to their sizes. For collision merger: 1) A small bedform (with length Lt) approaches a larger one (with length Ll) from behind. 2) When the small bedform is succinctly close, the intervening trough rises above the dashed zero-line, and they are considered merged. 3) Heights and lengths of colliding bedforms are combined additively to form the newly merged bedform (with length L0l). For pass-through interaction: 1) A small bedform approaches and 2) merge as before. 3) However, the resulting merged form would exceed Hmax. Instead, a merged form at the maximum height line is formed (with length L0t), and excess sediment is ejected as a small bedform in the front of the newly merged bedform (with length L0l) (from Martin and Jerolmack [2013]).

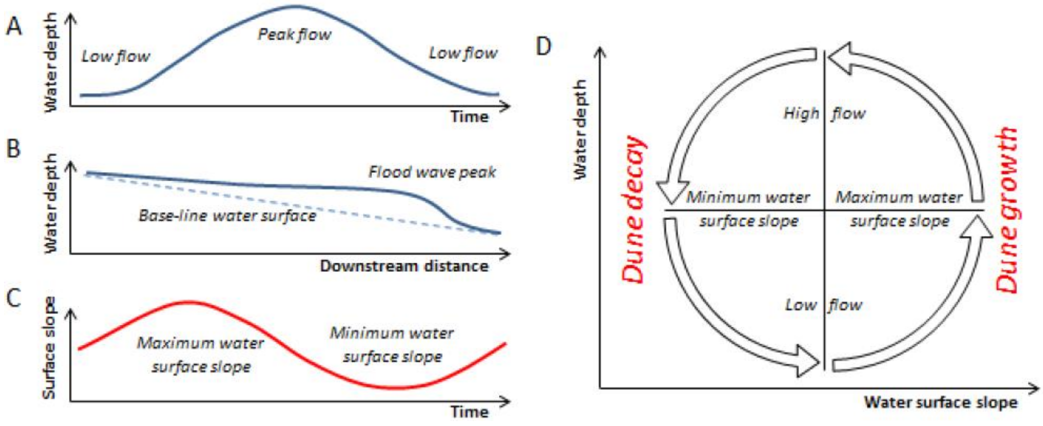

Figure 2-15. The passage of a flood wave at a location over time (A) and at a time over a downstream distance (B): both result in a water surface slope (C) that is out-of-phase with water depth at a location (A). This depth-slope association affects the nature of alluvial dune growth and decay in unsteady flows (D) (from Reesink et al. [2013]).

Reesink et al. [2013] also highlight that the shape of flood waves and the phase-relation between water surface slope and water depth vary between floods from highly asymmetrical flash-floods to monthly changes in base-flow. *Paarlberg et al.* [2010] investigated a similar phase divergence using a physically-based numerical model and concluded that hysteresis in dune height is larger for a sharp-peaked flood wave, but the total increase in dune height is larger for broad-peaked flood waves (Figure 2-16)

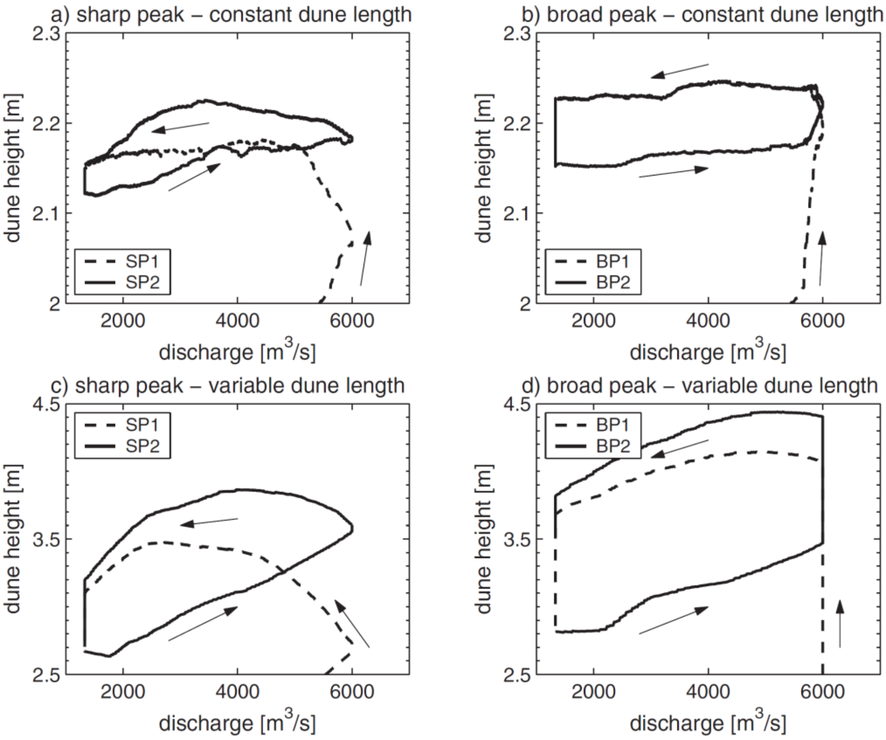

Figure 2-16. Hysteresis in dune height, for the two types of flood waves (Fig. 6). Results for both constant dune length (a-b), and variable dune length (c-d) are shown (note different scales on the y-axis). In the figures, the two subsequent flood waves in each simulation are plotted separately (see legend of subplot a) (from Paarlberg et al. [2010]).

The hysteresis-effect in dune height for both constant dune length (Figure 2-16a-b) changes little on dune height (~0.1 m) for both types of flood waves, while for variable dunes the influence (~0.7 m) was found to be more pronounced (Figure 2-16c-d). For both constant dune length (Figure 3.6a-b), the hysteresis effect for the sharp-peaked flood wave is more pronounced. This is because a maximum dune aspect ratio is obtained for the flow and sediment conditions (confirmed by *Carling et al.* [2000a]), and the dune height only changes due to small nonlinear effects if the water depth changes strongly between the low and high discharge [*Paarlberg et al.*, 2010]. However, for variable dunes, during the broad-peaked flood, higher dunes were generated at the start of the falling stage. This is important since at the end of the flood wave relict dunes are higher, which may cause a maximum impact of roughness changes and additional practical problems for river-based operations such as shipping.

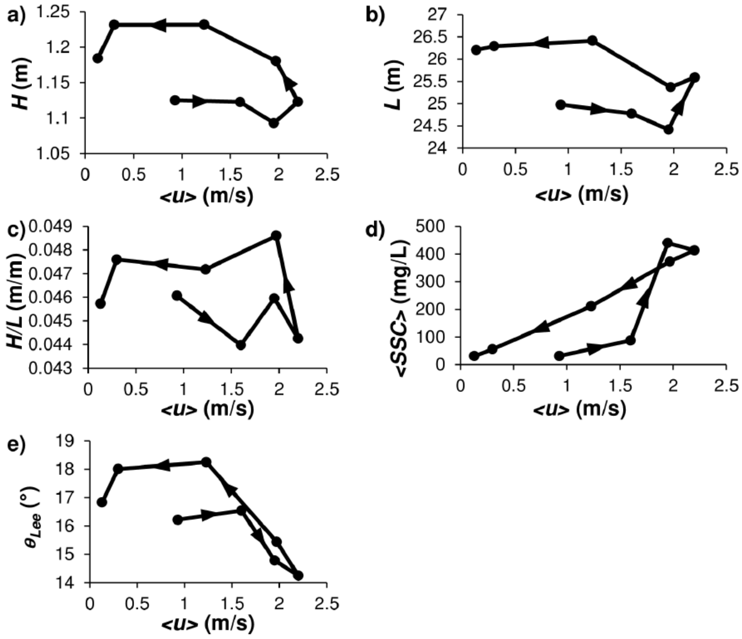

Figure 2-17. Relation between mean velocity <u> and a) dune height (H), b) dune length (L), c) aspect ratio (H/L), d) suspended sediment concentration <SSC> and e) lee slope angle θ_{Lee}. Arrows indicate the direction of the loop. (from Hendershot [2014]).

2.3.3. Tides

As shown above, understanding of hysteresis effects is based on bed response to floods, and there is little research on hysteresis effect about tides. As hysteresis can be affected by various factors, such as flow strength, water level and their variation rates, sediment supply etc., the time scale is generally the big issue for scaled flume experiments and their application to the natural environment. Therefore, there is a need for a range of future work to address hysteresis effects in tidal areas and how this varies in time and space and the impact this has on longer-terms system developments.

Hendershot [2014] explored the hysteresis effect of low -angle dunes in Fraser Estuary with high-resolution equipment. She found that the variation of bedform height and lee angle have an anticlockwise hysteresis with flow strength (Figure 2-17), while *Kostaschuk and Best* [2005] show clockwise hysteretic loops for height and aspect ratios. They proposed that it is probably the sampling bias results in the discrepancy, as *Kostaschuk and Best* [2005] employed single beam echo-sounder. The statistic geometry data highly depends on the accuracy of measuring lines, while dune height is recognised to be highly variable along the crestline of individual dunes [*Parsons et al.*, 2005].

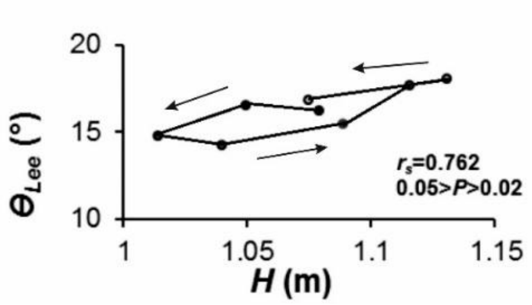

Figure 2-18. Relations between dune lee angle (θ_{Lee}) and height (H). Correlation coefficients (r_s) were calculated using Rank Spearman Correlation because the data are non-parametric. The P-value calculated from a t-distribution is inaccurate when there are < 11 observations, so the P-value is determined from a t-statistics table and reported as ranges of values. The arrows highlight an obvious complete hysteresis loop between H and θ_{Lee}. (from Hendershot [2014]).

The hysteresis loop of lee angle and height (Figure 2-18) indicates that the relaxation of the lee slope can be linked to sediment supply and is associated with a planning off of the dune crest which is proposed as a mechanism of low-angle dune development [*Hendershot*, 2014].

2.3.4. The influence of hysteresis on flow resistance

The total resistance for flows over bedforms consists of skin friction related to sediment particles and form drag associated with bedforms [*McLean*, 1992; *Kostaschuk and Villard*, 1996; *Lefebvre et al.*, 2011b]. A number of laboratory and field investigations have revealed that the existence of two different values of flow resistance under the same hydraulic conditions during temporally varying flows, that is, the change of bed roughness lags the change of discharge [*Shimizu et al.*, 2009]. *Shimizu et al.* [2009] also implied that this phenomenon is ascribed to the distinctive characteristics of bedform evolution or transition and, in turn, differences in flow resistance during rising and falling limbs of floods, even under the similar hydraulic conditions [*Yamaguchi and Izumi*, 2002; 2003]. Furthermore, hysteresis-effects on bed roughness (bed shear stress) is the main factor which can influence the accuracy of the process-based dune evolution model.

2.3.5. Hysteresis related to sediment transport

The developing boundary layers and coherent flow structures generated above the stoss of dunes have a huge potential to suspend, entrain and transport more sediment than predicted from spatially-averaged estimates of bed shear stress [*Unsworth*, 2015]. Consequently, the hysteresis-effect of areas covered by dunes is in turn also highly influenced by sediment transport.

The predominantly bedload-based laboratory experiments of dune hysteresis have focused on dune splitting and merging during periods of unsteadiness. However, the effect of dominant sediment transport type needs to be taken into account, as the change in phase between bedload dominated sediment transport and bedforms to suspended dominated sediment transport occurs [*Nittrouer et al.*, 2008; *Unsworth*, 2015]. This transition will be critical to the response of the bed to changes in flow, but significant uncertainty remains in the process changes that result across this transition.

CHAPTER 3

3. Bedform adaptation to changing flows

Abstract: River bedforms keep translating and deforming perpetually during their migration. During flow field unsteadiness they also change in size and shape over time and in space. However, our knowledge of how bedforms adapt to changing flows remains inadequately understood. This chapter herein reports a series of large flume experiments executed under a fully mobile bed and investigates how dunes response to changes in flow velocity and depth. The results show: (1) shear stress and grain size dominate the mechanisms of sediment transport and the progress of sediment transport subsequently controls how dune size alters with changes in water depth and flow velocity; (2) the correlation between sediment transport and sediment supply at the initial flow condition demonstrates different modes of dune initiation and development. Under degradation, dune initiation is controlled by the generation of deep scour pits, while under equilibrium, by the mounds remain in the initial bed; (3) Under BLD, in the falling limbs, the probability of occurrence of large relicts dominates how dunes adapt to falling flows. The probability of bedform superimposition increases gradually with decreasing flow velocity but increasing crest-to-crest distance. A large and dramatically varying step length enhances the instability of each dune but decreases the possibility of generation of small dunes whose wavelength is less than step length; (4) two separate types of sediment supply variation, were found to affect dune adaptation: i) systematic sediment supply variations related to net degradation/aggradation and ii) local sediment supply variations related to sediment redistribution over and among dunes. A systematic sediment supply is found to be a first order factor, affecting dune adaptation when net degradation/aggradation occurs; (5) the analysis of dune three-dimensionality reflects that the generation of the larger dunes is the main factor controlling sediment transport and thereby bedform adaptation. The processes of dune adaptation vary due to diverse sediment redistribution over and between dunes and dune adaptation is a spatially- and temporally- variable response of multiple, interacting dunes and broader scale redistribution of sediment. More attention thus should be taken when bedforms are not regular, and the average value for dune length and dune height maybe not the appropriate parameter to determine the adaptation coefficient.

3.1. Introduction

River dunes, the most prominent component of flow resistance, are ubiquitous in nearly all fluvial channels under subcritical flows [*Van Rijn*, 1993; *Best*, 2005a; *Bridge*, 2009]. They range from 10^{-2} to 10^{1} m in height and 10^{-1} to 10^{2} in length [*Bradley and Venditti*, 2016], formed by interactions between flow and sediment transport [*Allen*, 2009; *Ohata et al.*, 2017]. In the last 30 years, numerous studies have been focused on understanding the dune formative circumstances [*Van Rijn*, 1984b; *Southard and Boguchwal*, 1990; *Van Den Berg and Van Gelder*, 2009; *Ohata et al.*, 2017], as they are of vital importance for engineering, for example they may destroy river infrastructure [*Amsler et al.*, 1997], and for geological studies they are the foundation for paleoenvironmental reconstruction based on their sedimentary structures preserved in strata [*Allen*, 1982; *Leclair and Bridge*, 2001; *Leclair*, 2002; *Bridge*, 2009].

Based on the cross-sectional profile of dunes, in general, they are classified as high-angle, asymmetric dunes (HADs with ~ 30° lee slope) or low-angle, symmetric dunes (LADs with lee slope < 10°) [*Venditti*, 2013; *Hendershot et al.*, 2016]. The most significant distinction between HADs and LADs is that permanent flow separation zone (FSZ), in general, occurs in the lee-side of HADs, where sediment avalanching leads to bedforms migrating downstream, whereas only intermittent or even no flow separation is produced over the lee of LADs, and sediment deposits from suspension in the lower lee and trough [*Best and Kostaschuk*, 2002; *Best*, 2005a; *Hendershot et al.*, 2016]. Furthermore, recent research [*Kostaschuk and Villard*, 1996; *Kostaschuk and Best*, 2005; *Naqshband et al.*, 2014a; *Naqshband et al.*, 2014c] has revealed that different sand transport mechanisms can be attributed to these different formations of dunes: HADs occur under bedload dominant regime, while LADs develop under high suspension conditions. This finding is in line with traditional dune transitions, from dunes to upper stage plane beds [*Best and Kostaschuk*, 2002]: with the increase of flow strength, the stronger turbulence generates higher suspension, resulting in progressively lower dune lee slope (i.e. dune decay) until this is “swept out” [*Duin*, 2015; *Duin et al.*, 2016]. This conclusion also has been successfully applied in numerical models to simulate dune-flat bed transition via adopting different step lengths to represent different sediment transport regimes which is shown to control dune form [*Sekine and Kikkawa*, 1992; *Shimizu et al.*, 2009; *Duin*, 2015]. Additionally, *Naqshband et al.* [2014a] found that dune transition could occur under a smaller suspension threshold, compared with low Froude numbers. It indicates that it is the combination of flow depth, shear stress, grain size and even upstream dune morphology that can combine to control dune size and shape [*Carling et al.*, 2000b; *Best and Kostaschuk*, 2002].

Many studies have contributed to investigating the complex interactions between the turbulence, bed morphology and sediment transport, which is key to understand river dune dynamics [*Van Rijn*, 1993; *Best*, 2005a]. However, most research has focused on two-dimensional (2D) dunes, while natural dunes are eventually three-dimensional (3D), if given sufficient time [*Baas et al.*, 1993; *Venditti et al.*, 2005b]. This simplification of dune morphology, ignores the effect of lateral and secondary flows, inherently limits our interpretation and understanding on dune development [*Parsons et al.*, 2005]. Recent studies [*Maddux et al.*, 2003a; *Maddux et al.*, 2003b; *Venditti*, 2003; 2007; *Nabi et al.*, 2012; 2013c] have demonstrated that turbulence intensity is highly connected to the dune planform shape and crestline curvature. Additionally, *Parsons et al.* [2005] proposed that the morphology of the upstream dune is another controlling factor on the downstream form. However, links between the turbulence, dune 3D shape and sediment transport still remain poorly understood, and it highlights that there is an urgent requirement for quantifying them to advance our knowledge on overall dune dynamics and response to changes in flow stage [*Best*, 2005a].

Many past experimental studies on flow dynamics over dunes have focused on fixed beds under clear water conditions [*McLean et al.*, 1994; *Bennett and Best*, 1995]. It has the advantage that they allow detailed flow measurements without the complications of both a migrating and changing bedforms and the difficulties of flow measurement in the presence of sediment transport over a fully mobile bed [*Best and Kostaschuk*, 2002]. However, due to the presence of a dense sediment layer close to the bed and migrating secondary bedforms over the stoss side of the dune toward the dune crest [*Naqshband et al.*, 2014c], the near-bed flow and sediment processes are significantly different from the near-bed flow and sediment dynamics measured over fixed dunes, resulting in significant process gaps between the flume results and field observations [*Grant and Madsen*, 1982; *Naqshband*, 2014]. Therefore, more work is needed on mobile beds to accurately address links between the flow- and sediment-dynamics and dune development [*Best*, 2005a].

All natural fluvial environments exhibit perpetual variation in flows, resulting in the response of dune morphology and dynamics and variations in equilibrium bedform states [*Nelson et al.*, 2011; *Martin and Jerolmack*, 2013]. During flood events, the change of dunes (decay and growth) influences flood characteristics where the variability of bedforms, such as their height and shape [*Julien and Klaassen*, 1995; *Carling et al.*, 2000a; *Carling et al.*, 2000b; *Julien et al.*, 2002], changes roughness and influences river stage [*Parsons and Best*, 2013]. Furthermore, the hysteresis effect is known to differ for different flood wave shapes (sharp- or broad-peaked) [*Wilbers*, 2004; *Paarlberg et al.*, 2008]. Therefore, the key to fuller understanding the various dune adaptation to unsteady flows, such as superimposition, splitting and amalgamation [*Reesink et al.*, 2017], is accurately quantifying the physically-based hysteresis effect, which is still in its infancy [*Wilbers*, 2004; *Paarlberg et al.*, 2010; *Warmink et al.*, 2013; *Warmink*, 2014]. *Reesink et al.* [2017] proposed a comprehensive conceptual model to illustrate how dunes adapt to changing rates of water depth and velocity, which involves multiple processes: 1) the increase of flow velocity results in the increase of trough scour; 2) the increase of water depth enhances the occurrence of superimposition; and 3) the decreased flow depth flattens dunes. It also provides a basis for the understanding of the spatial distribution of dunes, as both flow and water depth varies in space and time [*Reesink and Bridge*, 2009; *Reesink et al.*, 2015].

There are a range of issues and interacting variables that are key to understanding dune dynamics and progress in this research area thus requires a complete understanding on the feedbacks between turbulence, dune form and sediment transport [*Best*, 2005a; *Parsons and Best*, 2013]. Herein, a series of mobile-bed ($D_{50} = 400\mu m$) flume experiments were designed and executed in a large recirculating flume, and the objectives of this study are: (1) to investigate what is the main factor that controls dune size across a range of different flow stages; (2) to investigate how dune morphology (size, shape and three-dimensionality) varies in response to changing flow depth and velocity; and (3) how the changing rate of hydraulic conditions affects the style and rate of dune adaptation?

3.2. Experiment design and data processing

Experiments were undertaken at the University of Hull's Total Environment Simulator

(TES) flume/wave tank facility. The TES is a large recirculating flume (16 m long, 2 m wide and 0.5 m deep) which was configured as a 1.6 m wide and 11 m long channel for the experiments (Figure 3-1). A baffle was installed at the upstream end of the channel to dissipate turbulence generated by the pumps and inlet and provide fully developed flow conditions. Water surface slope was controlled by a weir near the endbox to maintain uniform flow conditions for the test section. Additional slurry pumps were installed to enhance the movement of sand within the recirculating loop [*Reesink et al.*, 2017]. Twelve Ultrasonic Sensors (URSs) were mounted on a StebonTM 4.5m robotic traverse and set to move upstream and downstream automatically every 180 seconds to measure bed elevations over time. Sampling frequency was set at 3 Hz, resulting in the horizontal and vertical resolution at 10.7 and 0.5 mm respectively (Figure 3-1b). Water surface slope was measured along the channel at 2 Hz by 8 wave rods (HR Wallingford WG8 Twin-wire wave rod system), spaced 1 m apart (Figure 3-1a) along the channel. Five fixed Nortek ADVs, whose sampling rate was set to 25 Hz, were installed in order to measure flow velocities. One ADV was installed in the upstream inflow section at 40% of the water depth. Four ADVs were installed in the instrument box (Figure 3-1c) providing a stacked array to capture the velocity profile. An Acoustic Backscatter Sensor (ABS) system, with three frequencies of 0.5, 1 and 2 MHz, was also installed in the instrument box to monitor suspended sediment transport.

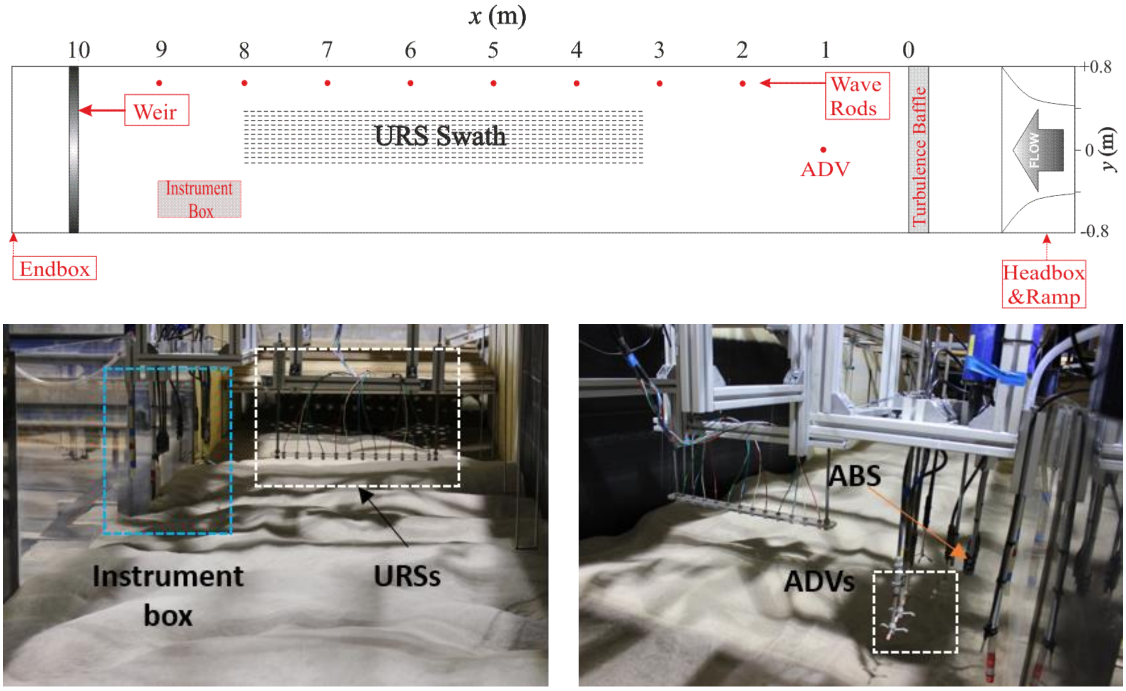

Figure 3-1. A) Diagram of the experimental set-up and photos of B) the drained flume bed, looking downstream, and C) instruments in the measuring box.

Six different basic state flow conditions, with two water depths and three flow velocities, were run. These were set based on the bedform phase diagram of *Southard and Boguchwal* [1990] to assure that dunes would be produced over the range of conditions (Figure 3-2 and Table 3-1). A total of 2250 kg narrowly graded, unimodal, washed and sieved white quartz sand with a median grain size D_{50}= 0.4 mm was added into the channel, providing a mean bed thickness of ~20 cm.

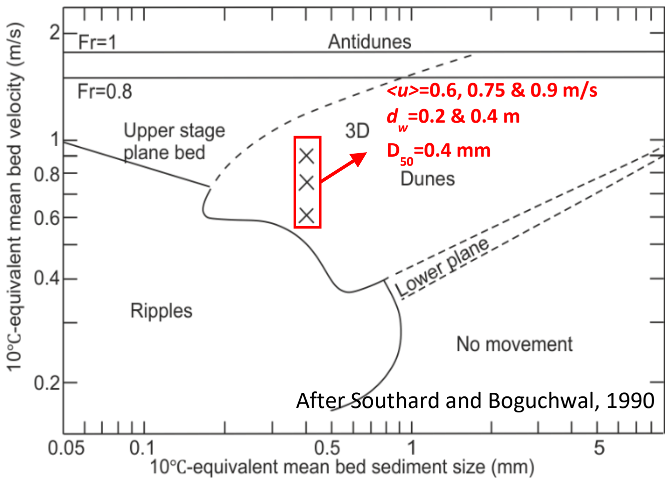

Figure 3-2. Hydraulic conditions in the bedform phase diagram (after Southard and Boguchwal, 1990).

Based on the six base states (S1 to S6), a series of experiments were run under imposed flow conditions (Appendix A). During the whole experiments, three different types of flow condition change were applied on both water depth and flow velocity: sudden, fast and slow change. A total of 18 experiments (a to r) with different flow condition change were explored and they were catalogued into four types: i) depth increase (and bed aggradation), ii) depth decrease (bed under degradation), iii) increasing discharge, and iv) decreasing discharge (错误!书签自引用无效。). For experiments a~g, the bed was roughly flattened before the experiments and they were used to analyze the initiation of the bedforms. However, for other ones, experiments were run over 6 hours under pre-imposed flow condition without any artificial destruction of the bed, afterwards, the designed flow condition change were applied. Discharge alterations were adjusted through the flume pump inverter, whilst water depth changes were achieved via addition or subtraction of water from the flume with pump system. For the series under gradual change, the time period of the rising limb for the fast and slow change was set at 72 and 153 minutes respectively, while that of the falling limb was 63 and 207 minutes, respectively. Both rising and falling limbs were divided into 16 steps with equal time and achieved step by step. After the flow conditions reached the designed values, experiments were run again over 6 hours under the post-imposed flow condition.

Table 3-1. Six basic flow conditions.

Name	d_w (m)	<*u*> (m/s)	*Q* (m^2/s)
S1	0.2	0.6	0.192
S2	0.2	0.75	0.24
S3	0.2	0.9	0.288
S4	0.4	0.6	0.384
S5	0.4	0.75	0.48
S6	0.4	0.9	0.576

Table 3-2. Summary of the 18 individual experiments. The time period of the rising limb for the fast and slow wave is 72 and 153 minutes, while that of the falling limb is 63 and 207 minutes, respectively. Each of the 18 experiments could be found in Appendix A. d is the water depth, u is the depth-averaged flow velocity and Q is the discharge. The subscript 1 and 2 indicate flow conditions for state 1 and state 2 for each experiment.

	Stages	d1 (m)	u1 (m/s)	Q1 (m3/s)	d2 (m)	u2 (m/s)	Q2 (m3/s)	u increased	u decreased	Q increased	Q decreased	Releveled	Sudden	Fast	Slow
a	S1-S4	0.2	0.6	0.192	0.4	0.6	0.384			√		√	√		
b	S3-S6	0.2	0.9	0.288	0.4	0.6	0.384		√	√		√	√		
c	S4-S5	0.4	0.6	0.384	0.4	0.75	0.48	√		√		√	√		
d	S4-S2	0.4	0.9	0.384	0.2	0.75	0.24		√		√	√	√		
e	S6-S3	0.4	0.9	0.576	0.2	0.6	0.192		√		√	√	√		
f	S2-S1	0.2	0.75	0.24	0.2	0.6	0.192		√		√	√	√		
g	S4-S1	0.2	0.9	0.288	0.2	0.6	0.192		√		√	√	√		
h	S1-S4	0.2	0.6	0.192	0.4	0.6	0.384			√			√		
i	S1-S4	0.2	0.6	0.192	0.4	0.6	0.384			√				√	
j	S1-S4	0.2	0.6	0.192	0.4	0.6	0.384			√					√
k	S2-S5	0.2	0.75	0.24	0.4	0.75	0.48			√			√		
l	S1-S6	0.2	0.6	0.192	0.2	0.9	0.288	√		√				√	
m	S1-S6	0.2	0.6	0.192	0.2	0.9	0.288	√		√					√
n	S4-S6	0.4	0.6	0.384	0.4	0.9	0.576	√		√					√
o	S4-S1	0.4	0.6	0.384	0.2	0.6	0.192				√				√
p	S4-S1	0.2	0.9	0.288	0.2	0.6	0.192		√		√			√	
q	S4-S1	0.2	0.9	0.288	0.2	0.6	0.192		√		√				√
−	S6-S4	0.4	0.9	0.576	0.4	0.6	0.384		√		√			√	

3.2.1. Quantification of bedform characteristics s

Post-processing was required to remove the noise: zero values and spikes induced by poor return voltages and localized suspended sediment respectively [*Unsworth*, 2015]. Two methods were utilized to detect noise: ‘bed slope detection’ and ‘3 bin wide moving detection'. Generally, in a sandy bed, bed slope should be always lower than the angle of repose. Therefore, positions whose bed slope larger than ±0.5 (±30°) were removed [*Lin and Venditti*, 2013]. Second, the noise was detected by setting a maximum threshold of the elevation difference between two successive pings. This threshold was set to 0.5 times the standard deviation of each time series and was applied across a 3 bin wide moving window [*Martin and Jerolmack*, 2013; *Unsworth*, 2015]. Figure 3-3 displays the results of data filtering. While the experiment was under higher discharge, high suspension significantly affects the quality of depth data from the URS, making extraction of depth data difficult.

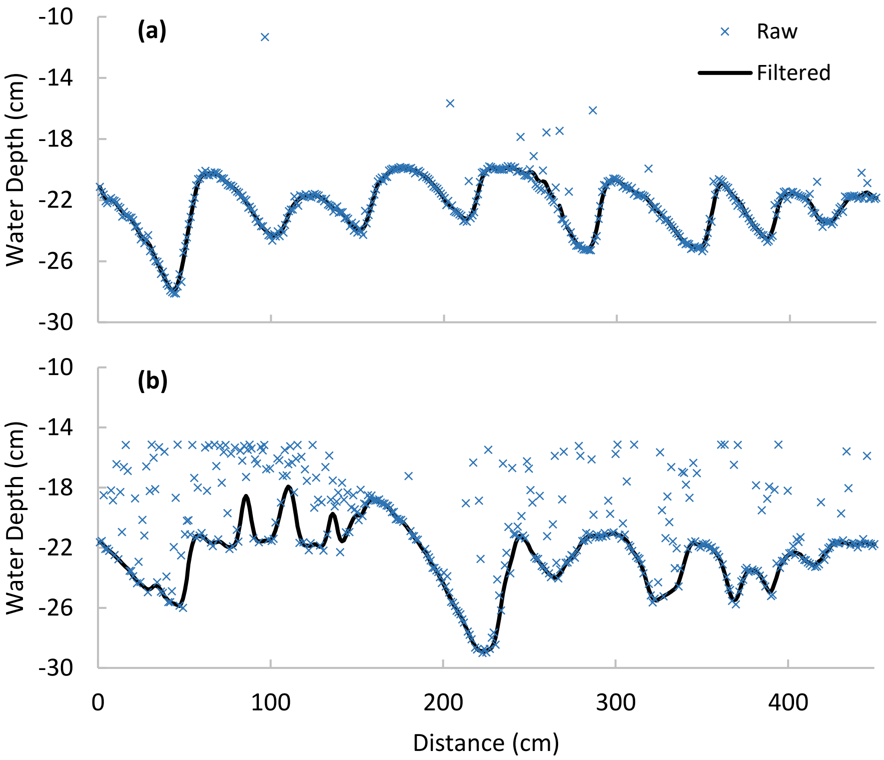

Figure 3-3. Depth sounder filtering: (a) example of bed profile under low discharge with slight suspension, and (b) example of bed profile under high discharge with significant suspension. Blue crosses are the original data, while black lines are the interpolated bed after filtering.

In terms of bedform geometry computation, individual bedform identification (IBI) was adopted [*van der Mark and Blom*, 2007], in order to generate objective data [*van der Mark et al.*, 2008] from each the 12 URS profiles. 'Zero-crossing' was used to identify crests and troughs for the filtered bed profiles [*van der Mark and Blom*, 2007]. Individual bedform height (H_i) was determined as elevation changes from troughs to downstream crests, while individual lengths (L_i) were calculated from inter-crest distances. Finally, all of the results obtained from the 12 URSs were averaged to calculate the spatially averaged values (H and L).

3.2.2. Transport stage

The dimensionless particle parameter (D_*) and dimensionless Shields stress (τ_*) are commonly used to determine sediment transport stages [*Van Rijn*, 2007; *Julien*, 2010]:

$$D_* = D_{50}\left[\frac{(s-1)g}{\nu^2}\right]^{1/3} \qquad 3\text{-}1$$

$$\tau_* = \frac{\tau}{(\rho_s-\rho_w)gD_{50}} \qquad 3\text{-}2$$

where D_{50}= median grain size, *s*= specific density (ρ_s/ρ_w, i.e. sediment density / water density, was assumed as 2650 kgm^{-3} and 1000 kgm^{-3}, respectively), g = gravitational acceleration and ν= kinematic viscosity coefficient.

Table 3-3. Summary of transport stages.

Condition	τ_*/τ_{*cr}	u_*/w_s
BLD	>3.3	<1
MXD	3.3~33	≥1
SSD	>33	≥1

The ratio of τ_* to $\tau_{*\mathrm{cr}}$ (the threshold for sediment entrainment) was used to determine sediment transport mechanisms [*Church*, 2006]: (1) $1 < \tau_*/\tau_{*cr} < 3.3$, bedload dominated (BLD); (2) $3.3 < \tau_*/\tau_{*cr} < 33$, mixed-load dominated (MXD); (3) $\tau_*/\tau_{*cr} > 33$, suspended-load dominated (SSD). However, the range of this parameter used to define sediment transport conditions was established empirically, thereby it was not intended to represent local particle dynamics [*Venditti et al.*, 2016]. The ratio of the shear velocity to the settling velocity (u_*/w_s, i.e. suspension threshold) is another useful parameter to define suspension event, whereby suspension occurs while $u_*/w_s > 1$ [*Bagnold*, 1966; *Abbott and Francis*, 1977; *Middleton and Southard*, 1984]. Therefore, combined both methods, sediment transport conditions were determined in Table 3-3.

The total boundary shear stress, τ_0, representing the sum of shear stresses, related to both bedform and grain size, was derived from the water slope:

$$\tau_0 = \rho_w ghS \qquad 3\text{-}3$$

in which, h denotes water depth and S indicates the water slope. In order to eliminate the sidewall effect, the empirical equation of *Williams* [1970] was adopted to correct the shear stress:

$$\tau = \frac{\tau_0}{(1+0.18h/w^2)} = \rho u_*^2 \qquad 3\text{-}4$$

where w means the width of flume, and u_* is shear velocity. The settling velocity was calculated followed with *Ferguson and Church* [2004] which works for all sizes of sediment:

$$w_s = \frac{RgD_{50}^2}{C_1\nu + (0.75C_2RgD_{50}^3)^{0.5}} \qquad 3\text{-}5$$

in which C_1 and C_2 are constants related to the shape and smoothness of the grains. For sieve diameters of natural grains, $C_1 = 18$ and $C_2 = 1$. R is submerged specific gravity = $(\rho_s - \rho_w)/\rho_w \approx 1.65$.

3.2.3. Sediment transport measurements

An automated method called 'lag distance detection' was applied to calculate translation distance between two consecutive alongstream profiles [*Nordin*, 1971; *Davis and Sampson*, 1986; *Jerolmack and Mohrig*, 2005]. As bedforms migrated continually downstream, measured bed profiles at different times were lagged by a distance called the translation distance. The sum of squared elevation discrepancy for each position was calculated for each lag distance. Translation distance between two surveys was taken as the lag distance that corresponded to the minimum value. Finally, 12 translation distances were averaged to get a spatially-averaged translation rate. This method can be applied when bedform migration and the translation is not significant between consecutive surveys [*McElroy and Mohrig*, 2009].

Simons et al. [1965] proposed an approach to compute sediment transport related to bedform translation:

$$q_T = \beta_b(1-p)V_bH \qquad 3\text{-}6$$

In which, p is the porosity of bed ($p = 0.4$), V_b is bedform migration speed, H is bedform height and β_b is the shape factor of bedforms. $\beta_b = 0.56$ is typical of asymmetrical bedforms [*Berg*, 1987; *Hoekstra et al.*, 2004; *Venditti et al.*, 2016]. Notably, this equation was built based on the assumption that bedforms migrate downstream without changes in the shape, size and spacing [*Lin and Venditti*, 2013].

3.2.4. Bed texture characterization

The influence of dune three-dimensionality in planform and cross-sectional morphology is one of the key challenges in bedform research. However, until recently, quantifying the 3D dune morphology has not been adequately addressed [*Best*, 2005a]. Technologies used by previous research [Allen, 1968a; Ashley, 1990; Venditti, 2003] have often meant that subjective procedures are required to identify certain crestlines prevent the universal use [*Friedrich*, 2010; *Coleman and Nikora*, 2011]. Most recently, the 2D autocorrelation method has been verified as a potentially effective tool to assess 3D characteristics of bedforms [*Nordin*, 1971; *Coleman and Nikora*, 2011], although more data should be applied to define the more exact thresholds for bedform transitions [Friedrich, 2010]. The 2D autocorrelation function was developed based on the normalised spatial 1D autocorrelation function (more details can be found in chapter 3.2.2 of Friedrich [2010]), defined as:

$$R(\Delta x, \Delta y, 0) = \frac{\sum_{i=1}^{N-k} \sum_{j=1}^{M-l} (z(x_i, y_j) - \bar{z})(z(x_{i+k}, y_{j+l}) - \bar{z})}{\sigma^2} \qquad 3\text{-}7$$

where z is topography data along x and y direction, which indicates along or across the channel. σ is the standard deviation for the random field. The 2D autocorrelation of topography reveals the 3D character of a recorded bed by characterising crests and troughs in *x*- and *y*-direction, respectively. The contour plot of the 2D autocorrelation function (Figure 3-4) highlights the existence of elliptical shapes at level of 50% around the centre, and both bedform size in *x*-direction and *y*-direction and spatial bedform alignment can be obtained by analysing the shapes of the ellipse [*Friedrich et al.*, 2006].

Five main parameters were marked: a and b are the major and minor axis of the ellipse; $x0$ and $y0$ are the longitudinal and transverse distance of the ellipse and θ means the angle of rotation of the ellipse. 2D dunes potentially have an infinite ratio a/b, while similar lengths along and cross channel result in $a/b \cong 1$ and the difficulty in θ assessment [*Coleman and Nikora*, 2011]. $\sin\theta$ is the parameter to determine the direction of crestline relative to flow: $\sin\theta$ tends to zero under flow-aligned pattern, whereas to unity under flow-normal condition [*Goring et al.*, 1999]. Moreover, *Friedrich* [2010] proposed that bedforms are wall-influenced when $x0/y0 < 1$, while flow-depth-influenced when $x0/y0 > 1$. Therefore, the distribution of the ratio $x0/y0$, a/b and θ trough time could reflect how bedforms develop and could be employed to investigate which factor affects dune three-dimensionality [*Coleman and Nikora*, 2011].

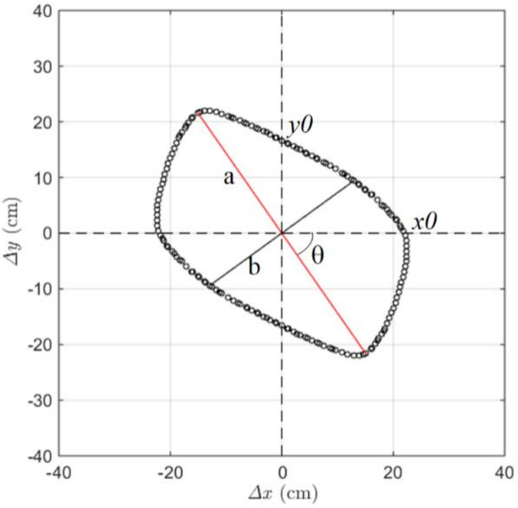

Figure 3-4. Schematic display of geometrical information describing the shape of the ellipse at a contour level of 50% for the 2D autocorrelation function for bedform development of experiment E13 at minute 444.

3.3. Results

In order to fully investigate dune evolution under the varying flows, dune longitudinal profiles of the middle probe (No. 6) were selected to present the continuous dune adaption (migration and deformation). For each survey, dune profiles between 1 hour prior to the imposed flow and depth changes and 3 hours after the changes were analysed, except those experiments whose bed were releveled to rough flatbed (Figure 3-5). Furthermore, bed elevation (Figure 3-6) and bedform features (Figure 3-7) were averaged from twelve bed profiles, and their variation could be used to represent bed state and any bed elevation changes, in terms of depth increase (aggradation) or depth reduction (degradation). Variation of bed elevation led to the different flow conditions along the channel (black lines in Figure 3-6). Additionally, dune deformation based on the residuals of the cross-correlation of consecutive profiles was plotted in sequence to visualise the relative changes between dunes while they were migrating downstream (Figure 3-8). Averaged sediment flux related to bedform migration is also plotted in Figure 3-9. The effects of the flow, bed conditions and topography were further analysed to better understand how bedforms response to the changing flows.

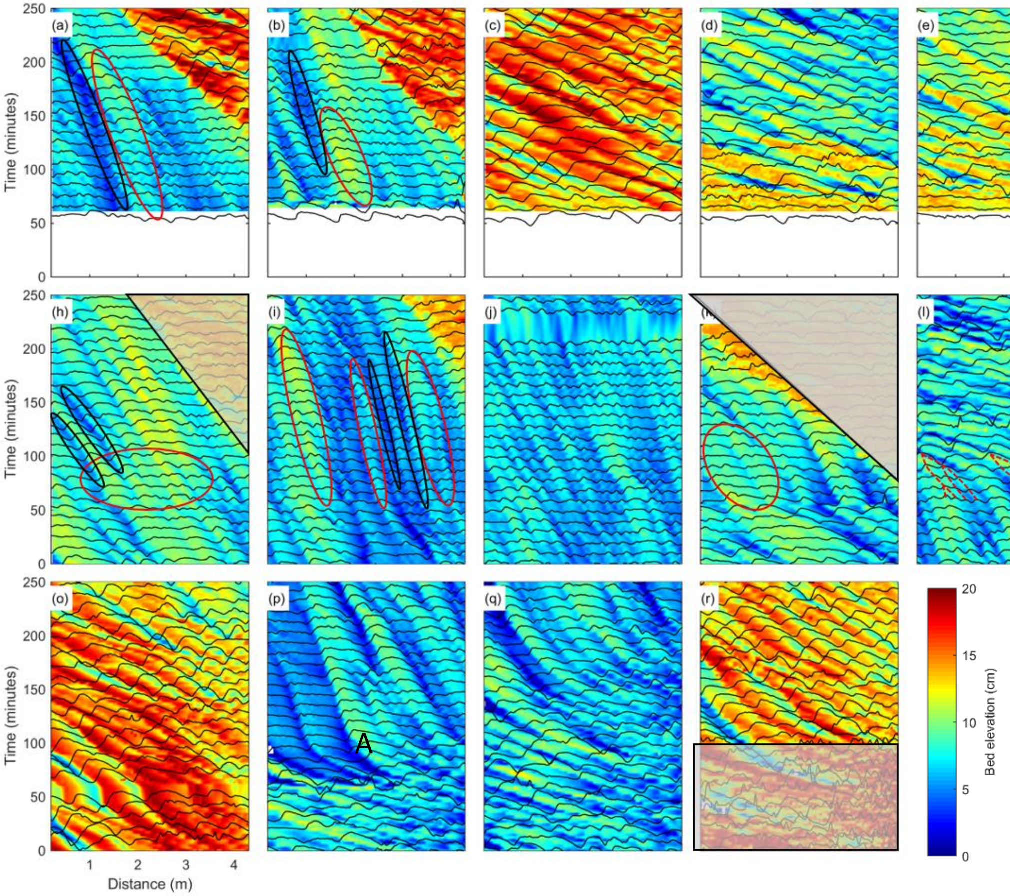

Figure 3-5. Consecutive bed elevation profiles plotted over time and coloured by bed elevation for the 18 experiments. Results illustrates the development of the bedforms and changes in time and space. The profiles depict bed profiles 60 minutes prior to the change in flow conditions and 180 minutes post-change conditions. Flows come from the right to left. Areas marked by grey are where profiles are significantly affected by high suspension and thus measurements are suspect. Red ovals indicate where sediment accumulation occurs and then large scale bedforms generate. Black ovals with solid lines denote that small dunes behind or over the leeside of the large dunes are washed out. Red dashed lines represent how bedforms grow and merge. Dune A, B and C denote three specific dunes which will be discussed in the discussion section.

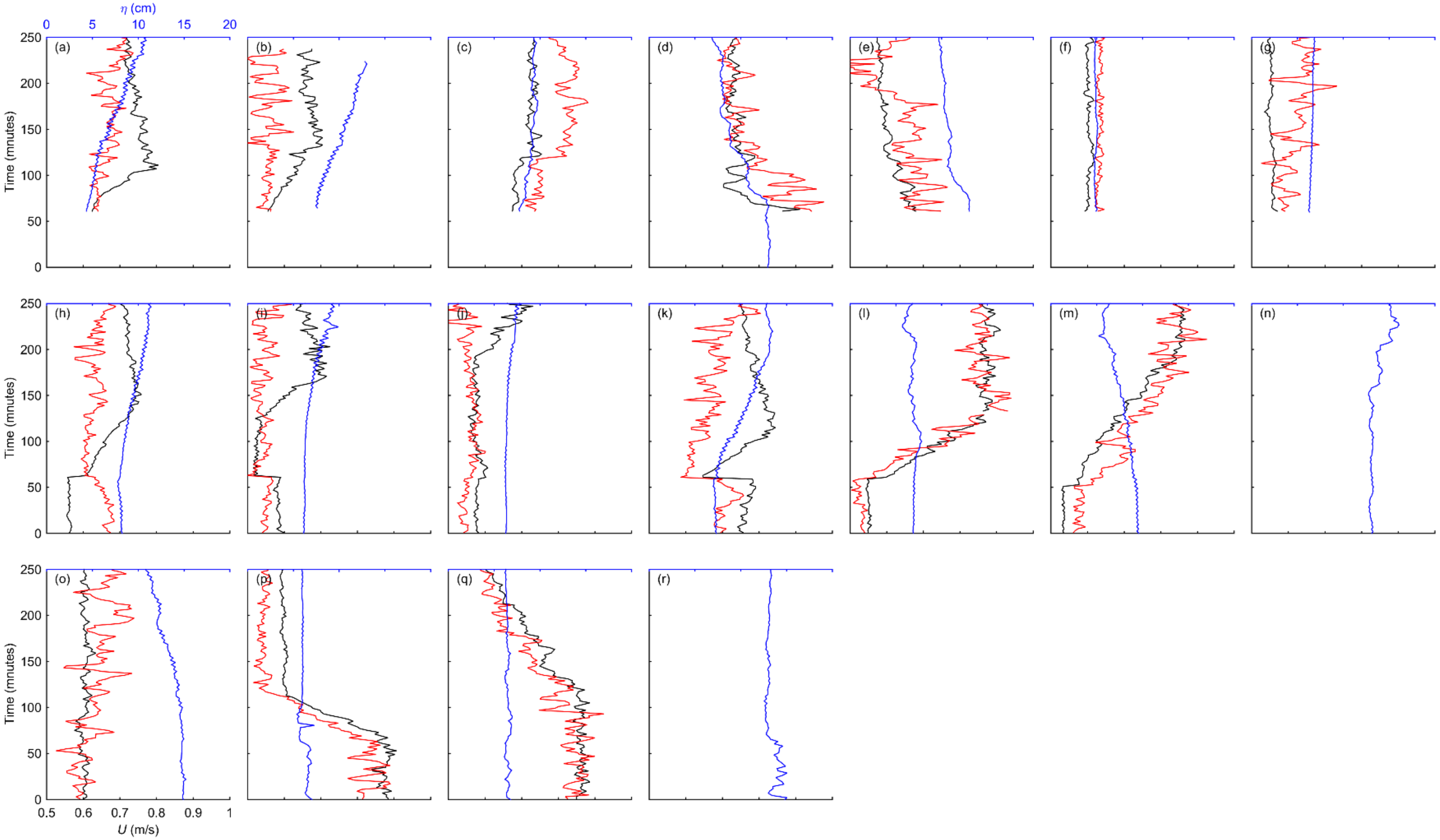

Figure 3-6. Variation of flow velocities over time for the 18 experiments (upstream location in black and downstream in red) and mean bed elevation (blue lines) over time. Bed elevation increase indicates bed aggradation, in contrast, bed elevation decrease means bed degradation. Note that for some cases, such as b, the sudden change of flow velocity at 60 minutes was observed. That is because sometimes experiments were stopped at the end the first day and restart on the second day. There is no velocity data available for experiment n and r.

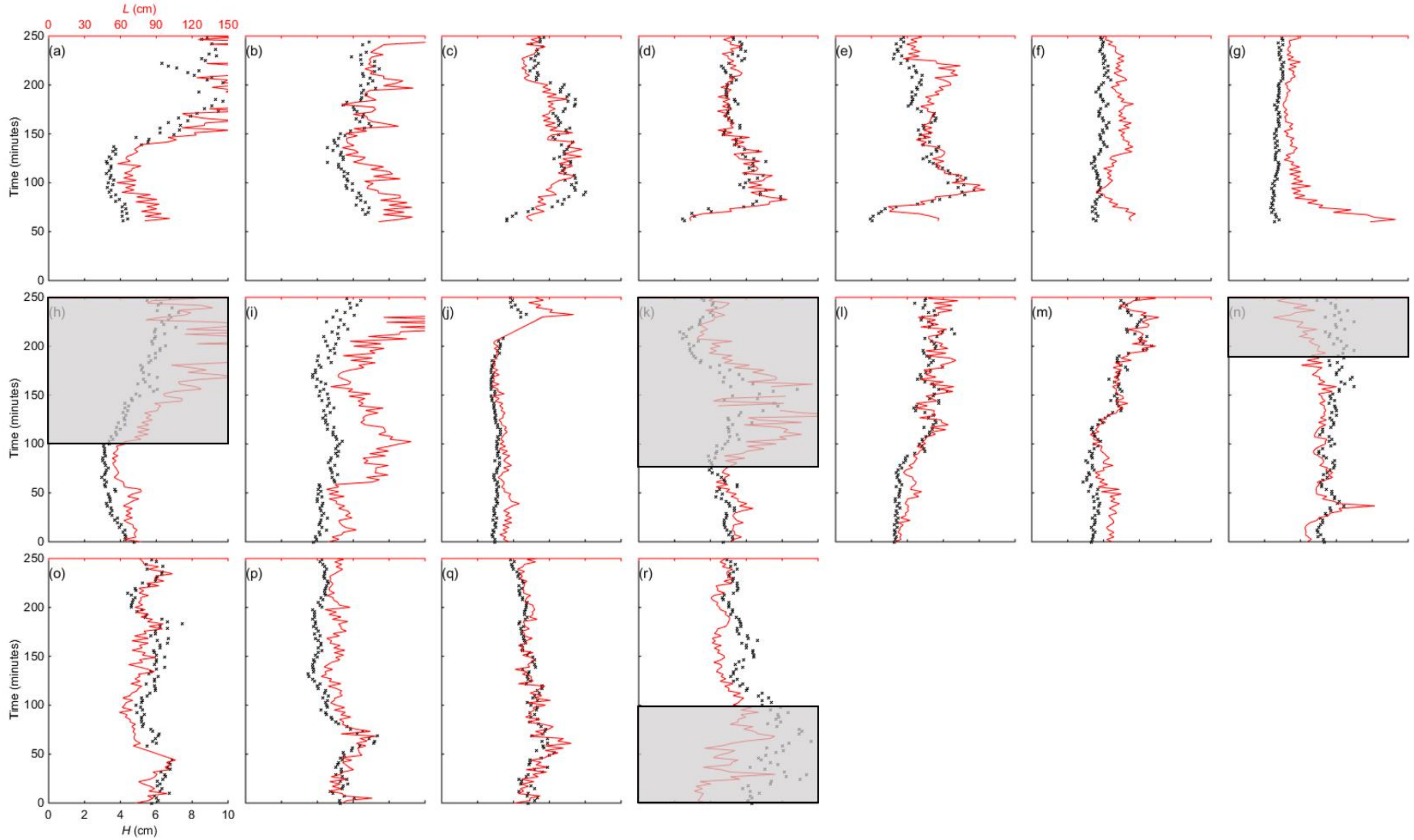

Figure 3-7. Variation of bedform features: height (black lines) and wavelength (red lines) for the 18 experimental runs. Areas marked by grey are where profiles are significantly affected by high suspension and thus measurements are suspect.

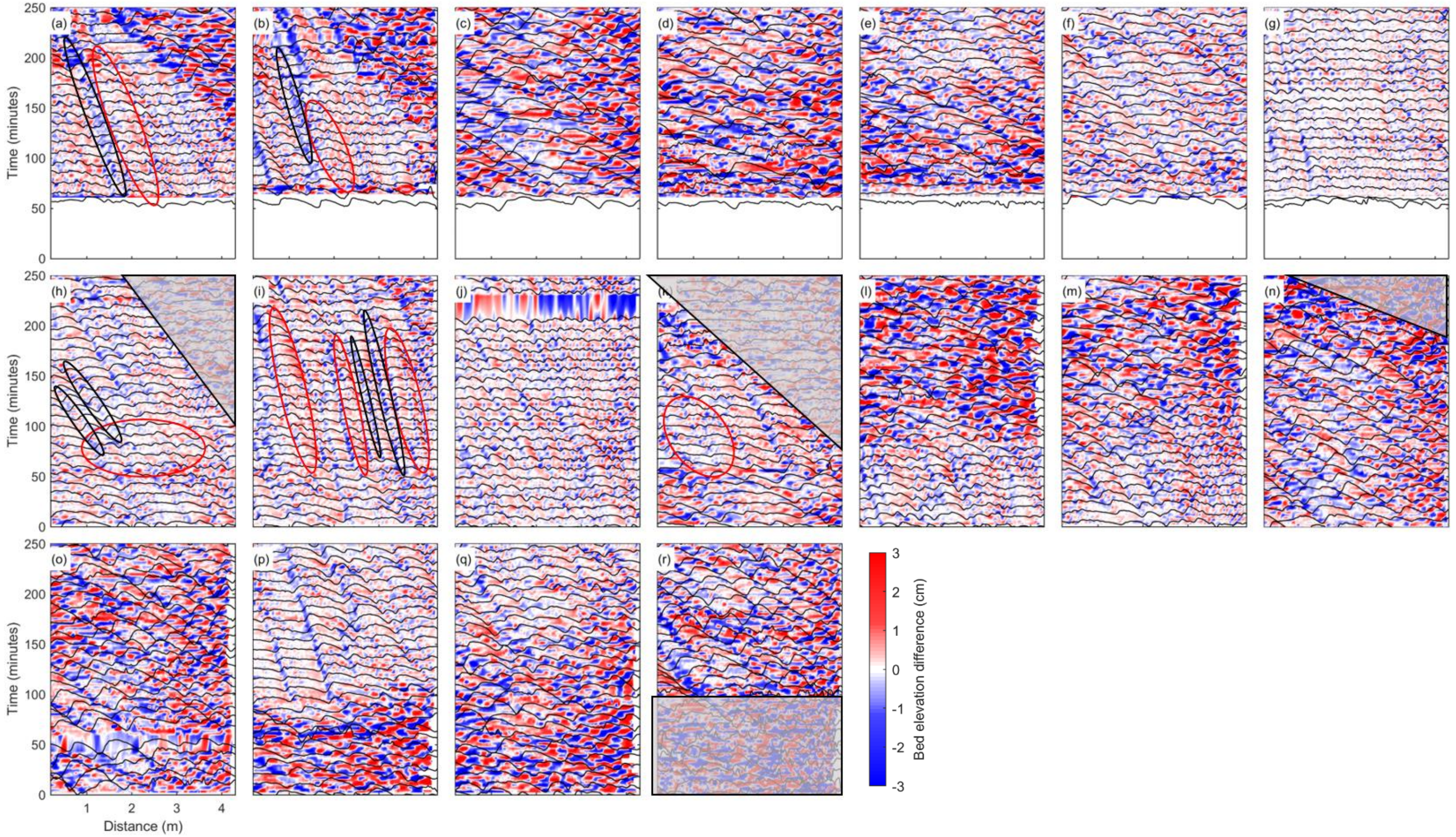

Figure 3-8. Consecutive profiles plotted over time and coloured by bedform deformation for the 18 experimental runs. Red ovals indicate where sediment accumulation occurs and then large scale bedforms generate. Black ovals with solid lines denote that small dunes behind or over the leeside of the large dunes are washed out. Flows come from the right to left. Areas marked by grey are where profiles are significantly affected by high suspension and thus measurements are suspect.

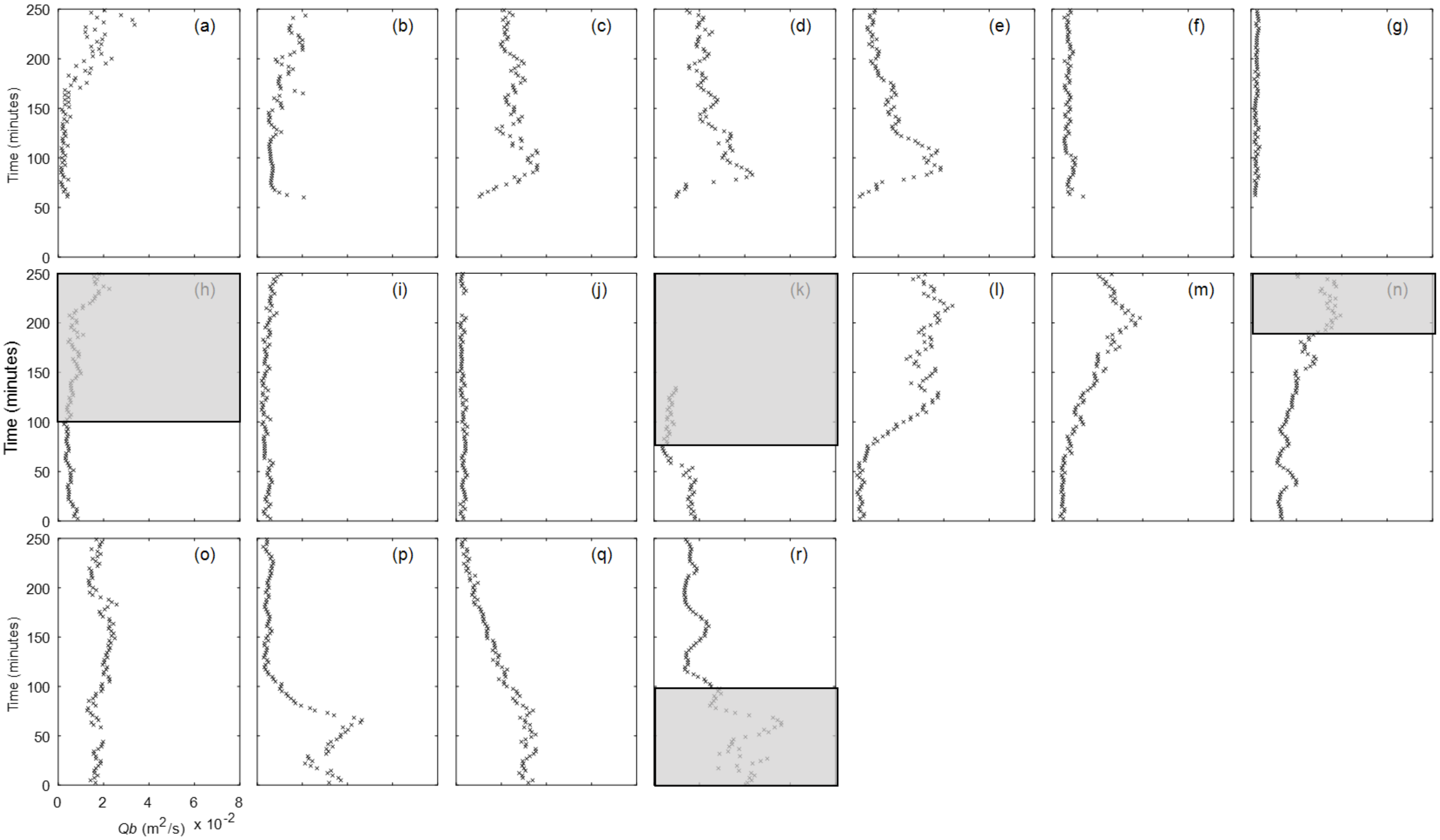

Figure 3-9. Variation of sediment flux related to bedform migration for the 18 experimental runs. Areas marked by grey are where profiles are significantly affected by high suspension and thus measurements are suspect.

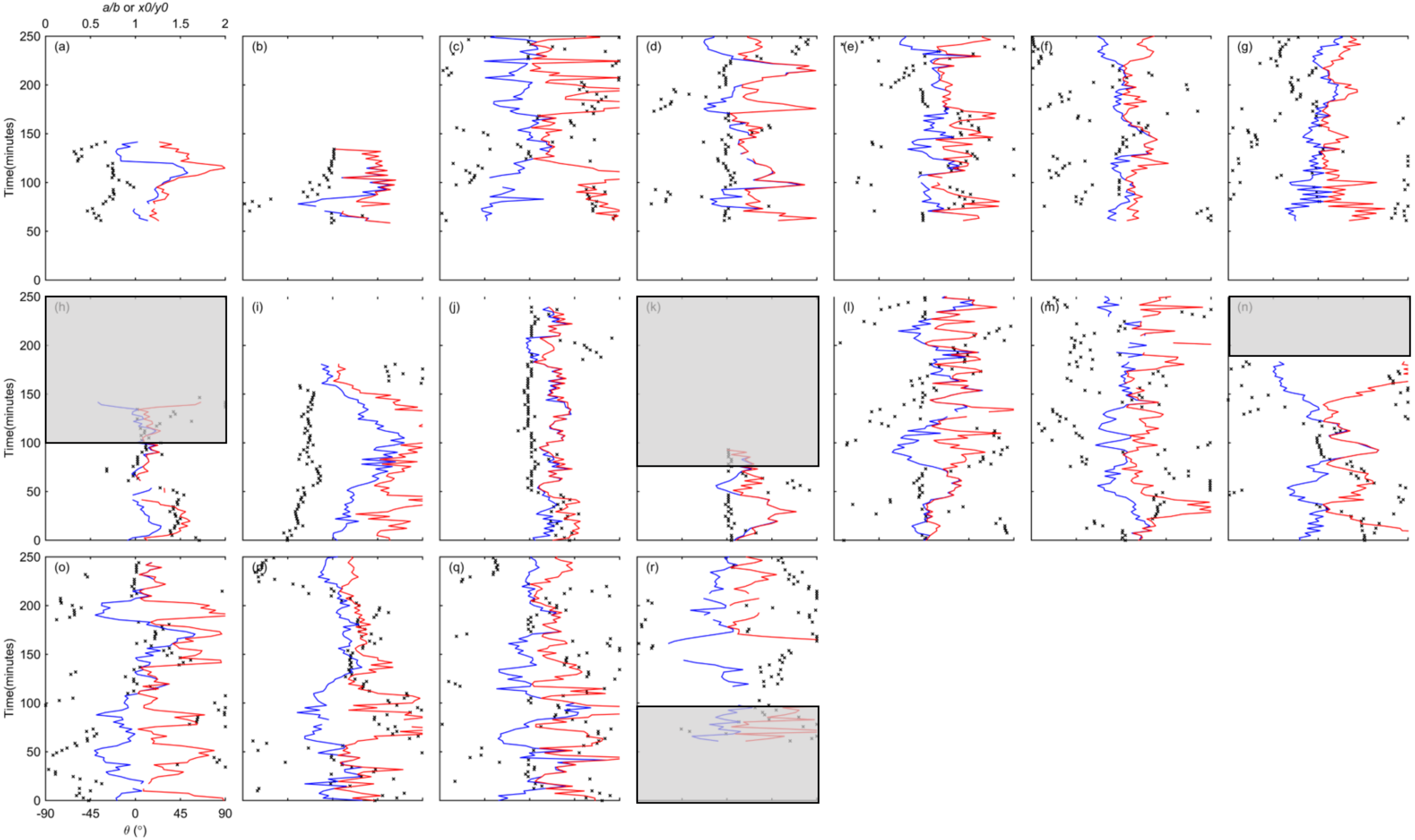

Figure 3-10. Variation of bedform 3D texture features: θ (black crosses) and ratios of a/b (blue lines) and x0/y0 (red lines) for all 18 experimental runs. Areas marked by grey are where profiles are significantly affected by high suspension and thus measurements are suspect.

3.3.1. Bed respond to flow changes

All experiments were catalogued into four types: bed under aggradation (i.e. water depth increase), degradation (i.e. water depth decrease) and bed elevation under equilibrium but increasing (i.e. flow velocity increase) or decreasing (i.e. flow velocity decrease) discharge (Based on the six base states (S1 to S6), a series of experiments were run under imposed flow conditions (Appendix A). During the whole experiments, three different types of flow condition change were applied on both water depth and flow velocity: sudden, fast and slow change. A total of 18 experiments (a to r) with different flow condition change were explored and they were catalogued into four types: i) depth increase (and bed aggradation), ii) depth decrease (bed under degradation), iii) increasing discharge, and iv) decreasing discharge (错误!书签自引用无效。). For experiments a~g, the bed was roughly flattened before the experiments and they were used to analyze the initiation of the bedforms. However, for other ones, experiments were run over 6 hours under pre-imposed flow condition without any artificial destruction of the bed, afterwards, the designed flow condition change were applied. Discharge alterations were adjusted through the flume pump inverter, whilst water depth changes were achieved via addition or subtraction of water from the flume with pump system. For the series under gradual change, the time period of the rising limb for the fast and slow change was set at 72 and 153 minutes respectively, while that of the falling limb was 63 and 207 minutes, respectively. Both rising and falling limbs were divided into 16 steps with equal time and achieved step by step. After the flow conditions reached the designed values, experiments were run again over 6 hours under the post-imposed flow condition.

Table 3-1. Six basic flow conditions.

Name	d_w (m)	$\langle u \rangle$ (m/s)	Q (m^2/s)
S1	0.2	0.6	0.192
S2	0.2	0.75	0.24
S3	0.2	0.9	0.288
S4	0.4	0.6	0.384
S5	0.4	0.75	0.48
S6	0.4	0.9	0.576

Table 3-2).

The change of pump speed and water column alters the total sediment flux in the main channel, as sediment input and output alter with resuspension and how much sediment passes over the mobile bed. In short, in the recirculating flume, the rate and composition of the sediment entering the flume are determined by some degree by the (selective) transport process [*Parker and Wilcock*, 1993; *Kleinhans*, 2005b]. As a consequence, bed aggradation or degradation occurs, when sediment transport rate exceeds or lags behind the upstream sediment supply [*Reesink and Bridge*, 2007]. As such these effects need to be monitored and accounted for when interpreting the results.

Previous research [*Kleinhans et al.*, 2002; *Kleinhans*, 2005b; *Reesink and Bridge*, 2007; *Tuijnder et al.*, 2009] has demonstrated that sediment mixtures significantly affect dune generation, evolution, and irregularity both in feed and recirculation flumes. The armour layer, composed of coarser bed material, is largely stable in a recirculation flume, whereas it is mobile in a feed flume. The bed material used in this study is relatively uniform (narrow mixture), thereby the armour layer induced hysteresis effect or vertical sorting is likely, not significant and sediment entering the flume section is independent of the flow discharge, and the generation of the larger dune or bar features (see Figure 3-5) is related to variations in sediment supply, rather than armouring due to sediment mixtures.

In a flume experiment, when the sediment feed from the upstream exceeds the capacity of sediment transport, unit bars develop (e.g. [*Reesink and Bridge*, 2009]). Herein, in experiments with imposed water depth increase, bed aggradation was observed. The self-fed sediment deposited (settled) quickly at the upstream inlet zone and the sediment transport rate was lower than the sediment deposition rate. As a consequence, the deposition of sediment at the upstream section of the channel results in an increase in the upstream bed elevation, thereby decreasing the water depth but increasing the flow velocity and shear stress, leading to the generation of unit bar (up to 0.16 m in height). Large dunes (6~12 cm in height and 45~70 cm in length) were generated over the back of the unit-bar, similar, but larger, than those observed in *Reesink and Bridge* [2009]. *Reesink and Bridge* [2009] observed that larger water depths allows the development of larger superimposed dunes on the back of the unit bar.

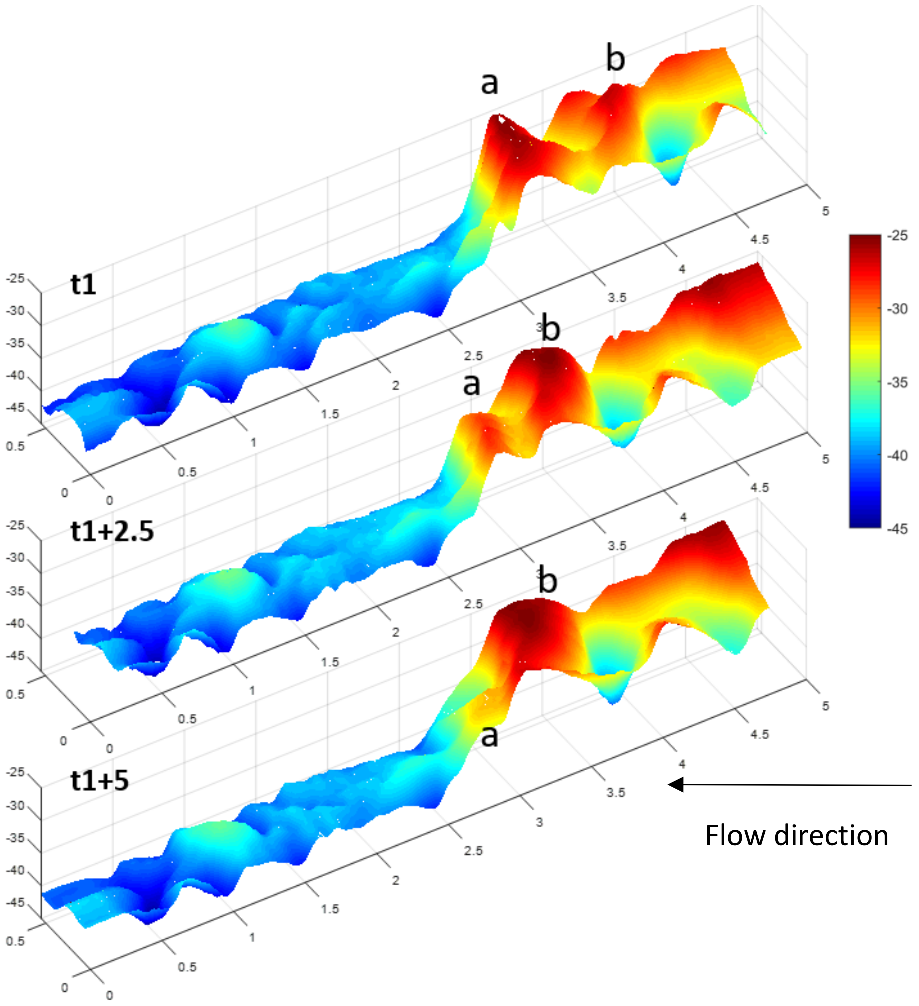

Figure 3-11. Visualization of bed topography under bed aggradation for the experiment a at time t, t+2.5 and t+5 minutes. Dune b migrated faster than dune a, and they interplayed at t+2.5 that dune b grew while dune a decayed and died out later on at t+5. This interaction was referred to dying-out [Gabel, 1993].As mentioned above, while the experiments are under higher discharge, the triggered high suspension significantly affects the measurement results of bed profiles. Moreover, data analysis, such as bed migration and 3D texture, highly depends on the accuracy of bed data. Therefore, bad data were picked out (grey shaded areas) and following analysis related to those bed profiles were removed.

Additionally, the interaction of the large dunes at the unit-bar front controlled the processes related to how sediment moved downstream (Figure 3-11). Herein, the area where bed elevation displays a significant increase is defined as the bar area (BA), and where with little elevation change was regarded as the normal area (NA). During the runs BA migrated downstream with some of the suspended sediment deposited in the NA, as the bar was attenuated during migration. This is also reflected in Figure 3-8 which shows how bed elevation differs between consecutive profiles and are positive in the NA zone. However, the effect of the sediment supply in the NA was constrained by the generation of larger scale dunes. The dunes were quite sensitive to local bed elevation, where sediment was accumulated on the stoss-side of high relief, leading to the generation of larger dunes, thus starving downstream sections. As a consequence, the trough of the high relief dunes was further scoured (Figure 3-5 and Figure 3-8). Thereby, sediment for the area in the downstream of the trough was supplied by the trough scouring, rather than by the bypass sediment from the BA. Moreover, the generation of deep trough scour slowed the migration speed of the high relief bedform. Some small dunes over high relief bedform did pass through but tended to be washed out in the less-side, which further slowed down crest migration speed (e.g. black and red ellipses in Figure 3-5a and b).

Unlike experiments with increasing depth and a sediment supply exceeding capacity to transport, the decrease of water depth results in the reduction of sediment supply (supply-limited, sediment passing the main channel exceeds sediment supply). As a consequence, the higher sediment transport leads to bed degradation. The upstream bed responded to this change more quickly. However, the effect of sediment supply-limitation on bedforms gradually weakened downstream, as eroded sediment from upstream fed the bedform development downstream, results in some instances of bed increasing the size of dunes downstream (Figure 3-5d, e and o).

Additionally, without imposed water depth change, changes in flow velocity did not alter sediment supply rates and no significant variation of mean bed elevation was detected in these runs (Figure 3-6).

3.3.2. 3D characteristics of dunes

Figure 3-10 displays the variation of θ (black crosses) and ratios of a/b (blue lines) and $x0/y0$ (red lines) for bedform development of each experiment. These parameters were computed from the shape of the ellipse at a contour level of 40% for the 2D autocorrelation function. It is obvious that both θ and a/b in runs with slower bedform migration rate remain relatively stable (a, b, g, h, I and j), whereas those in experiments with faster migration display relatively intense fluctuation (such as c, o and q). Moreover, in some experiments (e.g. experiment *i*), rotation of θ was observed, coupled with $x0/y0$ fluctuating around 1.

When lengths along- and cross-channel are similar, resulting in $a/b \cong 1$, θ is hard to be assessed [*Coleman and Nikora*, 2011]. If dunes are relatively two dimensional across the channel, *b* should be slightly larger than 55 cm, which is the measuring range of URSs across the channel. In some periods, the wavelength is nearly 55 cm (Figure 3-7), which will lead to somewhat misleading artifacts in the data processing method. More details on how these parameters change with dune evolution was analysed in the next section.

3.3.3. Dune dynamics

3.3.3.1. Dune dynamics under bed aggradation

For experiments *a-b* and *h-k* (Based on the six base states (S1 to S6), a series of experiments were run under imposed flow conditions (Appendix A). During the whole experiments, three different types of flow condition change were applied on both water depth and flow velocity: sudden, fast and slow change. A total of 18 experiments (a to r) with different flow condition change were explored and they were catalogued into four types: i) depth increase (and bed aggradation), ii) depth decrease (bed under degradation), iii) increasing discharge, and iv) decreasing discharge (错误!书签自引用无效。). For experiments a~g, the bed was roughly flattened before the experiments and they were used to analyze the initiation of the bedforms. However, for other ones, experiments were run over 6 hours under pre-imposed flow condition without any artificial destruction of the bed, afterwards, the designed flow condition change were applied. Discharge alterations were adjusted through the flume pump inverter, whilst water depth changes were achieved via addition or subtraction of water from the flume with pump system. For the series under gradual change, the time period of the rising limb for the fast and slow change was set at 72 and 153 minutes respectively, while that of the falling limb was 63 and 207 minutes, respectively. Both rising and falling limbs were divided into 16 steps with equal time and achieved step by step. After the flow conditions reached the designed values, experiments were run again over 6 hours under the post-imposed flow condition.

Table 3-1. Six basic flow conditions.

Name	d_w (m)	$\langle u \rangle$ (m/s)	Q (m^2/s)
S1	0.2	0.6	0.192
S2	0.2	0.75	0.24
S3	0.2	0.9	0.288
S4	0.4	0.6	0.384
S5	0.4	0.75	0.48
S6	0.4	0.9	0.576

Table 3-2) when the water depth was increased, the bed elevation displays an increasing trend (Figure 3-5 and Figure 3-6). The varying rate of bed elevation is related to both the magnitude and varying rate of the flow velocity. Experiment *k*, which had a sudden change and the highest post-change velocity (0.75 m/s), shows the fastest increase of the bed elevation, while experiment *j*, which had a slow change but with a constant flow velocity, displays the slowest change in bedform size (Figure 3-6).

The larger scale bedforms are firstly generated at the upstream section of the flume where the bed elevation and flow velocity are much higher (Figure 3-6). In contrast, at the downstream end where bed elevation and flow velocity are smaller, the bedforms are much smaller, although flow discharge is the same for the whole channel.

In terms of the bed profiles in the NA, both bedform initiation and development, in experiments with the increase of water depth, was found to be very sensitive to the local bed elevation. After the change of water depth, sediment accumulation (marked by red ellipses in Figure 3-5 and Figure 3-8) was observed over bedforms on the high relief (mound, whose length is normally more than 3 times of the length of the superimposed bedforms). The sediment coming from the upstream accumulated in the stoss of the high relief, leading to the sediment starvation of bedforms located downstream of the high relief, thereby resulting in the increase of trough scour (marked by black ellipses in Figure 3-5 and Figure 3-8). Furthermore, the most downstream bedform developed over the high relief generally diminished and finally vanished in the trough as the 'nourishment' for the bedforms in the downstream.

As the 2D autocorrelation function is relatively sensitive to the bed elevation, especially across the channel, the generation of the bar will significantly affect computational result and accuracy. Where measurements combined the NA and BA thus were removed, and the analysis of 3D texture is only focused on NA before the bar enters into our measuring area. Sediment transport related to bedform migration and deformation was found to be relatively small (Figure 3-9 and Figure 3-8), indicating both the variations of bedforms along and cross the channel are little. This result verifies that θ is varying between -30 and 30° with little fluctuation (Figure 3-10).

For experiment *a*, *b* and *i*, where the mounds existed in the initial bed, leading to the development of small dunes or ripples. Their a/b (>1.3) is relatively larger than that

($a/b < 1.3$) of experiment *j*, where ripples were regularly developed with no mounds observed (Figure 3-5).

3.3.3.2. Dune dynamics under equilibrium but increasing discharge

Without imposed water depth change (*c* and *l*~*n*), the bed elevation remains relatively stable, except in experiment *m* whose elevation declined (Figure 3-6). That is because, the flow condition for the first hour of experiment *m* was changed from S6 to S1, whose flow velocity is the lowest and thus bed response rate is relatively slow (refer also to experiment *e* and *o*). Therefore, the bed did not have sufficient time to recover (reach equilibrium) for a water depth at 0.2 m. After the new flow condition (0.9m/s) was imposed, the bed remained erodible as the sediment fed in the channel was less than the sediment moving downstream and depositing in the rear tank.

Bedform merging was commonly observed after the flow velocity was increased. Especially, in the shallow water experiments (*l* and *m*), bedforms were relatively sensitive to the local bed elevation, particularly over the high relief crests, which merged rapidly (marked by dashed red lines in Figure 3-5). This is also reflected in the variation of bedform features (Figure 3-7) that both bedform height and length increased with the change of flows. In contrast, in experiment *n* where bedforms were under deep water, the dune length displayed a slight decrease while dune height remained constant. Furthermore, in experiment *n*, individual dunes deformed dramatically such that they either attenuated or split in a short time (Figure 3-5).

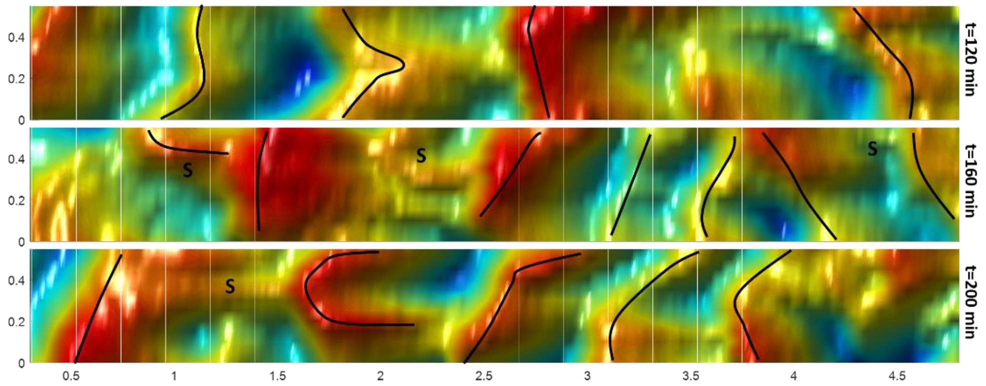

Figure 3-12. Visualization of bed topography experiment c at time t=100, 150 and 200 minutes. The black lines denote orientation of crestlines. Red colour indicates higher elevation while blue colour is lower elevation. S denotes Spur. Flow direction is from right to left.

Sediment transport related to bedform migration is relatively large (2~3×10^{-2} m^2/s)

(Figure 3-9), and parameters of 3D texture display significant fluctuations (Figure 3-10). Moreover, θ of experiment *c* and l both shows a rotation from around -80° to 80°, indicating that the orientation of crestline varies greatly but regularly. Figure 3-12 displays the topography of experiment *c* at *t*=100, 150 and 200 minutes when θ is -50°, 0° and 60°, respectively. This result corresponds well with the variation of the orientation of crestlines, which largely varies from left- to right-skewed.

3.3.3.3. Dune dynamics under depth decrease (bed degradation)

In contrast to the experiments with a water depth increase, the bed elevation of experiments *d, e* and *o* with water depth decrease (from 0.4 to 0.2 m) display an increasing trend (Figure 3-6). Unlike bed aggradation where bed elevation is caused by the migration of a bar (an abrupt increase boundary, dividing bed profiles into two parts: BA and NA), the bed elevation under a reduction in depth resulted in bed degradation, but at a lower bedform adjustment rate with no obvious boundary indicating the sudden change in conditions within the bed elevation changes (Figure 3-5).

Bedforms, in experiment *d* and *e*, initiated quickly through the generation of deep scours (Figure 3-5) and reached the maximum within 40 minutes with 8 and 120 cm in height and length respectively. In contrast, the decreasing rate of the mean bed elevation was greatest during dune growth, followed by a slight decrease of both dune size and bed elevation (Figure 3-6). Meanwhile, the sediment flux related to dune migration shows a similar trend with the variation of dune size (Figure 3-9). Under a certain flow discharge, the variation of the bed elevation altered the flow depth and flow strength, thereby the capability of sediment transport. Moreover, θ of experiment *d* was largely remained around 0° between t= 100 and 180 minutes, while that of experiment *e* nearly 40° (Figure 3-10), when dunes were decaying (Figure 3-7).

The results indicate that after the change of flow condition, bedforms in the upstream section of the flume responded to the new conditions more quickly, shown by the way in which bedforms there decreased and became smaller than those in the downstream (Figure 3-5). In contrast, bedforms in the downstream section generally maintained their size or even slightly grew, supported by the sediment sourced by the degradation from the upstream section. Therefore, bedform size displays a decreasing trend from the upstream to downstream. In a similar circumstance, smaller bedforms move faster than the larger ones, leading to the bedform amalgamation: such as bedform passing through or merging. Consequently, with bedforms migrating downstream, the bed elevation gradually declines (Figure 3-6).

3.3.3.4. Dune dynamics under equilibrium but decreasing discharge

In experiments without imposed water depth changes but with flow velocity decrease imposed, there is no obvious variation of the spatially-averaged bed elevation (*f, g* and *p-r* in Figure 3-6). Experiment *f* and *g* were re-flattened before a new flow condition was imposed, but their initial deviations of bed elevation were different (Figure 3-5). Bedforms developed from the relatively uniform flatbed (experiment *f*) were smaller (H=3.5 cm and L=55 cm) than those generated from an uneven bed, which were relatively larger (H=4 cm and L= 65cm, experiment *g* in Figure 3-7). Moreover, sediment transport of experiment *f* was found to be higher than that of experiment *g* (Figure 3-9), which also could be reflected by the slope of bedform migration in Figure 3-5. θ of both experiment f and g is largely very high, over 60°, while $x0/y0$ is small, fluctuating around 1 (Figure 3-10).

In experiment *p*, with a fast velocity decrease under shallow water, bedform height decreased quickly from 6.2 to 4 cm, while the decrease of wavelength was slower from 90 to 70 cm (Figure 3-7). A similar evolution in bedform change was observed in experiment *r* with fast velocity decrease under deep water. Furthermore, bedform height decreases was caused by both troughs filling in and crest erosion (Figure 3-5). Moreover, bedform superimposition was only observed in the experiments under shallow water. In terms of bedform 3D textures, the variation of θ was found to be smoother in the experiments with a fast decrease (*p* and *r*), while more noise was observed for experiment *q*, which had a slow decrease imposed (Figure 3-10).

3.4. Discussion

3.4.1. What controls the size of dunes?

Relationships between bedform characteristics (height *H* and length *L*) and flow conditions (velocity *U* and water depth *h*) were summarized in Figure 3-13. In general, under subcritical flow conditions, flow velocity plays a key role in bedform size. Flow depth also plays a role, with larger dunes found for experiment *a~c* and *h~k* under deeper water. Moreover, the relatively large standard deviation of wavelength indicates that dunes are quite unstable when flow velocity is high.

Numerous studies have illustrated that the increase of suspended sediment transport [*Fredsøe*, 1981; *Johns et al.*, 1990; *Kostaschuk and Best*, 2005; *Venditti et al.*, 2016] or ratio of suspended sediment to bedload [*Smith and McLean*, 1977; *Amsler and Schreider*, 1999; *Kostaschuk*, 2000] could result in the decrease of bedform height, as suspended sediment deposits in the trough or the lower lee-side. Similarly, Shimizu et al. [2009] proposed that dimensionless grain shear stress τ_* could be used to distinguish dune ($\tau_* < 0.5$), dune transition ($0.5 < \tau_* < 0.8$) and upper stage plane bed (USPB when $\tau_* > 0.8$) regime and τ_* highly affects the step length, thereby the sediment transport mechanisms [*Sekine and Kikkawa*, 1992; *Duin et al.*, 2016]. In this study, for almost all experiments under deeper flow depths, the experimental conditions were under mix-load or suspended sediment dominated conditions ($u_*/w_s > 1$) and under an USPB regime ($\tau_* > 0.8$, Table 3-4). It verifies that the effect of suspended sediment is non-negligible and explains the negative relationship between bedform height and flow velocity (i.e. shear stress) found in the deeper water experiments. *Naqshband et al.* [2014a] analysed 414 experiments and drew a similar conclusion: dune decays when $u_*/w_s > 1$, while dune grow in bedload dominated regimes (i.e. $u_*/w_s < 1$). These both illustrate the different influence of sediment transport mechanisms on dune morphology and elucidate the progressive generation of USPBs.

Naqshband et al. [2014a] also summarised that relative dune length (L/h) showed an increasing trend with a suspension threshold in both high and low Fr conditions. Our results are not consistent with this conclusion, but our finding fills the gap of their conclusion. For bedforms generating under similar flow depth but different suspension thresholds, their wavelength decreases slightly with the increase of mean flow velocity. Furthermore, bedforms under high suspension thresholds are unstable, leading to the rapid change of dunes size, through amalgamation, merging and washing out (Figure 3-5 and Figure 3-14). The intensive interactions between dunes also significantly influence the statistics of bedform characteristics via zero-crossing [*Ernstsen et al.*, 2009; *Martin and Jerolmack*, 2013], resulting in the large standard deviations, particularly in the higher flow velocity conditions (Figure 3-13).

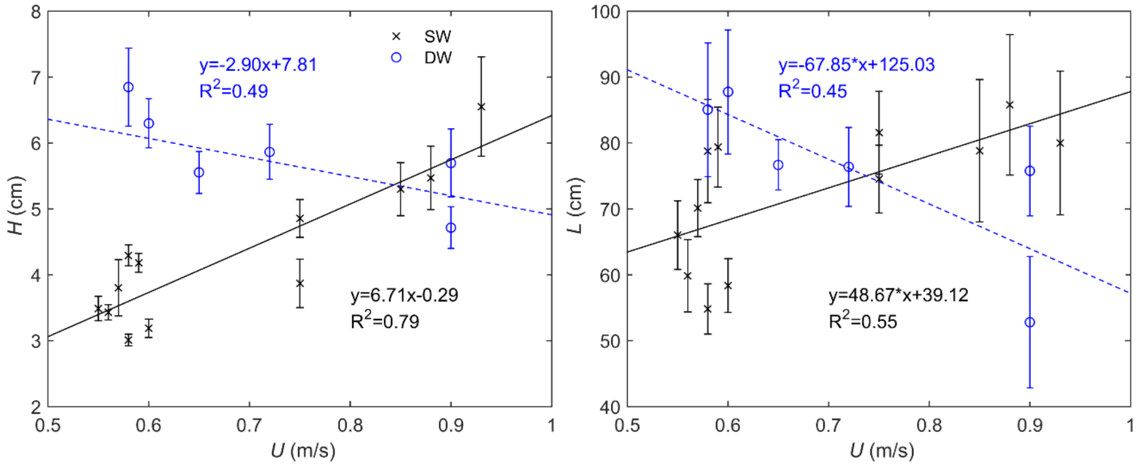

Figure 3-13. Summary of the relationship between bedform features and flow conditions: (a) bedform height and (b) bedform length. There were all calculated under equilibrium condition when bed elevation, bedform height, and length remain stable. SW means experiments taken in shallow water depth 0.2 m and DW indicates deep water depth 0.4 m. Black lines are the trendlines for shallow water while blue lines for deep water.

Ohata et al. [2017] proposed a set of new bedform phase diagrams based on abundant laboratory and fieldwork data. Similar to the phase diagram of *Southard and Boguchwal* [1990], experiments in our research are located in dunes regime (Figure 3-15). The high apparent errors at the boundaries of the upper regime bedforms in *Ohata et al.* [2017] indicates that they may not be accurately defined. Furthermore, *Naqshband et al.* [2014a] found a negative correlation between Froude number Fr and suspension threshold u_*/w_s (if sediment grain size is similar, the relationship between Fr and τ_* is negative). Therefore, in high suspension or shear stress conditions, dunes are easier to be transited into USPB regime at lower Froude numbers (red dash-dotted lines in Figure 3-15).

Shear stress and grain size dominates the mechanism of sediment transport [*Dade*, 2000; *Flemming*, 2000; *Ernstsen et al.*, 2005; *Church*, 2006] and the progress of sediment transport subsequently controls dune size under certain water depth and flow velocity conditions [*Venditti et al.*, 2005b; *Lin and Venditti*, 2013; *Venditti*, 2013; *Naqshband et al.*, 2014a; *Venditti et al.*, 2016]. Our results confirm that a high standard deviation exists when predicting bedform size simply from water depth [*Yalin*, 1972; *Van Rijn*, 1984b; *Bradley and Venditti*, 2016]. Thus, the processes of bedform adaptation to changing flows will vary for situations where different sediment transport mechanisms dominate due to diverse sediment redistribution processes [*Reesink et al.*, 2016; *Reesink et al.*, 2017]. Exactly quantifying the effect of suspension (ratio of suspended sediment to bedload) on various beds composed of different grain sizes under a range of flow strength needs be further understood in future work [*Kostaschuk et al.*, 2005; *Kostaschuk et al.*, 2009; *Bradley et al.*, 2013; *Naqshband et al.*, 2014c].

Table 3-4. Summary of sediment transport mechanisms for each stage.

	pre-stage				post-stage			
	τ_*	$\tau_*/\tau_{*\mathrm{cr}}$	u_*/w_s	Condition	τ_*	$\tau_*/\tau_{*\mathrm{cr}}$	u_*/w_s	Condition
a	0.38	11.3	0.8	BLD				
b	0.25	7.5	0.7	BLD	1.2	35.8	1.5	SSD
c	0.8	23.9	1.2	MXD	0.77	23.0	1.2	MXD
d	1.45	43.3	1.6	SSD	0.83	24.8	1.2	MXD
e	2.4	71.6	2.1	SSD	0.5	44.8	1.6	SSD
f					0.36	10.7	0.8	BLD
g	1.38	41.2	1.6	SSD	0.2	6.0	0.6	BLD
h	0.48	14.3	0.9	BLD	1.4	41.8	1.6	SSD
i	0.31	9.3	0.7	BLD	0.2	6.0	0.6	BLD
j	0.29	8.7	0.7	BLD	1.7	50.7	1.7	SSD
k	0.63	18.8	1.1	MXD	1.66	49.6	1.7	SSD
l	0.15	4.5	0.5	BLD	0.42	12.5	0.9	BLD
m	2.1	62.7	1.9	SSD	0.55	16.4	1.0	MXD
n				SSD				SSD
o	1.84	54.9	1.8	SSD	0.34	10.1	0.8	BLD
p	0.59	17.6	1.0	MXD	0.27	8.1	0.7	BLD
q	0.62	18.5	1.1	MXD	0.28	8.4	0.7	BLD
r	2.3	68.7	2.0	SSD	0.9	26.9	1.3	MXD

3.4.2. What controls the differences of dune 3D texture?

Dune three-dimensionality is widely recognised to be heavily linked to flow structure and sediment transport [*Maddux et al.*, 2003a; *Maddux et al.*, 2003b; *Parsons et al.*, 2005; *Venditti*, 2007], and exploring this link is a prerequisite to reconstructing paleoenvironments from the preserved dune cross sets [*Leclair*, 2002; *Best*, 2005a]. The 2D autocorrelation function applied in this study could quantify the 3D shape of dunes [*Friedrich et al.*, 2006; *Friedrich*, 2010; *Coleman and Nikora*, 2011], and the results largely reflect how dune 3D characteristics varied with changing flows (Figure 3-10).

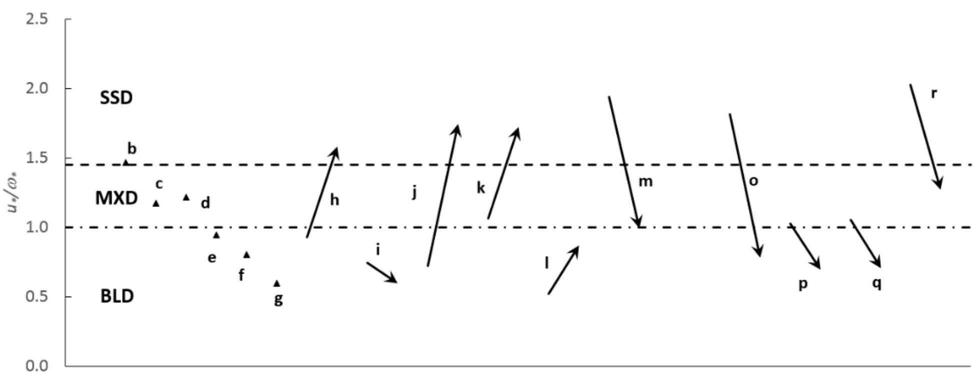

Figure 3-14. Variation of the transport stage for each experiment except a and n where there is no shear stress data collected. The dash-dotted line indicates the boundary between bedload dominated (BLD) and mixed-load dominated (MXD), while the dashed line is the boundary between MXD and suspended sediment dominated (SSD).

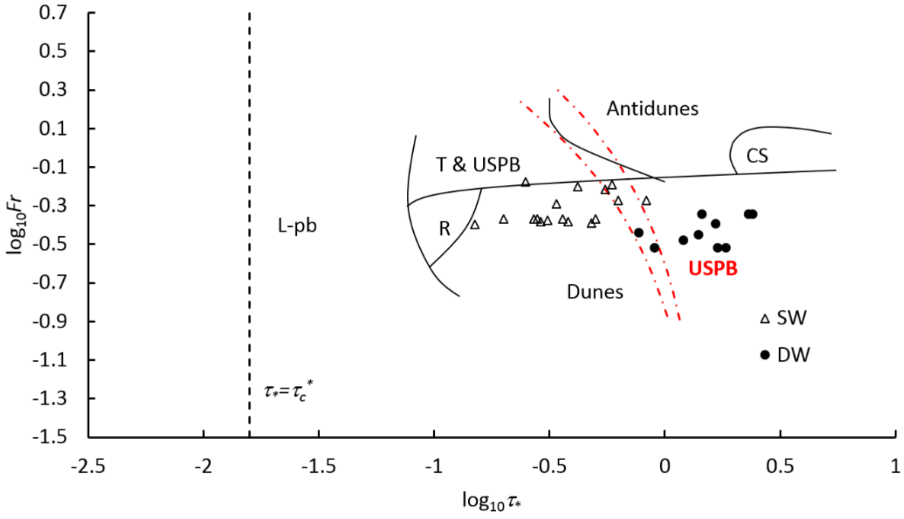

Figure 3-15. New schematic diagram of $log_{10}\tau_{*}{-}log_{10}Fr$ *for medium sand (*$D_{50}=0.354{\sim}0.707mm$*) after Ohata et al. [2017]. SW means experiments taken in shallow water depth and DW indicates deep water. The red dash-dotted lines, transformed from fig.2 in Naqshband et al. [2014a], mean the boundary between dune (left) and USPB regime (right). L-pb is Low-plane bed, T is dune transition, USPB is upper-stage plane bed and CS is cyclic step.*

In experiments with small bedload transport rates (Figure 3-9), the variation of three-dimensionality is relatively low (Figure 3-10), attributed to non-significant dune interactions (Figure 3-5). Figure 3-16 displays bed topography for experiment *g, i* and *j* at time T=150 minutes. For experiment *g* with several regular, 2D large dunes, as their crestlines are continuous and develop across the channel, the calculated θ is larger than 80°. After several minutes, the larger dunes decayed, resulting in the dramatic change of θ (Figure 3-5). In contrast, for experiment *i* with an irregular, large dune oblique to the mean flow direction, its θ is nearly 30°, while θ of experiment *j* is around 0°, as dunes are relatively irregular and crestlines are not continuous (Figure 3-16). Our results align with previous research [*Friedrich et al.*, 2006; *Friedrich*, 2010; *Coleman and Nikora*, 2011] which have shown θ tends to be higher in experiments with wall-restrained, relatively regular 2D dunes, while a value near 0° is found in experiments with water-influenced irregular 3D dunes.

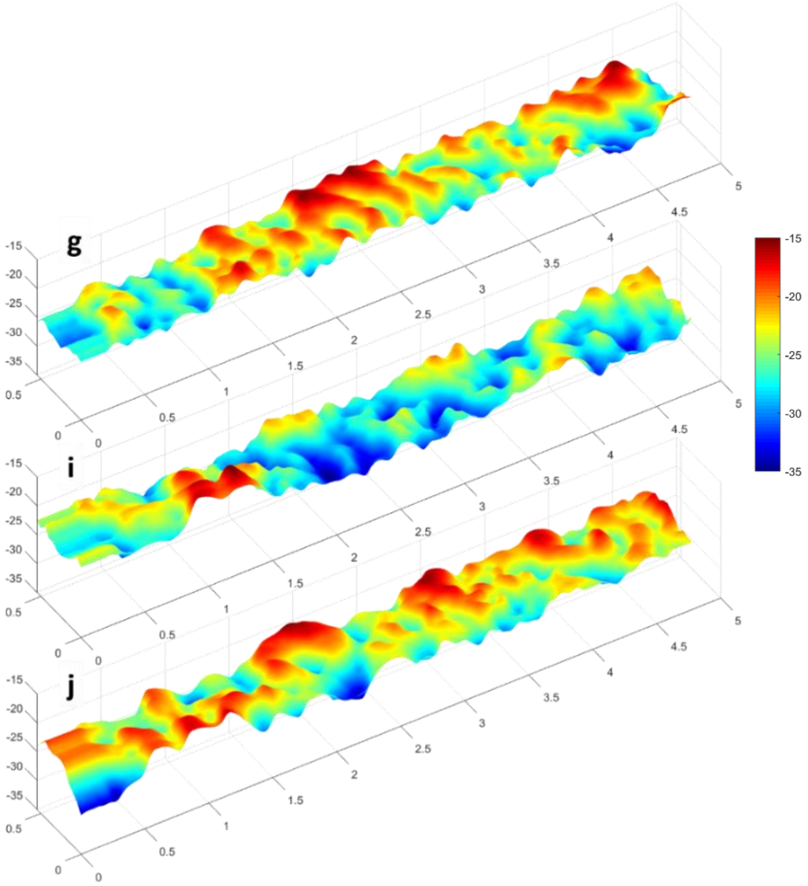

Figure 3-16. Visualization of bed topography for experiment g, i and j at time T=150 minutes in Figure 3-5. Red colour indicates higher elevation while blue colour is lower elevation. Flow direction is from right to left.

In contrast, in experiments with larger bedload transport rates, dunes are generally larger (Figure 3-5 and Figure 3-7) and deform significantly as they move (Figure 3-8 and Figure 3-9). Crestlines of larger dunes are generally longer, extending across the channel (Figure 3-12), and as a result, θ verifies previous research [*Goring et al.*, 1999; *Friedrich*, 2010], with a value of θ is in line with the average direction of the crestlines. However, this result is only valid on dunes with continuous crestlines and when $|\theta| > 30^{\circ}$. A θ tending to zero indicates that dune crestlines are aligned with flow direction [*Goring et al.*, 1999; *Coleman and Nikora*, 2011]. In our study, when crestlines are not continuous and dunes are relatively irregular, θ also ends to zero (Figure 3-16c). Furthermore, spurs widely generate in deep water experiments (Figure 3-12 and Figure 3-17), their normally flow-aligned direction [*Allen*, 1968a] could also result in some deviation on the result of 2D autocorrelation application. The generation of spurs alters the turbulence and sediment transport over stoss-side (e.g. [*Allen*, 1968a; *Swanson et al.*, 2017]), and the subsequent dramatic dune migration and deformation leads to the variation of crestilines and the 3D texture of dunes.

Limited by the range (55 cm) and resolution (5 cm) of bathymetry data across the channel and the interval time (2.43 minutes) of data collection, it is hard to distinguish whether these dunes are wall-influenced and flow-depth-influenced and capture the transition from ripples to dunes [*Friedrich*, 2010]. However, the variation of these parameters largely presents how the planform shape of dunes change with variable flow forcing. In future studies, the analytical methods should be applied to more data across different resolutions, in order to completely define the exact thresholds for these parameters corresponding to various 3D dune planform shapes, which could be applied to advance our understanding on links between turbulence and bed morphology [*Best*, 2005a].

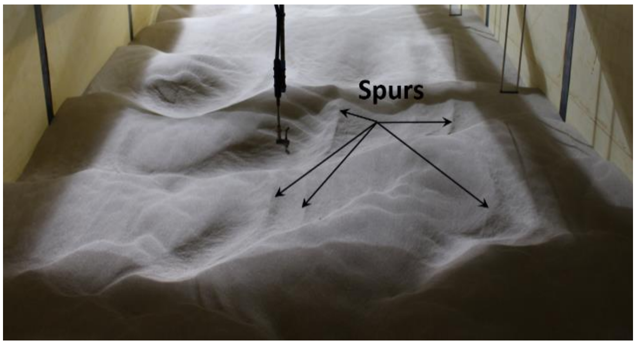

Figure 3-17. The drained flume bed at the end of the experiment with imposed 0.4m water depth and 0.9 m/s flow velocity, looking downstream.

3.4.3. How do dunes adapt to changes in hydraulic condition?

Spontaneous creation (i.e. superimposition), merging, splitting, dying-out and pass-through are well recognised as five main mechanisms of bedform adaptation to changing flows [*Warmink*, 2014; *Reesink et al.*, 2017]. These adaptation processes depend on sediment redistribution over and among dunes, and water depth and flow velocity have separate effects on sediment redistribution [*Reesink et al.*, 2017]. Therefore, any study on dune adaptation is a study on sediment dispersal between and over dunes [*Reesink et al.*, 2016; *Reesink et al.*, 2017].

The change of hydraulic conditions can lead to a variation of the bed elevation, due to an imbalances between sediment supply and sediment transport [*Kleinhans*, 2005b].

The variation of bed elevation seems to be a first order factor controlling dune development, as both flow strength and water depth will vary. Thus, bed elevation adaptations to changing flows, which lead to the change of sediment supply [*Villard and Church*, 2005], should not be ignored while investigating dune adaptation. The persist net aggradation could lead to the generation of larger dunes reaching 0.3~0.4 h in height, while dunes developed under little or no aggradation tend to fit equilibrium depth-scaling relations [*Villard and Church*, 2005].

3.4.3.1. Bedform development from rough flatbeds

Previous research (e.g. [*Venditti et al.*, 2005c]) on bedform initiation from hydraulically rough, flat beds have ascertained that flow strength can play different roles in bedform initiation. There are two separate modes which depend on the primary sediment transport mechanisms. Research conducted in laminar open channel [*Coleman and Melville*, 1996; *Coleman and Eling*, 2000] proposed that the initial ripple wavelength is only related to grain size, i.e. independent of flow strength, and did not require turbulence to generate ripples. While in turbulent flows, *Venditti et al.* [2005c] observed that the initial ripple wavelength displayed a negative relationship with flow strength. In contrast, *Kuru et al.* [1995], also in turbulent flow, found a positive correlation between the initial wavelength and the trajectory length (i.e. step/relaxation length in literature such as *Duin* [2015]) for a saltating particle. As the step length is widely known to increase with increasing flow strength [*Fernandez Luque and Van Beek*, 1976; *Nakagawa*, 1980; *Niño and García*, 1998; *Shimizu et al.*, 2009], higher flow strength could enhance initial wavelength. The different results of these observations could be due to the resolution of data, different bed material sizes and the influence of water depth employed.

Herein, bedform merging was widely observed in bedform initiation experiments *a~g* as the primary mechanism of bedform growth, except in experiment *d* and *e* (Figure 3-5). These two experiments were executed under conditions of reduced depth and bed degradation, and the initial shear stress was thus larger. They were both under MXD/SSD dominated conditions, and deep scours were initiated across the entire measuring area in a very short period, leading to the generation of relatively large dunes. Bed degradation enhances the size of the dunes with the decreasing flow strength, dunes decayed until sediment transport equals to sediment supply (Figure 3-6 and Figure 3-7).

However, limited by the interval time (180 seconds) of bed profile collection, our results are unable to interpret the initial generation of ripples, which could transit to a dune within tens of seconds in a sandy bed under lower flow strength [*Venditti*, 2003]. Experiment *d* and *e* under MXD conditions and bed degradation, the generation of deep scour pits determined the initiation of large dunes (Figure 3-5*d* and *e*), and the large dunes increased bed roughness and slowed down bed degradation rate (reflected by the mean bed elevation in Figure 3-6d and e). In contrast, for other experiments under MXD or BLD (NA of experiment *a* and *b* are under BLD with low sediment transport) but without net bed degradation or aggradation, dune initiation and development in the beginning are found to be highly related to the initial bed that the ripples superimposed over mounds and developed into large compound dunes while there was no scour pit development observed (Figure 3-5). Therefore, the correlation between sediment transport and sediment supply at the initial flow condition demonstrates different modes of dune initiation and development: under bed degradation (sediment supply < sediment transport), dunes initiate by the generation of deep scour pits, while under no net bed degradation or aggradation (sediment supply = sediment transport), dunes initiation and development are controlled by the mounds left in the initial bed. Moreover, the generation of compound dunes controls the rate and direction of sediment transport and the deep scour pits play a constraining role in the variation of dune 3D dimensionality (Figure 3-10).

3.4.3.2. Bedform adaptation from pre-bedform generated beds under BLD

i) when discharge increased

In experiments with low sediment transport, generally under BLD, for both pre- and post-change (Figure 3-9 and Figure 3-14), bedform growth (Figure 3-7) with increasing flow depth, is due to bedform merging (Figure 3-5), especially in the faster flow changing experiments (*h*, *I* and *k*). Bedforms are found to be more sensitive to local bed elevation than superimposed bedforms over the high relief from inherited topography, and under these conditions bedforms alternately merge and split (Figure 3-5). The merging and splitting of bedforms over high relief alters the lee slope of the compound form, leading to spatial unevenness in the flow-form feedback processes [*Martin and Jerolmack*, 2013; *Reesink et al.*, 2017], thereby adjust the rate of sediment bypassing which feeds downstream [*Reesink and Bridge*, 2009; *Naqshband et al.*, 2014b; *Naqshband et al.*, 2014c; *Kwoll et al.*, 2016; *Lefebvre et al.*, 2016; *Lefebvre and Winter*, 2016a; *Kwoll et al.*, 2017]. Planform of the compound forms (ripples or dunes superimpose over high reliefs) dominates the results of the 3D texture computed by the 2D autocorrelation method. The different values of θ (Figure 3-10) corresponding to various planforms (Figure 3-12) further verify that the compound forms control not only the rate but also the direction of sediment transport.

Similarly, in experiments when sediment transport increases, bedform merging is widely observed (*l* and *m* in Figure 3-5), leading to the growth of dunes. This dune interaction explains the previous results that under BLD with shallow water experiments, bedform size is found to increase with flow velocity (Figure 3-13). The high sediment transport results in faster bedform migration and greater deformation [*Venditti et al.*, 2016], and sediment redistribution is more even along the channel, compared with that in experiments with low sediment transport rates. Therefore, high crest reliefs, which have a significant role in dune adaptation, deform quickly in the course of superimposed dune merging, and their effect is weakened or even dispersed. However, the different variations of θ (*l* and *m* in Figure 3-10) which reflect the average direction of crestlines, indicate that the processes or effect of sediment transport on dune migration and deformation may be different [*Friedrich*, 2010; *Coleman and Nikora*, 2011]. In this study, we found that the disparate changes attribute to not only the rate of changing flows but also disequilibrium between sediment supply and transport. The first observation is that the merging responds very quickly to the increasing flows in both fast and slow flood waves [*Martin and Jerolmack*, 2013], leading to the a rapid change of dune three dimensionality (Figure 3-10). The smooth variation of θ for experiment *l* reflects that bedform merging occurs regularly and simultaneously along the channel in the rapid flood wave, while the variations of a/b or $x0/y0$ are more intricate, because of the irregular but sustained bedform merging during the rising limb (Figure 3-5). Moreover, experiment *m* is under slight degradation (the reason was explained in section 3.3.3.2), and it slightly affect the sediment dispersal between dunes, especially on dune troughs, leading to the enhanced stability of dune 3D shape.

ii) when discharge decreased

Martin and Jerolmack [2013] investigated the response of bedform size to slow and fast triangular flood waves, and found that when the time scale of hydraulic change is faster than that of bedform adjustment, the apparent hysteresis occurs (e.g. bedform adaptation lags behind the change of flows [*Reesink et al.*, 2017]). However, it simply treats bedform decaying as the generation and migration of secondary bedforms erode the relict crest and fill the relict trough, while it is, in effect, much more complicated [*Warmink*, 2014; *Reesink et al.*, 2017], especially in fast flood wave experiments. The bedforms in the upstream section adjust first to the changing flows, while the bedform downstream adapt not only to the change of flow strength but also the sediment redistribution induced by the change of upstream bedforms (Figure 3-5p). During the quick falling flow conditions, as long as the certain individual dune falls behind the flows, its marked feature, relative to the surrounding dunes, has a disproportionate effect on sediment redistribution. The 'slow-response' dune A in experiment *p*, which has a large relative size and slow migration rate (Figure 3-5), acts like a node separating the sediment transport for downstream and upstream: bedform height downstream declines, but their length remains largely constant; while bedforms in the upstream broadly reach equilibrium with little variation and interaction. The constrained variation of θ (Figure 3-10) also reflects that the marked dune A, to some extent, affects the sediment transport and redistribution. *Villard and Church* [2005] observed a similar bed response to a freshet in the field, and dune adaptation is spatially varying not only because of the spatial and temporal variation of water depth and flows, but also due to local condition [*Reesink et al.*, 2017], such as local aggradation and degradation and lateral sediment transport. However, in experiment *q* with the slow change in discharge, bedforms have a longer time to adjust to the changing flows, allowing enough sediment redistribution to affect bedform adaptation widely and homogeneously. Thus, the probability of occurrence of large bedform relicts is lower in the experiment with slow changing flows, resulting in a lack of apparent hysteresis (Figure 3-5q).

The analysis of dune three-dimensionality reflects that the generation of the larger dunes is the main factor controlling sediment transport and thereby bedform adaptation. This result indicates that more attention should be taken when bedforms are not regular, and the average value for dune length and dune height [*Wilbers*, 2004] is perhaps not the appropriate parameter to determine the adaptation coefficient.

3.4.3.3. Bedform adaptation from pre-bedform generated beds under MXD/SSD

The occurrence probability of bedform superimposition which is a key feature of bedform kinematics increases gradually with decreasing flow velocity but increasing crest-to-crest distance [*Reesink and Bridge*, 2009; *Reesink et al.*, 2017]. Our study confirms this finding with superimposition only observed in experiments with low bedload transport (Figure 3-5). It is most likely because that the high flow strength in the faster flow runs results in the greater sediment transport and homogeneous sediment distribution [*Shimizu et al.*, 2009; *Duin et al.*, 2016]. The step/relaxation length of sediment could increase exponentially from the order of millimetres in bedload dominant transport regime to several meters in suspended load dominant transport regime [*Naqshband et al.*, 2016], indicating that the effect of sediment suspension on dune migration and deformation becomes increasingly pronounced [*Kostaschuk et al.*, 2008; *Bradley et al.*, 2013]. The step length, to some extent, may influence bedform interaction. For example, in experiment *n* (Figure 3-5), the interaction of bedform merging (B and C) stopped and ended with the washed-out of the downstream dune B. It is because most sediments passed over the crest of dune B due to the large trajectory length, leading to the starvation of dune B, thereby its decay. This process is linked to the spatial lag between the shear stress and sediment transport along dunes [*Smith and McLean*, 1977; *Nakagawa*, 1980; *Duin et al.*, 2016], and the coexist of the washing out and increase of dunes reflects that step length varies along dune surfaces, at least in circumstances where the effect of suspended sediment is non-negligible. Therefore, the large and dramatically varying (exponentially linked to local shear stress) step length enhances the instability of each dune but decreases the possibility of generation of small dunes whose wavelength is less than step length (Figure 3-5).

3.4.4. Is dune adaptation affected by the changing rate of hydraulic condition?

Fluctuations of sediment transport, which may be caused by spatially and temporally variation of grain sizes [*Flemming*, 2000; *Bartholdy et al.*, 2005; *Ernstsen et al.*, 2005; *Van Rijn*, 2007], sorting in grains [*Flemming and Davis*, 1992; *Blom*, 2003; *Reesink and Bridge*, 2009; *Wang et al.*, 2016] and variations of sediment supply [*Kleinhans et al.*, 2002; *Tuijnder et al.*, 2009; *Dreano et al.*, 2010], play a pivotal role in generation and development of bedforms [*Lisle et al.*, 2001; *Turowski*, 2010; *Venditti et al.*, 2016; *Reesink et al.*, 2017]. Furthermore, the redistribution of sediment transport to the new circumstances along bedform surfaces leads to the deformation of bedforms [*Reesink et* *al.*, 2016]. In this study, narrowly graded sand was used, therefore, the effect of the fluctuations induced by the grain size is disregarded, and the variation of sediment supply related to changing flows is found to be a first order control on the response.

Limited by the number of our experiments, it is difficult to fully quantify the links between changing rate of flows and dune development, but the effect of the varying rate is apparent. Two separate types of the variation of sediment supply, affecting dune adaptation, were observed: systematic sediment supply related to net degradation/aggradation [*Villard and Church*, 2005] and local sediment supply related to sediment redistribution over and among dunes [*Reesink and Bridge*, 2009; *Reesink et al.*, 2016]. Thus, dune adaptation is associated to both systematic and local sediment supply, when net degradation/aggradation exists, due to the significant disequilibrium between the upstream and downstream (Figure 3-5*h*, *i*, *j*, *k* and m). In our extreme cases the increase of systematic sediment supply leads to the generation of a bar, the changing rate of flows controls the migration speed of the bar. Thus, the sediment supply for NA is controlled by the changing rate, as it is supported by the bypassing superimposed dunes (Figure 3-11).

The effect of the changing rate of flows on dunes in spatial scale is pronounced [*Reesink et al.*, 2017], but current models [*Wilbers*, 2004; *Martin and Jerolmack*, 2013] are mainly built on reach averaged features. This study enriches this knowledge and preliminary investigates how the rate of changing flows affect dune evolution. However, the effect of grain size is most important in some contexts [*Dade*, 2000; *Bartholdy et al.*, 2005], which are ignored in this study and requires further study. Moreover, accurate links between step length and flow strength need to be further investigated in order to better understand dune adaptation [*Duin*, 2015; *Duin et al.*, 2016], especially under MXD/SSD.

3.5. Conclusions

The present study investigates how dunes adapt to different changing flow conditions. The processes of dune adaptation vary in different sediment transport mechanisms due to diverse sediment redistribution over and between dunes. Dune adaptation is, therefore, a spatially- and temporally- variable response of multiple, interacting dunes [*Reesink et al.*, 2017]. Based on the results of 18 large flume experiments, the following conclusions can be reached:

1. The factor affecting dune size under equilibrium condition

a. Dune size is significantly connected to sediment transport mechanisms: positive relationships were found between dune size and mean flow velocity under BLD, while negative relations were found under MXD and SSD, when suspension plays a greater role in sediment transport and dune migration. Therefore, shear stress and grain size dominate the mechanisms of sediment transport and the progress of sediment transport subsequently controls dune size under certain water depth and flow velocity conditions.

2. Dune 3D texture

b. The results of 2D autocorrelation function concur with previous research that θ tends to be higher in experiments with wall-restrained, relatively regular 2D dunes, while it is near 0° in experiments with water-influenced irregular 3D dunes. However, when crestlines are not continues and dunes are relatively irregular, θ tends to zero as well (Figure 3-16c). Furthermore, the pervasive generation of spurs in experiments with larger flow strength alters the turbulence and sediment transport over stoss-side, and the subsequent dramatic dune migration and deformation leads to the variation of crestilines and the 3D texture of dunes.

3. Dune adaptation to changing flows

c. The correlation between sediment transport and sediment supply at the initial flow condition demonstrates different modes of dune initiation and development: dune initiation is related to sediment supply condition: under degradation bed, dune initiation is controlled by the generation of deep scour pits, while under no net bed degradation or aggradation, it is determined by the mounds left in the initial bed. The generation of compound dunes controls the rate and direction of sediment transport and the deep scour pits play a constraining role in the variation of dune 3D dimensionality.

d. Under BLD, in rising limbs, disequilibrium between sediment supply and transport plays a vital role in dune adaptation. As bedforms are more sensitive to local bed elevation that superimposed bedforms over the high reliefs left in the pre-topography alternately merge and split (Figure 3-5). Furthermore, the compound form dominates the results of the 3D texture, controlling not only the sediment transport rate but also the direction of sediment transporting downstream.

e. Under BLD, in falling flows, the probability of occurrence of large relicts dominates how dunes adapt to falling limb conditions. The probability decreases with the decreasing rate of flow change, thereby no apparent hysteresis occurs. If bedforms have sufficiently long time to adjust to the changing flows, sufficient sediment is redistributed, leading to no large relicts.

f. The occurrence probability of bedform superimposition increases gradually with decreasing flow velocity but increasing crest-to-crest distance. It is most likely that because the high flow strength in fast flows results in the greater sediment transport and homogeneous sediment distribution. The step/relaxation length of sediment could increase exponentially from bedload dominant transport regime to suspended load dominant transport regime, indicating that the effect of sediment suspension on dune migration and deformation becomes increasingly pronounced. The large and dramatically varying (exponentially linked to local shear stress) step length enhances the instability of each dune but decreases the possibility of generation of small dunes whose wavelength is less than step length.

g. Two separate types of variation of sediment supply, affecting dune adaptation, were also observed: systematic sediment supply related to net degradation/aggradation and local sediment supply related to sediment redistribution over and among dunes [Reesink and Bridge, 2009; Reesink et al., 2016]. Systematic sediment supply is a first order of factor, affecting dune adaptation when net degradation/aggradation occurs, which is keenly felt in rising depth and falling depth conditions respectively.

CHAPTER 4

4. Bedform development and morphodynamics in a recirculating flume under unsteady flows

Abstract: Dunes are ubiquitous features in sand bed rivers and estuaries, and their formation, growth and kinematics play a dominant role in controlling boundary-layer flow structure, flow resistance and sediment transport processes. However, bedform evolution and dynamics during the rising/falling limb of a flood wave remain poorly understood. Herein, we report on a series of flume experiments, undertaken at the University of Hull's Total Environment Simulator flume/wave tank facility, with imposed flow variations and hydrographs of different forms: i) a sudden (shock) change, ii) a fast flood wave and iii) a slow flood wave. Our analysis shows that, because of the changes in sediment transport mechanisms, the sediment flux rather than the bedform migration rate is a more appropriate parameter to relate to the transport stage. This is particularly the case under bedload transport dominated conditions at lower flow discharge, where a strong power law relationship was detected. In terms of varying processes across the hydrograph limbs, bedform evolution during the rising limb of a flood is dominated not only by bedform amalgamation but also by the washing out of smaller-scale bedforms. Furthermore, bedform growth is found to be independent of the rising rate of the hydrograph limb, while the evolution of bedform decay is affected by the rate of discharge decrease. This results in an anticlockwise hysteresis between the transport stage and total flux in fast wave experiment, indicating a significant role of the change in sediment transport mechanisms on bedform evolution. Moreover, analysis of the variation of deformation fraction (F) suggests that net degradation of the bed enhances bedform deformation and leads to a higher F (~0.65). This work extends our knowledge on how dunes generate and develop under variable flows and has delineated how variations in the transport stage can be coupled with the variation in the dominant sediment transport mechanisms.

4.1. Introduction

Dunes are ubiquitous features in sand bed rivers and estuaries [*Kleinhans*, 2005a; *Villard and Church*, 2005], and their formation, growth, and kinematics play a dominant role in boundary flow structure, flow resistance and sediment transport [*Nelson et al.*, 1995; *McLean et al.*, 1999b; *Best*, 2005a]. Previous research on bedforms has established relationships between hydraulic conditions and bedform geometries under equilibrium conditions and steady flows [*Van Rijn*, 1984a; *Best*, 1996; *Baas*, 1999]. However, all fluvial and estuarine conditions display temporal variations in flow discharge and water level, creating unsteadiness [*Martin and Jerolmack*, 2013; *Unsworth*, 2015]. The bed of rivers and estuaries adjust to changing flow strength through reorganisation and altered roughness. If bedforms do not adjust instantaneously to changing flows, hysteresis is generated in the relationship, and disagreement is introduced into the predictions (i.e. phase diagrams) obtained under steady flows emerges [*Lin and Venditti*, 2013].

Although, the argument on the mechanisms of bedform initiation and growth, especially the distinction between ripples and dunes still exists [*Allen*, 1976; *Baas*, 1999; *Jerolmack and Mohrig*, 2005; *Wijbenga and Klaassent*, 2009], each of these theoretical, empirical, and numerical models performs very well to some extent. It is easy to comprehend that bedforms of different dimensions occupy different migration velocities: small-scale bedforms with faster migrating rates catch up with the large ones with slower speed, thereby bedforms merge or bypass, leading to the growth of dunes with larger sizes. However, bedform evolution and dynamics during the falling limb of a flood wave (i.e. bedform decay) remain poorly understood, due to the formation of hierarchies of bedforms of various sizes, and few quantitative theory has been tested experimentally to predict the timescale of bedform decay in response to a reduction in discharge. *Martin and Jerolmack* [2013] proposed a distinctive model for bedforms to predict adjustment rates in terms of bedform reconstitution time and successfully applied this model to predict the occurrence of bedform hysteresis in natural flood waves. However, the accuracy of this type of time-lag model depends on the type of flood waves (fast or slow), and unsatisfactory results are often found in fast flood wave conditions [*Warmink*, 2014; *Warmink et al.*, 2014].

The coupled alteration of sediment supply and sediment transport processes during a flood wave is another factor often suggested as leading to differences commonly found between different research [*Venditti*, 2003]. *Fredsøe* [1981] observed that the increase of bedload transport results in dune height rising, while the increase of suspended sediment transport leads to the decrease of height, as suspended sand deposits in the trough [*Kostaschuk and Best*, 2005]. *Nabi et al.* [2013c] established a 3-D physics-based high-resolution modelling approach to simulate the dynamics of underwater ripples and dunes, but such models are computationally intensive and quite time-consuming [*Paarlberg et al.*, 2007]. In contrast, simplified models afford to simulate large-scale areas but highly dependent on the accuracy of parameterizations of small-scale processes [*Paarlberg*, 2008]. It is still poorly understood how suspended sediment contributes to dune morphology, migration and deformation and how its contribution compares to that of bedload transport [*Bradley et al.*, 2013; *Naqshband et al.*, 2014c].

Venditti et al. [2016] designed a series of flume experiments comprised of bedload dominated, suspended-load dominated, and mixed-load dominated conditions, classified by transport stage, to investigate how bedform morphology and kinematics vary with transport stage (i.e. flow strength). Besides, they also implied that the fraction of the total load contributed by translation changes with the increase of the transport stage leads to the different effects on bedform morphology. However, their results were obtained based on equilibrium conditions that bedforms were recognised to reach equilibrium under certain flows. Herein, we designed a series of flume experiments where imposed variable flows were used to test the impact of flow variability on bedform response. A series of hydrographs where explored where the rate of change in flow was altered (sudden change, fast and slow wave) to investigate how bedforms evolve under varying flow conditions. The results are used to address the following questions: (1) how do bedforms grow from a flat bed with different flow strengths; (2) how do bedforms evolve during rising and falling limbs with different flood wave flashiness; and (3) how does the fraction of deformation related flux affects bedform growth and decay?

4.2. Experiment design and data processing methods

Experiments were undertaken at the University of Hull's Total Environment Simulator (TES) flume/wave tank facility. The TES is a large recirculating flume which was configured as a 1.6 m wide and 10 m long channel (Figure 4-1). The flume was filled with ~2250 kg of narrowly graded, unimodal, washed and sieved white quartz sand with a median grain size D_{50}= 0.4 mm.

A series of experiments with different types of flow conditions were designed, but this work just presented three runs with a sudden, fast and slow change of flow condition, which were designed to investigate dune adaptation under changing flow velocity but constant water depth (Figure 4-3). The bedform phase diagram of *Southard and Boguchwal* [1990] was referred to choose the flow conditions to assure that dunes would be produced (Figure 4-2). In this series of runs, we investigated how bedforms response to flow velocity changing. Thereby, ideally, we need keep water depth unchanged. However, as bedforms response very quickly, resulting in the consequent change of water level, it is hard to adjust both the power of pump and water level to maintain constant water depth and designed instantaneous flow velocity. Flow discharge was varied via adjusting pump speeds, with the water volume in the flume kept constant.

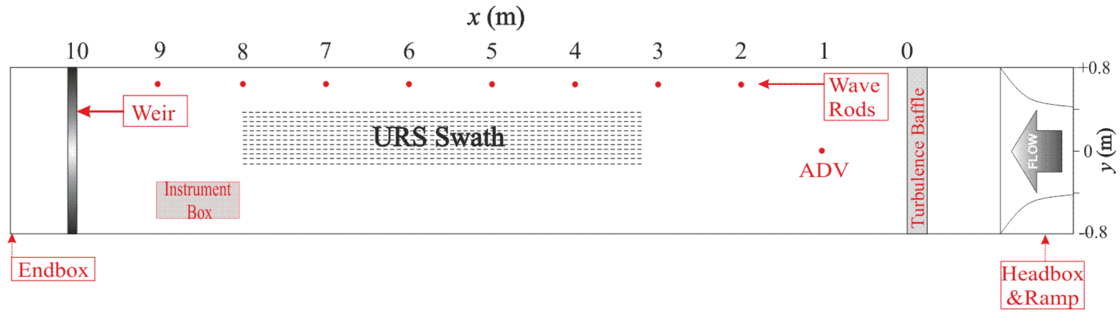

Figure 4-1. Schematic of Experiment design (to scale).

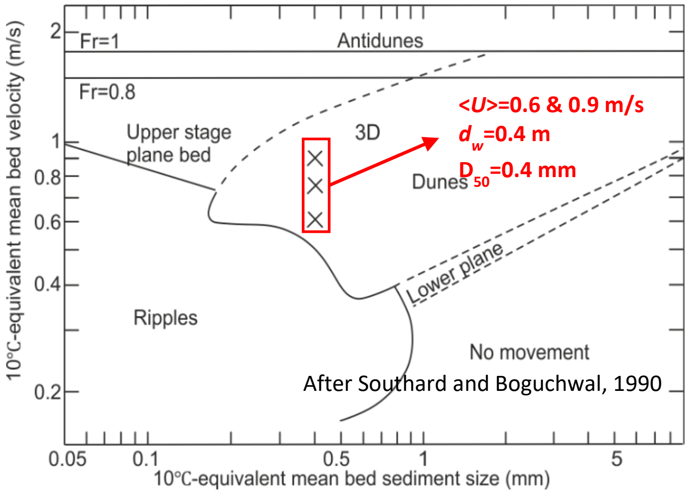

Figure 4-2. Hydraulic conditions used in the experiments based on the bedform phase diagram (after Southard and Boguchwal, 1990).

In each of these three experiments, we first ran the experiment in steady State 1 (S1 with low discharge) for six hours, which was found to be sufficiently long for bedforms to reach equilibrium. Then, for experiment E10 we suddenly increased flow condition to State 2 (S2 with high discharge), allowing bedforms to develop and achieve a new equilibrium within another six hours, while for fast (E13) and slow change (E15), step changes were conducted to increase the flow conditions to reach S2 (Figure 4-3a). The step changes were made by manually adjusting the intake valve pressure at appointed times. After six hours of steady-state bedform evolution under S2, we decreased flow conditions back to S3 (the same with S1) again, allowing bedforms to decay across another six-hour-steady-run period. The time for the rising and falling limbs varied in these two experiments (Figure 4-3), allowing us to distinguish the effect of changing rate of flow condition on bedform development.

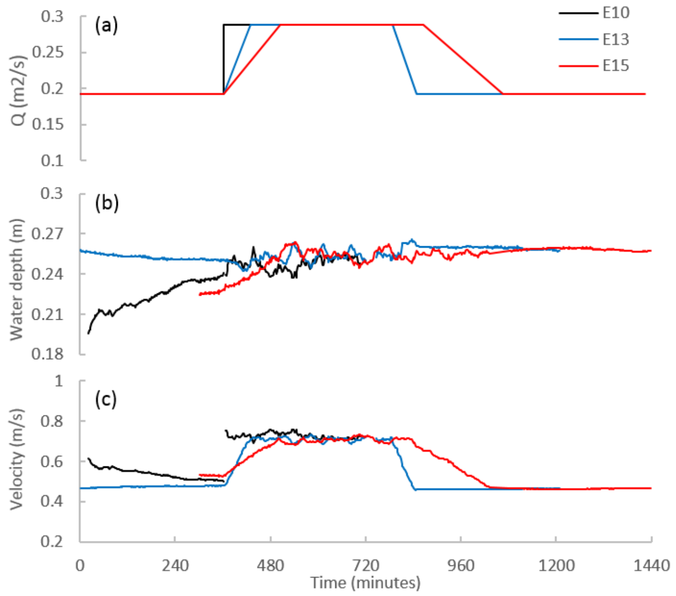

Figure 4-3. Summary of hydraulic conditions for each run: (a) designed flow discharge (b) measured water depth, and (c) depth-averaged velocity <u>. The black, blue and red lines indicate Experiment 10, 13 and 15 respectively.

A total of 12 ultrasonic sensors (URS), perpendicular to the main flow, were set in a straight line and used to continuously measure a 4.5m long and 0.55m wide swathe (the lateral interval is 5 cm) in the middle of the channel. These URSs swept up and down the length of the observation section along longitudinal transects, recording 420 depth values for each transect survey (i.e. the longitudinal resolution is 450/420=1.07 cm) with approximately 180 seconds, and the resolution of bed topography was submillimetre. A series of wave rods were employed in the right side of the flume to record water level with a frequency of 2 Hz, which can be used to estimate the variation of water depth and water slope along the flume channel.

A total of 2250 kg sand was added and in the following experiments, no more sand was added. The bed sediment thickness was set at 0.2 m, which should be larger than the maximum bedform heights and ensured that the experiments were not sediment supply limited.

4.2.1. Bedform characteristics calculation

Post-processing of the URS data was required to remove the noise/zero values and spikes induced by poor return voltages and localized suspended sediment respectively [*Unsworth*, 2015]. Two methods were utilized to detect noise: 'bed slope detection' and '3 bin wide moving detection'. Generally, in a sandy bed, bed slope should be always lower than the angle of repose. Therefore, positions whose bed slope larger than ±0.5 (±30°) were removed [*Lin and Venditti*, 2013]. Second, the noise was detected by setting a maximum threshold of the gradient between two pings of the bed return. This threshold was set to 0.5 times the standard deviation of each time series and was applied across a 3 bin wide moving window [*Martin and Jerolmack*, 2013; *Unsworth*, 2015].

Two automatic approaches are commonly adopted in bedform geometry estimation: (1) calculation based on individual bedform identification (IBI), following by *van der Mark and Blom* [2007]. In this tool, subjective choice has been avoided as much as possible, ensuring it is applicable to various datasets [*van der Mark et al.*, 2008]; and (2) autocorrelation method (AC), i.e. standard time series analysis based on the spatial bed elevation data, following as *McElroy* [2009].

For the first method, IBI, the method called 'Zero-crossing' was used to identify crests and troughs for the filtered bed profiles [*van der Mark and Blom*, 2007]. Individual bedform heights, $H1_i$ and $H2_i$, were determined as elevation changes from troughs to downstream crests and crests to downstream troughs, respectively, while individual lengths, $L1_i$ and $L2_i$, were calculated from inter-crest and inter-trough distances. Lee face slopes were computed as $H2_i/Ldowns_i$ ($Ldowns_i$, length of the lee face), and stoss face slopes as $H1_i/Lups_i$ ($Lups_i$, length of the stoss face). Finally, all of the results obtained from the 12 URSs were averaged to calculate the spatially averaged values (H and L).

For the second method, AC, the wavelength was determined from the spatial lag (R) corresponding to the strongest negative autocorrelation peak (see details in figure 4 of *Masselink et al.* [2007]) and wavelength is nearly two times of R *[Traykovski, 2007; Miles et al., 2014]*. However, if bedforms are irregular, a factor of two will over predict the wavelength [*Masselink et al.*, 2007].

Previous research on sandy bed proposed that bedform height can be calculated directly from the variance of the bed level (i.e. the root mean square, RMS) by $H = \sqrt{8}\sigma$ for a sinusoid, where σ is the standard deviation of the bed elevation profile [*Crawford and Hay*, 2001]. These approaches were thus adopted in the following analysis.

4.2.2. Transport stage

The dimensionless particle parameter (D_*) and dimensionless Shields stress (τ_*) are commonly used to determine sediment transport stages [*Van Rijn*, 2007; *Julien*, 2010].

$$D_* = D_{50}\left[\frac{(s-1)g}{\nu^2}\right]^{1/3} \qquad 4\text{-}1$$

$$\tau_* = \frac{\tau}{(\rho_s - \rho_w)gD_{50}} \qquad 4\text{-}2$$

where D_{50}= median grain size, s= specific density (ρ_s/ρ_w, i.e. sediment density / water density, was assumed as 2650 kg m^{-3} and 1000 kg m^{-3}, respectively), g= gravitational acceleration, ν = kinematic viscosity coefficient, u'_*= bed shear velocity related to grains, $u_{*.cr}$= critical bed-shear velocity according to *Schields* [1936], τ= bed shear stress.

The ratio of τ_* to $\tau_{*\mathrm{cr}}$ (the threshold for sediment entrainment) can be used to determine sediment transport mechanisms [*Church*, 2006]: (1) $1 < \tau_*/\tau_{*cr} < 3.3$, bedload dominated (BLD); (2) $3.3 < \tau_*/\tau_{*cr} < 33$, mixed-load dominated (MXD); (3) $\tau_*/\tau_{*cr} > 33$, suspended-load dominated (SSD). However, the range of this parameter used to define sediment transport conditions was established empirically, thereby it was not intended to represent local particle dynamics [*Venditti et al.*, 2016]. The ratio of the shear velocity to the settling velocity (u_*/w_s, i.e. suspension threshold) is another useful parameter to define suspension event, whereby suspension occurs while $u_*/w_s > 1$ [*Bagnold*, 1966; *Venditti et al.*, 2016]. Therefore, combined both methods, sediment transport conditions were determined in Table 4-1.

Table 4-1. Summary of transport stages.

Conditions	τ_*/τ_{*cr}	u_*/w_s
BLD	>3.3	<1
MXD	3.3~33	≥1
SSD	>33	≥1

The total boundary shear stress, τ_0, representing the sum of shear stresses, related to both bedform and grain size, was commonly derived from the water slope:

$$\tau_0 = \rho_w g h S \qquad 4\text{-}3$$

in which *h* denotes water depth and S indicates the water slope. In order to eliminate the sidewall effect, the empirical equation of *Williams* [1970] was adopted to correct the shear stress:

$$\tau = \frac{\tau_0}{(1+0.18h/w^2)} = \rho u_*^2 \qquad 4\text{-}4$$

where w means the width of flume, and u_* is shear velocity. The settling velocity was calculated based on *Ferguson and Church* [2004] which works for all sizes of sediment:

$$w_s = \frac{RgD_{50}^2}{C_1\nu+(0.75C_2RgD_{50}^3)^{0.5}} \qquad 4\text{-}5$$

in which C_1 and C_2 are constants related to the shape and smoothness of the grains. For sieve diameters of natural grains, $C_1 = 18$ and $C_2 = 1$. R is submerged specific gravity = $(\rho_s - \rho_w)/\rho_w$ ≈ 1.65.

4.2.3. Sediment transport measurements

The sediment within a sandy bed is commonly moved simultaneously as bedload and suspended load. Bedload moves by rolling, sliding, and saltating (or hopping) over the bed, and moves at a small fraction of the fluid flow velocity. In contrast, suspended load is carried in the lower to middle parts of the water column and moves at a large fraction of the mean flow velocity. When bedforms exist, not only the bedload but also the portion of the suspended load which comprises material derived from the bed (the sum of them is called bed material load) play a major role in controlling the topography

[*Kostaschuk and Villard*, 1996; *Villard and Kostaschuk*, 1998].

Thus, for trains of movable bedforms, translation (dominated by bedload transport) and deformation (dominated by bedload transport and suspension event) are two independently representative manners of sediment transport. Translation represents the mean bedform migration that defines the Lagrangian reference frame of the bed, while bed deformation is specifically the difference between bed topography that is invariant in the bed's Lagrangian reference frame and the real, stochastically changing bed elevations [*McElroy and Mohrig*, 2009].

4.2.3.1. Bedform translation rate

An automated method called ‘lag distance detection’ was applied to calculate translation distance between two consecutive along stream profiles [*McElroy and Mohrig*, 2009]. As bedforms migrated continually downstream, measured bed profiles at different time were lagged by a distance called the translation distance. The profiles were lagged relative to one another as long as bedforms did not deform dramatically, and the sum of squared elevation discrepancy for each position was calculated for each lag distance. Translation distance between two surveys was taken as the lag distance that corresponded to the minimum value. Similarly, 12 translation distances were averaged to get a spatially-averaged translation rate. This method can be well applied when bedform deformation is not significant between consecutive surveys.

Simons et al. [1965] proposed an approach to compute sediment transport related to bedform translation:

$$q_T = \beta_b (1 - p) V_b H \qquad 4\text{-}6$$

in which, p is the porosity of bed ($p = 0.4$), V_b is bedform migration rate, H is bedform height and β_b is the shape factor of bedforms. $\beta_b = 0.56$ is typical for asymmetrical bedforms [*Berg*, 1987; *Hoekstra et al.*, 2004; *Venditti et al.*, 2016]. Notably, this equation was built based on the assumption that bedforms migrate downstream without changes in the shape, size and spacing [*Lin and Venditti*, 2013]. Thereby, the bedform translation rate calculated via equation 4-6 is irrespective of bedforms deformation.

4.2.3.2. Bedform deformation rate

Saltation load is defined as particles that bounce along the channel, partly supported by the turbulence in the flow and partly by the bed, following a distinctively asymmetric trajectory. They are important to promote bedform evolution, while ignored by most geomorphologists as a special case [*McElroy and Mohrig*, 2009].

Simons et al. [1965] found that when the bedload transport calculated by individual bedform tracking is always smaller than the direct measurement, as part of the sand is suspended from the bed during high transport conditions. Therefore, *McElroy and Mohrig* [2009] proposed to take constant of integration to be the fraction of bed material load that moves intermittently in near-bed suspension. The equation they suggested to calculate deformation rate is based on two along stream bed profiles, and the average of elevation changes (D) associated to bedform deformation flux and independent of translation are computed as:

$$D = \frac{\Delta x}{2N\Delta t}\sum_{x}|\Pi(x)| \qquad \text{4-7}$$

$$\frac{\partial \eta}{\partial t} + V_b\frac{\partial \eta}{\partial x} = -\Pi \qquad \text{4-8}$$

where D is summed over the bed profiles, indicating mean volume change in two consecutive topography. Δx is the length of the translated bed profiles, Δt is the time difference between the two profile measurements, and N is the total number of measurements in the profile. $\Pi(x)$ calculated by Equation 4-8, means the elevation difference between the translated bed profiles.

Sediment exchanging between suspended load and bedload denotes the exact bed deformation related sediment which is the topographic aggregate of all changes in size, shape, and spacing of traditionally defined bedforms but is irrespective of their delineation [*McElroy and Mohrig*, 2009].

In order to make the calculated deformation flux comparable to bedform translation flux, deformation flux should be calculated over the same time scale as the translation flux [*Ganti et al.*, 2013], a further calculation similar to the equation to estimate translation flux was proposed by *McElroy and Mohrig* [2009]:

$$q_D = (1-p)D\frac{V_s}{w_s} \tag{4-9}$$

where V_s is the horizontal sediment velocity calculated from the empirical equation related to shear velocity (u_*) and critical shear velocity (u_{*cr}) [*Fernandez Luque and Van Beek*, 1976]. The ratio V_s/w_s is the ratio of the distances that a grain travels in each direction during its trajectory. However, the data used to get the empirical equation based on the transport stage (τ_*/τ_{*cr}) is lower than 8 which means the sediment transport is highly bedload transport dominated. As long as the transport stage increases, the V_s increases but should be less than near bottom fluid velocity (u_{BT}, it is hard to define the near bottom fluid velocity and the near bottom velocity should be smaller than depth averaged velocity, $\bar{u}$, so in the following calculation, u_{BT} was replaced by $\bar{u}$) [*McElroy and Mohrig*, 2009]. When $\tau_*/\tau_{*cr} \cong 33$ which is the lower boundary of SSD, V_s reaches approximately $\bar{u}$; when $\tau_*/\tau_{*cr} > 33$, V_s computed via the empirical equation becomes larger than $\bar{u}$, which is impractical in the nature. Thereby, when$\tau_*/\tau_{*cr} > 33$, we take $V_s = \bar{u}$.

Besides, the deformation fraction, F, was chosen to reflect the ratio of the deformation flux (Q_D) to the total bed material flux (i.e. $Q_{tot} = Q_T + Q_D$):

$$F = \frac{Q_D}{Q_T + Q_D} = \frac{q_D\Delta t}{q_D\Delta t + q_T\Delta t} \tag{4-10}$$

in which Δt is the time difference. The time difference (i.e. interval) is the main factor affecting deformation flux that longer time lead to greater underestimates of actual deformation flux which can be calculated by employing a surveying strategy with at least two survey repeats and extrapolating to apparent deformation fluxes at short timescales, the most accurate estimate of deformation flux [*McElroy and Mohrig*, 2009]. This conclusion is applicable under steady flow conditions, while part of our flow conditions is variable. Therefore, in order to make the calculated results of all experiments comparable, the minimal interval (nearly 4.5 minutes) of topography surveys in the same direction were chosen as the interval for computing D, q_D and q_T. Then F can simply be expressed by $q_D/(q_D + q_T)$.

4.2.3.3. Suspended sediment transport

An Aquascat$^{\text{TM}}$ Acoustic Backscatter Sensor (ABS) system, which was used to quantify suspended sediment dynamics, was set up at the instrument box downstream of the end of URS measurement area. Recent research has highlighted that the multi-frequency acoustic techniques have the potential to measure the profiles of suspended sediment concentration with a high spatio-temporal resolution [*Thorne and Hanes*, 2002]. Moreover, the concentration and particle size profiles can be calculated independent of reference measurements, as long as k_t, the parameter of the measurement system, which is related to signal frequency, pulse width, transducer radius, and conversion function between sound and electricity, is known from the explicit solution [*Thorne and Hanes*, 2002]. k_t used in this study was calibrated using the calibration sediment tower at National Oceanography Centre, Liverpool.

4.2.4. Bed texture characterization

The influence of dune three-dimensionality in planform and cross-sectional morphology is one of the key challenges in bedform research. However, until recently, quantifying the 3D dune morphology and systematically understanding the processes concerning the formation and controls of three-dimensionality have not been addressed [*Best*, 2005a]. Technologies proposed by previous research [*Allen*, 1968a; *Ashley*, 1990; *Venditti*, 2003] are not easy to obtain 3D information and also the subjective procedure to identify certain crest lines prevent their universal use [*Friedrich*, 2010]. Most recently, the 2D autocorrelation method is verified as a potentially useful tool to estimate 3-D characteristics of bedforms, although more data should be applied to define the more exact thresholds for bedform transitions [*Friedrich*, 2010].

The 2D autocorrelation function was developed based on the normalised spatial 1D autocorrelation function [*Friedrich*, 2010], defined as:

$$R(\Delta x, \Delta y, 0) = \frac{\sum_{i=1}^{N-k} \sum_{j=1}^{M-l} (z(x_i, y_j) - \bar{z})(z(x_{i+k}, y_{j+l}) - \bar{z})}{\sigma^2} \qquad \text{4-11}$$

where *z* is topography data along x and y direction, which indicates along or across the channel. σ is the standard deviation for the random field. The 2D autocorrelation of topography existing bedforms reveals the 3D character of a recorded bed by characterising hills and troughs in *x*- and *y*-direction, respectively. A contour plot of the 2D autocorrelation function (Figure 4-4) highlights the existence of elliptical shapes at the level of 50% around the centre and both bedform growth in *x*-direction and *y*-

direction and spatial bedform alignment can be obtained by analysing the shapes of the ellipse [*Friedrich et al.*, 2006].

Five main parameters were marked: a and b are the major and minor axis of the ellipse; $x0$ and $y0$ are the longitudinal and transverse distance of the ellipse and θ means the angle of rotation of the ellipse. 2D dunes potentially have an infinite ratio a/b, while similar lengths along and cross channel result in $a/b \cong 1$ and the difficulty in θ assessment [*Coleman and Nikora*, 2011]. $\sin\theta$ is the parameter to determine the direction of crestline relative to flow: $\sin\theta$ tends to zero under flow-aligned pattern, whereas to unity under flow-normal condition [*Goring et al.*, 1999]. Moreover, *Friedrich* [2010] proposed that bedforms are wall-influenced when $x0/y0 < 1$, while flow-depth-influenced when $x0/y0 > 1$. Therefore, the distribution of the ratio $x0/y0$, a/b and θ trough time could reflect how bedforms develop and could be employed to investigate which factor affects dune three-dimensionality [*Coleman and Nikora*, 2011]. These approaches were used to analyse the datasets herein.

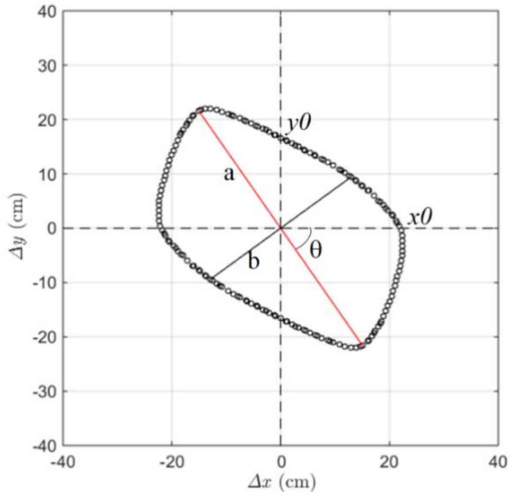

Figure 4-4. Schematic display of geometrical information describing the shape of the ellipse at a contour level of 50% for the 2D autocorrelation function for bedform development of experiment E13 at minute 444.

4.3. Results

The water surface elevation (measured from water surface to flume bottom including the thickness of sand layer) for these three experiments were set to 0.4 m (the initial thickness of bed material is 0.2 m and the water depth is 0.2 m). However, the sediment transport during the experiments changed the bed level, especially, when water depth was changed. Among all experiments, it was found that bed elevation rises with the increase of water depth, nearly 8 cm when water surface elevation grew from 0.4 m to 0.6 m (compared to the equilibrium condition). This was also reflected at the beginning of Experiment E10 and E15 (Figure 4-5): A large bed level variation (colour changes) was detected. The mean bed elevation displays a decreasing trend in S1, indicating that net degradation occurred, while it is approximately unchanged afterwards. That is because a run with 0.6 m water surface elevation was conducted before both of these two experiments. When water surface elevation decreased to 0.4 m, the whole system (sediment transport and hydrodynamics) was changed and sediment supply was less than sediment transported outside of the flume. *Venditti et al.* [2016] also observed the similar behaviour of bed level adjustment in SSD transport stage. The initial bed of E15 was not flattened but developed via a falling limb with the decrease of water depth. Therefore, the first 5 hours was removed in the following analysis, but data of the last hour with constant flow strength reached equilibrium and was kept.

Water depth of E10 increased from nearly 0.19 m to 0.25 m before S2, implying bed level was scoured by around 6 cm, while that of E13 showed a very slight decrease (Figure 4-6). In contrast, after S1, water depth of all of these three experiments basically kept constant, around 0.25 m, but those in S2 displayed a more dramatic fluctuation than those in S3 which kept relatively stationary.

Corresponding to the variation of water depth, the water slope S showed some differences between the three experiments (Figure 4-6). In S1, the S of E10 displayed a declining trend, but that of E10 remained higher. In contrast, in the first 100 minutes, the S of E13 approximately kept negative, followed by a nearly constant S=2.4D-4. During S2, all of the water depth of the three runs displayed a large variation between 0 and 0.004 but kept quite smooth in S3. Similarly, the transport stage τ_*/τ_{*cr} calculated from S presented similar variabilities like S and all of the three transport stages were observed (Figure 4-6). The unexpected bed level change in S1 lead to variation of the transport stage: (1) SSD, E10; (2) BLD, E13; (3) MXD, E15. In S2, the range of transport stage for all the three was similar, spanning from BLD to SSD, but differences existed in the average values (Table 4-2): (1) MXD, E10 and 1E5; (2) BLD, E13. All of these patterns of variability can be mirrored in the bedform dimensions and translation rates [*Venditti et al.*, 2016].

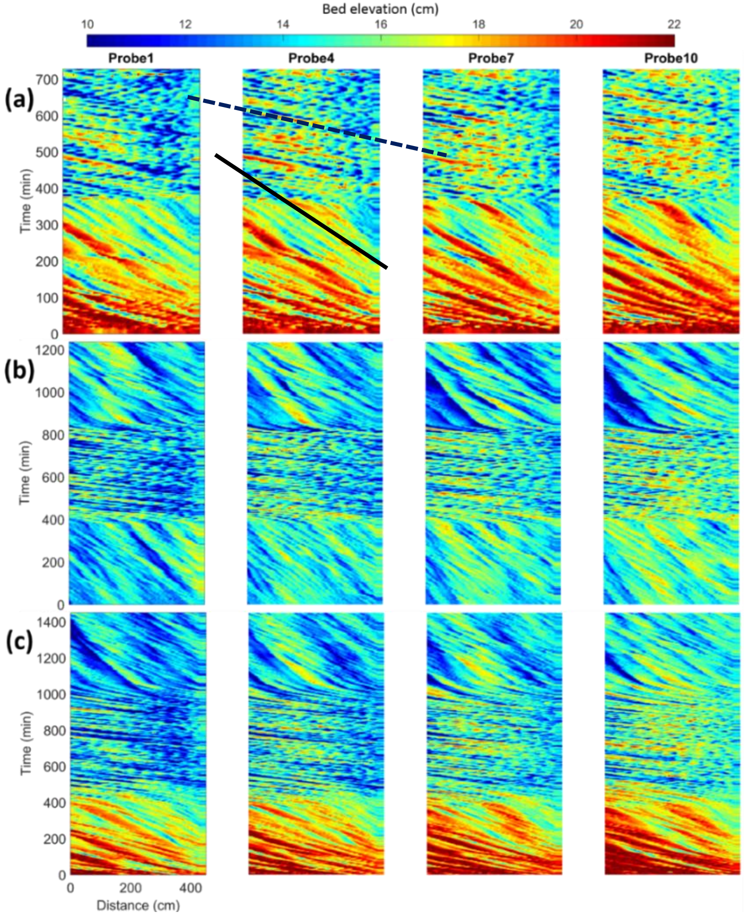

Figure 4-5. Visualization of bedform development for several Probes of (a) E10, (b) E13 and (c) E15. The slope of solid black lines reflects the bedform migration rate.

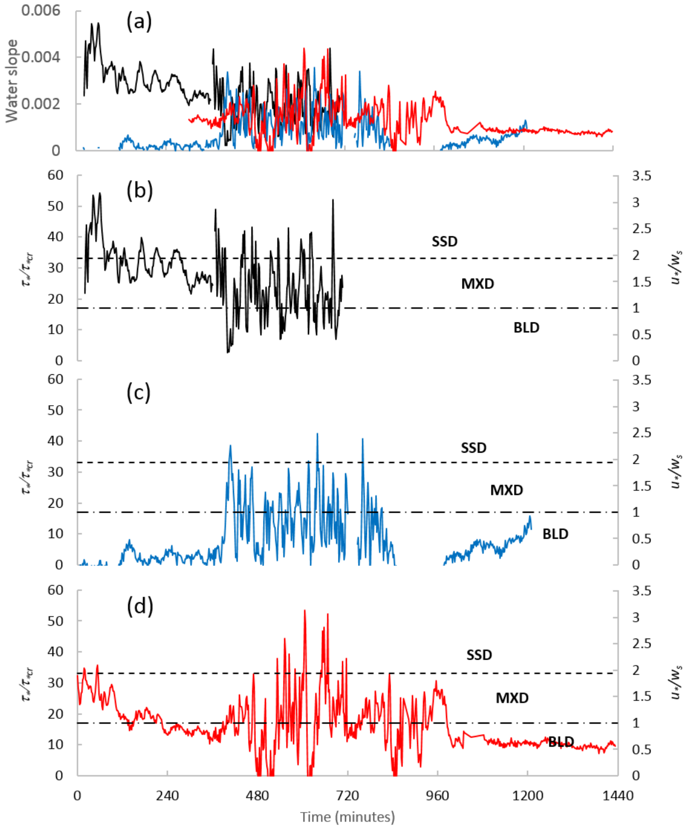

Figure 4-6. Time series of water surface slope, water depth, transport stage (τ_*/τ_{*cr}) and the ratio of the shear velocity to the settling velocity (u_*/w_s) for Run 10, 13 and 15. The dashed line indicates the suspension threshold $u_*/w_s = 1$. BLD, bedload dominated conditions; MXD, mixed-load dominated conditions; SSD, suspended-load dominated conditions.

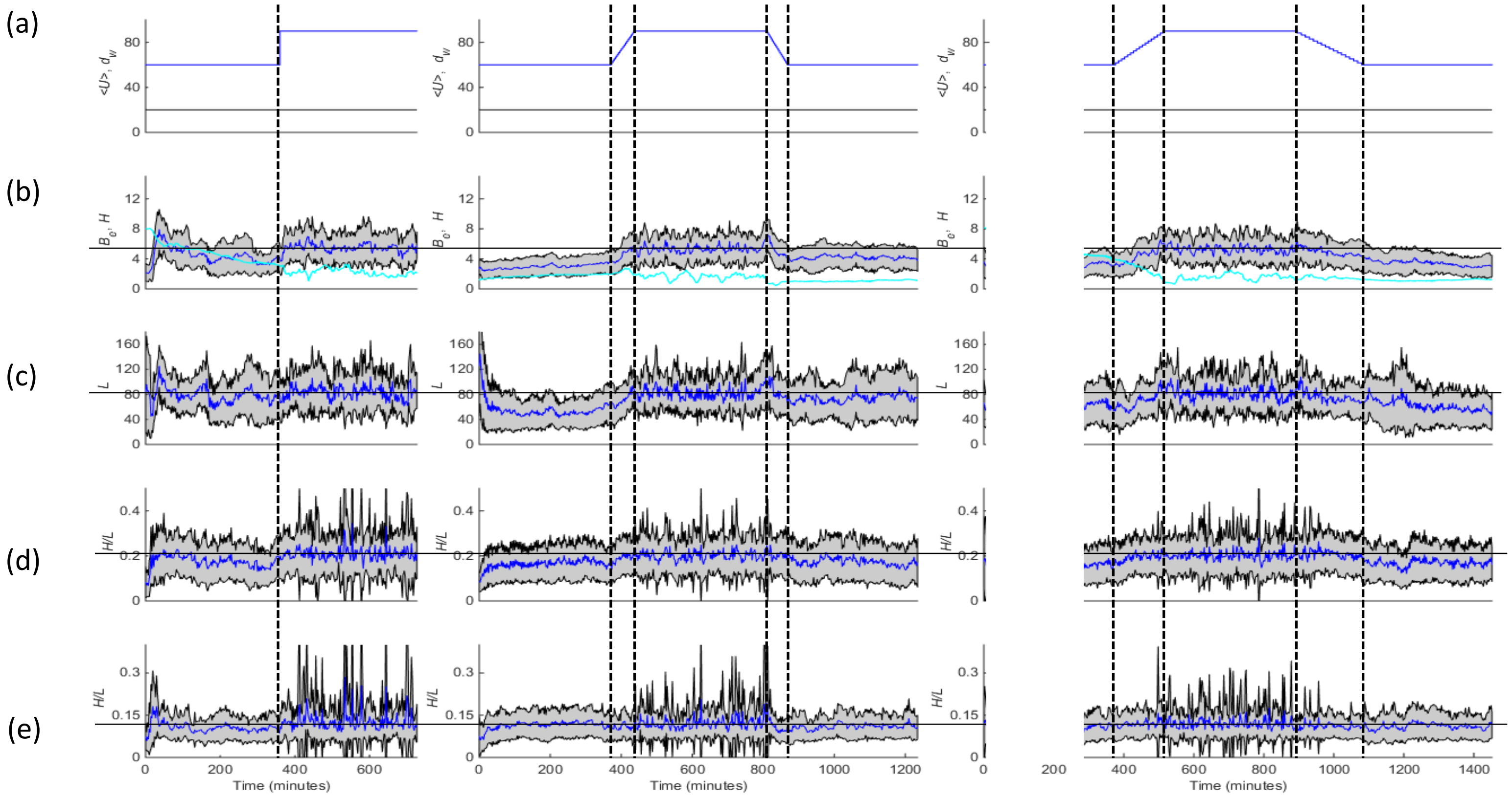

Figure 4-7. Summary of bedform characteristics for three runs (E10, E13 and E15): (a) imposed flow depth and flow velocity, (b) bedform height and bed elevation, (c) wavelength, (d) lee-side slope and (e) stoss-side slope. The grey shadow indicates the standard deviation.

Additionally, from Figure 4-6, bedform size in S1 and S3 with lower flow velocity is identifiable that both the crests (warmer colour) and troughs (cooler colour) are recognizable. Furthermore, bedform migration rate which can be reflected by the slope of the contour line (Slope=time difference/bedform migration distance, i.e. higher slope represents lower migration rate) is also identifiable with the variation of the hydraulic condition. The slope in lower hydraulic conditions (S1 and S3) is sharper but flatter in higher condition (S2). The variation of slope during hydraulic condition change is observed. However, as hydraulic condition increased to S2, bedform morphology became unstable, resulting in difficulty in tracking individual bedforms, but the migration-rate-related slope is still identifiable and consistent. Notably, the distinction of bed profile on lateral direction existed, but this effect on statistics of bedform size was small to negligible) Thereby, the following processing was based on the average values of these twelve profiles.

4.3.1. Bedform dimensions

Figure 4-8 compares the bedform geometry: (a) bedform height and (b) wavelength, obtained via IBI and AC technique. The result shows that the IBI method yielded smaller H and L values than those calculated via AC (for wavelength) and RMS approach (for height). As *Masselink et al.* [2007] suggested, occasionally, the overprediction of wavelength by two times of R attributes to bedform irregularity. A linear trend line with high correlation (R^2=0.89) was obtained that $L = 2.35\sigma$ based on data from all of these three experiments. It manifests that both of these two methods work well, because they are both sensitive to large scale bedforms (i.e. host bedforms). In contrast, wavelength estimation is more complicated due to bedforms deformation (merging, splitting, cannibalization et al.). Wavelength estimation via IBI is an average value, depending on how many bedforms are captured: (1) sometimes small scale bedforms which are identified as superimposed secondary bedforms, could not be captured based on 'zero-crossing' [*Lin and Venditti*, 2013], (2) and sometimes small scale bedforms are recognised as splitting bedforms, resulting in more bedforms being captured. However, the AC method relies more on larger bedforms over bed profiles, reflecting in Figure 4-8b that with the increase of R, L is increasingly under-estimated. Besides, the poor relationship (R^2 = 0.15) of the trend line demonstrates that wavelength is more difficult to define, and wavelength evolution is quite complicated under variable flows. In order to investigate bedform wavelength and height synchronously, in the following, bedform characteristics obtained via IBI were used for further analysing and discussion.

Figure 4-7 summaries how bedform geometry varies based on IBI (i.e. *van der Mark and Blom* [2007] method). On the whole, bedform size and lee-side slope responded rapidly with the variation of flow discharge, while some differences are manifest between different experiments even under the same imposed discharge.

Experiment E10 (sudden change), with net degradation (i.e. bed erosion), developed relatively large bedforms across the initial period, reaching 7.8 cm in height and 120 cm in wavelength, followed by a decrease to 4 cm (H) and 70 cm (L) at around 160 minutes. After a quasi-equilibrium status was reached, before bedforms increased rapidly in response to the hydraulic condition jump and reached equilibrium within 30 minutes.

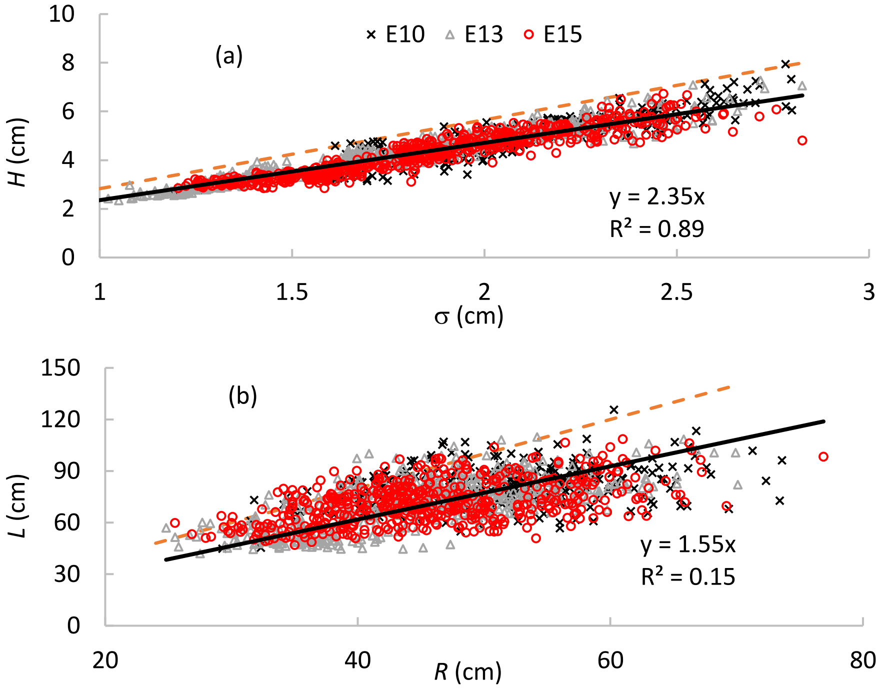

Figure 4-8. Comparison of bedform geometry: (a) bedform height obtained via individual bedform identification (IBI) and autocorrelation technique (AC) and (b) wavelength obtained by IBI and RMS. Data here is the average values from 12 profiles. The dashed line in the upper diagram presents $H = \sqrt{8}\sigma$ *concluded by Crawford and Hay [2001], and that in the bottom diagram means* $L = 2 * R$ *suggested by Masselink et al. [2007]. Solid lines are linear trend lines with the intercept equal to zero.*

For E13 with fast change of water discharge, bedform height displayed a slight increase to 3.6 cm while the wavelength remained constant, 60 cm during S1. With the fast increase of flow discharge, both bedform height and length grew rapidly and even approximately reached equilibrium with 5.0 cm in height and 80 cm in wavelength.

Similarly, during the falling limb to S3, the decrease of bedform size responded very well to the falling of flow velocity, reaching equilibrium with H=4.0 cm and L= 65 cm at the end of the run. Note however that the final equilibrium bedform size of S3 of 4.2 cm (H) and 75 cm (L) is larger than that of S1, even though they are with same flow condition. The standard deviation of bedform size during equilibrium period of S2 is larger than that of S1.

During the last hour of S1 for E15 with slow flow change, bedforms reached equilibrium with 3.6 cm and 65 cm in height and length, respectively. Bedforms grew with the slow increase of water discharge and reached a similar equilibrium to E13. However, bedform decay during falling limb is different. With the slow decrease of flow discharge, bedforms fell slightly but did not reach equilibrium at the end of the falling limb. A hysteresis about 60 minutes was detected, and afterwards, bedforms decayed with a slighter rate, reaching 3 cm (H) and 55 cm (L) at the end of the run.

4.3.2. Sediment transport

Figure 4-9a shows spatially averaged bedform migration rates $\langle V_b \rangle$ of each run. The variation of $\langle V_b \rangle$ corresponded very well with changing of hydrodynamics, except during the initial period of S1 for E10. The bedform migration rate of E10 increased dramatically to a rate of 9 cm/min $\langle V_b \rangle$ during S2, followed by a decline to 2 cm/min at the end of S1. However, during the initial period of E13, bedform migration rate is seemingly independent of bedform initiation processes.

Variation of the bedform translation flux rate (q_T, Figure 4-9b) and deformation flux rate (q_D, Figure 4-9c) displayed similar patterns with that of $\langle V_b \rangle$, but q_D displayed a more complicated pattern of variation. The variation of deformation fraction (F) displays an opposite trend, however, indicating a negative relationship between flow strength and F.

Table 4-2 summaries q_T, q_D and F for the equilibrium period of each state and run. The result shows that, q_T and q_D in the period with higher flow discharge (S2) are larger and their standard deviations are greater, as well. Furthermore, In the equilibrium period of S1, both q_T and q_D of E10 and E15 are much higher than that of E13. F of E10 and E15 is 0.65 above 0.5, reflecting that bedform deformation is more significant, while F of E13 is smaller than 0.5. For S2 with higher flow discharge, both q_T and q_D in E10 are the highest, reaching 68.5 gs^{-1}m^{-1} and 62.8 gs^{-1}m^{-1}, respectively. E13 exhibits a high q_T but small q_D, while high q_D but smallest q_T is found in E15. Meanwhile, F of all these runs decreases to lower than 0.5. Subsequently, as flow discharge decreases to the initial condition, both q_T and q_D fall to low values. *F* in E13 increases to around 0.5 and that of E15 rises to 0.65, which are similar with those in S1.

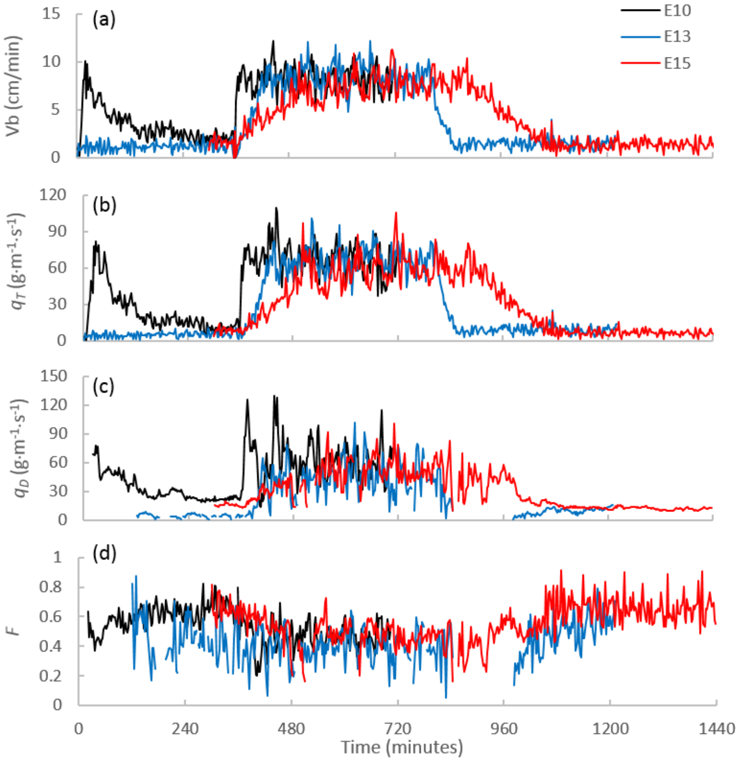

Figure 4-9. Time series of spatially averaged bedform (A) migration rates <Vb>, *(B) bedform-related sediment transport rate* q_T *and (C) the ratio of translation and deformation flux* (q_T/q_D) *for each experiment. The black, blue and red lines indicate Experiment 10, 13 and 15 respectively.*

The suspended sediment transport variation calculated via ABS obviously shows how suspended sediment transport varies under variable hydrographs and bedform evolution (Figure 4-10). In principle, both suspended sediment concentration and transport rate increase with the increase in flow strength and bedform size, and more intense sediment concentration over stoss-sides were detected. Otherwise, during the initial part of S1 for E10, the strong suspension was identifiable, coupled with high transport stage, bedform migration rate, and deformation rate.

4.3.3. Bedform texture characterisation and morphodynamics

Figure 4-11 displays how the ratio of $x0/y0$ and θ change with the development of bedforms. The filled red triangles imply where θ changes, compared with the prior value, are larger than 45°, indicating dramatic variation between two consecutive measurements. However, when ellipses get close to circles that $x0/y0 \approx 1$ and also *a/b* ≈ 1, the difficulty in calculating the accurate θ may also lead to the dramatic variation. This scenario is reflected by data in S1 and S3 where you can see for the majority of red triangles, $x0/y0$ approaches 1, except at the beginning of E10 where dramatic bedform evolution occurs, leading to the dramatic change of θ.

Table 4-2. Summary of migration flux, deformation flux, and deformation fraction during the equilibrium period. t_e *is the time of equilibrium period for each state and run, and it denotes the last how many hours for each state.*

State	Exp No.	t_e (h)	$\langle V_b \rangle$ (cm/min)		q_T (gs^{-1}m^{-1})		q_D (gs^{-1}m^{-1})		*F*		τ_*/τ_{*c}	
			Mean	Std	Mean	Std	Mean	Std	Mean	Std	Mean	Std
S1	E10	2	2.1	0.5	12.1	3.9	21.9	1.7	0.65	0.07	28.4	4.0
	E13	2	1.2	0.5	5.6	2.5	4.6	1.8	0.46	0.14	2.7	1.4
	E15	1	1.6	0.6	8.8	2.7	17.3	2.4	0.67	0.07	14.2	0.9
S2	E10	2	8.3	1.3	65.6	13.5	59.7	16.6	0.46	0.11	29.8	6.5
	E13	2	8.4	1.4	66.7	9.4	45.5	17.8	0.39	0.10	14.1	10.0
	E15	2	7.5	1.3	58.8	8.7	48.9	14.4	0.44	0.08	16.2	8.0
S3	E13	2	1.5	0.5	8.6	2.8	10.5	2.5	0.56	0.10	7.6	2.9
	E15	2	1.3	0.5	6.3	2.1	11.2	1.1	0.65	0.09	9.4	0.8

Both $x0/y0$ and θ shift relatively more smoothly during periods with low discharges, while those with high flow discharges change dramatically, reflected by plenty of red triangles. Furthermore, differences in the distribution of θ are large. The majority of θ in S1 of E10 are positive, while that in E13 is negative, and also differences of distribution in S3 are apparent. In the following section, a more detailed analysis on bedform textural character will be displayed, coupled with analysis of the morphodynamics of the bedforms.

4.3.3.1. Bedform morphodynamics on an initial flatbed

As experiments of variable hydraulic conditions were conducted and no more sand was added during our experiments, bed level adjustment was observed, especially when water elevation was changed. An experiment with 0.6 m water surface elevation was conducted before E10, while a run where $d = 0.4\,m$ was conducted before E13, resulting in a higher bed elevation (i.e. lower water depth) for E10 (Figure 4-6). Water depth of E10 increased from nearly 0.19 m to 0.25 m, implying bed level was scoured by around 6 cm, while that of E13 showed a very slightly decrease, of around 0.6 cm.

Furthermore, although discharge was set to the same for these experiments, the adjustment of net sediment transport and water depth (*h*) lead to the different behaviours of water slope (S) and transport stage (τ_*/τ_{*cr}). Transport stage of E10, under lower water depth and net degradation, is largest at the initial S1 period, reaching 60, and decreases to nearly 40 by around 160 minutes, followed by a nearly constant value with small fluctuations. In contrast, E13 with constant and higher water depth is under relatively low transport stage, less than 10. It indicates that E10 is suspended sediment dominant, while E13 is bedload dominant during the whole period. This is confirmed by suspended sediment transport in Figure 4-10, which shows that suspension in E10 is more significant than E13.

Figure 4-12 displays 3D bed morphology for five bed surveys from an initial flatbed (T=0 min) to around 40 minutes and bed elevation changes between these surveys. All of the above factors lead to different processes of bedform development: (1) For E10 with smaller *h* but larger S & τ_*/τ_{*cr}, bedforms developed dramatically, and large scour pits were observed, resulting in three-dimensional irregular morphology. Furthermore, sediment transport related bedform migration was quite significant. (2) For E13 with higher *h* and smaller S & τ_*/τ_{*cr}, bedforms also developed very quickly. However, compared with those of E10, bedforms were smaller but quite regular, nearly two dimensional, which also can be reflected by the distribution of $x0/y0$ and θ (Figure 4-11). E10 with larger undulation on initial bed results in $x0/y0 > 1$ and $\theta \approx 0°$, while for E13 with smaller fluctuations, $x0$ is smaller than $y0$, and θ fluctuates around $\pm$ 90°. Consequently, for E10, the dramatic development of bedforms leads to the decrease of $x0/y0$ to around 1, while θ displays an increased trend with the increase of bedform height. In contrast, for E13 with a smooth evolution of bedforms, $x0/y0$ keeps increasing slightly, and θ keeps fluctuating around $\pm$ 90° during the first two hours. It is reasonable that, for E10, although bedform length increases (Figure 4-7a), the scour pits extend laterally more dramatically, leading to the decrease of $x0/y0$. For E13, bedform evolution is slow and bedforms are quasi two dimensional, resulting in non-change of orientation of ellipses and a smooth increase of $x0/y0$, as $y0$ nearly keeps constant while $x0$ increases slowly.

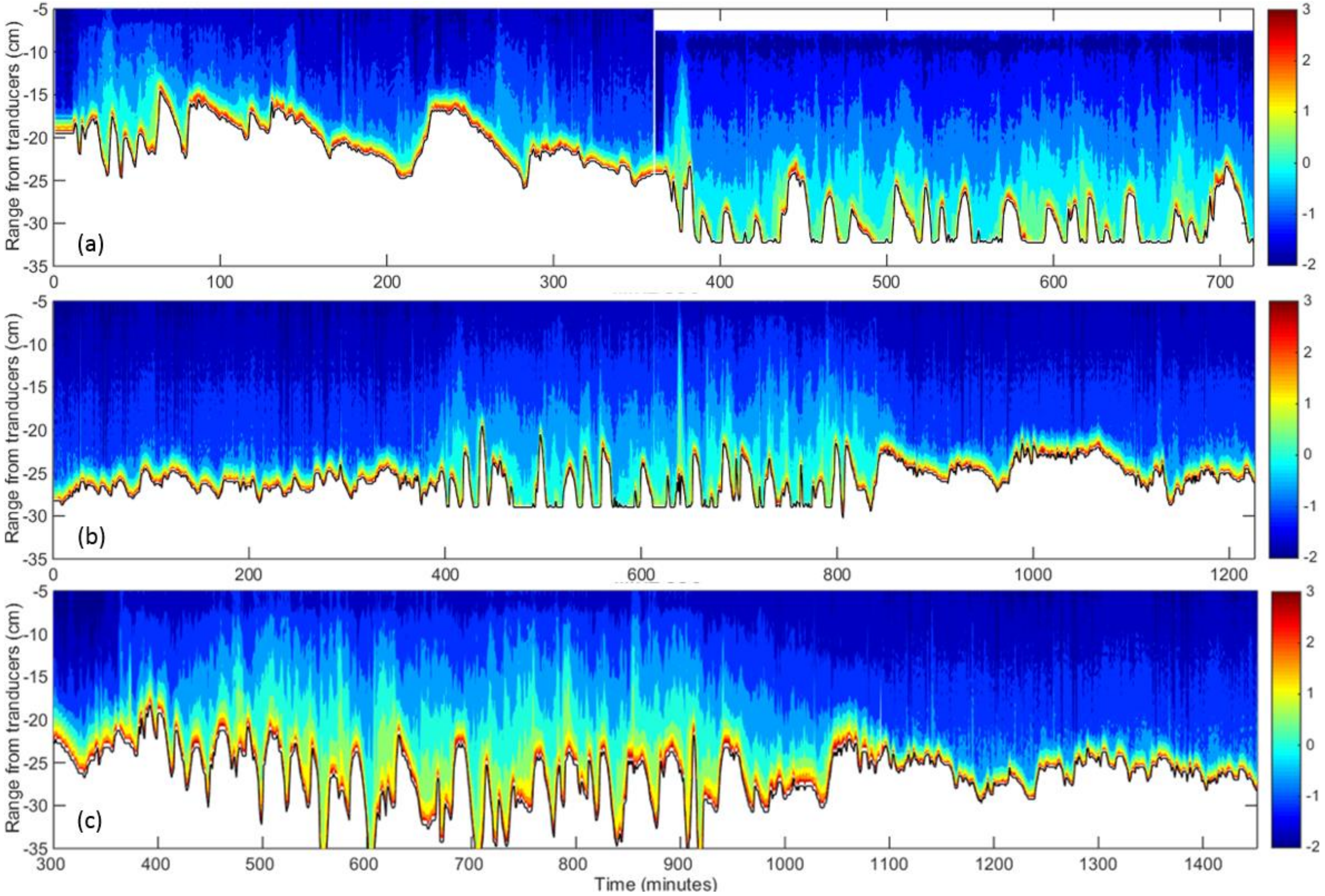

Figure 4-10. Suspended sediment transport over bedforms: (a) E10, (b) E13 and (c) E15. Unit of the colourbar is mg/L. Flow direction is from right to left.

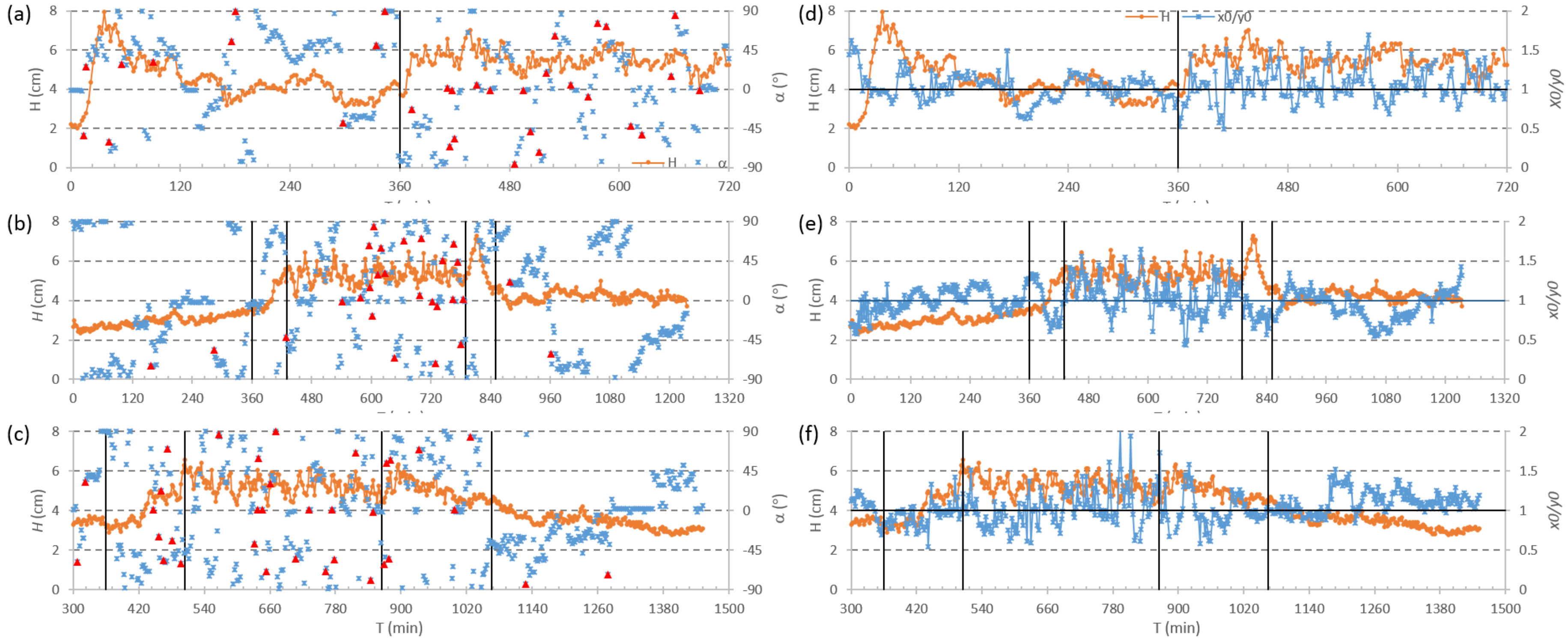

Figure 4-11. Change in θ (left column) and $x0/y0$ (right column) for bedform development of E10 (a, d), E13 (b, e) and E15 (c, f) for autocorrelation level of 0.5. Vertical lines indicate where hydraulic condition changes and the filled red triangles imply where θ changes are larger than 45° indicating dramatic variation between two consecutive measurements.

After bedforms are well developed, for E10, θ fluctuates around 45°, except between minute 120 and 160 where θ decreases to -45°, followed by a rising to 45° again. For E13, θ decreases to nearly 0° between minute 150 and 280. Variation of θ in E10, between positive and negative values, attributed to bedform merging, wash-out and splitting (Figure 4-14a), while θ of E13 which decreases to 0° is caused by the break of crestlines and troughlines across the channel (Figure 4-14b).

It is obvious that after 5 hours of steady-state run, mean bed elevation of E15 is the highest and that of E13 is the lowest (Figure 4-7 and Figure 4-13). Notably, one lager-size bedform is generated in the middle of the flume in E10 and downstream in E15, while a similar form cannot be detected in E13. This behaviour is also reflected in bed elevation changes (Figure 4-15). However, as the large-scale bedforms were located at the downstream area close to the ABS, this resulted in the more significant suspension events than the other two (Figure 4-10). The result suggests that great care is needed when we compare suspended sediment transport with bedform migration and development. Suspension over bedforms may be exaggerated as ABS reflects suspension over one individual bedform, which cannot represent local mean bedform characteristics, which we discovered above.

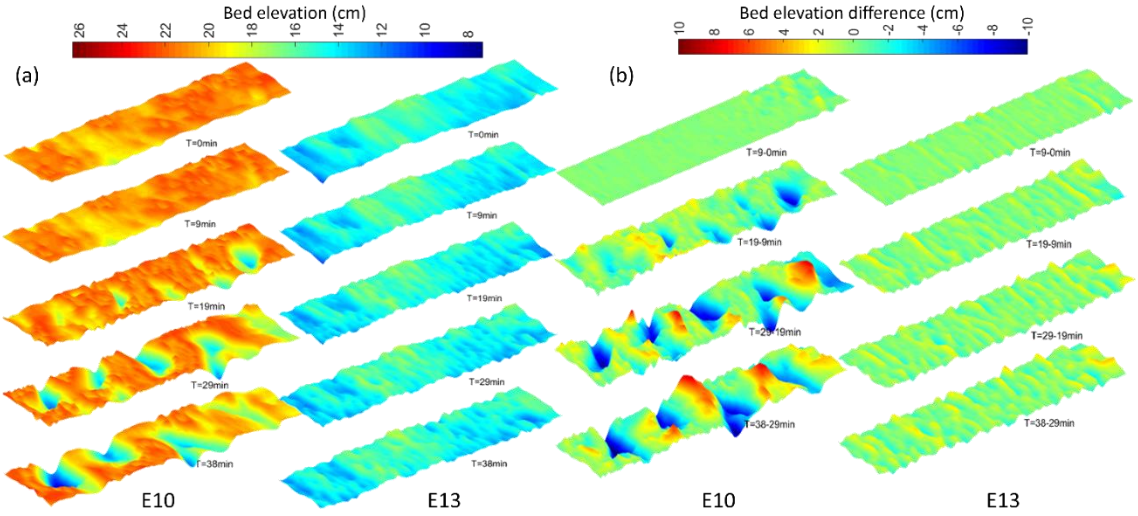

Figure 4-12. Bed topography (a) and elevation change (b) at the first 40 minutes of S1 of Run 10 (left rows) and 15 (right rows). Flow comes from right.

Furthermore, from the view of planform in bed elevation changes, crest lines basically parallel to each other in E13, except areas marked by rectangles where intersections are observed. In contrast, patterns in E10 and E15 are with larger amplitude and spacing, and intersections of crest lines are more common.

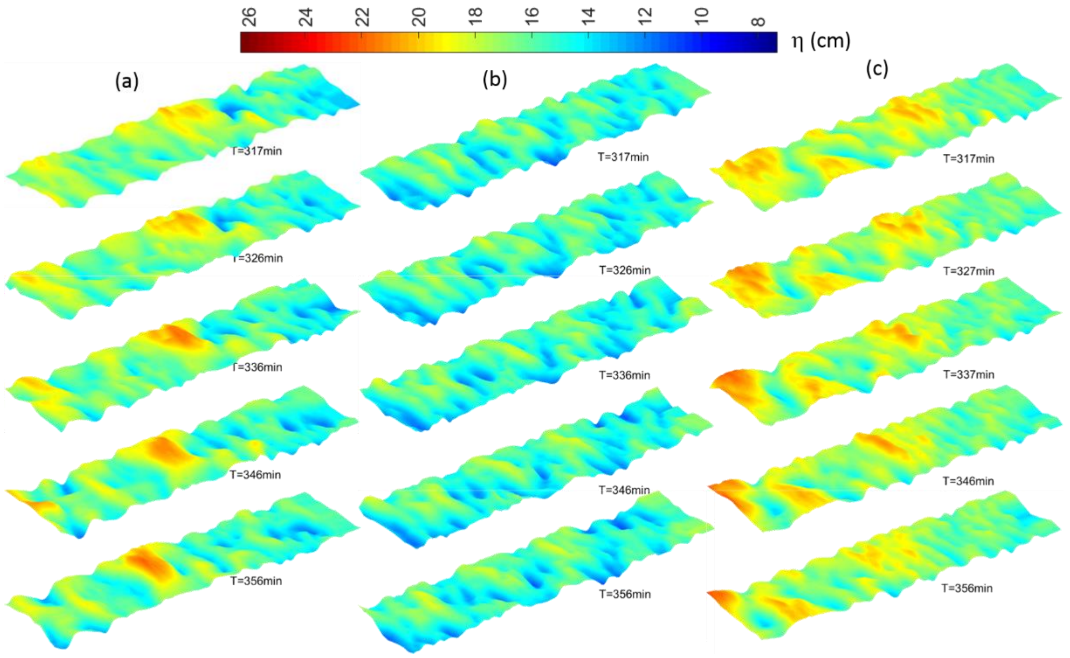

Figure 4-13. Visualization of bedform development of (a) E10 and (b) E13 at the last 40 minutes of S1. Flow direction is from right to left.

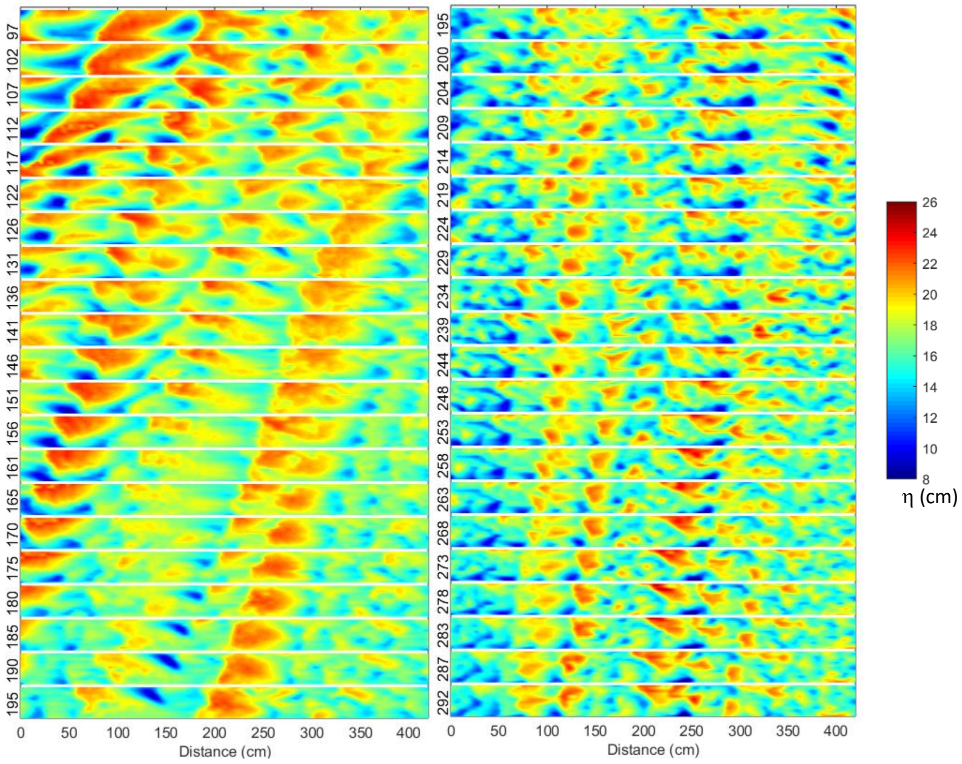

Figure 4-14. Visualization of bedform evolution between minute 97 and 195 of E10 (a) and between 195 and 292 minutes of E13 (B). Flow direction is from right to left.

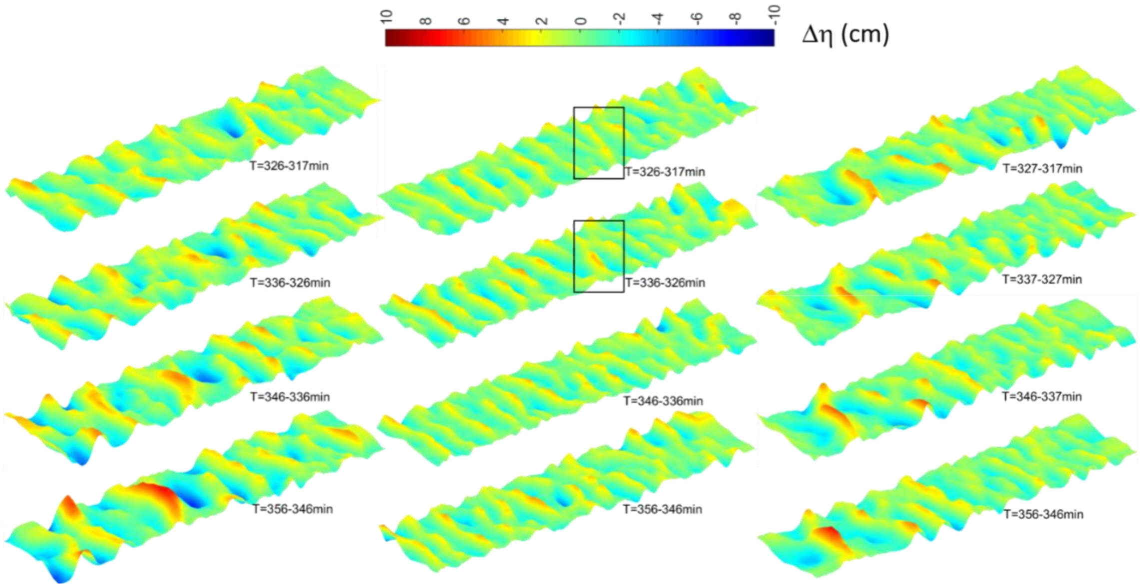

Figure 4-15. Bed elevation changes of (a) E10, (b) E13 and (c) E15 at the last 40 minutes of S1. Flow direction is from right to left.

4.3.3.2. Bedform morphodynamics during rising limbs and the following high discharge period

Before hydraulic conditions started to increase, the bed elevation of E15 was largest, 2 cm higher than that of E13 and 1 cm higher than E10 (Figure 4-7). For E10 with the sudden increase, mean bed elevation fell dramatically, decreasing 1.5 cm within 20 minutes. Moreover, both bedform length and height increased rapidly and reached a similar level in S2 for all these three experiments. Bedform height was nearly 5 cm and length were 80 cm when reached dynamic equilibrium. However, whether bedforms are saddle-shaped or lobe-shaped is not obvious in our experiment, as the width of swathe (55 cm) is not wide enough.

For E10, the sudden change of bedform deformation and translation rate at the first 30 minutes after flow condition increase leads to the dramatic transformation of planform, resulting in difficulty in bedform tracking. However, for E13 and E15 with a step change of water discharge, bedform transformation is lower, and the increase of bedform size is related to both the sediment accumulation in crests and scouring in troughs (black ovals in Figure 4-16). Furthermore, the migration rate increases linearly with the rising of water discharge (Figure 4-9), indicating that the bedform size variation has an insignificant role in bedform migration.

Notably, herein, during rising limbs, both bedform merging which marked by black ellipses and small-scale bedforms washed out behind a large-scale bedform marked by red ellipses are detected during bedform adaptation. Bedform merging (amalgamation) and splitting are the most common behaviours during bedform migration and small-scale bedforms' dying out attributes to the starvation of sediment, as they are trapped in the flow separation zone of a larger bedform [*Gabel*, 1993]. Furthermore, *Gabel* [1993] observed bedform dying out during both rising and falling limbs, while it was only detected in the falling limb of *Wijbenga and Van Nes* [1986] lab experiments [*Warmink*, 2014]. The gaps between these conditions observed here are probably caused by the three-dimensional geometry of bedforms which cannot be reflected by data measured via single-beam scan rather than multi-beam scan. In our data, lateral variation of bed topography is remarkable (Figure 4-16): (1) the larger scale bedform develops along the black solid line, becoming larger and showing an increasingly lateral growth, (2) crest of small bedforms in right bank declines firstly while that in left bank displays a slight increase (dashed line); (3) after the dying out of the bedform in the right bank, that in the left bank starts vanishing. Furthermore, from the process of 2D bed profile evolution (Figure 4-17), differences in bedform adaptation are prominent laterally.

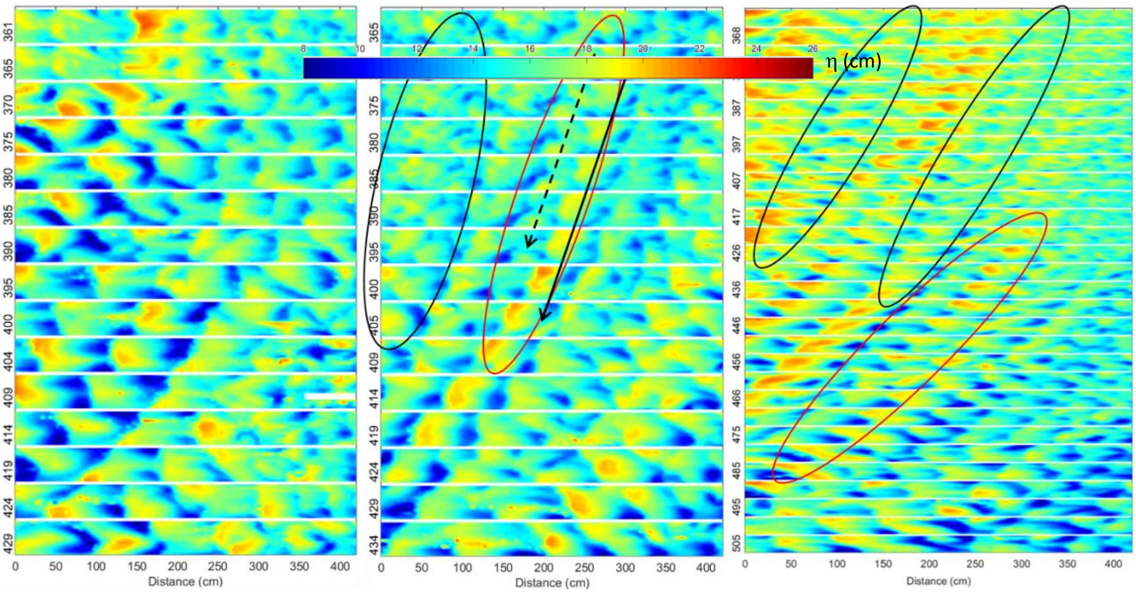

Figure 4-16. Visualization of bedform development (a) E10, (b) E13 and (c) E15 during rising limbs. The black ovals indicate sediment accumulation in crests and scouring in troughs leading to the increase of dune size. The larger scale bedform develops along the black solid line, becoming larger and showing an increasingly lateral growth. The dashed line represents that the crest of small bedforms in right bank declines firstly while that in left bank displays a slight increase. Flow direction is from right to left.

Additionally, during the rising limbs of E13 and E15 and first 30 minutes of E10, variation of θ displays an opposite trend compared with that before hydraulic condition changes: (1) for E10 and E15, θ fluctuates around -45°, while it undulates around 45° before changes; (2) for E13, θ fluctuates between -90° and -45°, while undulating between 45° and 90° before the rising limb (Figure 4-11). Similar trends can also be observed in the distribution of $x0/y0$.

Bed elevation of these three experiments reached the same level during the equilibrium period in S2 (Figure 4-7 and Figure 4-18). However, the spikes in the topography were quite obvious, reflecting abundant suspended sediment transport, which can be verified in Figure 4-10. Furthermore, bedforms were irregular with dramatic deformation, resulting in dramatic changes of θ and difficulty in individual bedform tracking between consecutive surveys.

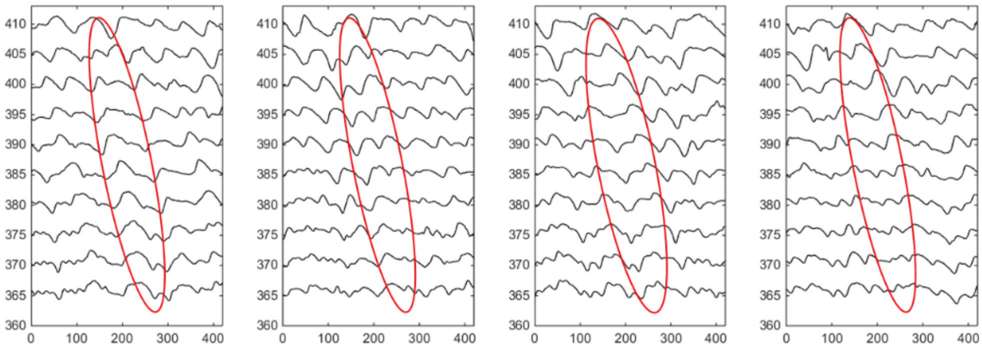

Figure 4-17. Bed profiles evolution for rising limb of E13: (a) Probe1; (b) Probe4; (c) Probe7; (d) Probe10. The red ellipses are corresponding to that in Figure 4-16b. Flow direction is from right to left.

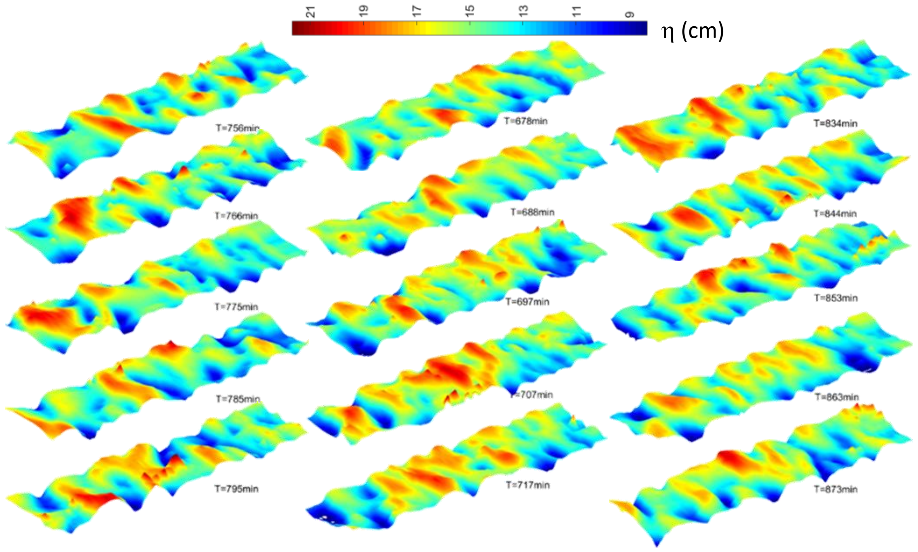

Figure 4-18. Visualization of bedform development of (a) E10 and (b) E13 at the last 40 minutes of S2. Flow direction is from right to left.

4.3.3.3. Bedform morphodynamics during falling limb and S3

After 6 hours running under S2, the total sediment transport in measuring area seems to reach equilibrium, as bed elevation of both of these two experiments remained unchanged (Figure 4-7 and Figure 4-19a). Thereby, the effect of bed level adjustment on bedform development should be negligible. Distinctions of bedform evolution between two runs were observed during falling limbs. For E13 with fast change, both bedform height and length decreased immediately with a reduction in flow strength, approximately reaching equilibrium at the end of the falling limb. In contrast, for E15, obvious hysteresis was detected for both wavelength and height and bedforms constantly decayed during the whole transition to S3, resulting in smaller bedforms compared with those of E13.

It is obvious that for E13, large-scale bedforms developed under S2 migrated downstream, coupled with persistent decay, because flow strength declined constantly and bedforms entering into the measuring area from upstream were smaller (Figure 4-19a). At the end of the falling limb (T=868 min), the left part (downstream) of bed topography evolved from the original large-scale bedforms displayed a different size compared with the right (upstream) part. Its crest elevation was reduced, but trough elevation still kept very low. Moreover, the spacing of the patterns on bed elevation changes of E13 became increasingly smaller (Figure 4-19b), indicating a continuous decline of the capability in moving sediment. Generation and migration of small-scale bedforms also can be recognised since T=868 min, the end of the falling limb in Figure 4-19a.

Furthermore, for bedforms in the middle of measuring area, their crests are eroded but wavelengths remain unchanged, while for bedforms in the upstream part of the channel, their troughs are filled in and wavelengths increasingly become smaller, leading to the decrease of bedform size. Unlike bedform development in E13, bedform migration and deformation are more dramatic at the beginning of the falling limb for E15, as flow strength maintains a longer time. E15 with slow change allows bedforms to have enough time to migrate and evolve, and the characters of initial bedforms cannot be recognised.

In terms of bedform texture characteristics, θ displays a similar trend for both E13 and E15 during the falling limb: (1) within the initial 40 minutes of falling limbs, bedform height of both of these two experiments increases coupled with negative θ varying between -90° and -45°; (2) subsequently, bedform height displays a declining trend and, in principle, θ becomes positive, fluctuating between 45° and 90°.

At the initial period of S3, both bedform height and length of E13 remain unchanged and bedforms seem to even reach equilibrium, but θ keeps changing. Besides, the transport stage shows a slight growth but keeping under BLD (Figure 4-6). In contrast, for E15, bedforms continuously decay, while the transport stage decreases slowly and θ increases slightly from around -45°to 45°.

Figure 4-20 displays how bedforms evolve during the last 40 minutes of S3 when both of these two experiments reached equilibrium. The obvious discrepancy between them is the apparent large-scale bedform which developed in E13, leading to the larger standard deviation of bedform length and variation of θ. Furthermore, bedforms of both of these experiments are quite irregular.

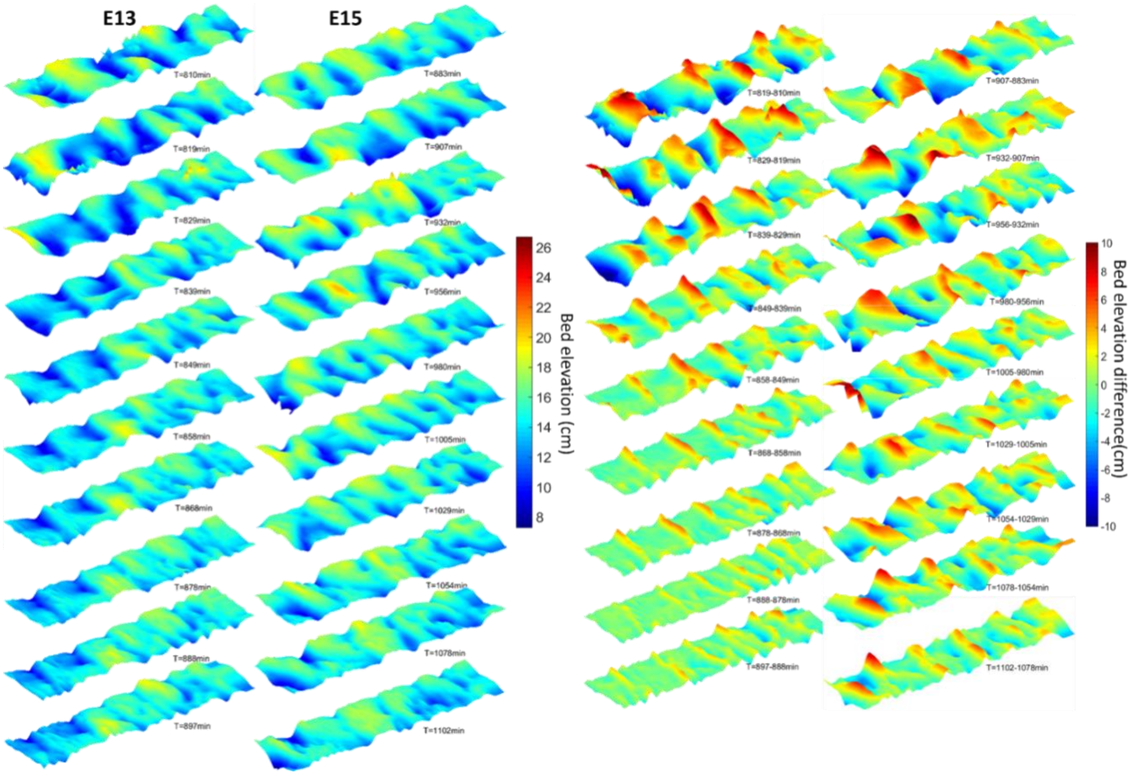

Figure 4-19. Bed topography (a) and elevation change (b) for the falling limb of E13 and E15. An extended 20-minute development after rising limb (the first 20 minutes of S3) was also added for both E13 and E15. Time interval of E13 and E15 is 9.5 and 24.5 minutes respectively, in order to keep the varying rate of flow discharge same. Flow direction is from right to left.

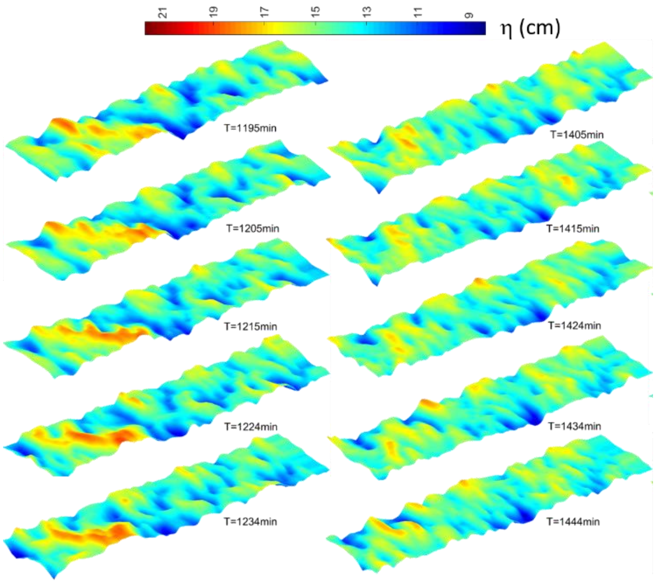

Figure 4-20. Visualization of bedform development of E13 (a) and E15 (b) at the last 40 minutes of S3. Flow direction is from right to left.

4.4. Discussion

Considerable research has established numerical models which can successfully simulate bedform initiation and development [*Nikora et al.*, 1997; *Paarlberg*, 2008; *Shimizu et al.*, 2009; *Nabi et al.*, 2013c]. However, as all of these models were built based on disparate data from flume experiments and fieldwork, gaps between them are apparent. Moreover, parameterizations of small-scale processes are somehow empirical, and their accuracy plays a decisive role in the simulation. According to our results, not only bed material or flow discharge but also transport stage (i.e. shear stress) and coupled sediment transport contribute to different bedform evolution processes under changing flow conditions.

4.4.1. What is the relationship between bedform migration rate and transport stage?

For a given depth to grain-size ratio, migration rate increases with the increase of the transport stage [*Lin and Venditti*, 2013]. In principle, our result follows this trend, but apparent data scattering is observed. *Venditti et al.* [2016] suggested that the different methods used to calculated translation rates lead to the scattering problem, as our data is spatially averaged across the channel while *Lin and Venditti* [2013] derived the relationship by tracking individual dunes. Furthermore, part of shear stress dissipated by suspending sediment into water column probably attribute to the bias of underestimation during high flow discharge when suspension frequently occurs (Figure 4-10 and Figure 4-21). Moreover, a small part of data with relatively low transport stages (highlighted by a circle) still occupies the large migration rate. That is because, the wave rods, utilized to estimate water slope, were fixed and its accuracy on shear stress calculation significantly depends on whether water surface was affected by underneath bedforms. Evidence showed that data during high flow discharge was affected when bedforms pass through, leading to the bias.

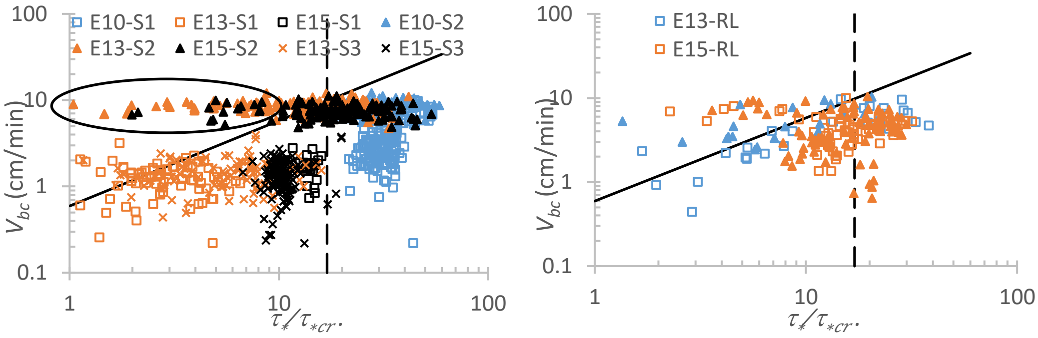

Figure 4-21. Bedform migration rate versus transport stage τ_*/τ_{*cr}*: (a) steady stage and (b) unsteady stage (Rising limb and falling limb). RL indicates rising limb and FL means falling limb. The solid line is calculated via* Lin and Venditti *[2013] and the dashed vertical line denotes the suspension threshold.*

Additionally, several apparent clustering is overpredicted (under the relation curve): E10-S1, E13-S3, and E15-S3 in Figure 4-21a; E15-RL and E15-FL in Figure 4-21b. Herein, several reasons may lead to the discrepancy: sediment suspension, net degradation, and generation of secondary bedforms [*Martin and Jerolmack*, 2013]. For E10-S1, E15-S1, and E15-RL, net degradation occurs (Figure 4-3b), indicating that sediment input is less than output, and part of sediment was not captured in the dune trough, which was not involved in bedform migration [*Naqshband et al.*, 2014c]. In other words, part of shear stress was dissipated by moving the bypassing sediment and sediment related to suspension (Figure 4-10), leading to the underestimation of migration rate.

However, for E13-S3 and E15-S3 without net degradation nor significant sediment suspension, the bias attributes to the generation of secondary bedforms and our method for migration rate calculation [*Martin and Jerolmack*, 2013]. As small bedforms are superimposed during the bedform decay period, the secondary bedforms are dominant on sediment transport. However, the autocorrelation method, which is more sensitive to large-scale bedforms [*Masselink et al.*, 2007], estimates the migration rate of large bedforms, leading to the underestimation.

The dune adaptation is ultimately related to sediment transport. Therefore, relationship between shear stress and dune migration speed [*Lin and Venditti*, 2013] can only apply to the instance that dunes migrate without size and shape change under bedload dominated condition. But, almost, in all circumstances, dunes migrate along with deformation, especially under unsteady flows. Thus, building relationship between shear stress and sediment transport is more adequate.

4.4.2. What is the relationship between sediment flux and transport stage?

In order to eliminate the influence caused by the above factors in the last section, the total sediment transport flux was calculated as $q_{tot} = q_T + q_D$ and utilised to establish a relationship with the transport stage (Figure 4-22). Generally, the relationship between τ_*/τ_{*cr} and q_{tot} depends on the status of sediment transport: (1) a quite intimate connection is found under steady and low discharge (BLD), exhibiting a power law relationship; (2) while the connection during unsteady and high discharge (MXD and SSD) is not as strong.

q_T was estimated by equation 4-6 that both migration rate and bedform height were probably representative of the primary bedforms, when superimposed bedforms exist, as the autocorrelation method is more sensitive to large scale bedforms [*Masselink et al.*, 2007]. q_D calculated via equation 4-9 contains part of bypass or locally suspended sediment which participates in bedform evolution, but what percentage of the sediment involved in this equation is unclear. Furthermore, as *Naqshband et al.* [2014c] concluded the bypass fraction increases with the rising of Froude Number (i.e. flow strength, generally), whether the percentage of bypass sediment estimated in that equation changes with variation of transport stage is not exactly understood. Besides, the development of 3D patterns accompanied with lateral sediment movement will lead to the overestimation of deformation flux in equation 4-9 [*Venditti et al.*, 2016], reflecting in Figure 4-22 that data with high transport stage expect E10-S1, generally coupled with high 3D forms were overestimated.

Furthermore, the manifestation of sediment transport by secondary bedforms promotes the migration and deformation of host bedforms. Therefore, the total sediment flux avoids the bias induced by incoordination between migration rate and transport stage when superimposed bedforms generate in Figure 4-21.

Figure 4-22b displays the relationship between the transport stage (τ_*/τ_{*cr}) and total sediment flux (q_{tot}) during rising and falling limbs. In principle, q_{tot} shows a positive correlation with τ_*/τ_{*cr}, indicating how the transport stage transits from BLD to MXD. Notably, E13 with fast changing presents an anticlockwise correlation, while not seen in E15 with slow variation.

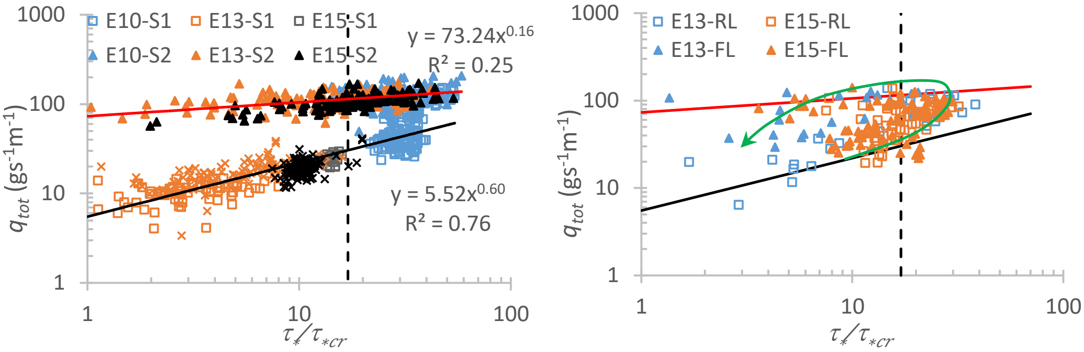

Figure 4-22. The relationship between total flux ($q_{tot} = q_T + q_D$) and transport stage (τ_*/τ_{*cr}). The solid black and red lines are least-squares regression through data in Figure 4-21a. The green arrow presents an anticlockwise correlation in E13 with fast changing.

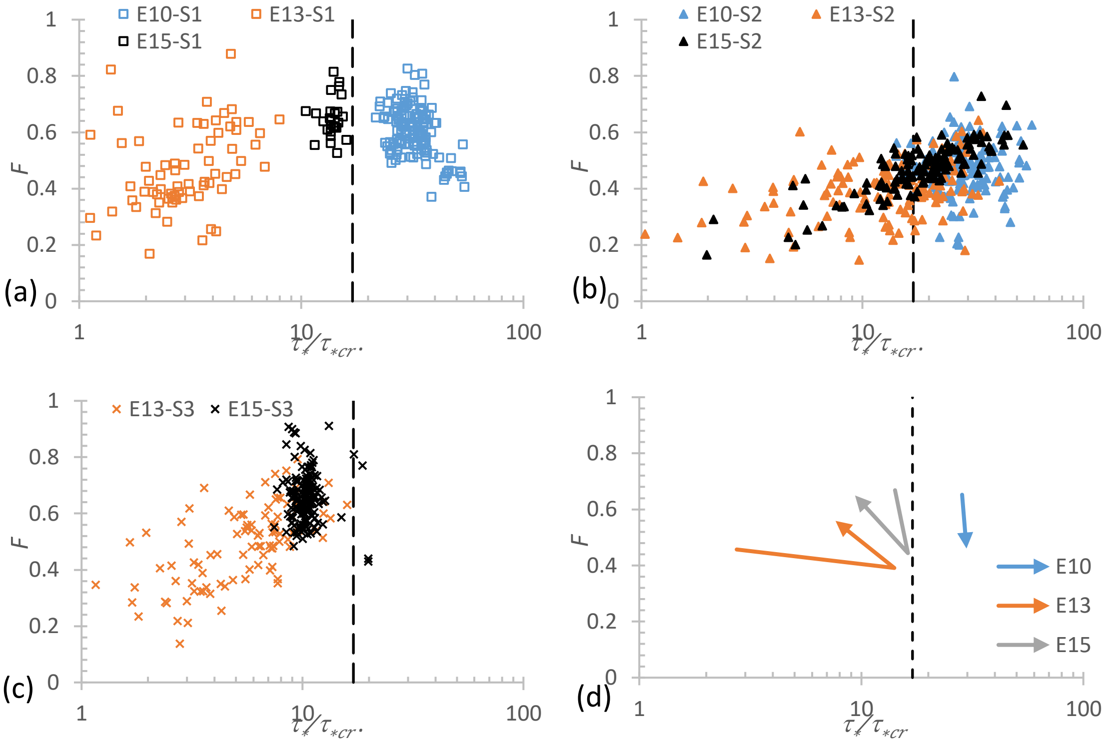

Figure 4-23. The fraction of the sediment flux related to deformation: variation during S1 (a); S2 (b); S3 (c) and overall trend (d).

In order to investigate how sediment transport mechanism affects bedform evolution, the relationship between τ_*/τ_{*cr} and the deformation fraction F were analysed (Figure 4-23). The results show that, in periods with low flow discharge, F increases with the increase of τ_*/τ_{*cr}, but when τ_*/τ_{*cr} approaches or exceeds the suspension threshold, F keeps constant nearly 0.6~0.7 (Figure 4-23a and c). Similarly, for data with high discharge, F keeps a positive relationship with τ_*/τ_{*cr}, but below 0.6 (Figure 4-23b).

Figure 4-23d summarized how F varies with hydraulic conditions and data was averaged from periods when bedforms reach equilibrium (S1-S2-S3, see Table 4-2). For bedforms with net degradation during S1 (E10 and E15), it is reasonable that deformation flux ($F \approx 0.65$) occupies a higher proportion compared with those without net degradation or aggradation (E13, $F \approx 0.5$). Furthermore, the transport stage seems to have little effect on F, as E10 is MXD while E15 is BLD. When flow condition increases to S2 which are all MXD, F of all of these three runs drops to lower than 0.5, indicating the effect of migration on sediment transport is enhanced. *Venditti et al.* [2016] found the similar result that F decreases with an increase of the transport stage when flow condition rose from BLD to MXD. They attribute this unexpected result to the growth of bedforms and increase of migration rate. In principle, as bedforms become bigger, leading to the larger roughness, the greater part of shear stress contributes to sediment movement related to bedform migration.

Notably, for E10 whose transport stages are nearly the same in S1 and S2, their F is quite different. That is because, sediment supply during S1 was limited, leading to the net degradation, and sediment transport related to net degradation is the main part of deformation. After flow condition dropped back to lower discharge (S3), F of both E13 and E15 rose back to the higher proportion (over 0.5).

In this study, sediment flux related to dune deformation was derived from differences between the consecutive bed profiles [*McElroy and Mohrig*, 2009], while it was assessed from the direct collection of the suspended sediment in the study of *Venditti et al.* [2016]. The difficulty in exactly quantifying the varying bypassing sediment transport over dunes under different flow strength [*Kostaschuk et al.*, 2009; *Bradley et al.*, 2013; *Naqshband et al.*, 2014c; *Naqshband et al.*, 2017] affects our ability in determining the thresholds of deformation fraction for different sediment transport conditions. However, the results of both studies demonstrate the similar trend between the transport stage and deformation fraction: the increase of transport stage results in the increase of the fluxes attribute to both dune translation and deformation, but the deformation fraction declines when bed condition transits from BLD to MXD. Moreover, in this study, both the sediment fluxes related to translation and deformation were calculated via the topography changes and bed degradation/aggradation leads to the enhancement of the calculation on dune deformation. Furthermore, in similar imposed flow conditions ($u = 0.6\mathrm{m/s}$) under BLD, deformation fraction increases from 0.45 to 0.65, while the transport stage rises from 3 to 16 (Figure 4-23d).

4.4.3. The initiation and development of bedforms from a flattened sand bed?

Development of quasi-two-dimensional bedforms over a flattened sand bed during the initial period of the experiment is commonly observed, such as *Venditti et al.* [2005b] and *Nelson et al.* [2011]. However, in our experiments, both 2D and 3D bedforms were detected at the initial period with the same flow discharge. One reasonable reason here to interpret the discrepancy is the differences of flow strength, i.e. shear stress, that the shear stress of E10 during the initial period is one order larger than that of E13 (Figure 4-6). The low shear stress of E13 remains the experiment is bedload transport dominant, as transport stage τ_*/τ_{*cr} is far smaller than 33 and u_*/w_s far smaller than 1. Thereby, the relatively steady sediment transport leads to the generation of quasi-two-dimensional bedforms (Figure 4-12). With the continuous several hours running, bedforms increasingly become larger and converted to 3D forms, which confirmed by *Venditti et al.* [2005b] who concluded that as long as running time is enough, there was an eventual transition to 3D forms. The conjunctions of crest lines in Figure 4-12 reflect the interactions between bedforms that some bedforms with smaller size but higher celerity overtake the host bedforms resulting in the transformation. In contrast, E10 with much higher τ_*/τ_{*cr} (ca 50) and larger u_*/w_s (ca 3) is suspended sediment dominant, resulting in several stochastic (random) scours and these deep scours laid the foundation of following bedform development during the initial period (Figure 4-12). Afterwards, the on-going bed level decline leads to the corresponding flow strength and water depth adjustment, and simultaneously, the changing of flow strength and water depth altered the equilibrium bedform size that the crests were washed and the deep scours were filled (Figure 4-12).

Coleman et al. [2005] proposed new expressions for both the times (t_e) required for ripples and dunes to achieve equilibrium magnitudes based on 91 laboratory experiments:

$$t_* = t_e u_*/D_{50} = 2.05 \times 10^{-2}(D_{50}/h)^{-3.5}(\tau_*/\tau_{cr})^{-1.12} \qquad 4\text{-}12$$

in which t_* is normalised time and t_e is time reaching equilibrium. Thereby, t_e can be calculated by local shear stress, grain size and water depth which are all available in our experiments. As some parameters in our experiment is not set constant, the average value was used here to assess t_e. The equilibrium time for E10 is nearly 54 minutes which correspond well with the bedform development of E10 (Figure 4-24). Herein, bedforms reached a higher level, followed by a decrease to the equilibrium condition, which also observed by *Nelson et al.* [2011] in his Experiment B on wavelength. In their experiment, a higher water discharge was set at the beginning, followed by a sudden change to the low flow for the remainder of the experiment. Unlike their experiment, our discharge was set constant at the whole S1, and the water and bed slope were adjusted by the bed itself rather than manually. Thereby, the increase-decrease trend was driven by the variation of shear stress, water depth and flow velocity simultaneously. In contrast, bedforms in E13 with much lower τ_*/τ_{cr}, whose equilibrium time is nearly 1000 minutes, keeps growing and migrating approximately constantly downstream, corresponding well with τ_*/τ_{cr}.

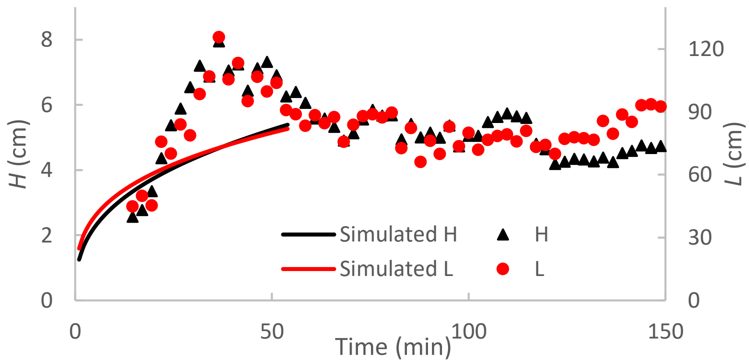

Figure 4-24. Comparison of reaching equilibrium for E10 between prediction and measured data.

The result indicates that bedform size prediction simply via water discharge was not appropriate, that the coupled changes of shear stress, water depth, and sediment supply should be taken into account, especially in events with dramatic alteration of these parameters, such as flooding.

4.4.4. What is the relationship between texture characteristics and bedform development?

Friedrich [2010] concluded that the 2D autocorrelation function is an important tool on 3D texture analysis, but in order to define more exact thresholds for bedform transitions, more data should be applied to this method. Her research defined analytically the restricting boundaries for bedform development: (1) when $x0/y0 < 1$, bedforms are wall-affected; (2) when $x0/y0 > 1$, flow-depth-affected. However, this method is subject to record length and in order to ensure the accuracy of data analysis, only less than 10% of the recorded length can be used [*Friedrich et al.*, 2006]. It means 45 cm for our 4.5 m measuring length, which is larger than half of the wavelength of the majority of bedforms during the whole experiments, indicating it is applicable to our data. Furthermore, in our experiments, the only area in middle channel (width is 55 cm measured by 12 URSs) was measured occupying only 35% of the whole width of the channel (1.6 m), forbidding our analysis across the channel. However, herein, as bedforms developed in our experiments are relatively three-dimensional, part of the 3D texture characteristics are still extractable (Figure 4-11).

Friedrich [2010] attributed different behaviours of θ to varying water depth: θ fluctuates around ±90° in deep flows, while around 0° in shallow flows. However, it is obvious that in experiments with deep flows (ratio of width to water depth is nearly 10), bedforms are well developed and generally, crestlines develop continuously across the whole channel, resulting in θ fluctuates around ±90°. Similarly, for shallow flows, around minute 60, similar behaviour is observed, verifying the importance of crestlines on θ. However, after 1.5 hours running in shallow flows, bedforms develop to relatively irregular morphology and crestlines are not continues across the channel, resulting in θ fluctuates between -45° and 45° [*Friedrich*, 2010].

Similarly, in our research, θ fluctuates around 0° (i.e. -45°~45°) when crestlines are not continuous across the measuring area (Figure 4-14b). In contrast, θ fluctuates around 45° while crestlines develop across the whole area. Furthermore, it is obvious that crestlines are perpendicular to flows but have a nearly 50° angle with the flow, resulting in θ fluctuates around 45° rather than 90° (see first 20 minutes in Figure 4-14a).

In summary, when the crestlines develop continuously across the whole measuring area and keep perpendicular to flows, θ tends to fluctuate around ±90° and $x0/y0 < 1$, while crestlines are not continuous, θ fluctuates around 0° and $x0/y0 > 1$. Moreover, θ highly depends on the angle of main crestlines and troughlines with flows. The distribution of θ and $x0/y0$ implies that in 3D bedform circumstances, judging whether bedforms reach equilibrium only by bedform size is not appropriate. It is because even bedform size keeps unchanged, their 3D texture characters may still vary, indicating the non-equilibrium condition. Especially, exactly quantifying bedform morphology plays a significant role in investigating interactions between hydrodynamics and morphology [*Best*, 2005a; *Coleman and Nikora*, 2011].

Previous research on both ripples [*Baas*, 1999] and dunes [*Venditti et al.*, 2005b] observed that the 2D-3D transition is inevitable as long as the running time is sufficiently long. In contrast, the result of the variation of θ in our experiments reveals that under steady flow conditions, bedforms keep switching between 2D and 3D, although bedform size reaches equilibrium. However, if we look through the data of *Venditti et al.* [2005b] (figure 8 where NDS, the non-dimensional span, estimated by those crests whose cross-stream extent exceeds 0.8 m) carefully, we can observe that after bedforms reach equilibrium, NDS variation is obvious and varies to less than 1.2 (the threshold used to define 2D and 3D: NDS < 1.2, 2D; NDS > 1.2, 3D.) intermittently, which is widely recognised in his experiments with higher velocities. This indicates bedforms transform between 2D and 3D intermittently but cannot be kept for a long time in 2D Moreover, limited by measuring size, after bedforms well developed, only 1 or 2 crestlines can be observed [*Venditti et al.*, 2005b]. They removed those crests whose cross-stream extent is less than 0.8 m which can inordinately bias NDS. This procedure magnifies the role of larger bedforms, as the crestlines of large ones or host bedforms can extend more broadly across the channel. Similarly, as mentioned above, the result calculated by autocorrelation function highly depends on larger scale bedforms. Therefore, it is reasonable, to some extent, both of these two methods are capable to quantify bedform three-dimensionality and estimate bedform 2D-3D transition. In our experiments, bedform merging and washing out within the measuring area plays a significant role in

3D quantifying (Figure 4-11 and Figure 4-14), as the characters of large bedforms dominate the result.

From the above, for the non-dimensional span method, the threshold (NDS=1.2) defined to distinguish transition between 2D and 3D bedforms is very subjective and identifying certain crestlines is the big challenge and very time-consuming as well. For the 2D autocorrelation function technique, the variation of bedform crestlines can be estimated, but particular patterns will significantly affect the result. This is because crestlines and troughlines across the channel keep varying between consecutively and non-consecutively with bedform migration. During the rising limbs, θ displays an opposite trend compared with those before flow condition changes, indicating that the rising of flow velocity not only increases bedform size but also alters sediment transport and bedform migration processes, especially on the lateral direction. During the falling limbs, as bedforms decay based on the initial large-scale ones generated on the high flow discharge, bedform three-dimensionality approximately remains on the same level although some variation exists.

4.5. Conclusions

This work extends our knowledge on how bedforms generate and develop under variable flows and also has begun to explore how flow strength variations can be coupled with variation in sediment transport mechanisms and/or supply:

1. Based on the results of our experiments, it is total sediment flux rather than bedform migration rate which is the more appropriate parameter to build the relationship with flow strength (i.e. transport stage), especially when the bed is bedload dominated and with lower flow discharge. Besides, whether there is a net degradation or aggradation plays a significant role in the calculation of deformation flux, and timescale is still a problem to calculate deformation flux, leading to the gaps on the correlations between BLD and MXD.
2. For rising limbs with increasing flow strength, not only bedform merging but also small-scale bedform washing out were detected. It is because the condition changes between BLD and SSD (i.e. the dramatic variation of sediment transport mechanism). However, as sediment transport in our experiments is dramatic, the growth of bedforms corresponded very well with hydraulic graphs, resulting in no apparent

hysteresis was detected during the rising limbs of these runs with smooth changes;

3. For falling limbs, different behaviours of the transport stage and the coupled of the fraction of deformation flux were observed. An anticlockwise relationship between transport stage and total flux was found in E13 with the fast wave, while cannot be seen in E15 with the slow wave, indicating the effect of decreasing rate of flow strength on bedform decay.
4. The 2D autocorrelation function is a potentially valuable tool for quantifying bedform 3D texture characters. When the crestlines develop continuously across the whole measuring area and keep perpendicular to flows, θ tends to fluctuate around $\pm 90^\circ$ and $x0/y0 < 1$, while crestlines are not continuous, θ fluctuates around 0° and $x0/y0 > 1$. Besides, θ highly depends on the angle of main crestlines and troughlines with flows.
5. The result of the variation of θ reveals: i) under steady flow conditions, bedforms switch between 2D and 3D, although bedform size reaches equilibrium. This is because crestlines and troughlines across the channel keep varying between consecutively and non-consecutively with bedform migration; ii) during the rising limbs, θ displays an opposite trend compared with those before flow condition changes, indicating that the rising of flow velocity not only increases bedform size but also alters sediment transport and bedform migration processes, especially in the lateral direction; iii) during the falling limbs, as bedforms decay based on the initial large-scale ones generated on the high flow discharge, bedform three-dimensionality approximately remains on the same level although some variation exists.

CHAPTER 5

5. Bedform dynamics in the middle reach of the Yangtze Estuary

Abstract: Bedforms are ubiquitous features existing in various environments ranging from deserts to oceans and even to other planets. Comprehending their development is vital to understand flow and sediment dynamics, and paleoenvironmental reconstruction of the geological record. Although abundant studies have been conducted on investigating fluid dynamics associated with bedforms in the past half-century, the vast majority of them focus on bedform dynamics under steady flows in a sandy bed. Therefore, how bedforms evolve under unsteady flows in cohesive beds is poorly understood. This paper presents two surveys analysing bedform development with different water/flow stages. They were conducted in the middle Yangtze Estuary, where bed material is composed of fine sand, silt and clay. Results show that compound bedforms exist in the late flood season, while only single type of bedforms are found in the late dry season. Results indicate that the superimposed bedforms in the late flood season and single-type bedforms in the late dry season are spring-neap tide controlled, and host bedforms are relicts of large dunes generated during the freshet. For compound dunes, relatively larger secondary dunes were discovered forming over the lower part of primary dunes. That is because bedforms decay from spring to neap tide and the crests of primary dunes respond to the flow structure more significantly, resulting in greater bedform translation and deformation. For single-type dunes, from neap to spring tide, trough scouring, rather than accretion or bedform amalgamation, results in bedform growth. Additionally, according to grain size analysis and morphometry measurements, our results highlight that clay content is a first-order control on bedform aspect ratio. Bedforms undergoing regenerative/constructive processes lead to the under-/over-estimation of bedform size, with key implications for bed roughness.

5.1. Introduction

Bedforms are ubiquitous features existing at various spatio-temporal scales and display a range of morphologies in environments ranging from deserts to oceans and even on Mars [*Best*, 2005a; *Rubin*, 2012; *Parsons and Best*, 2013]. Considerable research has been conducted on bedforms ranging from centimetres to meters in height and decimetres to kilometres in length in sand-bedded alluvial rivers, estuaries and coasts [*Rubin and McCulloch*, 1980; *Best*, 1996; *Wilbers and Ten Brinke*, 2003; *Goff et al.*, 2005; *Kostaschuk and Best*, 2005; *Parsons et al.*, 2005; *Ernstsen et al.*, 2006b; *Nelson et al.*, 2011; *Malarkey et al.*, 2015], where most large population centres are located.

Bedform phase diagrams, which were drawn based on data collected in laboratory flumes and under field conditions, display the relationships between various bed phases, and hydraulic and bed conditions, such as grain size, water temperature, flow velocity, water depth and other non-dimensional parameters [*Allen*, 1982; *Van Rijn*, 1984b; *Southard and Boguchwal*, 1990; *Kleinhans*, 2005a; *Van Den Berg and Van Gelder*, 2009] (see Table 5-1). These diagrams further define the boundaries and narrow the overlap between all sorts of bedform phases [*Baas et al.*, 2016]. Furthermore, prediction of dune dimensions is very important for the accurate estimation of bedform roughness, and the consequent stimulation of water level, especially for the construction of flood prevention measures [*Warmink et al.*, 2013; *Bradley and Venditti*, 2016]. In addition, reconstructing past fluvial environments on Earth and other planets depends heavily on estimated dune size based on cross-strata [*Bridge and Tye*, 2000; *Leclair*, 2002; *de Almeida et al.*, 2016]. Therefore, modern river prediction and paleoenvironmental reconstructions both critically depend on accurately building links between dune size and their ambient environment [*Bradley and Venditti*, 2016].

Numerous studies on ‘scaling relations’ [*Bradley and Venditti*, 2016] have built the links between bedform dimensions and boundary conditions, such as sediment supply [*Kleinhans et al.*, 2002; *Tuijnder and Ribberink*, 2008], shear stress [*Van Rijn*, 1984b; *Southard and Boguchwal*, 1990; *Bartholdy et al.*, 2005], water depth [*Yalin*, 2015; *Bradley and Venditti*, 2016] and grain size & virtual boundary layer (for ripples, e.g. *Coleman and Melville* [1996] and *Bartholdy et al.* [2015]). *Bradley and Venditti* [2016] has re-evaluated scaling relations, based on a large amount of flume and field data, and revealed that none of the previous predictors could accurately estimate bedform dimensions. Moreover, care must be taken when predicting bed phase in deep water, as bedform phase diagrams are mostly flume-based and developed from data generated from flow depth rarely greater than 1 m [*Venditti*, 2013] or 2.5 m [*Bradley and Venditti*, 2016]. The scale relationships between bedform size and water depth are vastly different in flumes and deep natural flows due to the change of the dominant process controlling dune size [*Kostaschuk and Church*, 1993; *Kostaschuk and Villard*, 1996; *Venditti*, 2013]. Therefore, the various scaling relations reflect not only the lack of consensus on the mechanisms controlling dune dimensions but also the complexity of bedform generation and development. However, in spite of nearly two orders of magnitude variation in dune size at any given flow depth, the positive relation between water depth and bedform dimension objectively exists [*Bradley and Venditti*, 2016].

Table 5-1. Comparison of bedform classification schemes, after Venditti et al. [2005a].

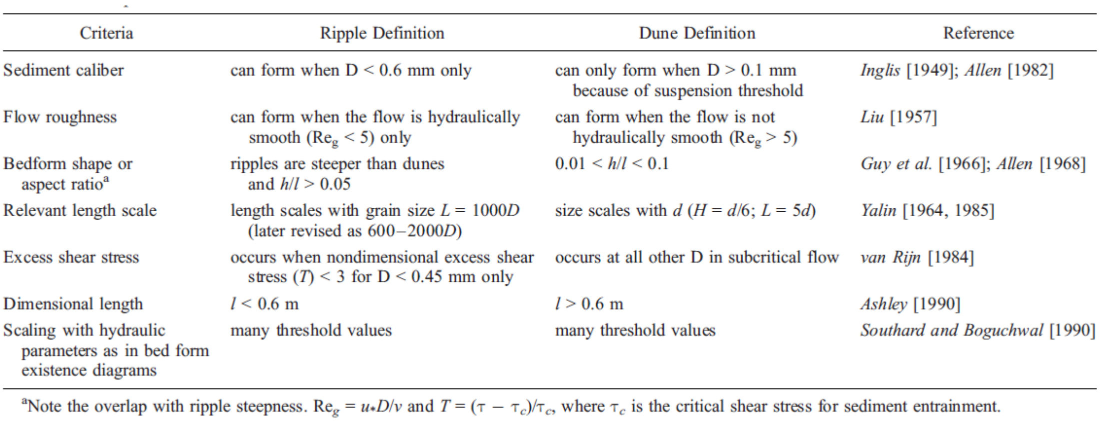

Criteria	Ripple Definition	Dune Definition	Reference
Sediment caliber	can form when D < 0.6 mm only	can only form when D > 0.1 mm because of suspension threshold	*Inglis* [1949]; *Allen* [1982]
Flow roughness	can form when the flow is hydraulically smooth ($Re_g < 5$) only	can form when the flow is not hydraulically smooth ($Re_g > 5$)	*Liu* [1957]
Bedform shape or aspect ratio[a]	ripples are steeper than dunes and $h/l > 0.05$	$0.01 < h/l < 0.1$	*Guy et al.* [1966]; *Allen* [1968]
Relevant length scale	length scales with grain size $L = 1000D$ (later revised as $600–2000D$)	size scales with d ($H = d/6$; $L = 5d$)	*Yalin* [1964, 1985]
Excess shear stress	occurs when nondimensional excess shear stress (T) < 3 for D < 0.45 mm only	occurs at all other D in subcritical flow	*van Rijn* [1984]
Dimensional length	$l < 0.6$ m	$l > 0.6$ m	*Ashley* [1990]
Scaling with hydraulic parameters as in bed form existence diagrams	many threshold values	many threshold values	*Southard and Boguchwal* [1990]

[a] Note the overlap with ripple steepness. $Re_g = u_*D/v$ and $T = (\tau - \tau_c)/\tau_c$, where τ_c is the critical shear stress for sediment entrainment.

According to the bedform phase diagrams, each phase originates from a certain set of circumstances. Nevertheless, the hierarchical nature of bedforms in the low flow regime has been recognised for nearly half-century highlighting that several distinct scales of bedform may generate in the same system [*Allen*, 1968b; *Jackson*, 1975; *Bridge*, 2009]. How one type of bedform superimposes on another is a key unknown [*Rubin*, 2012]. For example, ripples commonly occur on dunes [*Warmink et al.*, 2014], and smaller dunes are usually superimposed on larger ones [*Parsons et al.*, 2005; *Ernstsen et al.*, 2006b]. Some studies attribute this to multiple different flows (such as a response to both non-uniform and unsteady flow and hysteresis effects within a flood hydrograph [*Best*, 2005a]). The larger (host) bedforms are the remnant of some pre-existing flow condition, while the smaller (secondary or superimposed) ones form in the present new circumstance [*Allen*, 1968b; *Carling et al.*, 2000a; *Wilbers and Ten Brinke*, 2003; *Martin* *and Jerolmack*, 2013]. However, multiple studies have demonstrated that several scales of bedforms may develop simultaneously, and they could be active at the same time [*Best*, 2005a; *Parsons et al.*, 2005; *Venditti et al.*, 2005a; *Villard and Church*, 2005]. In contrast, an alternative view ascribes the generation of bedform superimposition to the development of the internal boundary layers created on the stoss-side of large bedforms [*Rubin and McCulloch*, 1980]. These layers lead to hydraulically smooth flows on the stoss, resulting in the generation of ripples [*Parsons and Best*, 2013]. This standpoint highlights the significant effect of flow structure on bedform morphology and consequently the mechanisms of sediment transport to bedforms. Superimposed bedforms growing and migrating on the stoss-side to the crests over primary bedforms are the mechanisms by which large dunes migrate downstream [*Reesink and Bridge*, 2007].

Superimposed bedforms commonly occur on the stoss-side of host bedforms and increase in height and wavelength from the trough towards the crest [*Harbor*, 1998; *Wilbers*, 2004]. Some cases also show that small-scale bedforms are absent on the lee-side and troughs (e.g. *Ernstsen et al.* [2006b] and *Parsons et al.* [2005]). This commonly occurs where the lee-side slope of bedforms reaches the angle of repose, preventing the generation of secondary bedforms on the lee and the trough. However, *Terwindt* [1971] and *Ernstsen et al.* [2006a] both observed “backflow ripples” on the lee-side related to flow separation which generally occurs on the lee-side of angle-of-repose dunes. Furthermore, *Parsons et al.* [2005] ascribed this phenomenon to flow acceleration at the crest of the larger dune forms and emphasised that further detailed investigations on fluid mechanics and sediment transport are needed.

Growing evidence from field observations suggests that symmetrical dunes with smaller lee-side angles (i.e. low-angle dunes, generally less than 10° [*Paarlberg et al.*, 2009]) are the prominent bedforms in large rivers [*Smith and McLean*, 1977; *Kostaschuk and Villard*, 1996; *Carling et al.*, 2000a; *Best and Kostaschuk*, 2002; *Chen et al.*, 2012; *Hendershot et al.*, 2016]. Due to the low-angle geometry, secondary bedforms are usually easier to be generated on the lee-sides without flow separation [*Best*, 2005a]. Therefore, interactions between topography, flow and sediment transport are inextricably linked and have been described as “chicken-or-egg problems” [*Costello and Southard*, 1981] or “self-organisation” [*Gyr and Kinzelbach*, 2004]. It further implies that predicting bedform phases based on phase diagrams or bedform predictors can be problematic, because these tools are based on highly-simplified physical parameters with simplistic assumptions [*Parsons and Best*, 2013].

Considerable research has been carried out on bedforms, most of them focused on equilibrium and unidirectional flow conditions. However, all fluvial and estuarine circumstances display temporal variations in flow discharge and water level, creating unsteadiness [*Martin and Jerolmack*, 2013; *Unsworth*, 2015]. Consequently, the rivers and estuaries strive to maintain balance with the changing flow strength by adjusting the roughness elements. Meanwhile, the variation of topography alters the local form drag (flow resistance), and thereby the level of river stages [*Reesink et al.*, 2013]. Most bedform research has focussed on non-cohesive sand beds, while more recent research has highlighted the effect of cohesive material (mud, clay and microorganisms, i.e. cohesive bed) on bedform geometry and dynamics, indicating that present bedform phase diagrams and predictors are overly simplistic [*Malarkey et al.*, 2015; *Schindler et al.*, 2015; *Baas et al.*, 2016]. Therefore, advancing our understanding of these interactions is the key to improving our ability to accurately predict the evolution of bedform [*Parsons and Best*, 2013].

This paper aims to investigate how bedforms respond to changing flood and tidal flows in the middle Yangtze Estuary, where bed material is composed of clay and fine sand. Both seasonal and tidal variations were studied in combination, and gaps between the rising and falling limbs of the hydrographs were identified. Our findings will also be valuable for paleoenvironmental reconstruction applied to the geological record.

5.2. Methods

5.2.1. Field setting

The Changjiang River, also known as the Yangtze River, has a total length of about 6,300 km and is the longest river on the Eurasian continent and the third in the world [*Dai et al.*, 2014]. It originates from the Tibetan Plateau, and flows eastward into the East China Sea at Shanghai, draining a total area of 1.81 million km^2, approximately one-fifth of the land area of the People's Republic of China (PRC) [*Yang et al.*, 2007]. The Yangtze basin supports the world's largest river-basin population, more than 450 million people [*Yang et al.*, 2014]. From the source in the west to the estuary in the east, it is divided into three segments by Yichang and Hukou: the upper, middle and lower reaches.

The Yangtze River, once regarded as the whole Changjiang River, is actually the very lower segment from Nanjing to the river mouth, which is tidally influenced (Figure 5-2). The tidal reach is called the Yangtze Estuary and starts from the tidal limit Datong located nearly 600 km upstream from the entrance to the East China Sea. Therefore, the Datong hydrology station is the controlling station for measuring hydrodynamics and sediment discharge into the sea [*Yang et al.*, 2002]. The annual-mean water and sediment discharges during 1950-2010 recorded at the Datong hydrology station were 896 km^3/yr and 390 Mt/yr, respectively [*CWRC*, 2014]. They also exhibit strong seasonal variations which show that during the flood season from May to October in response to monsoon rains in the upper basin occupies nearly 70% and 87% respectively of the annual total [*Chen et al.*, 2008; *Song et al.*, 2013].

Additionally, the monthly discharge varies widely, from 4140 m^3/s to 84,200 m^3/s, a nearly 20 times difference (Figure 5-1). Human activity, such as the building of dams within the river basin, has made an impact. Subsequently, the runoff discharge and its distribution are constantly changing [*Yang et al.*, 2010]. This monthly variation of runoff leads to the movement of the tidal current limit, between Zhenjiang and Jiangyin (ZJR, Zhenjiang–Jiangyin Reach) [*Song*, 2002]. The Changjiang Estuary is characterized as a meso-tidal estuary in terms of tidal range [*Fan and Li*, 2002; *Wu et al.*, 2009], varying from 2m (neap tide) to 4m (spring tide) [*Li et al.*, 2012]. The ZJR is affected by tidal currents depending on both the season and tidal conditions. The impact of tides on flow conditions is more significant in the dry season and spring tide, and less in flood season and neap tide.

The research site for this study is a slightly curved reach. It is located in the lower part of ZJR, nearly 15 km upstream from the Jiangyin Yangtze River Bridge (Figure 5-2). The runoff comes from the upstream reach (Yangzhong reach) in a southeasterly direction and turns left at Zaogangkou, flowing downstream to the east at a slight southerly angle. As a result, the riverbed thalweg is located on the south of the channel. However, the soil property of the south bank is quite compacted, preventing the erosion by the flows. Consequently, the planform of this reach has changed very little in the past decades.

Median bed material grain size (D_{50}) displays a fining trend, decreasing from nearly 300 µm at Zhenjiang Reach to around 20 µm at the mouth, in spite of some slight fluctuations [*Chen et al.*, 2012]. Dunes of various scales were observed in the Changjiang Estuary [*Zhou*, 1993; *Yang et al.*, 1999; *Cheng et al.*, 2004; *Chen et al.*, 2012; *Shuwei et al.*, 2017]. The scale of the dunes is dependent on the river discharge, with large dunes occurring in the high-discharge regime and medium dunes in the low-discharge regime.

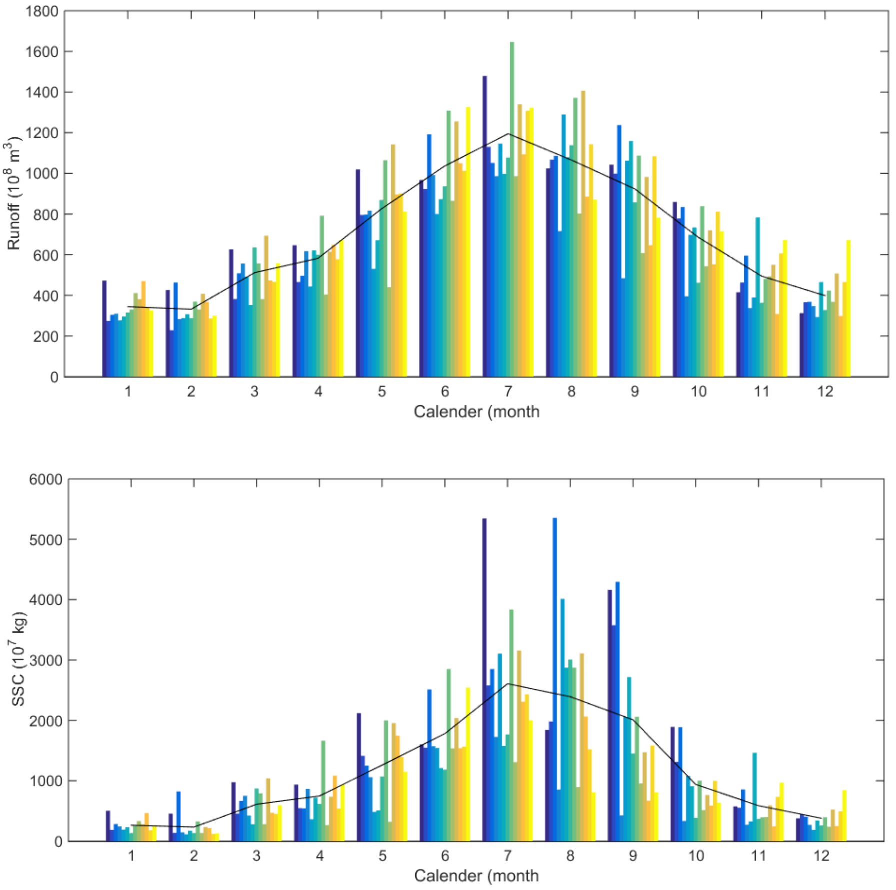

Figure 5-1. Monthly discharge and suspended sediment concentration at Datong Station from 2003 to 2015. The black line indicates the monthly mean value between 2003 and 2015.

5.2.2. Data collection

5.2.2.1. Data collection during the late flood season in October 2016

A Reson Seabat 7125 Multibeam Echo-Sounder (MBES) was employed to record three-dimensional (3D) bathymetry between the 20th and 22nd October 2016 (Figure 5-3a). The transducer of the MBES was mounted on the left side of the survey ship (18×3.8 m in length and width) by cables. The multibeam sonar system was configured for 512 beams operating in equi-distance mode at a frequency of 400 kHz, and a 150° wide swath was obtained perpendicular to the vessel track. The maximum ping rate is 50 Hz (±1 Hz), and the highest theoretical depth resolution can reach 6 mm [*RESON*, 2007]. The threshold of the ping rate was set to 20 Hz (automatically adjusted with water depth). Heave, pitch and roll (representing navigation, orientation, and attitude data) were recorded using an Applanix POS MV V3 gyroscope inertial guidance system mounted inside the vessel set as the origin of the coordinates.

Simultaneously, a Teledyne RD Instruments 600 kHz Rio Grande Workhorse acoustic Doppler current profiler (aDcp), mounted on the right side of the boat, was used to quantify the 3D flow velocities throughout a vertical column of water over each longitudinal section. The position of both MBES and aDcp was provided by a Trimble real-time differential global positioning system (DGPS), and the horizontal accuracy typically at +/- 0.3 m.

The aDcp has four transducers inclined at an angle of 20 degrees with respect to the vertical [*RD*, 2011]. It emits acoustic pulses of energy that are backscattered by scatters in the water column. Generally, scatters are regarded as materials carried by flows and having the same speed as the flow. The Doppler shift principle is applied to convert the change in frequency into weighted averages of components of flow velocity within each depth range bin [*Parsons et al.*, 2006]. However, the obtained velocities, called relative velocities, are measured with respect to the transducer. Thus, transducer speed must be known to calculate absolute flow velocities referencing to the earth. The transducer is fixed on the boat, so the boat speed is equal to the transducer speed. The boat speed can be estimated by two approaches: (1) by DGPS or (2) bottom tracking. The DGPS records the boat position and estimates boat speed (v_{DGPS}) via displacement. The accuracy and precision of calculated speed is highly dependendt on the accuracy of the DGPS [*Rennie and Rainville*, 2006]. The bottom tracking emits an independent acoustic pulse, different from the pulses to record water column information, to the river bed to quantify the relative movement between the bed and boat [*Rennie and Villard*, 2004]. Thus, the bottom tracking velocity (v_{BT}) is assumed to be the boat speed when the bed is fixed. However, if the river bed material is movable, the ‘bottom-tracking boat speed’ is biased by the bed movement. *Rennie* [2002] first applied this bias into estimating apparent bedload speed by comparing the boat velocity, $v_{bed} = v_{DGPS} - v_{BT}$.

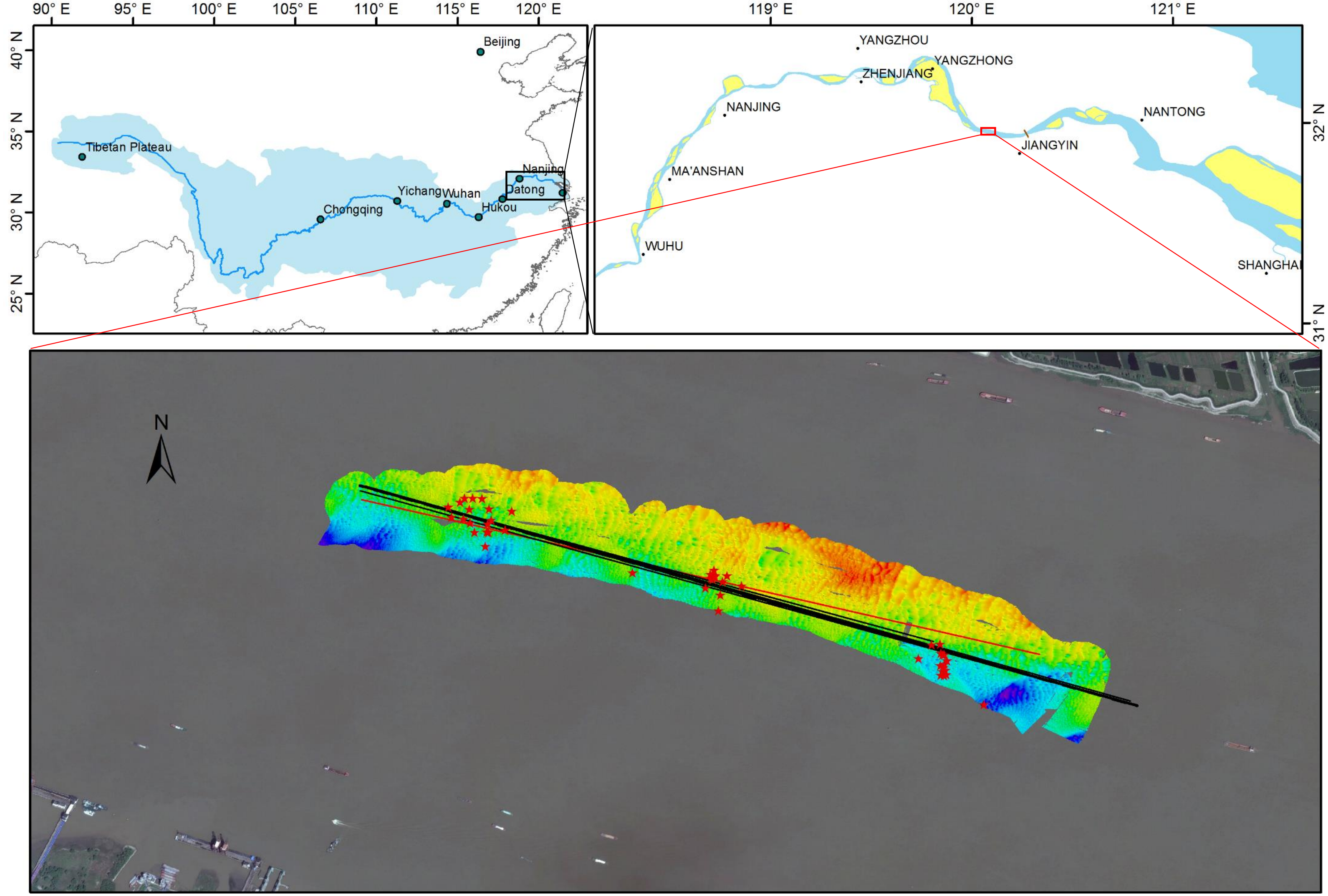
90° E
95° E
100° E
105° E
110° E
115° E
120° E
40° N
35° N
30° N
25° N
Beijing
Tibetan Plateau
Nanjing
Datong
Yichang
Wuhan
Hukou
Chongqing
119° E
120° E
121° E
32° N
31° N
YANGZHOU
YANGZHONG
ZHENJIANG
NANJING
NANTONG
JIANGYIN
MA'ANSHAN
WUHU
SHANGHAI
N

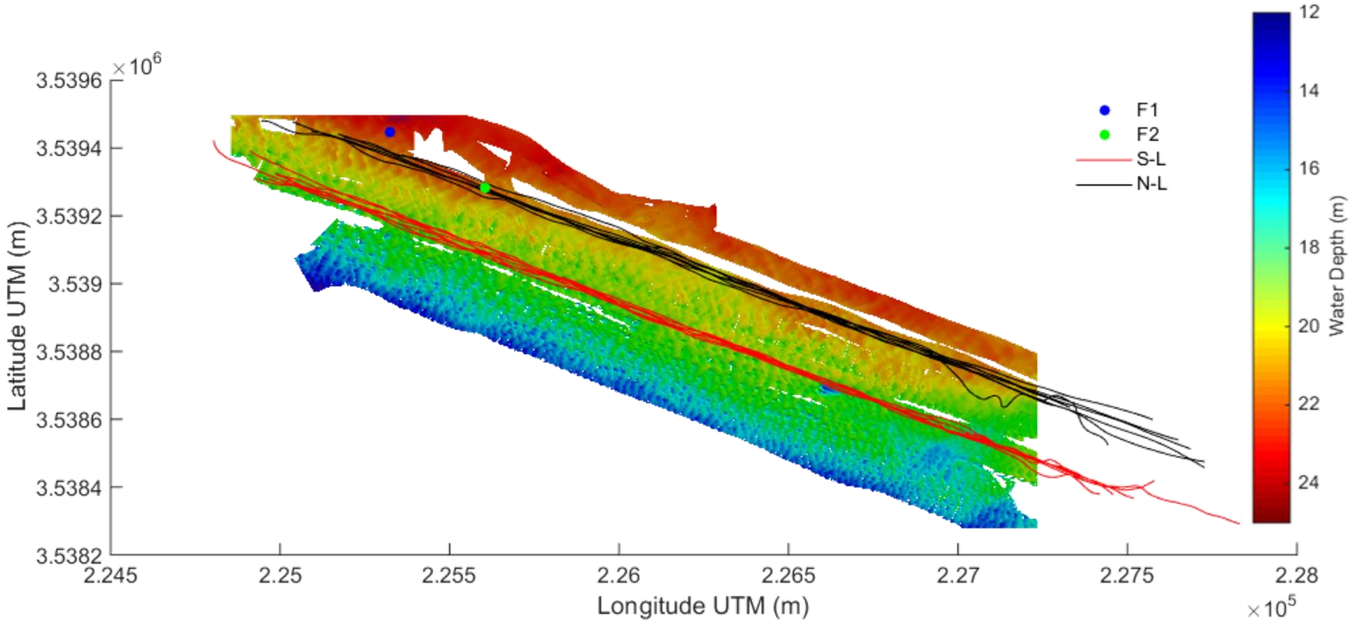

Figure 5-2. Location of (a) the Yangtze Basin, (b) the Yangtze Estuary and (c) measurement area. Red stars in (c) present fixed point sites; the red line indicates tracking line of Transect 1 and other five black lines mean tracking lines of Transect 2-6.

The aDcp transducer was inserted into the water at a distance of 0.8 m ensuring that data recording will not be affected by the wave, and aDcp data was collected at an interval of 3 seconds with the vertical bin size of 0.5 m. Five ‘pings’ were averaged before data was outputted to increase the signal/noise ratio. The blanking distance near the surface due to instrument command settings and near the bottom due to acoustic interference effects was 1.68 m and 6% of local water depth.

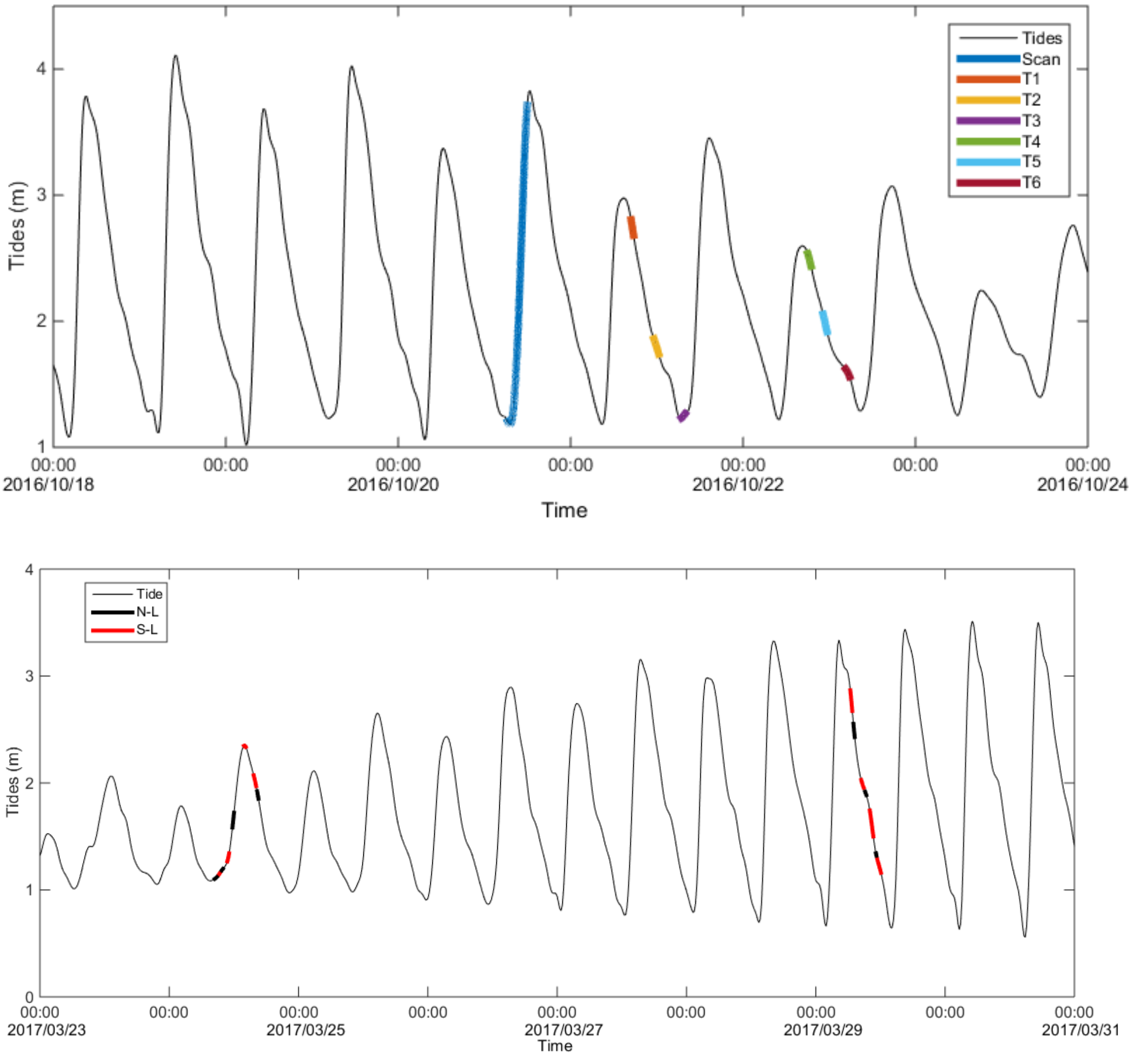

Figure 5-3. Hydrograph for tides and time for each measurement during the late flood (a) and late dry season (b). During the late flood survey, one area scan was done in advance to determine the research area, and six measurements were conducted after that within two tides. During the late dry season, 8 and 7 measurements were conducted during neap and spring tide respectively.

A first MBES measurement was made on the 20th October 2016 by scanning a field area, which is nearly 2 km long and 300 m wide, located on the north side of the shipping lane (Figure 5-2). Consequently, six repetitive aDcp coupled with MBES measurements were made, along with the longitude transect, during the following two days (3 on each day). Each measurement was taken in the upstream direction and, on the way back to the start point before the next measurement, three in-situ (fixed point) measurements were made. At each fixed location, three water samples were collected at the different layers: near surface (1 m depth), middle layer and near the bottom. Also, an OBS-3A turbidity sensor with 1 Hz sampling rate, which was used to self-record turbidity, salinity, and temperature (OBS-3A Turbidity and Temperature Monitoring System; Washington, USA), was lowered down from the surface to the bottom and pulled up via a manual winch. This was repeated three times for each point. Two riverbed samples were collected by a grab sampler, one for each day, and were further analysed in the laboratory.

5.2.2.2. Data collection during the late dry season in March 2017

The same MBES, aDcp and surveying ship used in the flood season were employed, and measurements were conducted in the same area. In order to investigate the effect of water depth and spring/neap tides on bedform evolution, two survey lines (North line, N_L, and South line, S_L) were measured in both neap tide (2017/03/24) and spring tide (2017/03/29) (Figure 5-3d). Measurements on the south line were always taken in the upstream direction, while those on the north line were in the downstream direction. Four measurements were conducted for the north line during the neap tide and three during the spring tide, named N1_1 to N1_4 and N2_1 to N2_3 respectively. Similarly, eight surveys were taken on the south line, four each for neap and spring tide, named S1_1 to S1_4 and S2_1 to S2_4 (Figure 5-2, N/S means north or south line, and the following 1 and 2 donate neap and spring tide respectively).

Additionally, two in-situ aDcp measurements (Figure 5-2d) were carried out during the neap (2017/03/25) and moderate tide (2017/03/28). As the south part of our research area is quite close to the navigation channel, and fishing events were relatively frequent during our measuring period, a location further north was chosen as the fixed point measurement area. Three water samples at the different layers (surface, middle layer and near the bottom) were collected hourly. An OBS-3A turbidity sensor tied together with a LISST 100X (laser in situ scattering and transmissometry) instrument, developed by Sequoia Scientific Inc., were lowered down from the surface to the bottom and pulled up via a manual winch at hourly intervals. That was done in order to measure volume concentrations and size spectra of vertical profiles.

Four riverbed samples for each survey were collected by a grab sampler during the neap and spring tides and were further analysed in the laboratory.

5.2.3. Bedform translation flux calculation

Simons et al. [1965] proposed an approach to compute sediment transport related to bedform translation:

$$q_T = \beta_b (1-p) V_b H \qquad 5\text{-}1$$

In which, p is the porosity of the bed ($p = 0.4$), V_b is the bedform migration rate, H is the bedform height and β_b is the shape factor of the bedforms. $\beta_b = 0.56$ is typical for asymmetrical bedforms [*Berg*, 1987; *Hoekstra et al.*, 2004; *Venditti et al.*, 2016]. Note that this equation was built based on the assumption that bedforms migrate downstream without changes in the shape, size and spacing [Lin and Venditti, 2013]. Therefore, the bedform translation rate in equation 5-1 is calculated irrespective of bedforms deformation.

An automated method called 'lag distance detection' was applied to calculate translation distance between two consecutive streamwise profiles [*Nittrouer et al.*, 2008; *Venditti et al.*, 2016], consequently, bedform migration speed is equal to lag distance divided by the interval time. As bedforms migrate continually downstream, measured bed profiles are lagged by a distance between two surveys, called the translation distance. The profiles are lagged relative to one another, as long as the bedforms do not deform dramatically. Translation distance between two surveys is taken as the lag distance that corresponded to the minimum derived value. Similarly, translation distances of parallel bed profiles across the channel are averaged to get a spatially-averaged translation rate. This method can be successfully applied when bedform migration and translation are not significant between consecutive surveys [*McElroy*, 2009].

However, flows in the tidally influenced areas are perpetually variable, leading to a permanently varying migration rate. Therefore, a migration rate between specific survey periods cannot represent the proper rate. Here, equation 5-1 was transformed to calculate the sediment transport flux per unit width per length:

$$Q_T = \beta_b (1-p) D_{lag} H \qquad 5\text{-}2$$

where $D_{\mathrm{lag}} = V_b \cdot \Delta\mathrm{t}$, and $\Delta\mathrm{t}$ is the time difference between the two surveys.

5.2.4. Bedform deformation flux

Simons et al. [1965] reported that when the bedload calculated by individual bedform tracking is always smaller than the directly measured bed material transport rate, part of the sand is suspended from the bed during high transport conditions and transported as saltation or suspension [*Bagnold*, 1973; *Cheng and Emadzadeh*, 2014]. These particles are partly supported by the turbulence in the flow and partly by the collision force from the bed and follow a distinctively asymmetric trajectory [*Abbott and Francis*, 1977; *Wiberg and Smith*, 1985]. Moreover, they are important to promote bedform evolution but ignored by most geomorphologists [*Naqshband et al.*, 2014a; *Naqshband et al.*, 2014c].

McElroy and Mohrig [2009] proposed to take the constant of integration to be the fraction of bed material load that moves intermittently in near-bed suspension. The equation they suggested to calculate deformation rate is based on two along-stream bed profiles. The average of elevation changes (D), associated with bedform deformation flux and independent of translation, is computed as:

$$D = \frac{\Delta x}{2N\Delta t}\sum_{x}|\Pi(x)| \qquad 5\text{-}3$$

$$\frac{\partial \eta}{\partial t} + V_b\frac{\partial \eta}{\partial x} = -\Pi \qquad 5\text{-}4$$

where *D* is summed over the bed profiles, indicating mean volume change in topography. Δx is the length of the transport distance, Δt is the time difference between the two profile measurements, and N is the total number of measurements in the profile. $\Pi(x)$, calculated via equation 5-4 , represents the elevation difference between the bed profiles.

In order to make the calculated deformation flux comparable to bedform translation flux, deformation flux should be calculated over the same time scale as the translation flux [*Ganti et al.*, 2013]. However, the time difference (i.e. interval) is the main factor affecting deformation flux. A longer time interval leads to a greater underestimation of actual deformation flux. Actual deformation flux can be calculated by employing a surveying strategy with at least two survey repeats and extrapolating to apparent deformation fluxes at short timescales, the most accurate estimate of deformation flux

[*McElroy and Mohrig*, 2009]. This conclusion is applicable under steady flow conditions. However, flow conditions in our research are variable, therefore, a transformed equation is proposed here to calculate the deformation flux:

$$D' = \frac{\sum_x |\prod(x)|}{N} \tag{5-5}$$

$$Q_D = D' D_{lag}/2 \tag{5-6}$$

where q_D means translation flux per width per length and D' is the average elevation change. Bedform deformation is persistent with bedform migration. Therefore, in the calculation of deformation flux, we hypothesize that the transport distance for the sediment, related to deformation, equals to half of bedform translate distance.

5.3. Results

In fluvial and coastal research, bedform geometry quantification is necessary and extremely important for engineers and scholars to understand interactions between the flow and bed morphology [*Kostaschuk*, 2006], explain the formation of cross-strata [*Reesink and Bridge*, 2011] and quantify sediment transport over bedforms [*Wilbers and Ten Brinke*, 2003]. Moreover, in many sedimentary environments, it is commonly recognised that bedforms are present as superimposed states that several scales can be observed in the same reach (e.g. *Parsons et al.* [2005]). Therefore, an effective method is vital to bedform geometry dependent research.

Gutierrez et al. [2013] proposed a standardization of the nomenclature and symbolic representation of bedforms and detailed the combined application of robust spline filters and continuous wavelet transforms, developed by *Torrence and Compo* [1998]. It was used to discriminate these morphodynamic features and provides the quantitative recognition of bedform hierarchies. This approach was successfully applied to a detailed 3-D bed topography from the Rio Parana, Argentina, whose large-scale dunes are superimposed by smaller bedforms.

An open source MATLAB software (GNU General Public License software) - bedforms-ATM V 1.1 - was developed as a joint collaboration between the Pontifical Catholic University of Peru (Pontificia Universidad Católica del Perú); the University of Technology and Engineering, Peru; and the Technical University of Braunschweig, Germany. This

Bedforms Analysis Toolkit for Multiscale Modelling presents an improved version of the method proposed by *Gutierrez et al.* [2013] and comprises four main applications: (1) bedforms wavelet analysis, (2) power Hovmoller Analysis, (3) bedforms multiscale discrimination, and (4) three-dimensionality analysis [*Gutierrez*, 2016]. Herein, we use this software to discriminate our filed morphodynamic data (applications (1) and (3) were applied).

However, statistical analysis is not available in version 1.1 of bedforms-ATM. Thereby, the method of *van der Mark and Blom* [2007] was applied here to compute bedform features, as this method avoids subjective code as much as possible, ensuring to be applicable to various data sets [*van der Mark et al.*, 2008]. Individual bedform heights, $H1_i$ and $H2_i$, were determined as elevation changes from troughs to downstream crests and crests to downstream troughs, respectively, while individual lengths, $L1_i$ and $L2_i$, were calculated from inter-crest and inter-trough distances. Lee face slopes were computed as $H2_i/Ldowns_i$ ($Ldowns_i$, length of the lee face), and stoss face slopes as $H1_i/Lups_i$ ($Lups_i$, length of the stoss face). Finally, all of the results obtained from the 12 URSs were averaged to calculate the spatially averaged values (H and L).

Additionally, features with a value below two standard deviations of the mean value for the transect were removed from the dataset. This effectively filtered out features with values too small (distorted by the 0.2 m resolution of the maps [*Hendershot*, 2014]) and too large (zero-crossing method may leave out some bedforms which may lead to a dramatic increase of bedform height or length or decrease of lee-side or stoss-side slope [*van der Mark and Blom*, 2007]).

5.3.1. Bedform variation during moderate tide in the late flood season

As displayed in Figure 5-2a, except for T1, the other five tracking lines (T2-6) are almost overlapping with each other. Therefore, only T2 to T6 were analysed in the following section, because the topography in the same area (2.23 km long and 40 m wide) can be extracted from each of these five transects for morphodynamic analysis (Figure 5-4). As we can see in Figure 5-4, multiscale bedforms dominate the whole reach, and they are relatively two dimensional. Bed elevation varies from -23 m to -15 m and the deepest part is located at the downstream end. Furthermore, the variation of bedform morphology within these five measurements is very tiny, and it is hard to observe in the global view.

The left column of Figure 5-5 represents the variation of bed profiles of three specific tracking lines, indicated in Figure 5-4, for each transect. It is obvious that there is considerable variation of bed profile in the lateral direction and that bedforms in the deeper and middle part comprise the large dunes superimposed with small dunes while bedforms in shallower part are composed of the bar superimposed with small dunes.

As illustrated in Figure 5-4 and Figure 5-5, during two tides, both migration and deformation of small dunes are tiny. Therefore, we presume only small-scale dunes are active during our measurements and, for the following data analysis, the topography of T2 is set as the basic reference. Bedforms wavelet analysis was first applied to all topography data. After that, the third application of bedforms-ATM was used to discriminate multiscale features. Results of each scale are given in Figure 5-6: bar (or remnant of larger scale bedforms produced due to flooding events or storms), large dunes and small dunes.

Table 5-2. Statistics of small superimposed bedform features in the late flood season.

Features	T2	T3	T4	T5	T6
H_{50} (H_{mean})	0.81 (0.88)	0.81 (0.88)	0.70 (0.77)	0.76 (0.83)	0.77 (0.84)
L_{50} (L_{mean})	16.77 (18.91)	17.12 (19.19)	16.07 (18.03)	16.87 (18.87)	16.92 (19.04)
Lup_{50} (Lup_{mean})	10.72 (11.86)	11.11 (12.23)	10.96 (12.17)	10.90 (11.85)	11.23 (12.34)
$Ldowns_{50}$ ($Ldowns_{mean}$)	4.92 (6.24)	4.76 (6.20)	4.08 (5.45)	4.84 (6.28)	4.66 (6.01)
Asy_{50} (Asy_{mean})	0.32 (0.30)	0.36 (0.32)	0.41 (0.37)	0.34 (0.31)	0.36 (0.33)
S_s_{50} (S_s_{mean})	4.04 (4.18)	3.88 (4.01)	3.70 (3.82)	3.69 (3.82)	3.72 (3.85)
S_l_{50} (S_l_{mean})	8.58 (9.71)	8.91 (9.90)	8.68 (9.56)	8.48 (9.32)	8.53 (9.47)
H/L_{50} (H/L_{mean}) %	4.62 (4.84)	4.56 (4.78)	4.68 (4.59)	4.37 (4.58)	4.38 (4.59)

H	*bedform height from both top to downstream trough (Htotr) and trough to the downstream top (Htrto);*
L	*bedform length calculated from both length between two subsequent crests and troughs;*
Lups	*length of the stoss face, the upward length;*
Ldowns	*length of the lee face, the downward length;*
Asy	*Asymmetry calculated via (Lups-Ldowns)/(Lups+Ldowns);*
S_l	*Lee face slope angle (degrees) computed as Htotr/Ldowns;*
S_s	*Stoss face slope angle (degrees) computed as Htrto/Lups;*
H/L	*Aspect ratio computed as (Htrto+Htotr)/Lups/2;*

Subscript 50 and mean here indicates median and mean value respectively.

To extract the bed profiles from the topographic maps, 41 stream-wise transects, spaced at 1 m cross-channel intervals, were laid over the base maps. Points were extracted at

0.2 m intervals along each of these lines and tagged with the position (transferred to the new coordinate that direction of stream-wise and cross-channel to the north bank was set to the new x-axis and y-axis) and depth of the bed below the water surface. Statistical results of bedform height (H), length (L), lee face angle (S_l), stoss face angle (S_s) and asymmetry (Asy) of small dunes for each transect are given in Figure 5-8 and Table 5-2. As the evidence from the figures shows, the variation of bedform features of small dunes is obvious and the variation tendency of median and mean values during tides is similar:

(1) Bedform height (H) increases between the high tide and the lower falling tide with the increase of flow velocity (T3-T4). It reaches equilibrium at some point before the low tide, remaining unchanged between this point and the low tide (T2-T3 and T5-T6);

(2) During the falling tides, bedform length (L) keeps increasing, while the variation of its components (upward length, $Lups$, and downward length, $Ldowns$) is more complicated. Upward length ($Lups$) continues to reduce, even after flow velocity starts accelerating (T4-T5), reaching its lowest value at some point in the lower falling tide. It is followed by a rise towards the low tide (T5-T6), and upward length in the low tide is slightly greater than that in the high tide. In contrast, downward length ($Ldowns$) rises to its maximum value at some point in the lower falling tide, followed by a decline towards the low tide. However, downward length in the low tide is much higher than that in the high tide. Additionally, the variations of stoss face angle (S_s) and lee face angle (S_l) shows a strong inverse correlation to the variations of $Lups$ and $Ldowns$.

(3) The bedform asymmetry (Asy) parameter displays a similar trend with that of upward length, but Asy reaches largest at the high tide. The more asymmetric the bedforms become, the higher the Asy is.

(4) Frequency polygons for all the calculated features (Figure 5-8) show that the distribution of each geometric property retains the same general pattern over the five measurements. The distributions for $H,\ L,\ Lups,\ Ldowns,$ and S_l are unimodal with positive skew, while the distributions for S_s and aspect ratio (H/L) are closer to being normally distributed. Otherwise, the distribution of Asy is unimodal with a negative skew.

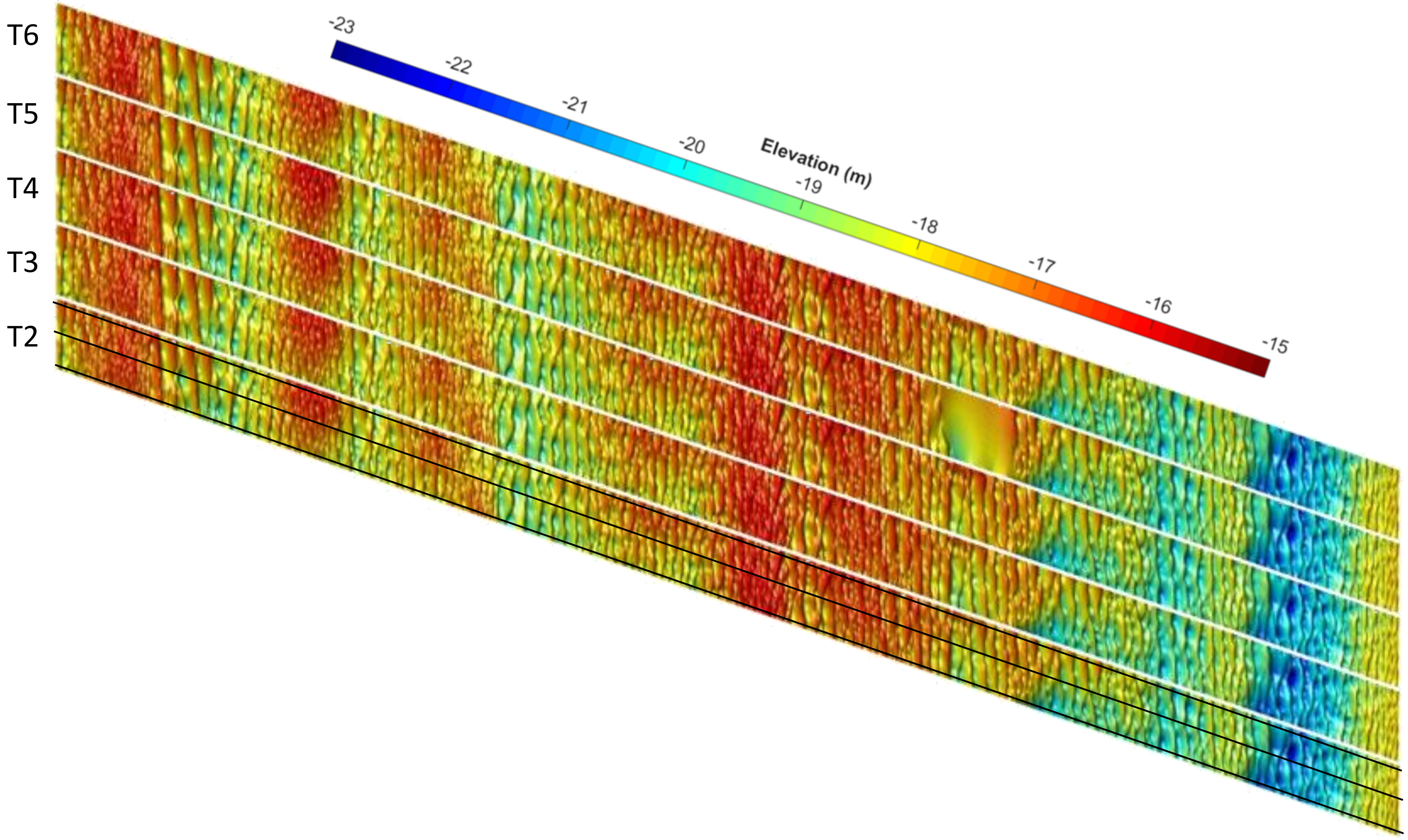

Figure 5-4. Bed topography of transect T2 to T6. Three black lines present locations of bed profiles in Figure 5-5. Bed elevation varies between -23 and -25m. Bedforms remain nearly unchanged during the whole survey.

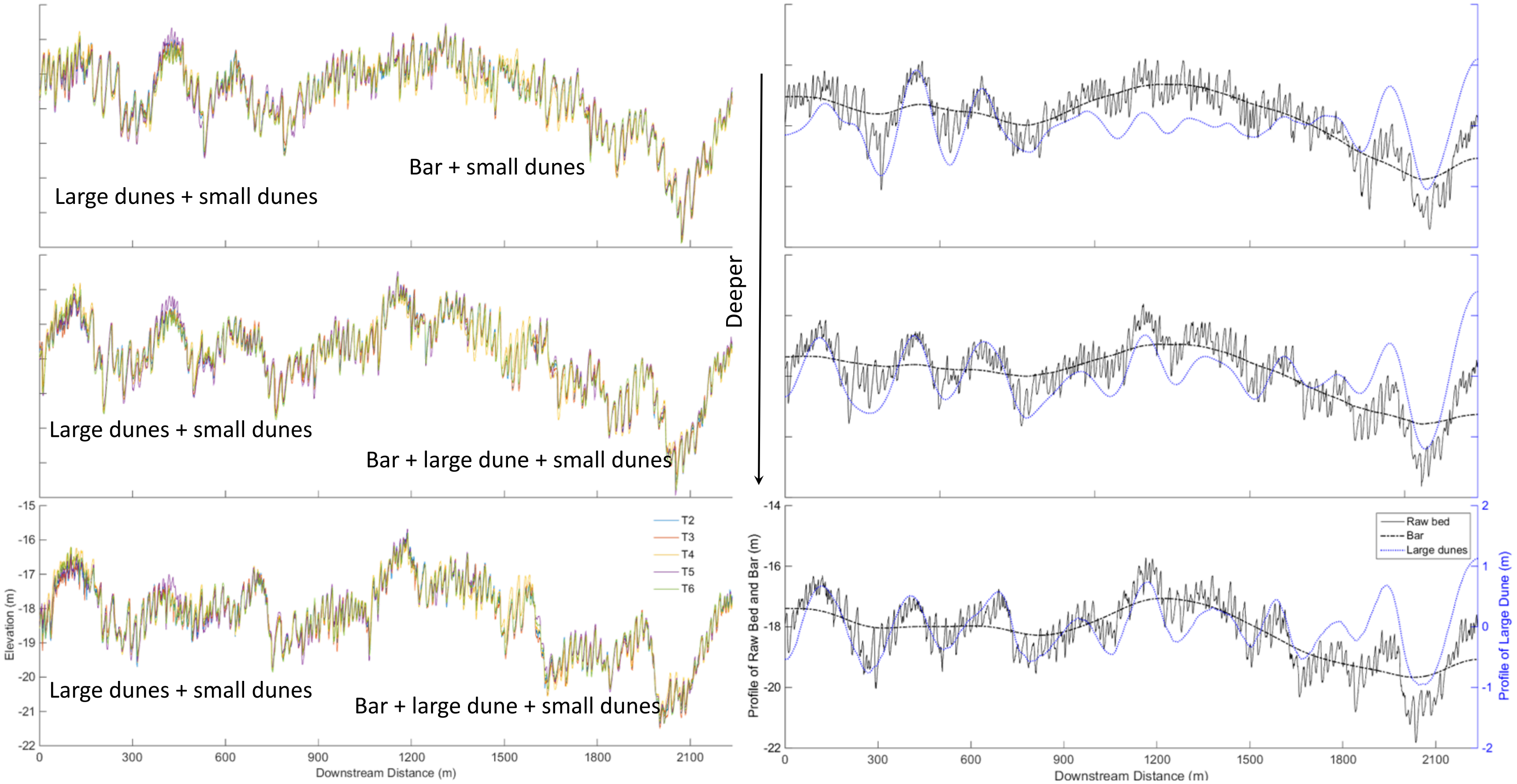

Figure 5-5. Variation of the topography of each transect (Left column) and bedform discrimination (Right column): Shallow part (first row), (b) Middle part (middle row) and (c) Deep part (bottom row). Locations of these profiles are defined in Figure 5-4. Three types of bedforms are distinguished: bar, large dune and superimposed smaller dunes.

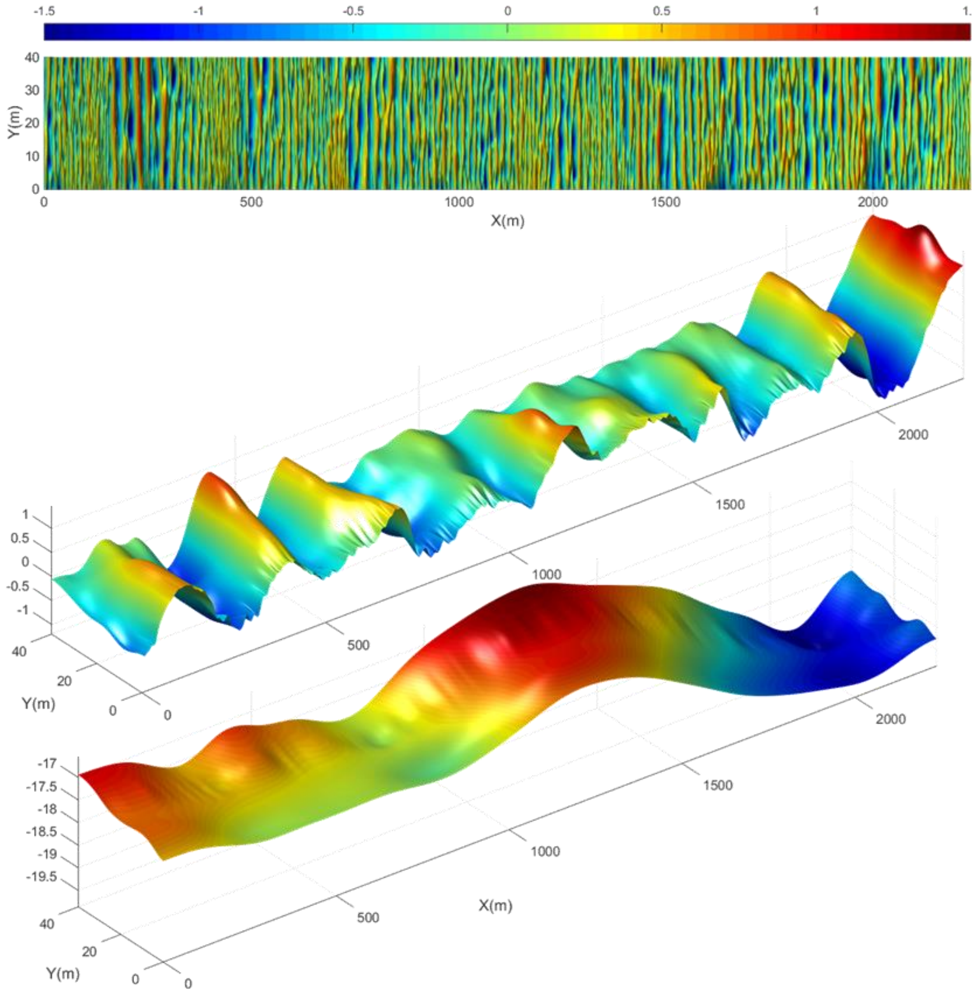

Figure 5-6. Bedform multiscale discrimination based on bathymetry of T2: (a) 2D view of superimposed dunes, and 3D view of (b) Large-scale dunes and (c) Bar.

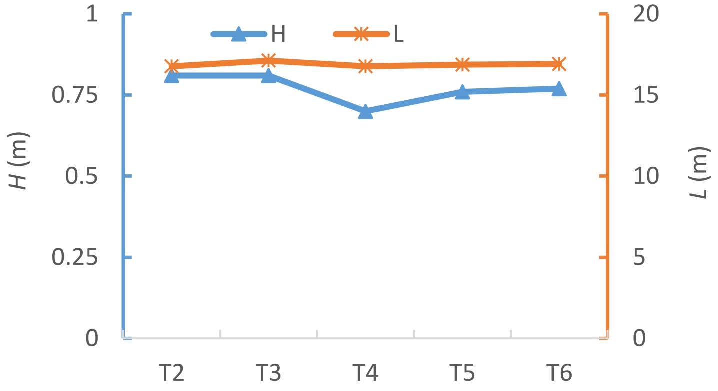

Figure 5-7. Variation of bedform size (height and length) within tides.

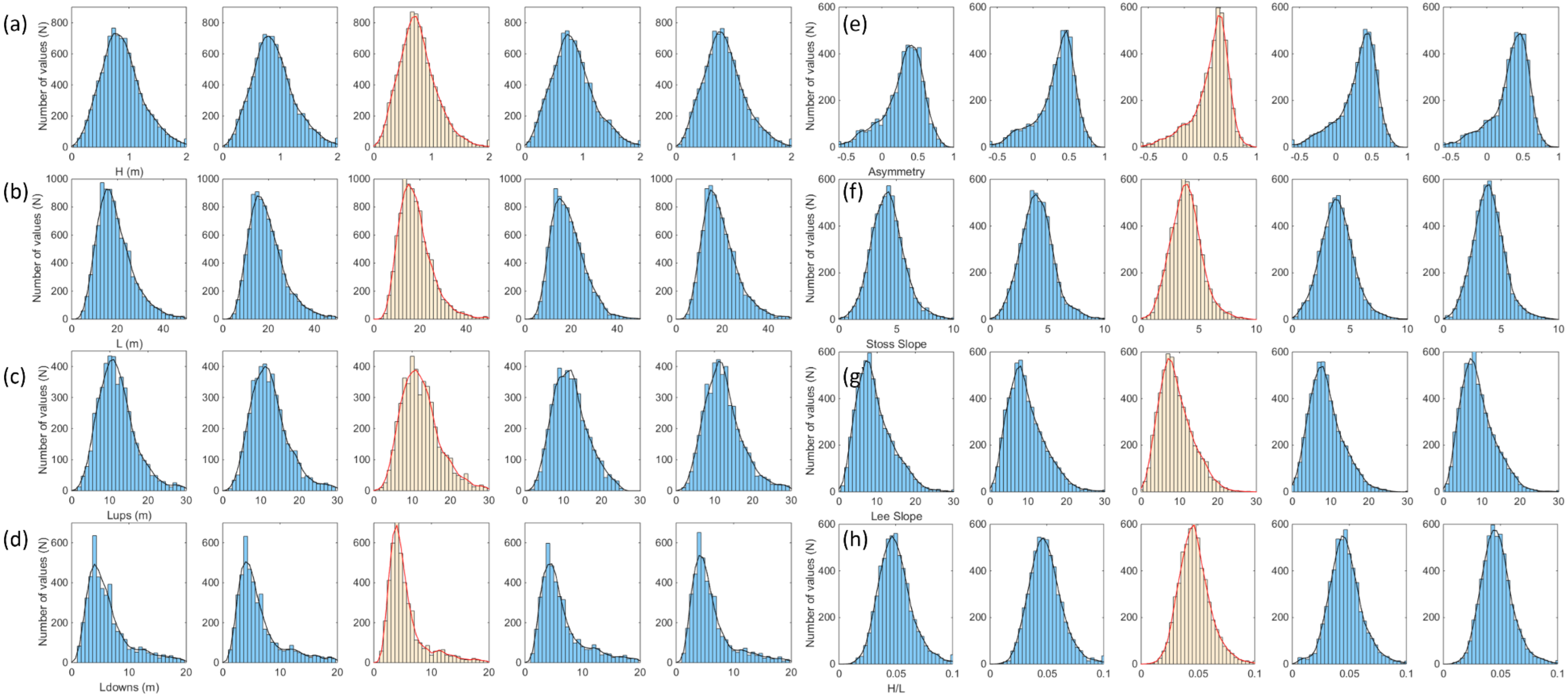

Figure 5-8. Statistics of characteristics of superimposed small dunes in the late flood season for T2-T6. Explanation of each characteristic from a to h, please see Table 5-2.

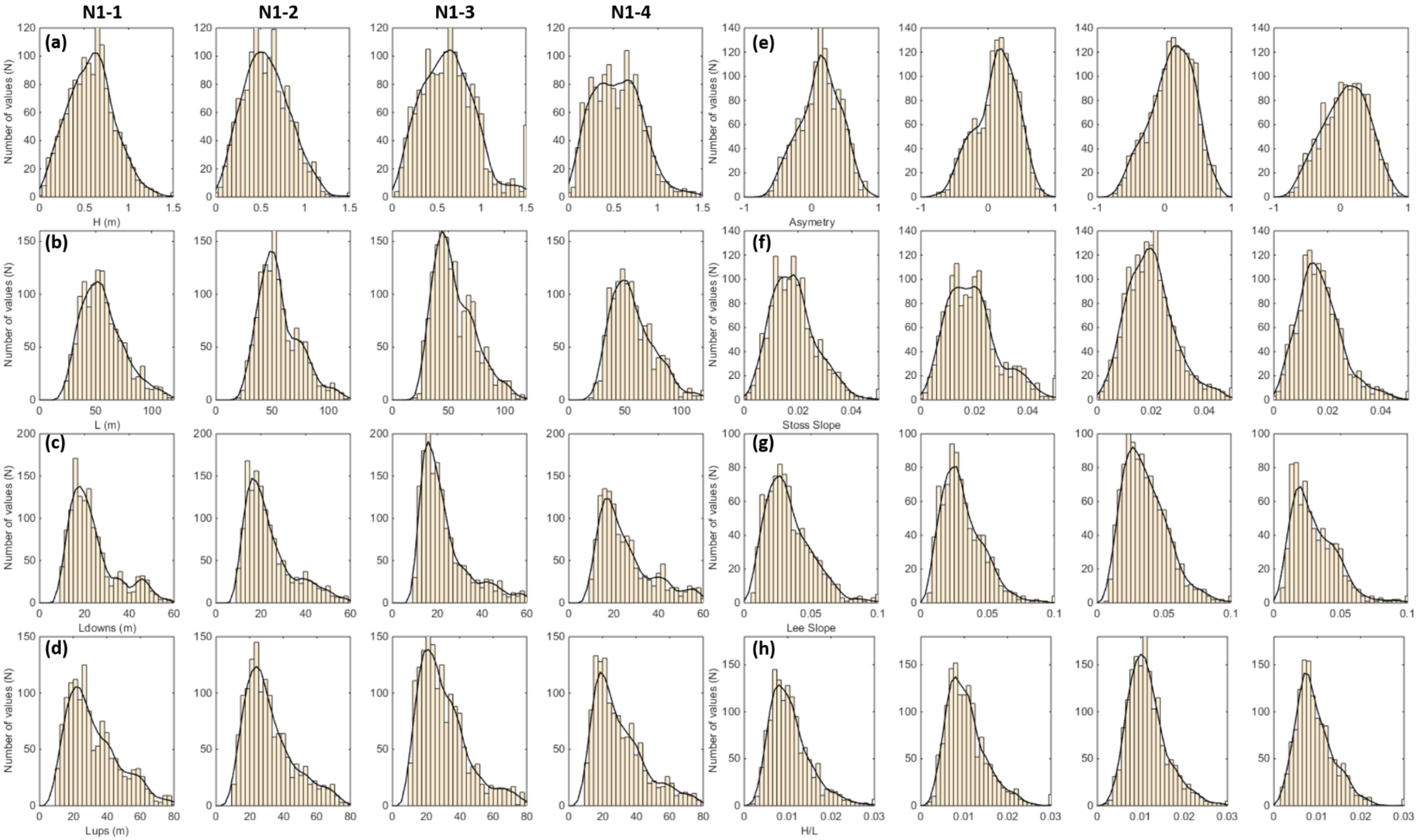

Figure 5-9. Statistics of dune characteristics of the North line during the neap tide. a to h displays the plot of H, L, Ldowns, Lups, Asymetry, Stoss slope, Lee slope, and H/L.

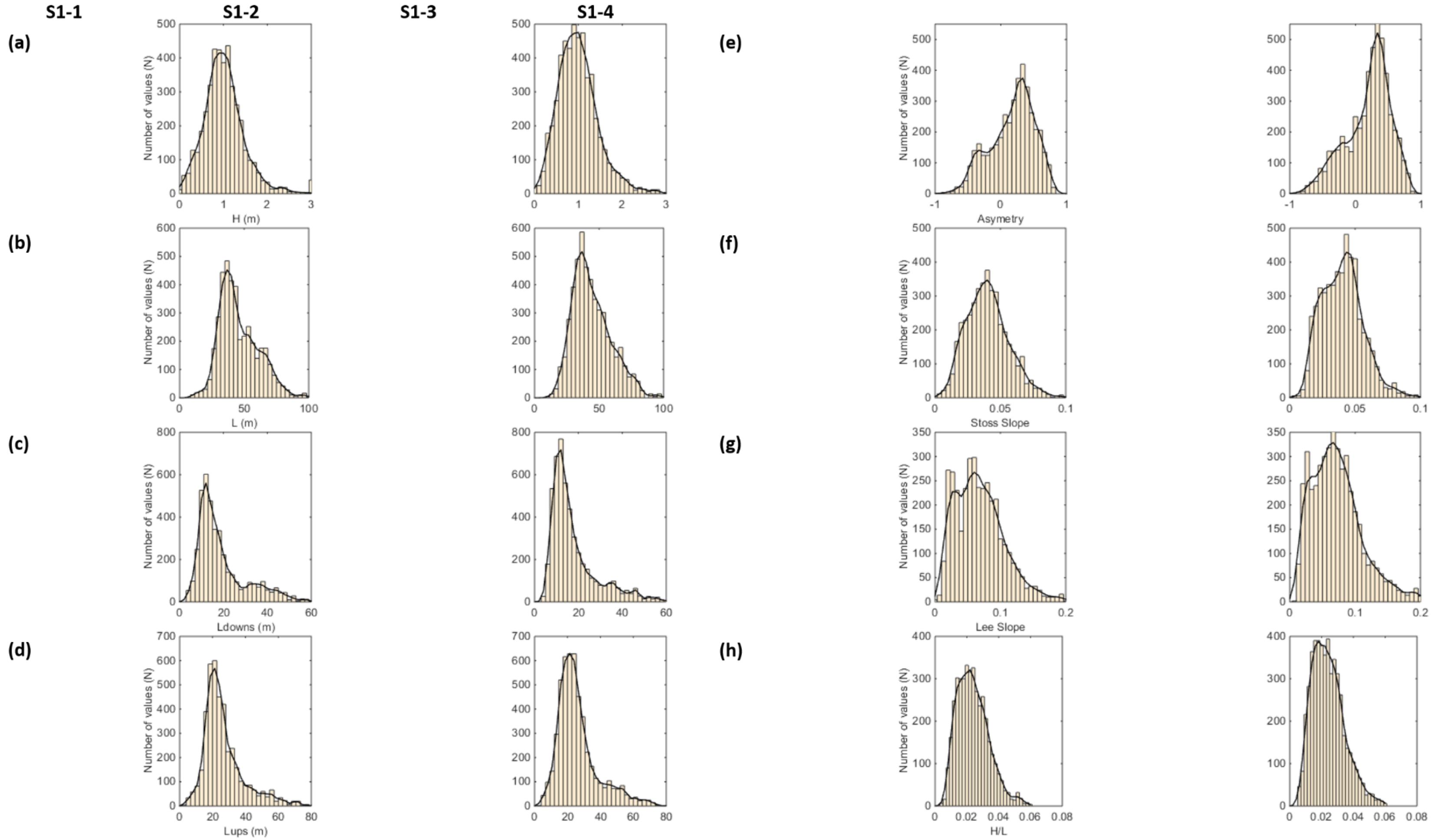

Figure 5-10. Statistics of characteristics of *superimposed small dunes of the South line during the neap tide. a to h displays the plot of H, L, Ldowns, Lups, Asymetry, Stoss slope, Lee slope, and H/L.*

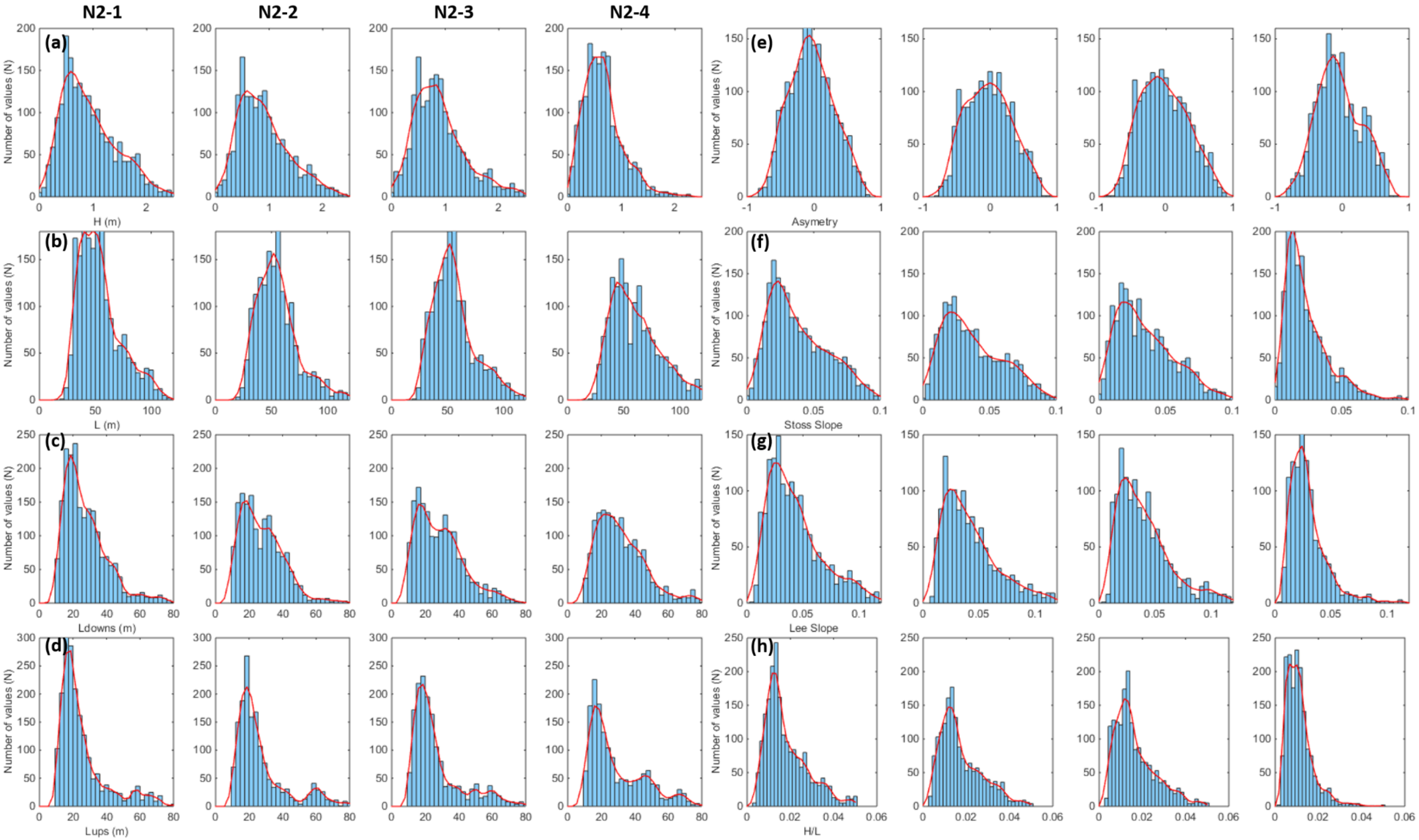

Figure 5-11. Statistics of dune characteristics of the North line during the spring tide. a to h displays the plot of H, L, Ldowns, Lups, Asymetry, Stoss slope, Lee slope, and H/L.

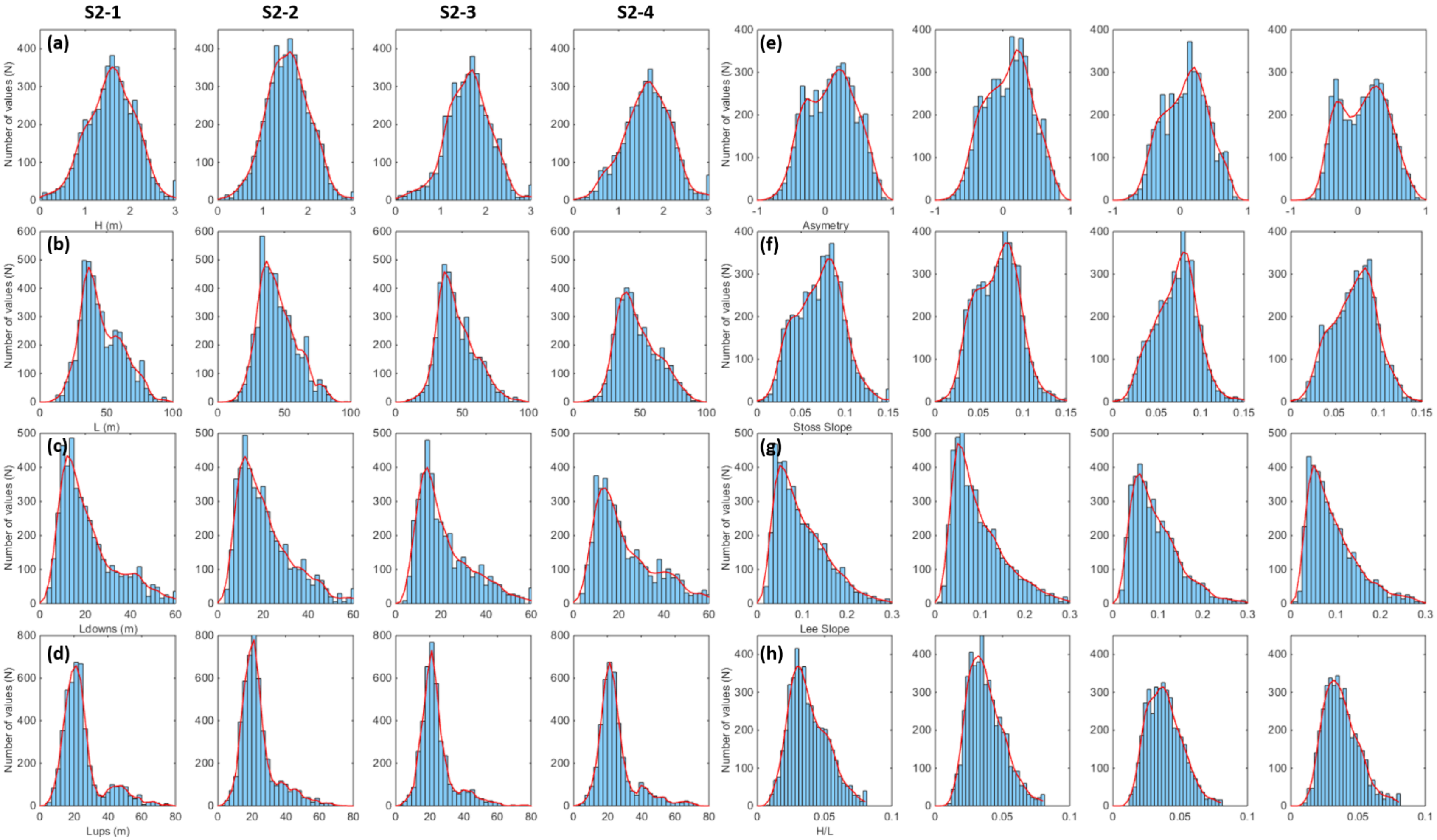

Figure 5-12. Statistics of characteristics of superimposed small dunes of the South line during the spring tide. a to h displays the plot of H, L, Ldowns, Lups, Asymetry, Stoss slope, Lee slope, and H/L.

5.3.2. Bedform variation during neap tide in the late dry season

Figure 5-13 and Figure 5-14 display the bed profiles of north and south survey line. Obviously, only one class of bedforms (dunes) can be observed from the north survey line, while two classes are detected from the south survey line where small dunes were superimposed over large dunes (bar scale, as $L > 500\ \mathrm{m}$). Following the same methods applied in late flood season (above), characteristics of N_L dunes and S_L superimposed dunes are calculated.

During the neap tide, the variation of the whole rising tide and the upper falling tide was captured (Figure 5-3). For the north line, the bedform height, length, and asymmetry keep constant, at ~0.6 m, ~ 53 m, and ~0.11 respectively.

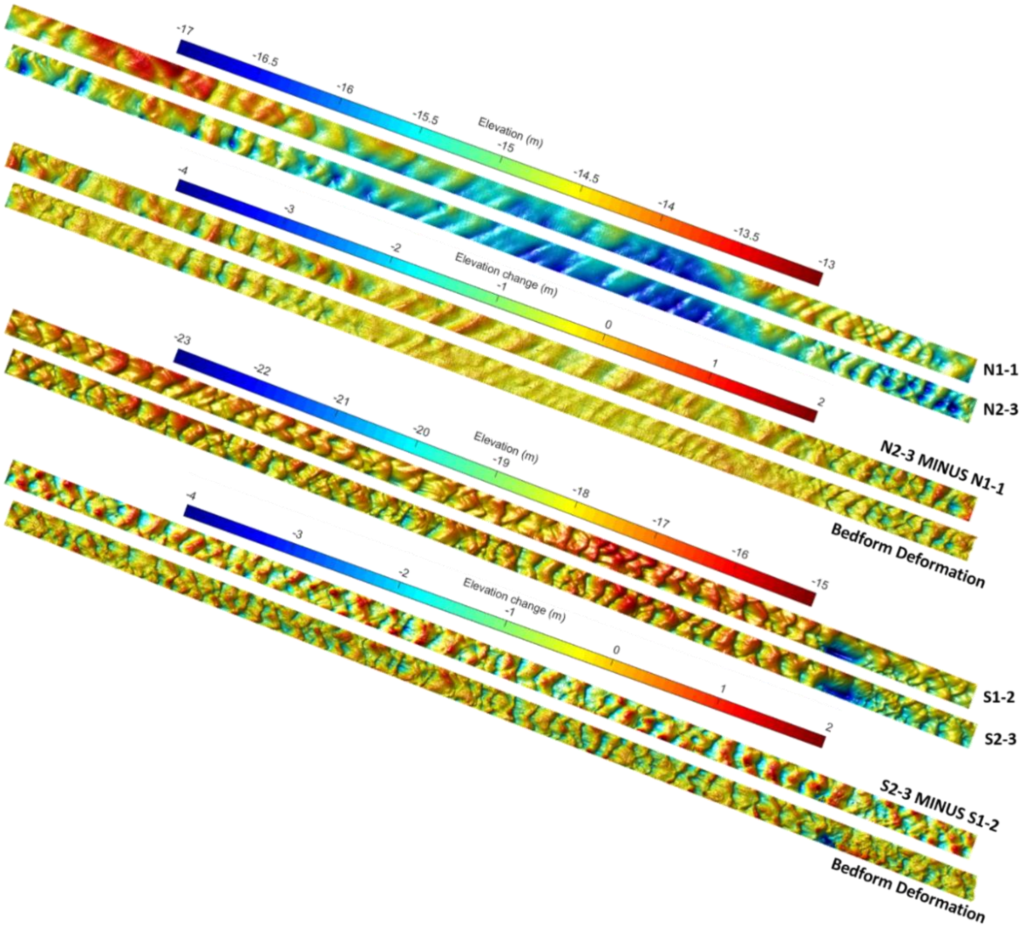

Figure 5-13. Bed topography of N1-1, N2-3, S1-2, and S2-3, bed elevation difference and bedform deformation between N1-1 & N2-3 and S1-2 & S2-3.

Similarly, for the south line, the bedform height, length and asymmetry changed little within the tidal cycle. Compared with the bedforms of the north line, bedform height (0.98 m) is larger but length (47 m) is smaller. Furthermore, bedforms display a more asymmetric shape with bedform asymmetry at 0.21, and this shape leads to greater lee-side and stoss-side slopes.

Table 5-3. Statistics of N_L (N1) and S_L (S1) bedform features during neap tide in the late dry season. Explanation of each characteristic please see Table 5-2.

Features	N1-1	N1-2	N1-3	N1-4
H_{50} (H_{mean})	0.58 (0.61)	0.58 (0.62)	0.61 (0.63)	0.50 (0.54)
L_{50} (L_{mean})	52.5 (57)	53 (57)	52.8 (56)	52 (57)
Lup_{50} (Lup_{mean})	27.3 (34)	27 (33)	26.3 (33.5)	25 (31.5)
$Ldowns_{50}$ ($Ldowns_{mean}$)	20 (25.2)	19.6 (25.4)	20.4 (26.4)	20.5 (27)
Asy_{50} (Asy_{mean})	0.12 (0.13)	0.11 (0.12)	0.10 (0.10)	0.05 (0.07)
S_s_{50} (S_s_{mean})	0.99 (1.12)	1.01 (1.13)	1.04 (1.2)	0.89 (1)
S_l_{50} (S_l_{mean})	1.6 (1.9)	1.6 (1.9)	1.6 (1.9)	1.4 (1.8)
H/L_{50} (H/L_{mean}) %	0.97 (1.07)	0.98 (1.07)	1.00 (1.11)	0.80 (0.96)
Features	**S1-1**	**S1-2**	**S1-3**	**S1-4**
H_{50} (H_{mean})	0.96 (1.03)	1.0 (1.1)		0.98 (1.10)
L_{50} (L_{mean})	46.9 (54.4)	46.3 (53.6)		46.9 (54.1)
Lup_{50} (Lup_{mean})	24.3 (34.3)	24.2 (33.7)		24.6 (34.7)
$Ldowns_{50}$ ($Ldowns_{mean}$)	14.8 (21.6)	15.4 (21.4)		15.2 (21.0)
Asy_{50} (Asy_{mean})	0.20 (0.21)	0.21 (0.19)		0.22 (0.21)
S_s_{50} (S_s_{mean})	1.88 (2)	2.07 (2.18)		2.03 (2.14)
S_l_{50} (S_l_{mean})	3.21 (3.59)	3.31 (3.74)		3.31 (3.71)
H/L_{50} (H/L_{mean}) %	1.9 (2.1)	2.0 (2.2)		2.0 (2.2)

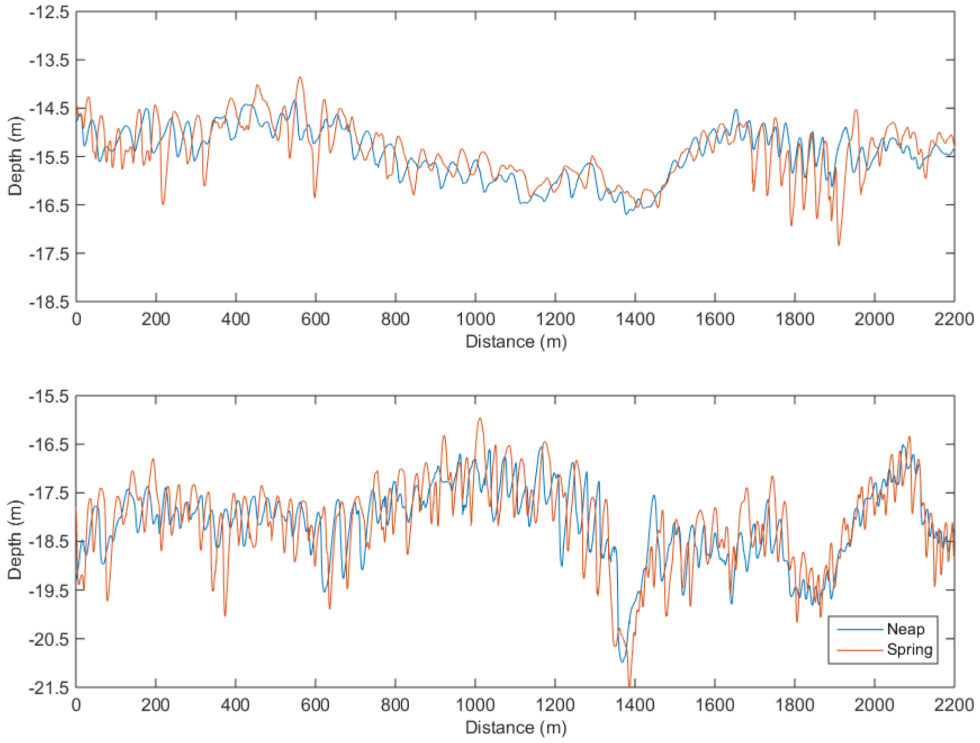

Figure 5-14. Variability of bed profiles for North (N_L) and South (S_L) survey line between neap and spring tide.

5.3.3. Bedform variation during spring tide in the late dry season

During the spring tide, the variation of bedforms within the falling tide was captured (Figure 5-3). For the north line, both the bedform height and length keep constant, ~ 0.8 and ~ 52 m. However, bedform asymmetry is negative, indicating that over 50 % of dunes display a reverse shape that stoss-side length is less than lee-side length. Similarly, for the north line, the bedform height and length keep constant, ~ 1.6 and ~ 47 m, but with a positive bedform asymmetry. Furthermore, like the situation in the neap tide, the superimposed small dunes of the south line still occupy higher H but smaller L.

Bedform length for both the south and north line changes little from the neap to spring tide. In contrast, bedform height shows increase trends that that of the north line increase 30%, while 60% for the south line (Figure 5-15).

Table 5-4. Statistics of N_L (N2) and S_L (S2) bedform features during spring tide in the late dry season. Explanation of each characteristic from a to h, please see Table 5-2.

Features	N2-1	N2-2	N2-3	N2-4
H_{50} (H_{mean})	0.79 (0.9)	0.78 (0.9)	0.79 (0.89)	0.56 (0.65)
L_{50} (L_{mean})	52 (56.5)	51.9 (56.4)	53 (57.3)	55 (60.7)
Lup_{50} (Lup_{mean})	20.8 (27.8)	20.9 (28.2)	21 (28.6)	21.5 (33)
$Ldowns_{50}$ ($Ldowns_{mean}$)	24 (28.9)	24.5 (29)	25.3 (29.6)	27.8 (33.5)
Asy_{50} (Asy_{mean})	-0.07 (-0.024)	-0.07 (-0.02)	-0.09 (-0.03)	-0.11 (-0.05)
S_s_{50} (S_s_{mean})	1.7 (2.1)	1.7 (2.1)	1.7 (2.1)	1 (1.35)
S_l_{50} (S_l_{mean})	1.9 (2.3)	1.9 (2.3)	1.9 (2.3)	1.35 (1.7)
H/L_{50} (H/L_{mean}) %	1.3 (1.7)	1.3 (1.7)	1.3 (1.7)	0.92 (1.12)
Features	S2-1	S2-2	S2-3	S2-4
H_{50} (H_{mean})	1.59 (1.66)	1.59 (1.66)	1.62 (1.68)	1.68 (1.72)
L_{50} (L_{mean})	47.0 (53.3)	46.4 (53.1)	48.2 (54.2)	47.8 (54.6)
Lup_{50} (Lup_{mean})	20.7 (27.9)	20.7 (28.2)	21.0 (28.5)	21.4 (29.3)
$Ldowns_{50}$ ($Ldowns_{mean}$)	20.4 (26.5)	20.3 (26.6)	20.9 (26.9)	19.9 (26.6)
Asy_{50} (Asy_{mean})	0.08 (0.09)	0.08 (0.09)	0.07 (0.07)	0.06 (0.07)
S_s_{50} (S_s_{mean})	4.06 (4.1)	4.01 (4.06)	4.1 (4.12)	4.12 (4.16)
S_l_{50} (S_l_{mean})	4.55 (5.62)	4.45 (5.59)	4.5 (5.44)	4.26 (5.35)
H/L_{50} (H/L_{mean}) %	3.2 (3.5)	3.2 (3.4)	3.2 (3.4)	3.2 (3.5)

5.3.4. Bedform variation between the late flood and dry season

Figure 5-16 displays how the bed looks like during the late flood and dry seasons. In general, after 5-month development, the large-scale topography (kilometres) basically remains unchanged, as some specific characteristics, circled in Figure 5-16, are still recognisable. However, in terms of dunes (tens meters), some changes have taken place that dunes generated in the late dry season (Mar. 2017) are relatively larger and more regular, compared with those detected in late flood season (Oct. 2016). Furthermore, crestlines of the superimposed bedforms in the late flood season are straighter, while those of single bedforms in the late dry season are relatively sinuous. In order to detail the changes of dunes between two seasons and different water depths, four lines were picked from the deeper to the shallower area, named from A-A to D-D, and those bed profiles were displayed in Figure 5-17.

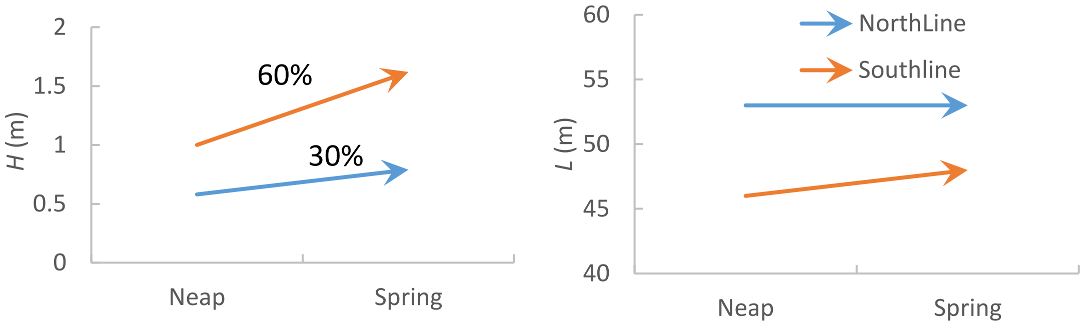

Figure 5-15. Variation of bedform size from the neap to spring tide: (a) bedform height and (b) bedform length. The yellow arrow in the left figure shows bedform height of the Southline increases from 1 m to 1.6 m by 60%, while the blue arrow represents bedform height of the Northline increases from 0.6 m to 0.79 m by 30%.

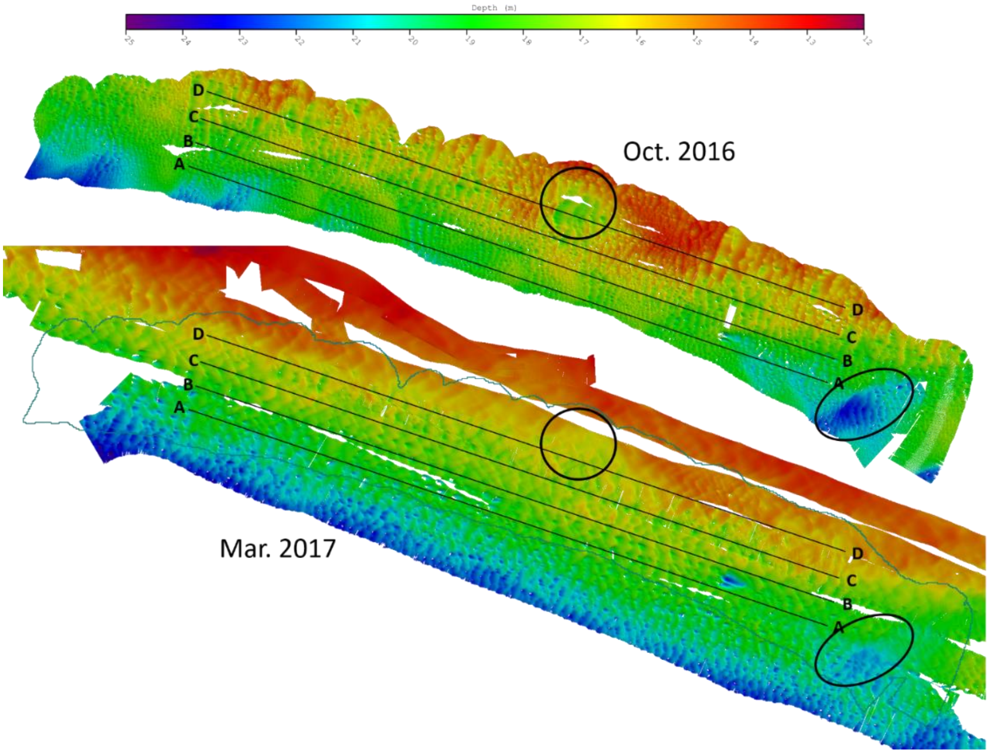

Figure 5-16. Topography from MBES for Oct. 2016 and Mar. 2017. Four bed profiles were selected across the channel: A-D. The areas marked by the ovals and circles indicate that after several months, some large dunes are still recognizable.

It is obvious that only one class of bedforms (dunes) were observed during the late dry season, while in late flood season, two classes of bedforms (large dunes and superimposed small dunes) were detected. Moreover, superimposed bedforms showed a decreasing trend over stoss-side from trough to crest, except D-D.

In total, fourteen host dunes were detected in these four bed profiles, and the dune height ranges from 1.4 to 3.2 m and length from 130 to 260 m. To some extent, the relatively larger superimposed dunes generating in the troughs affect the calculation of host dune height but slightly affect dune length. BRI ranged from 0.1 to 0.5, indicating that bedforms keep non-rounded, and BSI varied between 0.35 and 0.9, indicating the stoss-side length of the host dunes is larger than lee-side, except D1.

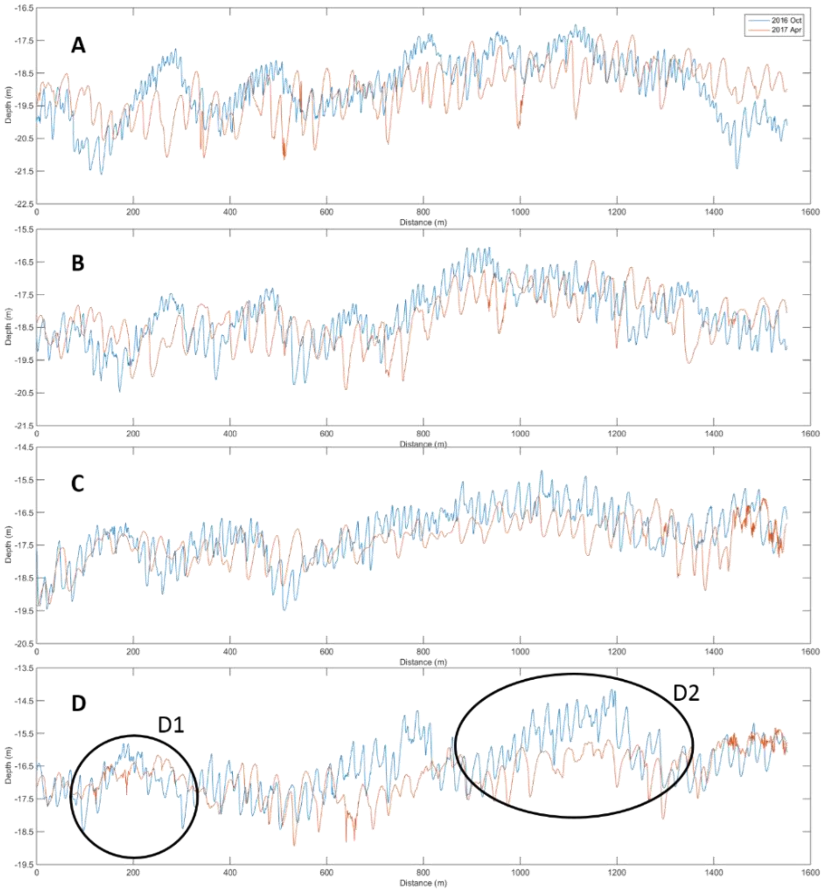

Figure 5-17. Four bed profiles from deeper to the shallower area. Exact positions please see Figure 5-16.

Additionally, the bedform height and length of the superimposed bedforms for Oct. 2016 vary between 0.6 and 1.1 m and between 12 and 20 m, while H and L of the primary bedforms for Mar. 2017 change between 0.9 and 1.2 m and between 30 and 35 m (Figure 5-18). Furthermore, in terms of bedform planar distribution, during the late flooding season (Oct. 2016), the mean dimension of superimposed small dunes shows an increasing trend from the deep to shallow water. In contrast, during the late dry season (Mar. 2017), mean bedform height decreases with water depth declining, while bedform length almost keeps constant and bedform dimension in shallower water displays a greater variability (Figure 5-18 and Figure 5-19).

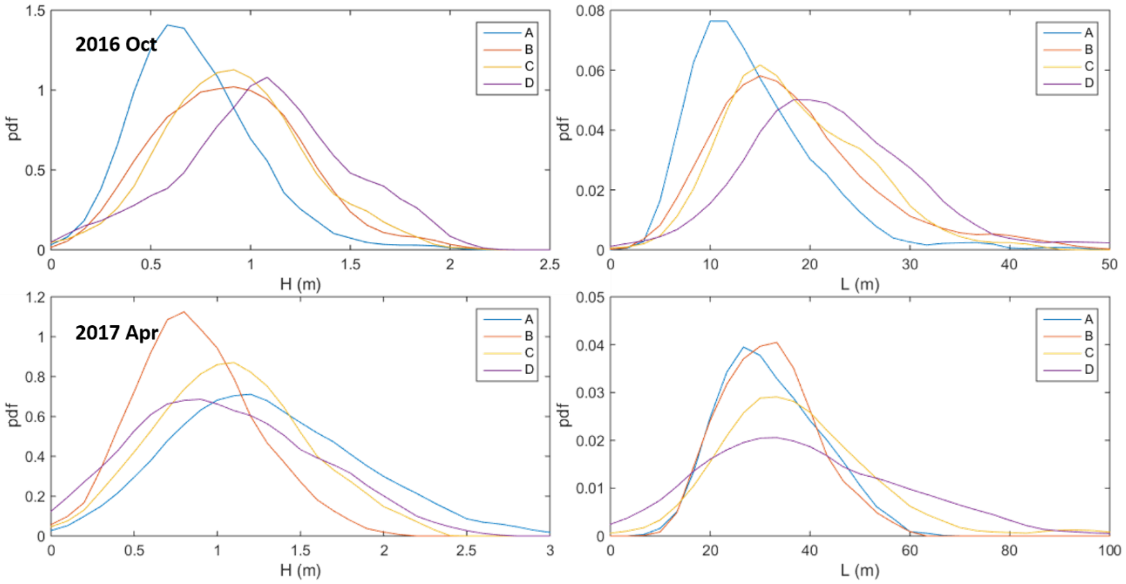

Figure 5-18. The histogram of bedform features across the lateral direction from A-A to D-D for superimposed bedforms of Oct. 2016 and primary bedforms of Mar. 2017.

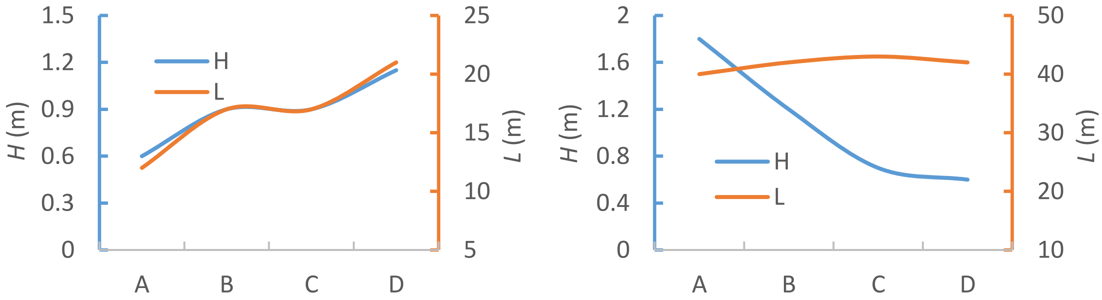

Figure 5-19. Lateral distribution of bedform size for (a) late flood and (b) late dry.

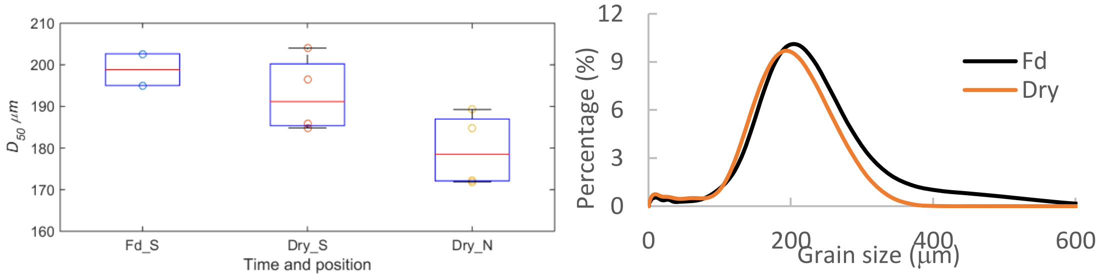

Figure 5-20. Median grain size (D_{50}) (a) and distribution of grain size (b). S and N represent south line and north line respectively.

5.3.5. Grain size distribution

Surface bed material is composed of fine sand, and the median grain size displays a slight decline between the late flood and dry seasons (Figure 5-20a). Furthermore, bed material over the deeper (south) line is coarser than those over the shallower (north) line. In terms of grain size distribution, clay was found contained in bed material (Figure 5-20b), indicating that bed may be affected by cohesive force [*Schindler et al.*, 2015; *Baas et al.*, 2016].

Clay content ranges from 6 to 13% (Figure 5-21). Variation for the south line between late dry and flood is little, while clay content for the north line during the late dry season is the largest.

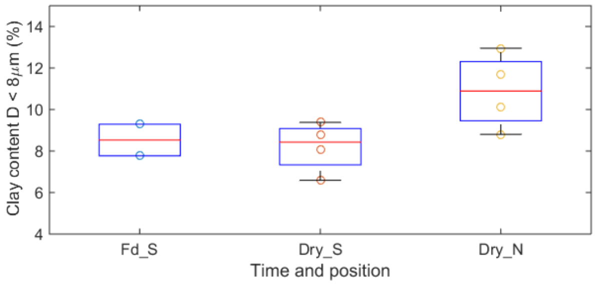

Figure 5-21. Clay content in bed material.

5.4. Discussion

5.4.1. How do compound bedforms form?

Previous research on bedform morphodynamics under tidal influence was summarised in Table 5-5: (1) compound bedforms were observed in *Lefebvre et al.* [2011b], *Lefebvre et al.* [2013a] and *Shuwei et al.* [2017] that primary bedforms are nearly one order of magnitude larger than the superimposed ones and compound bedforms commonly generated under circumstances with smaller Froude number ($F_r = U/\sqrt{gh}$); (2) only the single type of bedforms was detected in *Kostaschuk and Best* [2005] and *Hendershot et al.* [2016] with a relatively higher F_r. Therefore, relatively low Froude number (i.e. flow strength or stream power) is a determinant for the generation of compound dunes, which is also confirmed by previous research (e.g. *Chen et al.* [2012] and *Shuwei et al.* [2017]).

In this study, during the late flood season (falling limb of the freshet), different types of bedforms were observed: (1) in the deeper part, small dunes (SD) superimposed over large dunes (LD) on the bar (BA): SD+LD+BA; (2) in the middle part, small dunes superimposed on the bar: SD+BA; (3) in the shallow part, only small dunes superimposed over large dunes: SD+LD (Figure 5-17). Chen et al. [2012] reported that, in the lower Changjiang River, compound dunes commonly occur in the anabranching channels downstream (Reach C and D in their paper, called CD reach in the following part), due to the frequent variation of sediment transport altered by the diverging/converging flow during floods and low-flow periods. Research area in this study is near tidal current limit (where is the lower boundary of the CD reach), indicating a significantly ebb-dominant circumstance. The evidence shows that superimposed small dunes herein were not active within one tidal cycle but apparently varied after several tides (Table 5-2). This indicates that small dunes are most likely controlled by bi-weekly spring-neap tide [*Flemming and Davis*, 1992], especially the spring tides with stronger flow strength, as evidence of the late dry season shows that bedform variation of those larger dunes between neap and spring tides is considerable (Table 5-3 and Table 5-4).

Table 5-5. Summary of bedforms characteristics and flow strength.

	Lefebvre et al. [2011b]	*Lefebvre et al. [2013a]*	*Shuwei et al.* [2017]	This study (late flood)	*Kostaschuk and Best* [2005]	*Hendershot et al.* [2016]	This study (late dry)
D_{50} (mm)	0.3~0.7	0.5	0.095~0.27	0.2	0.4	0.27	0.17~0.2
h (m)	13~16	15	11.5~35.5	16~19	12~15	4~11	14~20
Fr (max)	0.08	0.08	0.07	0.07	0.17	0.3	0.12
	Primary bedforms				Single type		
S_l (°)	10~17	~12	4.1	1.8~4	8-25	14~18	1.6~4.5
H	3.5	5	4.1	3	1.5	1.16	0.6~1.6
L	196	180	204	260	30	25	47~53
	Secondary bedforms						
S_l (°)	-	-	4.5	8.5			
H	0.4	0.16	0.6~0.9	0.8			
L	5.4	3.3	8.2~14.2	17			

The orientation of the crestlines of large dunes is roughly outlined by red lines in Figure 5-16, presenting a nearly 30° obliquity with crestline direction of small dunes. It is because this research area is located at only 8 km downstream of the riverbend that flow direction could be influenced by different flow discharges. The direction difference between these two types of bedforms supports the hypothesis that those two types of bedforms are generated under different flow conditions: large dunes generated during high flow strength (floods) occupy a northeastward direction, while small dunes occupying an east-by-south direction are controlled by current flows with lower flow strength. Therefore, secondary bedforms are in equilibrium with the present flow, while primary dunes represent relict dunes related to the previous large discharge [*Southard*, 1991; *Allen*, 2009; *Bridge*, 2009; *Chen et al.*, 2012].

Variation of the primary bedform length is one of the main factors affecting secondary bedforms, especially in the falling limb of a flood wave, representing the mechanisms of bedform decay [*Martin and Jerolmack*, 2013; *Warmink*, 2014; *Warmink et al.*, 2014]. Dune splitting (break up) is defined as the quickest process of dune length reducing [*Gabel*, 1993; *Jerolmack and Mohrig*, 2005], highly related to bedform dynamics, but still remains poorly understood [*Parsons et al.*, 2005]. *Reesink and Bridge* [2009] quantified that when the height of secondary bedforms exceeds 25% of the host dune height, the lee-side of the primary dune could be affected. Furthermore, the lee-side slope of secondary bedforms determining the strength of flow separation is another important factor influencing dune splitting. However, neither of the superimposed or primary bedforms generate high-angle lee-sides, thereby there is no permanent separation zone existing over lee-sides, even no intermittent ones. Therefore, the secondary bedforms over the crests are unable to significantly affect the lee-side of primary bedforms [*Reesink and Bridge*, 2009; *Warmink et al.*, 2014]. It implies that the generation and migration of the superimposed small bedforms result in the decay of the primary dunes, but limited by their specific symmetric, low-angle geometry, thereby large dune splitting is unlikely to occur. As a result, the length of the large dunes decreases relatively slowly. It explains that although the large dunes in this research generating in previous large discharge keep decaying, they could still retain their form without significant length decreasing.

Except the small dunes superimposed over large dunes, there also exist bar-scale bedforms (Figure 5-5 and Figure 5-6). The possible mechanism of the bar initiation here is unlikely to be associated with bank direction and instability resulting from interactions between existing bars [*Rodrigues et al.*, 2015]. *Villard and Church* [2005] observed that large-scale bedforms develop in association with persistent aggradation, resulting in dunes remained large after the freshet peak. They attributed the unusual phenomenon (large dunes are superimposed on the bar) to the pre-freshet dredging, as the generation and growth of the bar took longer time than superimposed dunes. However, there is no or rare dredging events in our research area. Thereby, the generation of bar superimposed by large dunes is more likely to be the amalgamation of large dunes during the freshet with most significant sediment transport. After the freshet, the quick decrease of flow discharge (flow strength) significantly slowed down the amalgamation via the generation of small dunes in equilibrium with the present flows, leading to the occurrence of the bar-scale form.

5.4.2. What does control the distribution of superimposed small dunes over large dunes?

The large dunes in this study have similar length scale compared with those in *Lefebvre et al.* [2011b] and *Lefebvre et al.* [2013a] but with smaller lee-side angles and dune height. In terms of small superimposed dunes, in this study, they are relatively larger and did not reverse with tides. However, superimposed bedforms in *Lefebvre et al.* [2011b] and *Lefebvre et al.* [2013a] displayed a relatively smaller scale and reversed their direction during the flood tides [*Ernstsen et al.*, 2006b; *Ernstsen et al.*, 2009]. As the discrepancy of the variation of water level and flow velocity between the spring and neap tides is relatively small [*Ernstsen et al.*, 2009; *Lefebvre et al.*, 2013a], they could be defined as ‘tidal small dunes’ (i.e. tide-controlled). Thereby, their dimension is limited to the low level, as sediment transport related to bedform migration and deformation is restricted within a single tidal cycle.

Figure 5-22 shows the distribution of the lee slope (S_l) and stoss slope (S_s) of the large dunes for the middle stream-wise transect. The stoss slope shows a decreasing trend for the several large dunes upstream of the bar and then dramatically increases on the crest of the bar, followed by a significant drop to the minima and a slight increase on the lee of the bar. On the contrary, the lee slope exhibits an opposite variation, except that the lee slope reaches the maxima on the trough of the bar.

As illustrated by the previous section, although temporal variability of bedform characteristics exists, their changes are very small within these several tides, leading to the negligible temporal variability of spatial distribution. Therefore, the spatial distribution of bedform height, length, stoss slope and lee slope for T2 (Figure 5-23) is selected to represent these five measurements. It is obvious that spatial distribution of bedform height and length is similar: (1) relatively greater secondary bedforms generated on the lower lee-sides, stoss-sides, and troughs of the primary dunes and the largest ones existed on the trough of the most upstream large dune; (2) while smaller ones generated on the upper lee- and stoss-sides; (3) on the contrary, the distribution of the stoss slope and lee slope shows an inverse relationship with the distribution of bedform size; (4) the same distribution of stoss slope and lee slope results in the similar distribution of bedform aspect ratio.

Chen et al. [2012] and *Shuwei et al.* [2017] both observed that the dimension of secondary bedform increases from the trough to crest of primary large dunes [*Harbor*, 1998; *Wilbers*, 2004; *Parsons et al.*, 2005; *Ernstsen et al.*, 2006a; *Winter et al.*, 2008] in the adjacent region to this research, and they attribute this to flow depth change with different position over the surface of primary bedforms [*Jackson*, 1975]. Bedforms with smaller size move faster [*Best*, 2005a; *Venditti et al.*, 2005a; *Venditti*, 2013], resulting in bedform amalgamation (e.g. larger secondary bedforms) in the upper stoss of primary high-angle bedforms. However, the distribution of superimposed small dunes in this study displays a reverse trend (Figure 5-23). Furthermore, the superimposed small dunes over ebb lee-side were detected and they increase from the crest to trough.

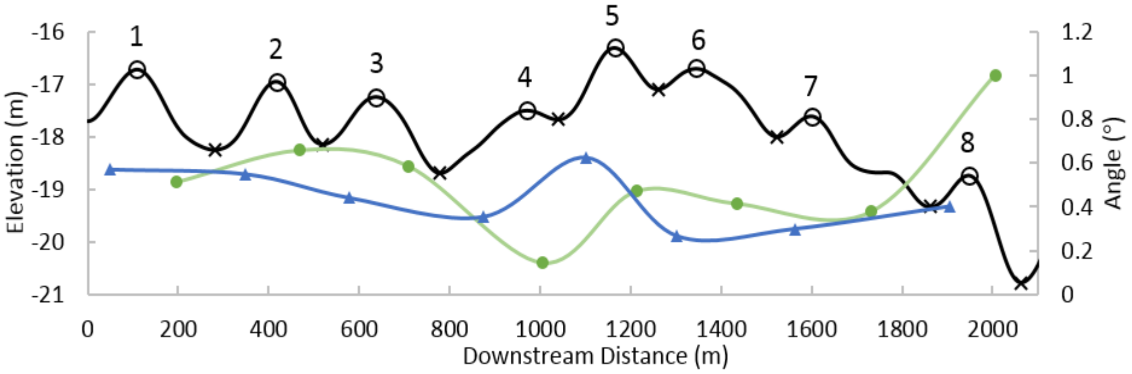

Figure 5-22. Distribution of lee slope (green line) and stoss slope (blue line) of the middle stream-wise transect. The black line displays the bed profile of large dunes plus bar. Hollow circles and crosses indicate positions of peaks and troughs of large dunes. Large dunes are named as 1~8.

As secondary bedforms are spring-neap tide controlled, they reach the maximum around the spring tide when flow strength is largest, followed by decaying to the neap tide. Our measurements were taken a couple of days before the neap tide (Figure 5-3a). For the secondary bedforms near the crest with lowest flow depth, they suffer the strongest sediment erosion [*Warmink et al.*, 2014], as flow velocity reaches the maximum, resulting in the most significant bedform decay. In contrast, secondary bedforms in the trough or over the lower stoss and lee sides migrate and deform relatively little, thereby bedforms remain their size.

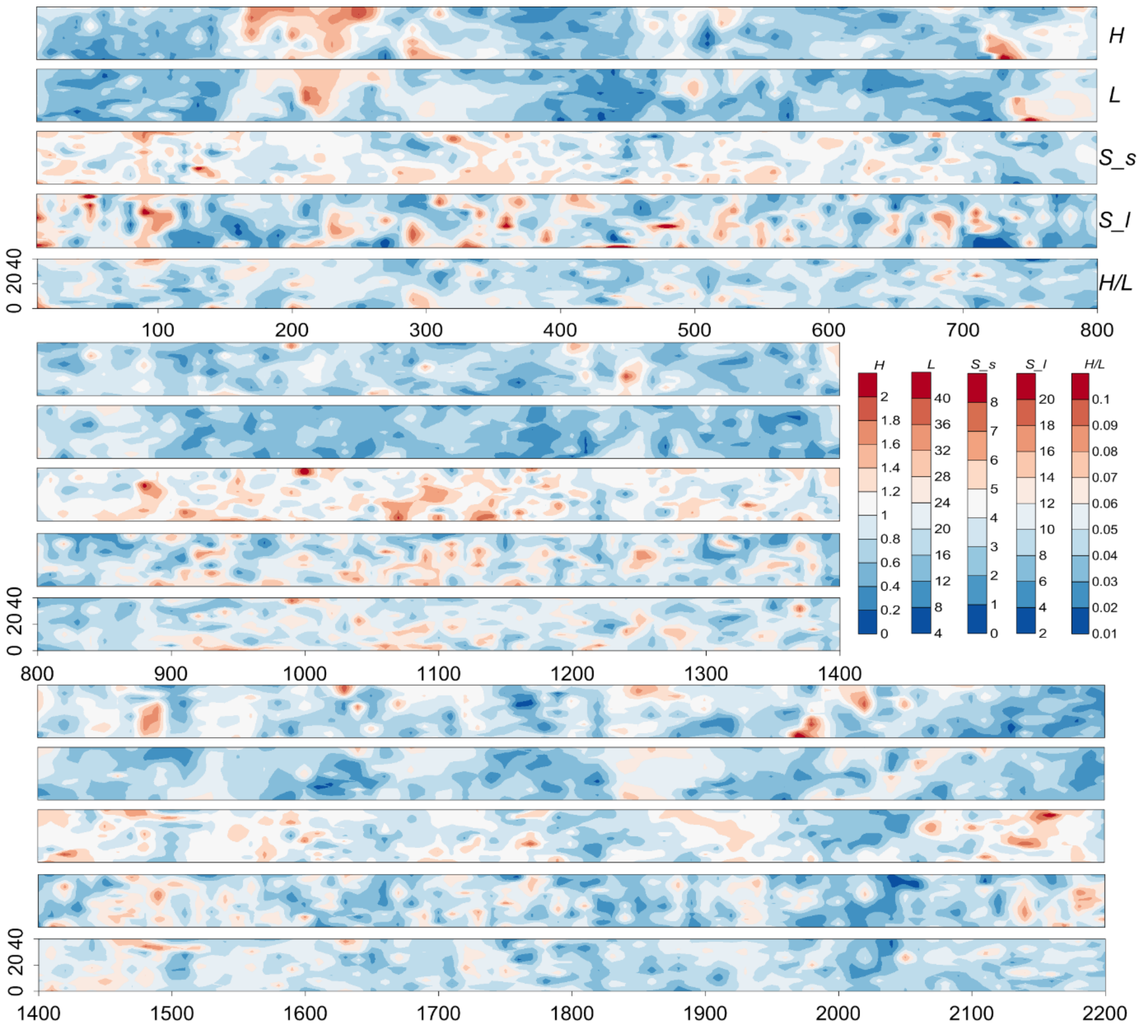

Figure 5-23. Spatial distribution of H, L, S_s, and S_l.

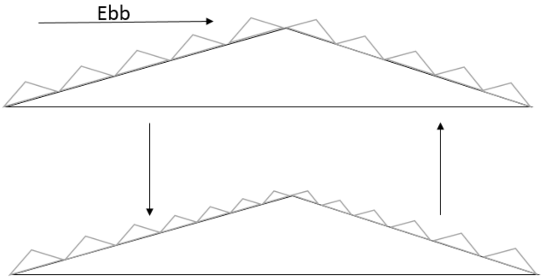

Figure 5-24. Superimposed bedform variation between spring and neap tides.

The above description elucidated how compound bedforms generate in the late flood season in the Changjiang Estuary and illustrated a scenario that how superimposed dunes, which are spring-neap tide controlled. The explicit process of bedform evolution could enhance our ability to establish accurate links between the flow, sediment transport and morphodynamics [*Wilbers*, 2004]. Furthermore, the unique distribution of the superimposed secondary dunes will result in a distinct pattern of cross-strata, which will enrich our knowledge of paleoenvironmental reconstruction in the fluvial-dominated reach of an estuary [*Visser*, 1980; *Leclair and Bridge*, 2001; *Leclair and Blom*, 2005].

5.4.3. Factors affecting bedform dimension

Prediction of dune dimension is important for accurate estimation of bedform roughness, and consequently simulation of water level, especially for the construction of flood protection measures [*Warmink et al.*, 2013; *Bradley and Venditti*, 2016]. In addition, reconstructing past fluvial environments on the Earth and other planets highly depends on estimated dune size based on cross-strata [*Bridge and Tye*, 2000; *Leclair*, 2002; *de Almeida et al.*, 2016]. Therefore, both of the modern river prediction and paleoenvironmental reconstructions depend critically on accurately building links between dune size and their ambient environment [*Bradley and Venditti*, 2016].

Numerous research on 'scaling relations' [*Bradley and Venditti*, 2016] has built the links between bedform dimensions and boundary conditions, such as sediment supply [*Kleinhans et al.*, 2002; *Tuijnder and Ribberink*, 2008], shear stress [*Van Rijn*, 1984b; *Southard and Boguchwal*, 1990; *Bartholdy et al.*, 2005], water depth [*Yalin*, 2015; *Bradley and Venditti*, 2016], grain size and virtual boundary layer (for ripples, e.g. *Coleman and Melville* [1996] and *Bartholdy et al.* [2015]). *Bradley and Venditti* [2016] reevaluated scaling relations based on abundant flume and field data and revealed that none of the previous predictors could accurately estimate bedform dimensions. Furthermore, they also found that dunes in shallow (less than 2.5 m) and deep water (larger than 2.5 m) exhibit different scaling relations due to the change of the dominant process controlling dune size. The various scaling relations, however, reflect the lack of consensus on the mechanisms controlling dune dimensions and also the complexity of bedform generation and development. However, in spite of nearly two orders of magnitude variation in dune size at any given flow depth, the positive relation between water depth and bedform dimension objectively exists [*Bradley and Venditti*, 2016].

This research identifies bedforms with different sizes during the late flood and late dry seasons, while flow depth is largely similar. In any measurement period, dune height is one order of magnitude smaller than the water depth, indicating that dunes are not flow-depth-restricted (flow-depth-restricted bedforms are characterized as dune height to water-depth ratio, H/h = 1/6 [*Holmes and Garcia*, 2008; *Yalin*, 2015]). In such circumstances, under subcritical flows, flow strength (i.e. shear stress or flow discharge) has a more significantly positive effect on bedform dimension [*Shuwei et al.*, 2017], as bedforms on both the north and south lines display growing trends from the neap to spring tide (Figure 5-3 and Figure 5-25).

It is widely recognised that compared with dune height, dune length displays a more stable scaling relation with water depth, varying between $L = 5 \sim 7.3h$ [*Van Rijn*, 1984b; *Julien and Klaassen*, 1995; *Yalin*, 2015]. However, according to the distribution of bedform size across the channel (Figure 5-18 and Figure 5-25), results show that at the same measuring time, bedform height in the deeper water is greater, while dune length is unexpected to be smaller. Previous research [*Yalin*, 1972; *Allen*, 1978; *Van Rijn*, 1984b; *Julien and Klaassen*, 1995; *Karim*, 1995; 1999] has pointed out the importance of the grain size (critical shear stress is estimated based on grain size as well) on bedform dimension. *Lin and Venditti* [2013] summarized dune data from previous research and proposed the strong correlation between aspect ratio (H/L) and transport stage (τ_*/τ_{*C}, where τ_* and τ_{*C} are Shields number and critical Shields number, respectively). It probably indicates that grain size is the main factor influencing bedform dimension, rather than water depth (flow strength is similar according to the aDcp data being analysed in the next chapter) under some certain conditions.

Additionally, some other academics [*Schindler et al.*, 2015; *Baas et al.*, 2016; *Parsons et al.*, 2016] emphasized the significant effect of physical cohesion imparted by cohesive clay within mixed sand-mud substrates on the generation, migration, and dimension of bedforms. Our result (Figure 5-25) largely confirms with the result reported by *Schindler et al.* [2015] that aspect ratio (H/L) has an inversely linear correlation with clay content.

The aspect ratio of bedforms in the late flood season (blue rectangle) is slightly greater than the predicted value. That is because those bedforms are under regenerative process [*Elbelrhiti et al.*, 2005; *Kocurek et al.*, 2010]. Especially for those superimposed bedforms over the crest of the primary dune, they decay a lot from the spring to neap tide, leading to bedform splitting, thereby significant increase of aspect ratio [*Reesink et al.*, 2017]. In contrast, the aspect ratio of bedforms in the late dry season is slightly smaller. Bedforms keep growing from the neap to spring tide, indicating that bedforms are under constructive process [*Kocurek et al.*, 2010]. Thereby, bedform height could continue increasing, resulting in the growth of aspect ratio until reaching equilibrium.

Furthermore, bedform length for the north line, where clay content is a little higher, is slightly greater than that of the south line (Figure 5-21 and Figure 5-25). This result is consistent with previous research that bedform length decreases with the increase of clay content [*Schindler et al.*, 2015]. Bedform migration and deformation are more significant under high flow strength dominating bedform size. Especially, bedform length highly depends on flow and bed condition during high flow strength, because it takes a much longer time to respond to the waning flows than bedform height [*Kostaschuk and Best*, 2005].

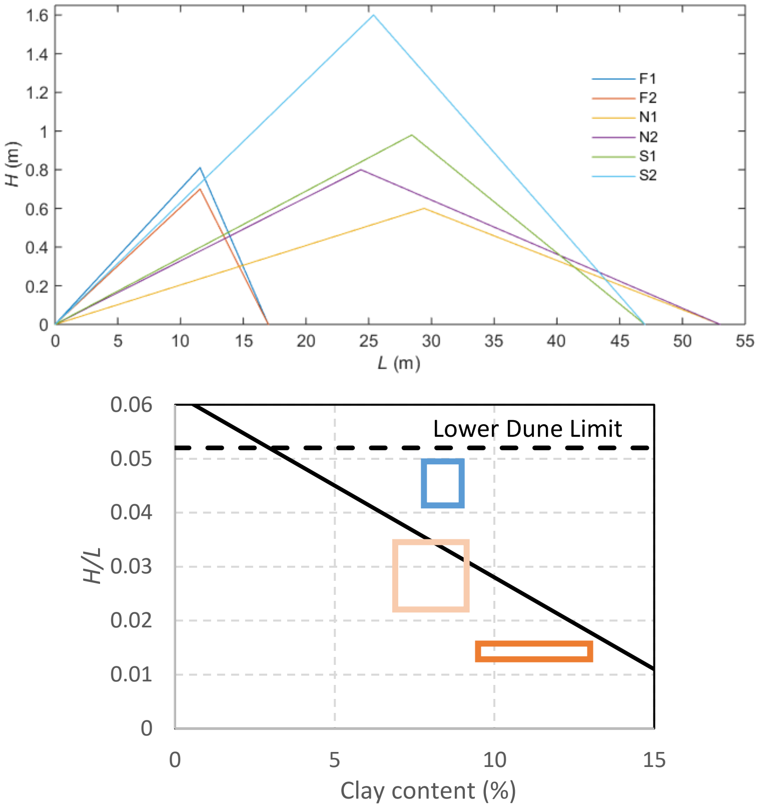

Figure 5-25. Variation of the shape of bedforms. Shapes were drawn based on H_{50}, Asy_{50}, and $Ldown_{50}$ (a), Relationship between H/L and clay content (b). Blue, light orange and dark orange rectangles donate bedforms during the late flood, neap tide and spring tide in late dry, respectively.

Table 5-6. Statistics of migration and deformation flux.

	D_{lag} (m)	q'_T (m^3)	q_D (m^3)	q_{tot} (m^3)	F
N_L	23.4	8.4	3.04	11.44	0.27
S_L	18.4	10.5	4.20	14.7	0.29

Bedform height increases, while the length of stoss-side decreases, resulting in a more symmetric shape (Figure 5-25a). This shape variation is related to significant trough scouring, which was pervasively occurred over the bed profile (Figure 5-14), rather than accretion or amalgamation [*Southard and Harms*, 1972; *Hendershot et al.*, 2016]. Furthermore, during our secondary survey (from the neap to spring tide), bedforms migrated nearly half of their wavelength and sediment flux related to migration is higher than that related to deformation with $F \cong 0.28$ (Table 5-6). The monotonous bedform deformation with trough scouring from the neap to spring tide results in a potentially specific cross-set. As trough scouring plays a vital role in changes of the thickness of cross-sets [*Allen*, 1973; *Leclair*, 2002], it could enrich our knowledge on paleo-hydraulic interpretation from sedimentary records in the tidally influenced area [*Leclair and Bridge*, 2001]. However, how grain size sorting [*Reesink and Bridge*, 2009] occurs and what the relationship between trough-scour depth and migration rate [*Leclair*, 2002] need be further investigated.

5.5. Conclusions

Field surveys examining the bedform dynamics under unsteady flows over a cohesive natural bed were conducted in the middle Yangtze River:

1. In the falling limb of the hydrograph (late flood season, first survey), multiscale bedforms were observed. The superimposed small dunes are spring-neap tide controlled, while primary bedforms are the relicts of large dunes generated during the earlier freshet flows.
2. The secondary dunes (symmetric shape) were discovered to generate over the lower part of the primary dunes. That is because, bedforms decay from spring to neap tide and crests of primary dunes respond to the flow structure more significantly, resulting in a greater control over sediment transport, thereby greater bedform translation and deformation.
3. In the initial rising limb (late dry season, second survey), single-scale bedforms were observed. They are also spring-neap tide controlled, and trough scouring results in the bedform growth, rather than accretion or bedform amalgamation.
4. Bedforms in deeper water responded to flow changes more quickly due to the enhanced sediment transport. During the late flood (decaying), bedforms increase from the deep to shallow water; while during the late dry (increasing), bedforms decrease from the deep to shallow water.

5. Finally, according to the grain size analysis and morphometrics, our results also highlight that clay content is a first-order control on bedform aspect ratio. Bedforms undergoing regenerative/constructive processes lead to the under-/over-estimation of size.

These findings enrich our knowledge of likely paleo-hydraulic interpretation from sedimentary records, in the tidally influenced area, near the tidal backwater zone.

CHAPTER 6

6. Flow and sediment dynamics over dunes in the middle part of the Yangtze Estuary

Abstract: Hydraulic roughness is a fundamental parameter in the understanding and simulation of hydro- and sediment- dynamics over dunes in fluvial and coastal areas. Completely understanding the links between the turbulent flow field, sediment transport and morphodynamics is key to better quantifying the evolving roughness in time and space. This paper presents two surveys, conducted in the middle Yangtze Estuary, analysing flow and sediment dynamics under different water/flow stages. Results show that when compound bedforms generate in the late flood season, flow structure was affected by the bed morphology and the velocity profile was segmented into two segments. Moreover, the lower segment is interpreted to reflect the friction induced by the superimposed small dunes. The increase of the velocity could increase the possibility of generating FSZ, consequently resulting in a further effect on flow structure, as the lee-side angles of small dunes fluctuate around 10°. The large superimposed dunes over the primary dunes play a significant role in roughness based on the result of flow structure. However, limited by the resolution of the instrument, it is hard to distinguish which roughness element dominants flow structure over compound dunes. The correlation between flow resistance and flow strength displays that both shear stress and roughness length over larger dunes in the deep water are more sensitive to mean velocity. That is because, the flow expansion over low-angle dunes is sensitive to both lee face and flow strength, resulting in the different correlations for low-angle dunes in the different water depth, thereby affecting their evolution. Furthermore, bedload transport calculated from empirical equations shows a satisfactory agreement with that estimated from bedform migration and deformation. This result implies that bedload transport induced by bedform related shear stress is little, and the clay contained in the bed material also has little effect on constraining bedload transport. This finding is significant to studies on migration and deformation of low-angle dunes in beds comprised of clay and sand.

6.1. Introduction

The migration of subaqueous dunes may cause bed-level aggradation [*Carling et al.*, 2000b] or degradation [*Villard and Church*, 2005], leading to the development of sedimentary structures of a distinctive style [*Leclair*, 2002; *Reesink and Bridge*, 2007]. Therefore, completely understanding the links between flows, sediment transport, and bed morphology is the prerequisite to interpret ancient sedimentary sequences in the rock record [*Carling et al.*, 2000b; *Best*, 2005a].

The hydraulic roughness is widely recognised as the effect caused by the bed roughness elements (ripples, dunes, bars) on the flow [*Smith and McLean*, 1977; *Smith*, 2014]. It is a fundamental parameter in the understanding and simulation of hydro- and sediment dynamics in fluvial and coastal areas [*Lefebvre et al.*, 2011b]. A range of empirical formulas have been built to estimate form roughness length only based on bedform morphological characteristics, which is associated with bedform height (H) and length (L), in unidirectional, oscillatory, or combined flows (e.g. [*Grant and Madsen*, 1982; *Van Rijn*, 1984b; *Soulsby and Whitehouse*, 1997]). Another approach to assess roughness length is from the velocity profile, called 'the Law of the Wall' [*Smith and McLean*, 1977; *McLean*, 1992]. Two segments could be detected on the spatially averaged log-linear velocity profile, if bedforms exist, and the roughness length is related to the y-intercept of the best-fit line. Furthermore, the lower segment was thought to be related to grain-induced friction, whereas the upper segment reflected the total friction [*McLean*, 1992; *Kostaschuk and Villard*, 1996; *Lefebvre et al.*, 2011b]. When several size classes of bedforms were present (e.g., ripples, small dunes, large dunes), the existence of several log-linear segments along the velocity profile were interpreted to reflect the friction induced by the differently scaled roughness elements [*McCann et al.*, 2011; *Lefebvre et al.*, 2013a]. Although this approach is not physically based [*Nelson et al.*, 1993], the upper segment seems adequately to represent the total resistance and the overall shear velocity of the flow [*Wiberg and Nelson*, 1992; *Lefebvre et al.*, 2013a].

However, recent research [*Paarlberg*, 2008; *Kwoll et al.*, 2016; *Lefebvre et al.*, 2016; *Lefebvre and Winter*, 2016b; *Kwoll et al.*, 2017] has revealed that not only bedform size but also bedform shape, i.e. lee side angle, and relative height (H/h) contribute to flow resistance and form roughness. Because, total roughness over dunes depends on the turbulent energy related to flow separation and the wake which forms over the lee side [*Lefebvre et al.*, 2014a; *Lefebvre et al.*, 2014b; *Lefebvre and Winter*, 2016b]. The lee side angle and bedform relative height was found to affect the presence and size of the flow separation [*Kwoll et al.*, 2016; *Lefebvre and Winter*, 2016a; *Kwoll et al.*, 2017]. Therefore, both the lee side angle and relative height are positively correlated to the Nikuradse sand roughness.

Roughness parameterization is widely recognised as the primary modelling consideration, as it has been proven to significantly affect velocity predictions in one-dimensional (1-D) and 2-D models [*Lane et al.*, 1999; *Lane et al.*, 2004; *Sandbach et al.*, 2012]. Increased computing power has dramatically shortened the time we use to simulate for the higher-dimension models, and enables us to investigate mechanisms generating in finer size, such as large eddy simulation, LES (e.g. [*Van Balen et al.*, 2010; *Nabi et al.*, 2012]) and direct numerical simulation, DNS (e.g. [*Bhaganagar and Hsu*, 2009; *Penko et al.*, 2013]). Although these physics-based models allow us to accurately investigate hydrodynamics, for large-scale applications, they are still time-consuming. Furthermore, for river-scale applications, resolving even dune-size bedforms (sub-grid scale) can be difficult due to the computational resources required as well as the availability of topographic data that are constantly evolving [*Sandbach et al.*, 2012]. Therefore, parameterizing roughness is the better way and could keep computational effort minimal [*Paarlberg et al.*, 2007; *Davies and Robins*, 2017].

Additionally, recent research [*McCann et al.*, 2011; *Davies and Robins*, 2017] emphasises that varying hydraulic roughness due to the variability of bedforms during the tidal circles significantly affects the pattern of the flows and sediment transport and the subsequent morphological change. However, few studies investigated feedbacks between the flows, morphology and sediment transport in a tidal flow, due to the difficulty in accurately measuring flow structure and topography in the field [*Lefebvre et al.*, 2013a; *Kwoll et al.*, 2014]. Recently, with the development of advanced equipment, increasingly detailed and intensive measurements are accessible in the field. For example, the multibeam sonars (MBESs) provide the opportunity to collect high-resolution 3D bathymetry, and the acoustic Doppler current profiles (aDcps) allow us to rapidly and accurately characterise the spatio-temporal flow structure in various types of water bodies [*Parsons et al.*, 2005; *Parsons et al.*, 2013].

In this chapter, these two advanced instruments (aDcp and MBES) were employed concurrently in two field surveys: one in the late flood (end of October, 2016) season and the other in the late dry (end of March, 2017) season, in the middle reach of the Changjiang (Yangtze) estuary, China, where compound bedforms widely exist [*Chen et al.*, 2012; *Shuwei et al.*, 2017]. This study quantifies the hydraulic roughness of large compound, ebb-oriented bedforms in the late flood season and that of single type bedforms in the dry season within tidal cycles. Sediment transport related to bedform migration and deformation is calculated and compared with results derived from empirical equations. Full understanding of the links between the flows, sediment transport, and morphological change is essential in advancing sediment transport modelling and the work herein may provide the realistic materials for the improvement of future modelling and prediction work in estuaries.

6.2. Methods

6.2.1. Field setting and Data collection

Details please see the last chapter.

6.2.2. Roughness length

The bed roughness (e.g. flow resistance) is a fundamental parameter in the understanding and simulation of hydro- and sediment- dynamics in coastal areas in numerical models. For a given boundary surface, the “energy losses” resulting in “flow resistance” is caused by the near bottom turbulence and the macro-flow structures within a prescribed channel reach [*Morvan et al.*, 2008].

The time-averaged current velocity profile ideally displays a logarithmic distribution above the bed and is commonly described by the physics-based approach – von Kármán-Prandtl Law of the Wall [*Lefebvre et al.*, 2013a]:

$$u(z) = \frac{u_*}{\kappa} ln\left(\frac{z}{z_0}\right) \qquad 6\text{-}1$$

where $u(z)$ is the time-averaged current velocity at the height z above the bed; u_* is shear velocity and z_0 (height z at which velocity is zero) is the roughness length, and κ is the von Kármán constant (0.41).

Spatially-averaged velocities are commonly applied to estimate bed roughness and shear stress [*Smith and McLean*, 1977]. However, the variability of flow depth along bedforms (i.e. z) leads to the discontinuity in the procedure of spatial-average. Therefore, z was normalised by dividing to water depth, $z_* = z/h$, before being spatially averaged and consequently a new Law of the wall was derived [*Lefebvre et al.*, 2011b]:

$$u\left(\frac{z}{h}\right) = \frac{u_*}{\kappa} ln\left(\frac{z}{h} - \frac{z_0}{h}\right) = \frac{u_*}{\kappa} ln\left(\frac{z}{h}\right) - \frac{u_*}{\kappa} ln(\frac{z_0}{h}) \qquad 6\text{-}2$$

Additionally, due to the side-lobe effects of the acoustic beams, velocities near the bottom (6% of the total water column, called near bottom blank area) are potentially erroneous [*RD*, 2011]. Furthermore, velocities near the top of the water column can be distorted by wave and boat motion. Thereby, velocities in these two parts were removed and only the middle part, $0.15 < z/h < 0.85$, was retained for further analysis. Shear velocity and roughness length estimated via the vertical velocity profile were calculated by following the detailed method in *Wilkinson* [1983].

However, the existence of bedforms alters the flow structure, reflected in the generation of a hierarchy of boundary layers (details in fig. 2, in *Lefebvre et al.* [2013a]). Therefore, in order to estimate the hierarchy of boundary layers, for each bed profile, linear regression was applied both from the bottom (lower segment) and top (upper segment) of the velocity profile (at least 4 points) to examine the variability of the coefficient of determination (R^2).

Furthermore, different velocity profiles were calculated to examine the effect of different scale bedforms on flows: (1) Spatial Average of Whole Transect (SAWT); (2) Spatial Average for each Large Dune (SALD); (3) Raw Velocity Profile (RVP), i.e. each aDcp collated velocity profile.

6.2.3. Telemac Model

The state-of-the-art model, Telemac-2D, an unstructured mesh finite element model, was employed for hydrodynamic simulation. Additional details could be found in *Hervouet* [2007] and from the Telemac website: http://www.telemacsystem.com.

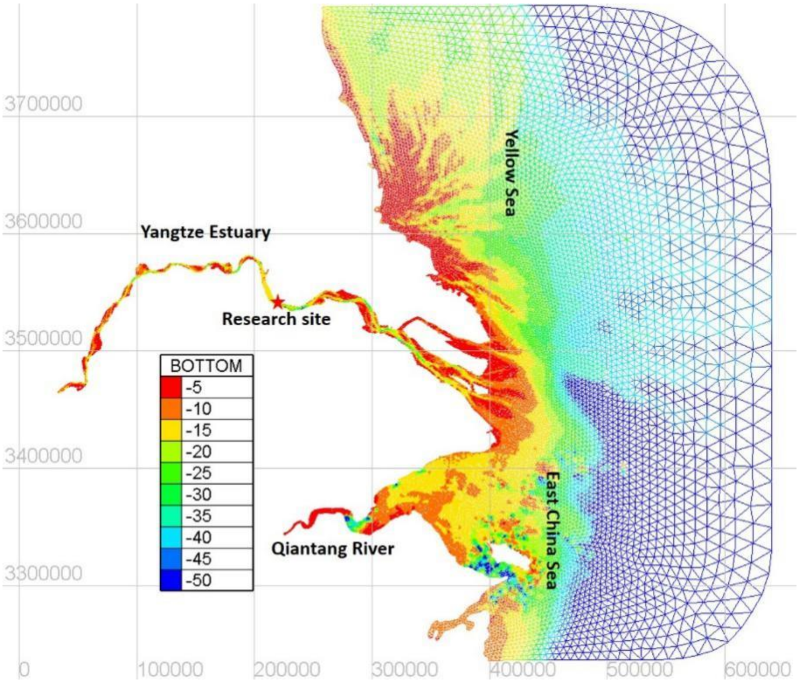

Figure 6-1. Mesh and Bathymetry of Yangtze Estuary, Hangzhou Bay and part of the Yellow and the East China Sea.

Figure 6-1 displays the mesh with the depth of Yangtze Estuary, and there are 88000 nodes in total with smallest grid space about 50 m in our research site and up to 20000 m in the sea boundary. Constant eddy viscosity model was selected, while density differences and waves were ignored.

The hydrodynamic model was employed and the result (flow depth and depth averaged flow velocity) would be used for the calculation of bedform migration rate (Figure 6-1).

Table 6-1. Summary of bedform migration rate prediction.

Authors	Bedform migrate rate (m/s)
Zhang et al. [1989]	$V_b = 0.0144\frac{U^3}{gh} = 0.0144UFr^2$
Shinohara and Tsubaki [1959]	$\frac{V_b h}{\sqrt{(s-1)gD_{50}^3}} = a(\frac{U_{cr}^2}{(s-1)gD_{50}}\frac{\theta'}{\theta_{cr}})^m$

Note: $a = 76.1$ and $m = 2.5$, when $0.1 < D_{50} < 0.21$ mm.

6.2.4. Bedform celerity calculation and prediction

Bedform celerity (V_b) could be calculated from the repetitive bed profiles between neap and spring tides, thereby sediment transport related to bedform translation q_T could also be computed [*Simons et al.*, 1965]:

$$q_T = \beta_b (1-p) V_b H \qquad \text{6-3}$$

in which, p is the porosity of bed ($p = 0.4$), V_b is bedform migration rate, H is bedform height and β_b is the shape factor of bedforms. $\beta_b = 0.56$ is typical for asymmetrical bedforms [*Berg*, 1987; *Hoekstra et al.*, 2004; *Vendittti et al.*, 2016].

Additionally, some empirical equations for estimating bedform migration rate were proposed based on flow and bed material characteristics (Table 6-1). These equations were derived based on fieldwork data.

Table 6-2. Formulas to Describe Bed Load Transport. Adopted after Garcia [2008].

Authors	Transport rate q_* (m^3/s)
Meyer-Peter and Müller [1948]	$8(\theta' - \theta_{cr})^{1.5}$
Wilson [1966]	$12(\theta' - \theta_{cr})^{1.5}$
Fernandez Luque and Van Beek [1976]	$5.7(\theta' - \theta_{cr})^{1.5}$
Einstein [1950]	$12f(\theta' - \theta_{cr})^{1.5}$
Yalin [1963]	$0.635T{\theta_{cr}}^{0.5}(1 - \frac{ln(1+aT)}{aT})$
Engelund and Fredsøe [1976]	$18.74(\theta' - \theta_{cr})(\sqrt{\theta'} - 0.7\sqrt{\theta_{cr}})$
Madsen [1991]	$F_M(\theta' - \theta_{cr})(\sqrt{\theta'} - 0.7\sqrt{\theta_{cr}})$
Niño and García [1998]	$\frac{12}{\mu_d}(\theta' - \theta_{cr})(\sqrt{\theta'} - 0.7\sqrt{\theta_{cr}})$
Van Rijn [1984a]	$0.053\frac{T^{2.1}}{D_*^{0.3}}$
Hanes [1986]	$6\theta'^{5/2}$
Nielsen [1992]	$12\sqrt{\theta'}(\sqrt{\theta'} - \sqrt{\theta_{cr}})$
Cheng [2002]	$13\theta'^{1.5}exp(-\frac{0.05}{\theta'^{1.5}})$

Note: D_* is the particle parameter, $D_* = \left[\frac{(s-1)g}{\vartheta^2}\right]^{1/3} D_{50}$; $s = \rho_s/\rho$ is the relative sediment density;
θ' is the grain-related Shield's parameter, $\theta' = \frac{u_f'^2}{(s-1)gD_{50}}$;
u_f' is the friction velocity, $u_f' = \sqrt{g}\frac{U}{C'}$; *U* is depth-averaged flow velocity;
C' is the grain-related Chezy roughness coefficient, $C' = 18log(\frac{12h}{k_s'})$, while *h* is water depth and k_s' is the grain roughness, 3*D*90;
f is a fitting parameter; g is gravity acceleration; *D*50 is median grain size;
T is transport stage parameter, $T = \frac{\theta'^2 - \theta_{cr}^2}{\theta_{cr}^2}$;
θ_{cr} is critical shear stress, which could be computed based on Shields curve [*Schields*, 1936], or could be calculated by $\theta_{cr} = \frac{0.30}{1+1.2D_*} + 0.055[1 - exp(-0.020D_*)]$ [*Soulsby and Whitehouse*, 1997];
$a = 2.45\frac{\sqrt{\theta_{cr}}}{s^{0.4}}$;
μ_d is the dynamic friction coefficient;
$F_M = 8/\tan \emptyset$ for sliding or rolling sediment while $F_M = 9.5$ for saltating sediment in the water.

6.2.5. Bedload transport prediction

Abundant research has been done on bedload transport calculation based on different principles, such as shear stress [*Yalin*, 1963; *Engelund and Fredsøe*, 1976; *Bagnold*, 1980; *Van Rijn*, 1984a], flow velocity [*Shamov*, 1952; *Levy*, 1956; *Goncharov*, 1962] and stochastic theory [*Einstein*, 1942; 1950; *Gomez*, 1991]. Several commonly used formulae for the dimensionless sediment transport rate (q_*) calculation are summarized in Table 6-2. Obviously, for all the formulae, relationships were established between effective shear stress and bed material speed [*Lajeunesse et al.*, 2010]. As both the magnitude and direction of flows vary during a tidal cycle, flow velocities/ transport rates are set to be positive during ebb tides and negative during flood tides [*Ernstsen et al.*, 2005; *Ernstsen et al.*, 2007]

6.3. Results

6.3.1. In-situ field measurement

How flow velocity changes through time is displayed in Figure 6-2 and Figure 6-3. Obviously, velocity directions were ~100 and 270 degrees for the ebb and flood tide respectively in both neap and spring tide, but maximum velocity magnitude increased from 1.0 to 1.3 m/s during the ebb tide and from 0.18 to 0.25 m/s during the flood tide. Furthermore, duration of flood tide remained the same, ~ 2.5 h, while the duration of high flows in ebb tides which was relatively steady kept longer, ~5.5 h (Figure 6-4).

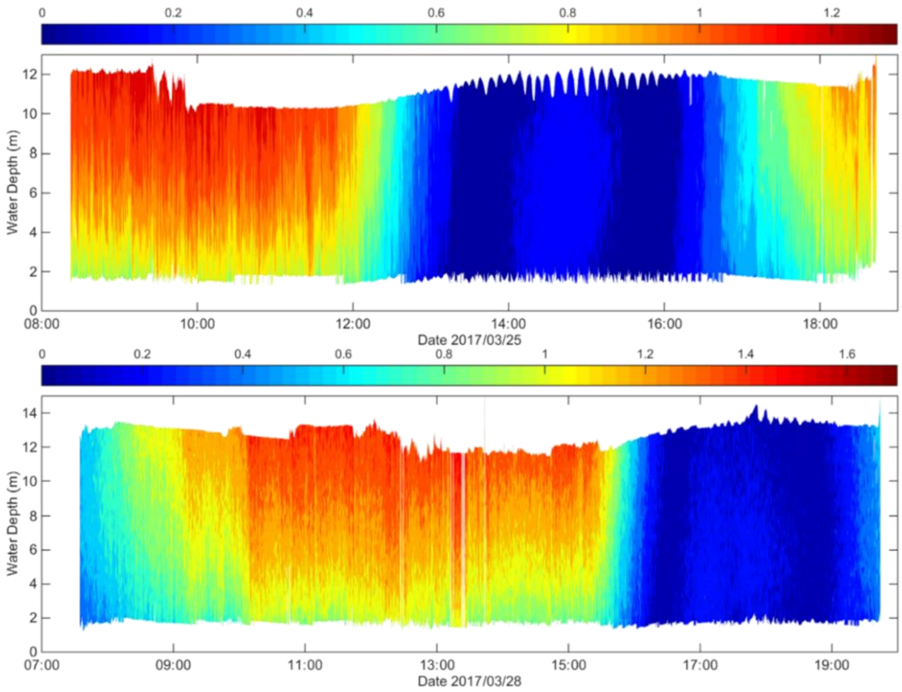

Figure 6-2. Velocity magnitude time series collected in the neap and moderate tide.

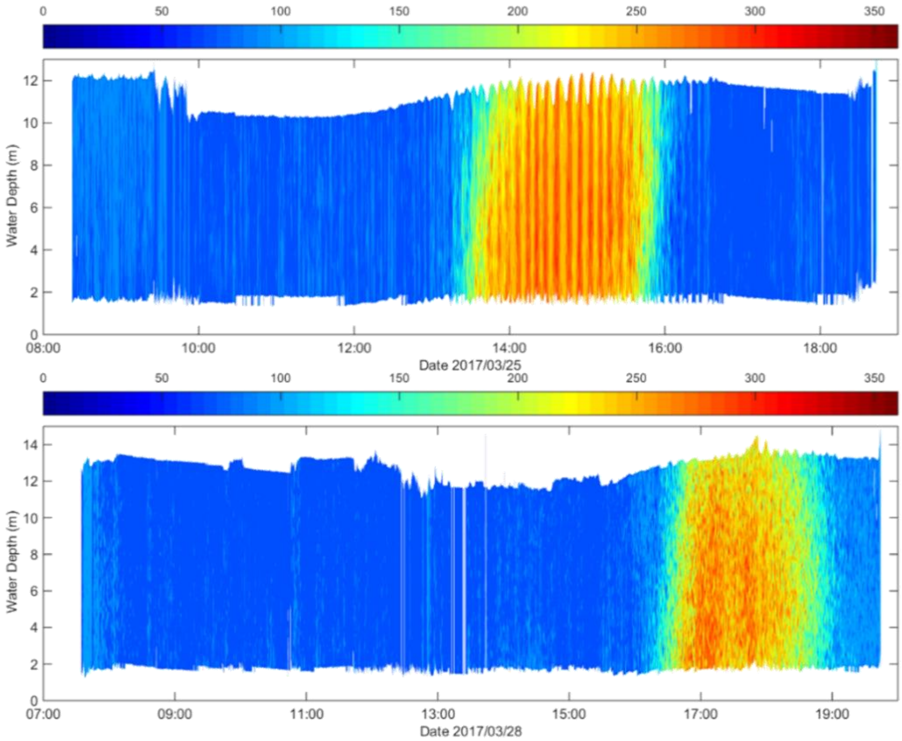

Figure 6-3. Velocity Direction time series collected in the neap and moderate tide.

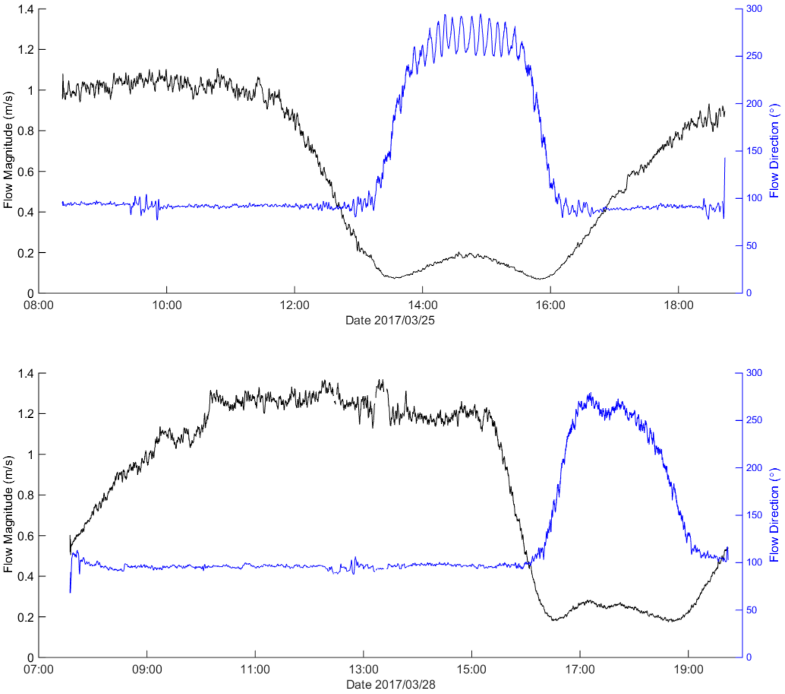

Figure 6-4. Time series of mean velocity magnitude and direction.

Additionally, fluctuation of velocity direction is found during the flood tide or when velocity is less than 0.4 m/s in the neap tide. That is because our measurement location is quite close to the navigation line of Jiagang Ferry, which connects Jiangyin city and Jinjiang city. The frequent ferry moving affected local flow field, especially when flow velocity was slow. Moreover, during the moderate tide, at the survey position, which is

400 m further downstream compared with that during the flood tide, there is no such effect being found, indicating that the effective range is less than 400 m.

6.3.2. Numerical model result

The TELEMAC-2D model was run for one month, starting at 00:00 UTC on 15 March 2017, and the field survey data was used to calibrate and verify the numerical model (Figure 6-5). The simulated results (depth-averaged velocities and tidal elevations) are consistent well with the observed (fieldwork) data, especially during the spring tide. Thus, the numerical results could be accepted to present the flow dynamics and water depth variation for the following bedload transport computation.

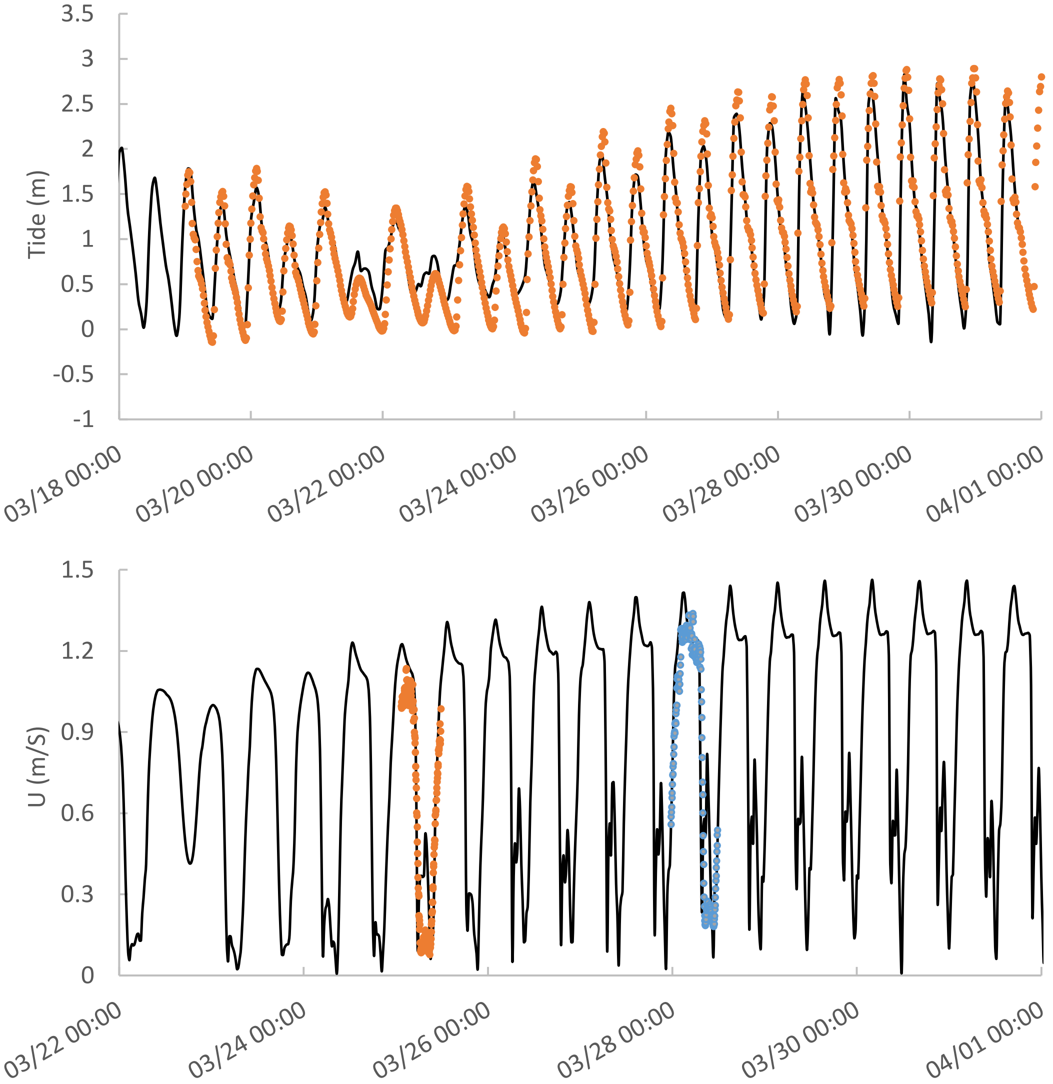

Figure 6-5. Validations of the current velocity and water elevation between 2017/03/18 and 2017/04/01. The solid lines represent the modelled results, while the dotted lines represent the observed results.

6.3.3. Flow dynamics over dunes

Aspect at a point presents the steepest downhill direction given as an azimuth angle (N = 0°) and Figure 6-6 shows the bimodal distribution of aspect for T2. The first crest around 100 degrees, equalling to mean flow direction of the ebb tide. The second nearly 278 degrees (98 degrees if transferred to downstream direction) indicates orientations of stoss-side and their difference is approximately 180 degrees.

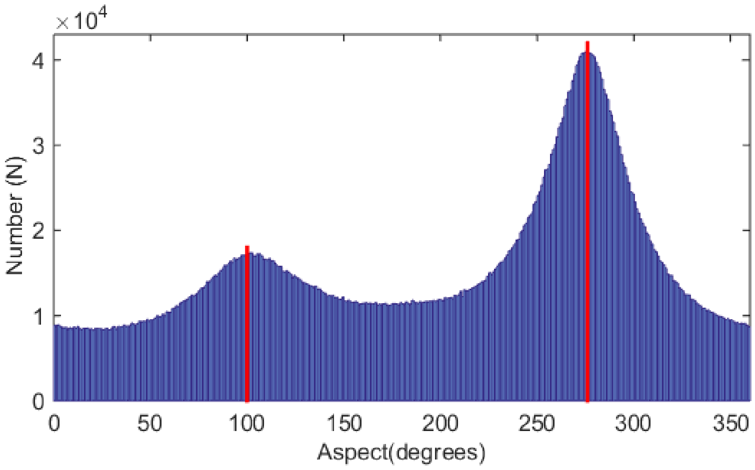

Figure 6-6. Distribution of Aspect (T2). Red line indicates the mode of the second peak, which is 278 degrees.

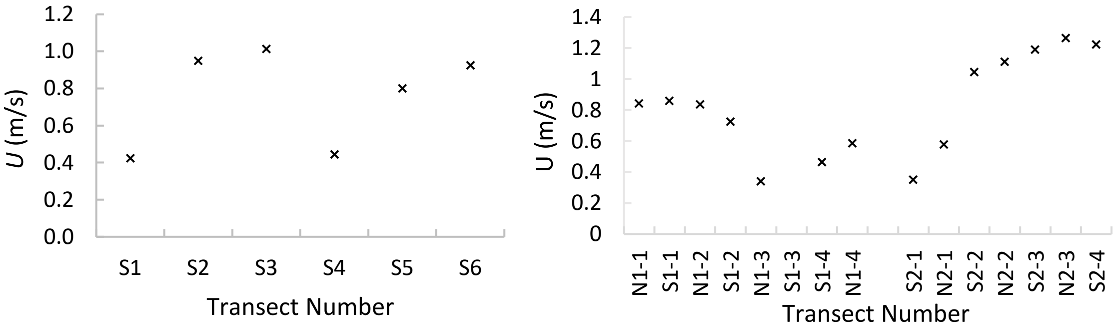

Figure 6-7. Spatially averaged flow velocities for each transect in time order during neap and spring tides in the late dry season.

It is widely recognised that the crestlines of two-dimensional ripples and dunes tend to be straight or slightly sinuous and are oriented perpendicular to the mean flow lines [*Venditti*, 2003]. From the topography of our measurement area, bedforms (late flood) are fairly two dimensional and orientation of stoss-side and lee-side, perpendicular to the crestlines, should be parallel to the flow which generates these bedforms. Therefore, in order to better analyse flow data coupled with the topography, a new coordinate was created based on aspect information that new x-axis (downstream direction) was calculated via the mean of mode aspects of both stoss-side and lee-side, equal to 99 degrees (azimuth angle), and thereby y-axis (cross-stream direction) equals to 9 degrees.

In the following data analysis, flows were transferred to the new coordinate.

Distribution of spatially averaged flow velocity of each transect was displayed in Figure 6-7. Results show that for the first survey (late flood season), measurements were taken during two ebb tides (3 for each), and flow velocity increased from 0.4 to 1.0 m/s. For the second survey (late dry season), both the ebb and subsequent flood tides were measured during the neap tide and only the ebb tide was measured during the spring tide. The greatest spatially mean flow velocity during neap tide is about 0.86 m/s while that in spring tide is larger, over 1.2 m/s.

Only the south line was investigated in the late flood season, during the repetitive measurements, each measurement was taken in the upstream direction. During the late dry season, one more north line was added. As surveys on north line and south line were taken alternately, the boat moved upstream along the south line and downstream along the north line, leading to the different space resolutions (Table 6-3). If the boat moves against the flows, boat speed referring to the bed could keep relatively slow, and simultaneously navigation line could remain straight, resulting in relatively high spatial resolution of flow data (south line). In contrast, if the boat moves along with the flows, in order to keep the straight navigation line, flow resolution is relatively low (north line). The speed and direction of boat movement affect the resolution of the collected flow field, limiting our analysis on turbulence less than that scale.

Table 6-3. Spatially averaged boat speed and along stream flow resolution.

Transect	Boat speed (m/s)	Resolution (m)	Transect	Boat speed (m/s)	Resolution (m)
N1-1	1.29	3.9	S2-1	2.19	8.3
S1-1	1.83	5.5	N2-1	3.25	12.3
N1-2	3.32	10.0	S2-2	1.67	4.1
S1-2	1.97	5.9	N2-2	3.38	6.9
N1-3	2.71	8.1	S2-3	1.43	2.9
S1-3			N2-3	2.85	5.7
S1-4	1.84	3.3	S2-4	1.51	3.0
N1-4	2.75	5.0			

As documented in past studies of flows over low-angle dunes [*Best and Kostaschuk*, 2002; *Bradley et al.*, 2013], flow separation occurs intermittently only or is absent above symmetric, low-angle dunes, but their topographic forcing of flow (expansion flow) contributes to similar gross patterns of flow acceleration and deceleration, which is widely recognised in research of angle-of-repose dunes. Appendix A displays the patterns of downstream flow in the late flood season and the result shows that neither of the flow acceleration and deceleration (macro flow structures) over large-scale low-angle dunes is apparently observed in low or high flow period, indicating that those large-scale dunes with quite low stoss and lee slope (less than 1°) have little effect on flows. However, small dunes, superimposed above large dunes, with larger lee side slope may affect the flow field near the bottom, but because of the presence of blanking zone above the bottom from aDcps, it is unable for us to detect whether there are separated zones existing over the lee-side of small-scale dunes. Besides, the diameter of the area that aDcp measures for flow computation, which is about 15 m (water depth is nearly 20 m), is larger than the length of flow separation zone which is about 4~6 times of bedform height [*Best*, 2005a]. Furthermore, both measurements (T1 and T4), which were carried out during the high tides, clearly capture the flow structure about the turn of flows from upstream to downstream. The result shows that the flows were highly mixed, but there was no wedge observed.

However, although the relationship between flow structure and large-scale bedforms is hard to observe, flow structures along the whole transect for measurements taken during a similar tidal condition (T1 vs. T4, T2 vs. T5 and T3 vs. T6) typically are similar in patterns, especially obvious in the distribution of flow direction. It indicates that small dunes superimposed over large-scale dunes slightly affect flow structure near the bottom, but this is hard for us to investigate due to the limits of the instrument.

Table 6-4. Summary of roughness length (z_0) and shear velocity (u_*) for velocity profiles of Spatial Average of Whole Transect (SAWT).

Transect	z_0		u_*	
	Upper	Lower	Upper	Lower
T2	0.153	0.034	0.101	0.059
T3	0.091	0.033	0.089	0.059
T5	0.231	0.037	0.077	0.045
T6	0.093	0.012	0.070	0.044

In terms of flow patterns over single-type dunes in the late dry season (Appendix C), morphology induced flow structures are not detected or hard to be detected due to the low streamwise resolution and relatively small dune size. Although there are some patterns in flow velocity contour, links between flow structures and dunes are relatively weak.

6.3.4. Bedform roughness

6.3.4.1. Bed roughness of compound dunes in the late flood season

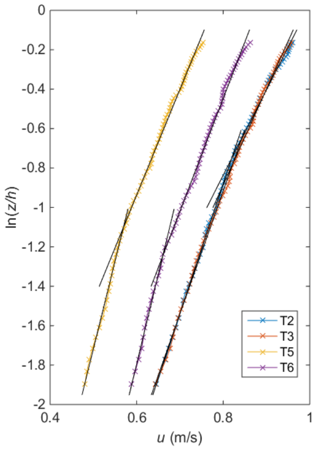

Figure 6-8. Downstream velocity profiles of Spatial Average of Whole Transect (SAWT): T2, T3, T5, and T6. Black lines indicate two segments were detected.

The patterns of the vertical velocity profiles display that the velocity profiles were segmented, being made of two log-linear segments. Lower and upper segments converge at the normalised height $z/h = 0.3$ (i.e. $\ln(z/h) = -1.2$) for T5 and T6, whose velocities are relatively lower, and at the normalised height $z/h = 0.43$ (i.e. $\ln(z/h) = -0.85$) for T2 and T3 with relatively larger velocities, lower and upper segments converge at the normalised height $z/h = 0.45$ (i.e. $\ln(z/h) = -0.8$) (Figure 6-8). Calculated roughness lengths via the Law of the wall for all segments shows a similar trend between four measurements, presenting a negative correlation with the variability of spatial mean velocity, while the variabilities of shear velocity are different for each segment (Figure 6-9 and Table 6-4).

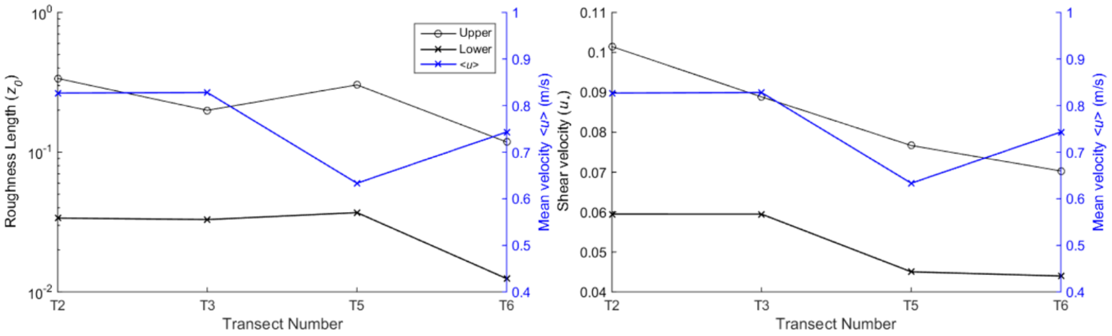

Figure 6-9. Variability of roughness length z_o and shear velocity u_* between measured transects.

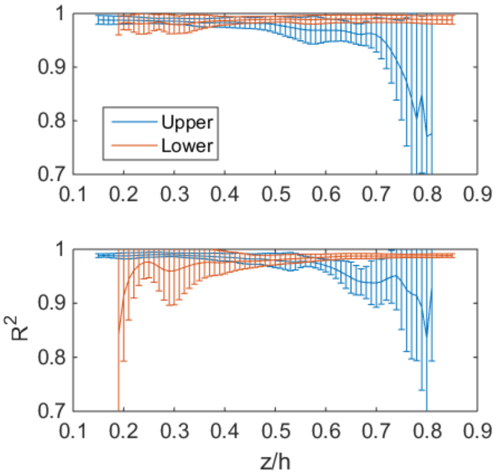

Figure 6-10. Average coefficients of determination (R^2) of the log-law applied to the lower segments (red line) and upper segments (blue line) of the large dune profiles (SALD) for each transect as a function of the normalised depth (z/h=height above the seabed normalised by water depth) vertical bars show 1 standard deviation.

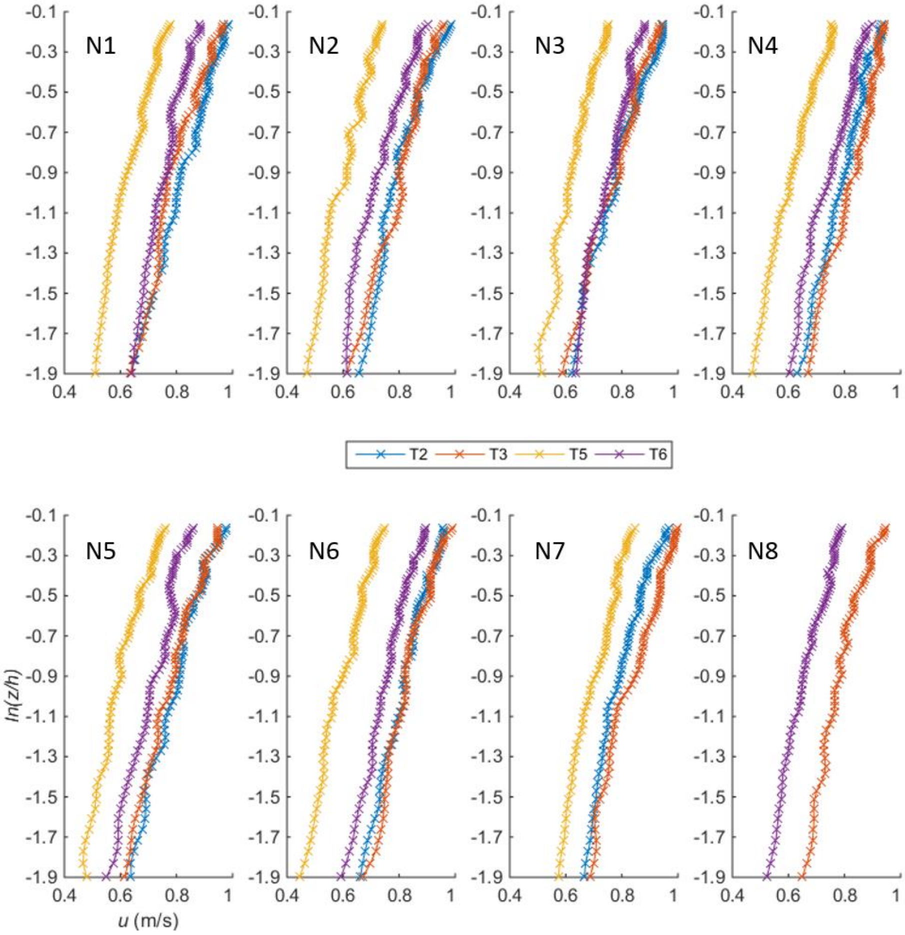

Figure 6-11. Spatial averaged velocity profiles over each large dune for transects T2, T3, T5, and T6.

Similarly, the patterns of the velocity profiles show that the majority of them were segmented into at least two parts that converged at the normalised height between 0.3 and 0.5 (i.e. $-1.2 < \ln(z/h) < -0.7$, grey background) above the bottom (Figure 6-10 and Figure 6-11). Roughness length of two segments were calculated: the lower part, $\ln(z/h) < -1.2$ and the upper part, $\ln(z/h) > -0.7$.

However, fluctuations of velocities along individual profile are also obvious, locating at upper segments except for N5, fluctuating along the whole profile. Thereby, to some of the profiles, these fluctuations dramatically affect the calculation of roughness length (N3 and N4 in Figure 6-12). However, in general, roughness lengths computed from upper segments are larger than those from lower segments. Furthermore, although the variability of roughness for each individual dune is obvious, they are basically in the same order of magnitude with those calculated via SAWT.

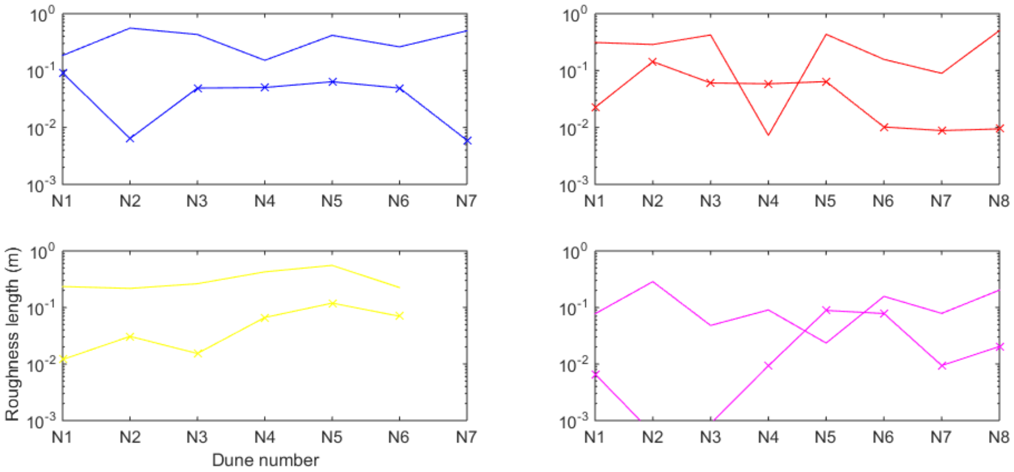

Figure 6-12. Variability of Roughness length over each individual large dune for T2 (a), T3 (b), T5 (c) and T6 (d).

6.3.4.2. Bed roughness of single-type dunes in the late dry season

Unlike velocity profiles over compound bedforms, velocity profiles over the single type of bedforms in the late dry season were not obviously segmented (Figure 6-13). It was also observed that the velocities of the upper part were distorted by wave and vessel moving, as it was strongly windy during our measurements. It is hard to quantify the influence of waves. Therefore, the upper velocities were removed in the following bed roughness calculation. It is also expected that the removal did not dramatically affect the estimation, as the law of the wall is not sensitive to the velocities of the upper part [*Lefebvre et al.*, 2011b].

Results of roughness length and shear stress estimated via the law of the wall are displayed in Table 6-5 and Figure 6-14. The roughness length of the north transect is relatively constant, fluctuating between 0.03 and 0.06. In contrast, that of south transect reaches 0.14 m for the transect collected at maximum velocity. Furthermore, a similar trend was observed for the shear velocity.

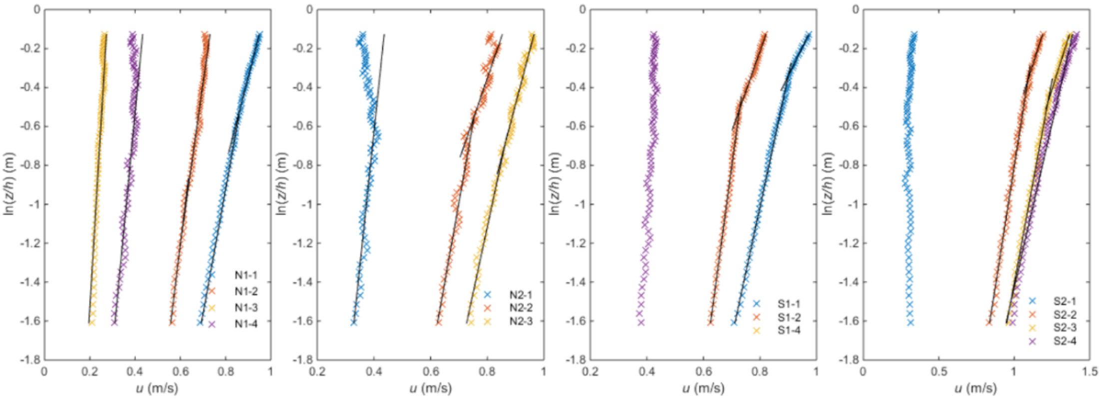

Figure 6-13. Downstream velocity profiles of Spatial Average of Whole Transect (SAWT).

Table 6-5. Summary of roughness length (z_0) and shear velocity (u_*) for velocity profiles of Spatial Average of Whole Transect (SAWT).

Transect	z_0 (m)	u_* (m/s)	Transect	z_0 (m)	u_* (m/s)
N1-1	0.0437	0.066	S1-1	0.0284	0.061
N1-2	0.0390	0.066	S1-2	0.0041	0.038
N1-3	0.0308	0.025	S1-3		
N1-4	0.0561	0.048	S1-4		
N2-1	0.0600	0.050	S2-1		
N2-2	0.0480	0.089	S2-2	0.0582	0.083
N2-3	0.0342	0.096	S2-3	0.0650	0.098
N2-4	0.0287	0.097	S2-4	0.1407	0.122

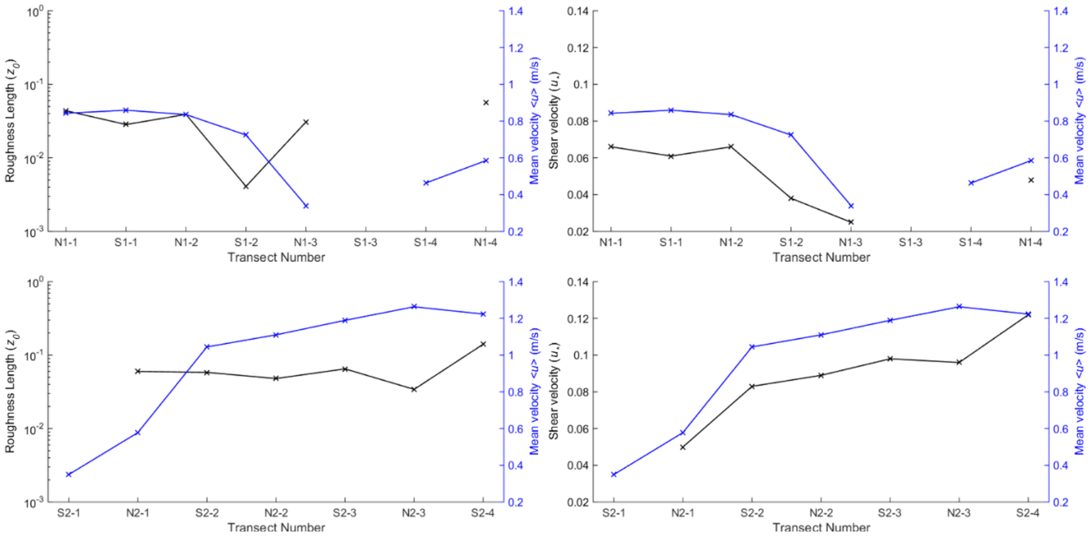

Figure 6-14. Variability of roughness length z_0 and shear velocity u_* between measured transects. Dark lines indicate roughness length in left two figures, while shear stress in right two figures. Blue lines denote mean flow velocities.

6.3.5. Bedload transport flux

Bedload transport flux between the first transect survey (08:00 am in 24/23/2017, neap tide) and the last transect survey (12:00 pm 29/03/2017, spring tide) during the late dry season was calculated via measured bedform migration distance (M_d) (Table 6-6) or predicted by some other derived equations (Table 6-7). All the predicted bedload transport fluxes are at the same order of the measured value estimated via bedform migration. Among those, *Wilson* [1966], *Engelund and Fredsøe* [1976], *Nielsen* [1992], *Cheng* [2002], and *Zhang et al.* [1989] predicted better results, while the others all display a underestimated trend.

6.4. Discussion

Due to the longer adaptation of bedform length, bedform decay during falling limbs or an abrupt drop occurred through quicker response (decrease) of bedform height or formation of smaller superimposed bedforms cannibalizing the original, relict features [*Martin and Jerolmack*, 2013; *Warmink*, 2014; *Warmink et al.*, 2014]. However, *Reesink et al.* [2013] proposed that generation of superimposed bedforms is not unique to dune decay by cannibalizing, as he observed that superimposed bedforms over the stoss-sides of larger dunes were only developed when water depth was increasing.

Above conclusions were mainly drawn based on bedload dominated lab experiments or fieldwork data, while suspended sediment transport is also a non-negligible effect on bedform migration and transformation. *Kostaschuk et al.* [2009] found that about 17% of the coarser suspended-load transported over the crest is deposited in the lee-side before it reaches the trough. Furthermore, *Naqshband et al.* [2014c] suggested that, even in an equilibrium condition, the contribution rate of suspended-load depends on the Froude number (F_r) that if the F_r is higher, the suspended-load contributions less to bedform migration. In conclusion, the disequilibrium between bedform geometry and flows over bedforms (especially near the bed surface) leads to the change of sediment transport mechanism [*Villard and Kostaschuk*, 1998], thereby bedforms transform in the process of migration (cannibalizing), deformation (superimposed bedforms) or both. There are a lot of impacts that can affect bedform transforming, and research on how bedforms exactly respond to changing flows is still in its infancy.

Table 6-6. Statistics of migration and deformation flux related to bedforms.

	D_{lag} (m)	Q'_T (m^3)	Q_D (m^3)	Q_{tot} (m^3)	F
N_L	23.4	8.4	3.04	11.44	0.27
S_L	18.4	10.5	4.20	14.7	0.29

Table 6-7. Summary of bedload transport via different equations.

Methods	M_d (m)	Q_* (m^3)
Meyer-Peter and Müller [1948]	/	5.98
Wilson [1966]	/	8.96
Fernandez Luque and Van Beek [1976]	/	4.26
Yalin [1963]	/	5.23
Engelund and Fredsøe [1976]	/	11.43
Van Rijn [1984a]	/	7.45
Hanes [1986]	/	2.69
Nielsen [1992]	/	9.50
Cheng [2002]	/	9.94
Zhang et al. [1989]	36.4	~17.1

6.4.1. The validity of roughness length of compound dunes in the late flood season

The variability of roughness length (Figure 6-9) confirms previous research (Fig. 11 in *Lefebvre et al.* [2013a]) that during ebb tides of the tidal cycle, roughness length computed from the upper segment of the velocity profile shows a negative relationship with spatial mean velocity, while those calculated from lower segment does not see any trend with velocity and changes little (except T6).

Except for the Law of the wall, some scholars (see detailed information in Table 1 of *Lefebvre et al.* [2011b]) suggest that bedform roughness length also could be computed via the ratio H^2/L with the universal equation [*Soulsby*, 1997]:

$$z_0 = a\frac{H^2}{L} \qquad \text{6-4}$$

where a, the empirical coefficient, ranges from 0.3 to 3, and its typical value is 1. The variation of a indicates that roughness length is related to bedform type (such as asymmetry) and flow condition (ebb or flood). Furthermore, in general, a is lower for superimposed bedforms and higher for primary ones [*Lefebvre et al.*, 2013a].

According to Figure 6-15, for small dunes, we take $H = 0.8\,m$ and $L = 17\,m$, thereby, bedform roughness length based on this scale (SD) ranges between 0.0113 and 0.113 m. Roughness lengths computed from the lower segment (0.012~0.037, see Table 6-4) fit this range estimated via bedform size. Similarly, for large dunes, we take $H = 3\,m$ and $L = 260\,m$, and the computed bedform roughness length ranging from 0.0117 and 0.117 m fit the empirical range of a, as well. Moreover, the inversed a via roughness length calculated from Law of the wall for middle and lower segment ranges from 0.32 to 1, except middle one of T5 ($\alpha = 3.6$), confirming that α, estimated from the lower segment, is generally lower [*Soulsby*, 1997; *Lefebvre et al.*, 2013a].

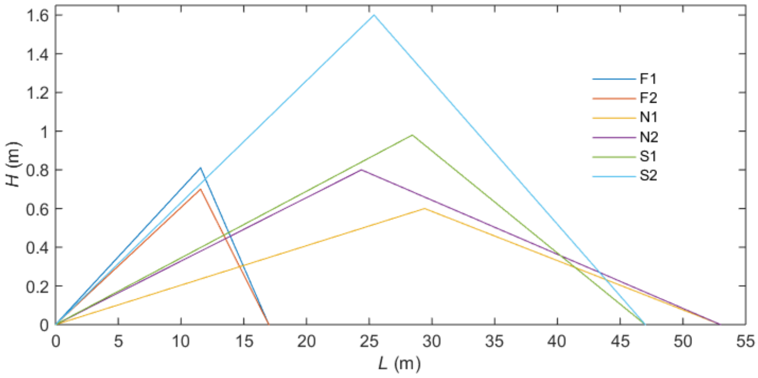

Figure 6-15. Variation of the shape of bedforms. Shapes were drawn based on H_{50}, Asy_{50}, and $Ldown_{50}$.

Lefebvre et al. [2014a] concluded that during the ebb, three segments were observed on the spatially-averaged velocity profiles. The lower segment, $z/h < 0.09$, is related to local grain roughness, while the middle segment, $0.09 < z/h < 0.23$ or 0.18 (the upper boundary is controlled by bedform height), results from the secondary bedforms. Finally, the upper segment, $z/h > 0.23$ or 0.18, attributes to large compound bedforms. However, in this research, the segment related to grain roughness could not be characterized due to the limitation of the instrument (velocities near the bottom were not reliable). Therefore, only two apparent segments of profiles were captured in our ADCP data. The change of roughness length computed from the lower segment of velocity profiles and size of small superimposed dunes is very little, indicating that roughness length of the lower segment is extremely likely to attribute to the small dunes. However, roughness length of the upper segment is more complicated, as it presents total hydraulic roughness [*Villaret et al.*, 2011; *Lefebvre et al.*, 2013a]:

$$k_s = k_{sbf} + k_{sg} = \sqrt{{k_{sr}}^2 + {k_{smr}}^2 + {k_{sd}}^2} + k_{sg} \qquad 6\text{-}5$$

where k_{sbf} is form related roughness, including k_{sr}, ripple-related roughness, k_{smr}, mega-ripple-related roughness and k_{sd}, dune related roughness; k_{sg} is grain related roughness. This formula is still the most efficient for the lower alluvial regime (ripples and dunes, when *Fr* < 1) [*Huybrechts et al.*, 2011; *Villaret et al.*, 2011].

The shape of bedform is one of the most important impacts that may affect flow structure. *Kostaschuk and Villard* [1996] and *Villard and Kostaschuk* [1998] pointed out that bedform asymmetry influences the range of effect, and asymmetric bedforms result in larger roughness length and have a greater range of influence than symmetric ones. In terms of low-angle dunes (lee-side slope less than 10°), *Best and Kostaschuk* [2002] suggested that macroturbulence, the main reason affects flow structures, is generated by intermittent flow separation or shear layer generated by the lee-side flow expansion. When the lee-side angle is larger than 10°, permanent flow separation happens [*Paarlberg et al.*, 2009; *Lefebvre et al.*, 2014a]. Although, when velocity magnitude is higher than some certain value (0.4 m/s in case of *Lefebvre et al.* [2014a]), flow separation zone (FSZ) forms and it does not change with the increase of velocity, but it does not explain whether the effect of the FSZ with unchangeable size is variable or not during the tidal cycle.

The compound bedforms in this research area are relatively complex, composed of three possible types: bar, large and small dunes. Although both the bar and large dunes are low angles, their combination could alter the flow structure over small dunes. It is reflected in Figure 5-6 in the last chapter that larger scale small dunes generate on the lower area of dunes and in Figure 5-5 in the last chapter that different scales and shapes of large dunes distribute on the 'bar'. Thereby, the most reasonable explanation for the results here is:

(1) The lower segment is interpreted to reflect the friction induced by small dunes. H and S_l of small dunes generated when velocities are relatively higher are slightly greater than those generated under lower velocities (Table 3-1 in the last chapter) and both the increase of H and S_l leads to stronger effect on flow structure, reflecting in the increase of its range of effect on velocity profiles (Figure 6-8). Besides, the lee-side angles (not the steepest angle for each bedform) of small dunes here are fluctuating around 10°, which is the lowest lee-side angle to generate permanent FSZ [*Paarlberg et al.*, 2009; *Lefebvre et al.*, 2014a], so nearly 50% of them generate intermittent FSZ. The increase of velocity could also increase the possibility of generating FSZ, consequently resulting in a further effect on flow structure.

(2) The upper segment is likely attributed to the combined effect of small and large dunes. Flow expansion over the lee-side of low-angle large dunes could generate

a shear layer resulting in macroturbulence, reflecting in Appendix B that, for the majority of less-side of large dunes, corresponding velocity gradients over lee-side are apparent, representing the effect of flow deceleration on flow energy dissipation. However, in some specific locations, such as the lee-side of the first large dune with relatively larger scale small dunes superimposed, it is obvious that the effect of the small dunes with larger lee-side angle, possibly flow separation happened, on flow structure is stronger than that of large dune, and this is also reflected in Figure 6-11, that differences of these specific individuals within middle segments are obvious, compared with others. In our research, it is hard to distinguish which element dominants flow structure. It is because that velocities were calculated by 4 beams of the aDcp, with a 20° angle perpendicular to the vertical direction, and with the increase of distance between the transducer and measuring position, the area for the velocity calculation increases, reaching 15 m diameter at water depth 15 m. This scale is close to the length of small dunes, therefore, flow structure over small dunes in this research was unable to present properly.

6.4.2. How does the hydraulic condition affect roughness and bedform development in the late dry season?

Roughness length and shear stress are two main parameters affecting water level, flow structure, and capability of sediment transport. They were computed via the law of the wall, and their correlations with mean flow velocity are displayed in Figure 6-16. For south survey line, z_0 shows a slight increase trend with increasing flow velocity, while for the north line, z_0 remains slightly fluctuating around 0.05 m. In terms of shear velocity, positive correlations were found in both two surveys, but south line occupies the larger slope (Figure 6-14 and Figure 6-16). This result indicates that, for the south line, both shear stress and roughness length are more sensitive to mean velocity.

Figure 6-17 displays the bed profiles of north and south survey line during the neap and spring tide in the late dry season. Obviously, two classes of bedforms (superimposed dunes and bar) can be observed from both survey lines. The roughness length, calculated from the upper segment, presents total hydraulic roughness [*Kostaschuk and Villard*, 1996; *Lefebvre et al.*, 2013a]. For the north transect, the combined effect of the bar and superimposed dunes on flows results in variation of roughness. As both of the bar and superimposed dunes varied little, there are no large-scale coherent flow structures (CFS) being observed, thereby, their effect on turbulence, especially macroturbulence, is confined [*Best*, 2005b; *Kwoll et al.*, 2016; *Kwoll et al.*, 2017]. In contrast, bed profiles of the south line are more complicated that superimposed dunes are larger with higher lee slope, and lee face of the bar is steeper as well (Figure 6-17). Flow structure is observed to be affected by the compound form (Appendix C), verifying that z_0 derived via velocity profiles could change with flows.

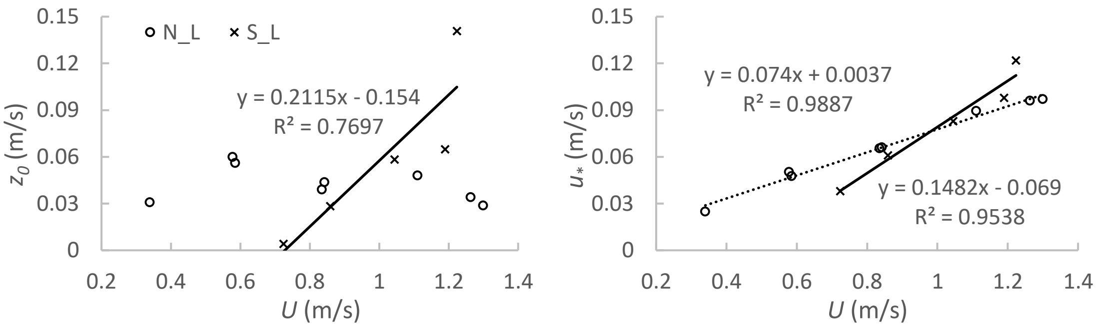

Figure 6-16. The relationship between mean flow velocity & roughness length (a) and mean flow velocity & shear velocity (b) in the late dry season.

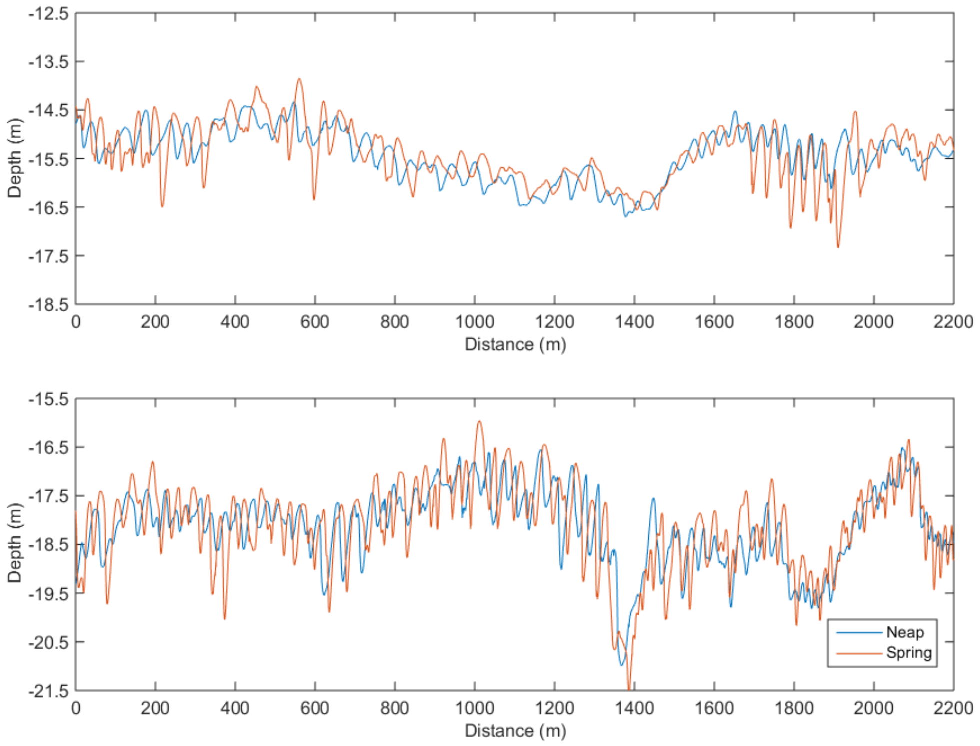

Figure 6-17. Variability of bed profiles for North (N_L) and South (S_L) survey line between neap and spring tide in the late dry season.

The lee slope angle plays a nonlinear effect on turbulence, implying that small changes in the lee slope for less steep dunes may induce relatively small variations in turbulence production, wake structure characteristics, and flow resistance [*Kwoll et al.*, 2016]. Both the lee slopes of superimposed dunes are small: less than 2° for the north transect while that of the south transect is a little bit higher, but less than 5°. The low lee slopes indicate that there is no flow separation occurring over the lee face and trough [*Paarlberg et al.*, 2007; *Bradley et al.*, 2013; *Lefebvre et al.*, 2016], but their topographic forcing of flow (expansion flow) could contribute to similar gross patterns of flow acceleration and deceleration [*Best and Kostaschuk*, 2002]. Therefore, it probably because the flow expansion over low-angle dunes is sensitive to both lee face and flow strength, resulting in the different correlations.

Lefebvre et al. [2016] proposed that bedforms with very low slip face (< 8°) should not be considered as additional roughness elements because they only have a shear stress which is less than 10% higher than that over a flatbed. In this study, it is confirmed by the equivalent results of bedload transport flux calculated from two different methods (Table 6-6 and Table 6-7). The empirical equations were generally summarized from experiments only considering flatbed, and the form related shear stress on sediment transport was ignored. Therefore, the similar results reflected that bedload transport induced by bedform related shear stress is little. Moreover, the clay contained in the bed material also has little effect on constraining bedload transport.

Bedform dimensions were determined based on *van der Mark and Blom* [2007], and stoss and lee slopes were calculated via ratios of $Htrto/Lups$ and $Htotr/Ldowns$ respectively, which may not correctly present the true slopes. *van der Mark and Blom* [2007] also proposed that the angle of the slip face, estimated by removing a distance of one sixth of the bedform height below the crest and above the trough (i.e. upper and lower segments of lee sides), better represents the true slope than the mean lee slope, $Htotr/Ldowns$. However, some research [*Kornman*, 1995; *Lefebvre et al.*, 2016] argues that both the morphology of the lower and upper lee side has an impact on flows. In this study, both stoss and lee sides are relatively low, and bedforms are relatively symmetric. Therefore, any algorithm will not dramatically change the calculating results of slip face. Although, the slip face at the very low lee side may reach over 10° or even angle-of-repose, at where flow separation occurs [*Best*, 2005a], its size is too small to affect flow structure, thereby the total hydraulic roughness.

Additionally, the intersection in Figure 6-16b, at where the flow velocity is nearly 1 m/s, separates the effects into two different parts. When U is lower than 1 m/s, the shear velocity of the north line is higher than that of south line. In contrast, when U is greater than 1 m/s, the shear velocity of the south line is larger. According to Figure 6-5b, during the tidal circles from moderate to spring tides, the period of high flow velocity ($U > 1m/s$) is relatively long. It results in that bedload transport of south line is higher.

6.5. Conclusions

Two advanced instruments (aDcp and MBES) were employed concurrently in two field surveys, one in the late flood (end of October, 2016) season and the other in the late dry (end of March, 2017) season, in the middle reach of the Changjiang (Yangtze) estuary, China, where compound bedforms widely generate [*Chen et al.*, 2012; *Shuwei et al.*, 2017]. The hydraulic roughness of ebb-oriented bedforms was calculated within tidal cycles and sediment transport related to bedform migration and deformation is calculated, compared with results derived from empirical equations:

1. Two segments were detected from the bed profiles in the late flood season, when compound bedforms, comprised of the bar, superimposed large dunes and small ones, generated. In contrast, velocity profiles over the relatively simple type of bedforms in the late dry season were not obviously segmented.
2. For compound dunes in the late flood season, the lower segment is interpreted to reflect the friction induced by small dunes. The lee-side angles of small dunes fluctuate around 10°, which is the lowest lee-side angle to generate permanent FSZ, Therefore, the increase of velocity could increase the possibility of generating FSZ, consequently resulting in a further effect on flow structure. The upper segment is likely attributed to the combined effect of small and large dunes. The large superimposed dunes over primary dunes play a significant role in roughness based on the result of flow structure. However, limited by the resolution of the instrument, it is hard to distinguish which roughness element dominants flow structure over compound dunes.
3. For dunes in the late dry season, south survey line, z_0 shows a slight increase trend with increasing flow velocity, while for the north line, z_0 remains slightly fluctuating around 0.05 m. In terms of shear velocity, positive correlations were found in both two surveys, but south line occupies the larger slope (Figure 6-14 and Figure 6-16),

indicating that, for the south line, both shear stress and roughness length are more sensitive to mean velocity. The flow expansion over low-angle dunes is sensitive to both lee face and flow strength, resulting in the different correlations.

4. Bedload transport calculated from empirical equations shows a satisfactory agreement with that from bedform migration and deformation. This result implies that bedload transport induced by bedform related shear stress is little. Moreover, the clay contained in the bed material also has little effect on constraining bedload transport.

Full understanding of the links between the flows, sediment transport and morphological change is essential in advancing sediment transport modelling. A growing number of studies [*Bradley et al.*, 2013; *Naqshband et al.*, 2014c] have revealed that suspended sediment transport plays a crucial role in sediment transport and bedform morphology and development. Future work must be coupled with concurrent suspended sediment transport [*Kostaschuk et al.*, 2005] and more detailed flow structure [*Kwoll et al.*, 2017], especially near the bed, in order to resolve the origin and development of low-angle dunes.

CHAPTER 7

7. Low-angle dunes in the Changjiang (Yangtze) Estuary: flow and sediment dynamics under tidal influence

Abstract: It has long been highlighted that important feedbacks exist between river bed morphology, sediment transport, and the turbulent flow field and that these feedbacks change in response to forcing mechanisms. However, current comprehension of bedform dynamics is largely based on studies on steady flow environments and cohesionless bed conditions, and few investigations were made under rapidly changing flows. Here, we examined flow and sediment dynamics over low-angle dunes in unsteady flows of the Changjiang (Yangtze) Estuary, China. Topography, flow, and sediment data were collected over a field *ca* 1.8 km long area through a semi-diurnal tidal cycle in a moderate tide of flood season. The results show that: (1) roughness length derived from the upper flow changes little with the flow reversing and displays the same level in both the ebb and flood tide. Moreover, the variability of individual bedform features plays an important role in roughness length variation. (2) Shear stress over the crest of low-angle dunes can roughly represent total stress of spatially averaged over dunes in this study area, which has significant implications for advancing numerical models. (3) Changes in morphology, flow and sediment dynamics over dunes through time reveal how low-angle dunes evolve within a tidal cycle. (4) The clockwise hysteresis loops between flow dynamics and bedform features (height and aspect ratio) are also observed. The combination of suspended sediment transport and bedload transport on dune transformation and migration attributes to the clockwise hysteresis. The specific sediment composition of the riverbed, in some extent, affects the mechanism of sediment transport related to the exchange between suspended sediment and riverbed, but further investigation is needed to figure out the mechanism behind this for extended series of tides, such as spring/neap tide and tides in flooding and dry season.

7.1. Introduction

Dunes are ubiquitous features in sand bed rivers and estuaries [*Kleinhans*, 2005a; *Parsons et al.*, 2005], and play a significant role in the connection between boundary flow structure and sediment transport [*McLean et al.*, 1994; *Nelson et al.*, 1995; *Best*, 2005a]. There have been many studies attempting to understand the feedbacks between turbulence, dune form and sediment transport [*Best*, 2005a; *Parsons and Best*, 2013], however, most of them have focused on fixed dune experiments (e.g. [*Bennett and Best*, 1995; *Maddux et al.*, 2003a; *Maddux et al.*, 2003b; *Venditti*, 2007]), ignoring the effect of movable bed, resulting in discrepancy between the flume results and field observations [*Grant and Madsen*, 1982; *Naqshband*, 2014; *Naqshband et al.*, 2014c]. Moreover, they have also mainly focused on unidirectional and uniform flow conditions (e.g. [*Guy et al.*, 1966; *Best*, 1996; *Nelson et al.*, 2011]), limiting the actual presence of the natural hydrology and sediment condition over dunes, especially in tidal environments on the time scale as short as single tidal cycle [*McLean et al.*, 1994; *Bennett and Best*, 1995; *Best and Kostaschuk*, 2002; *Kostaschuk and Best*, 2005; *Ernstsen et al.*, 2006b; *Lefebvre et al.*, 2011b; *Bradley et al.*, 2013; *Lefebvre et al.*, 2013a; *Kwoll et al.*, 2014; *Hendershot et al.*, 2016].

Both flows and sediment transport in natural rivers and estuaries are largely influenced by the generation, development, and transmogrification of dunes and controlled by dune geometry [*Clifford et al.*, 1992; *Yang et al.*, 2005; *Parsons et al.*, 2007; *Venditti*, 2013]. The flow separation generally occurred over the angle-of-repose lee-side results in the generation of turbulence and thereby alters the sediment dynamics [*Best*, 2005a]. However, growing evidence from field observations suggests that symmetrical dunes with smaller lee-side angles (i.e. low-angle dunes, LADs, generally less than 10° [*Paarlberg et al.*, 2009]) are the prominent bedforms in tidally influenced, suspended sediment dominated, sand-bedded rivers and estuaries [*Smith and McLean*, 1977; *Kostaschuk and Villard*, 1996; *Carling et al.*, 2000a; *Best and Kostaschuk*, 2002; *Kwoll et al.*, 2016; *Lefebvre and Winter*, 2016a]. As documented in past studies on flow dynamics over low-angle dunes [*Best and Kostaschuk*, 2002; *Bradley et al.*, 2013; *Hendershot et al.*, 2016; *Kwoll et al.*, 2016; *Lefebvre et al.*, 2016], flow separation occurs intermittently or is absent, but their topographic forcing of flow (expansion flow) contributes to similar gross patterns of flow acceleration and deceleration, which is widely recognised in research of angle-of-repose dunes [*Best*, 2005a]. Moreover, sediment deposits from suspension in the lower lee and trough, leading to the dune migration and deformation [*Best and Kostaschuk*, 2002; *Best*, 2005a; *Bradley et al.*, 2013; *Hendershot et al.*, 2016]. Additionally, increasing studies [*Kostaschuk and Villard*, 1996; *Kostaschuk and Best*, 2005; *Naqshband et al.*, 2014a; *Naqshband et al.*, 2014c] have revealed that different sand transport mechanisms contribute to these different formations of dunes: high-angle dunes (HADs) occur under bedload dominant regime, while LADs develop under high suspension circumstances.

Most of the existing research of dune morphodynamics has focused on non-cohesive bed conditions where median grain size D_{50} is larger than 150 µm [*Field et al.*, 1981; *Németh et al.*, 2006] and the classic bedform stability diagram proposed by *Allen* [1985] is established based on cohesionless sediments. However, recent studies have highlighted the effect of cohesive material, or ′′sticky stuff′′ (mud, clay and microorganisms, i.e. cohesive bed) on bedform geometry and dynamics, indicating that present bedform phase diagrams and predictors are overly simplistic [*Malarkey et al.*, 2015; *Schindler et al.*, 2015; *Baas et al.*, 2016; *Parsons et al.*, 2016]. Previous research observed that various scales of dunes existed in beds with clay contained, for example, the Changjiang (Yangtze) Estuary [*Cheng et al.*, 2001; *Wu et al.*, 2009]. However, their studies have mainly focussed on classifying their geometric characteristics [*Li et al.*, 2003; *Cheng et al.*, 2004; *Shuwei et al.*, 2017] or exploring how to predict bedload transport rate based on dune migration [*Yang et al.*, 1999], while how these LADs evolve under this specific condition has been rarely studied.

Therefore, this study aims to enrich current understanding of bedform dynamics in large tidal environments composed of fine bed materials. Here, seven repeated, high-accuracy measurements on bed topography and flow velocities within a single tidal cycle were carried out in the Changjiang (Yangtze) Estuary, China. Bed roughness and flow resistance were quantified to address how they responded to tidal-scale variable flows. Moreover, morphological changes, flow structure, and sediment transport over dunes through time were all quantified to elaborate how dunes evolved across different tidal stages. The findings are expected to help advance the understanding of generation and migration of low-angle dunes in large, tidally influenced areas and give significant implications for long-term modelling of estuarine sediment transport.

7.2. Methods

7.2.1. Study area

The Changjiang Estuary, well known as Yangtze Estuary, is a multi-channel estuary with a three-level bifurcation down-estuary and four distributaries separated by islands or banks. The mean annual discharge at Datong Station (the tidal limit, ~600 km upstream to the estuary) was 896 km^3 during 1950~2010 [*CWRC*, 2011] and high discharge occurs in the summer in response to monsoon rains in the upper basin. The mean (and maximum) tidal range is 2.66 m (4.62 m) at Zhongjun station near the mouth and decreases up-estuary to 2.43 m (3.96 m) at Gaoqiao station and 2.21 m (4.48 m) at Wusong station in the South Channel [*Yun*, 2004].

The mean sediment load transported into the estuary reached 390 Mt annually during 1950~2010 [*Luan et al.*, 2016] and median bed material grain size (D_{50}) in the estuary is 80~161 μm, composed of coarser silt to very fine sand in the dry season and very fine to fine sand in the flood season, with little seasonal and spatial variation [*Cheng et al.*, 2004; *Wu et al.*, 2009].

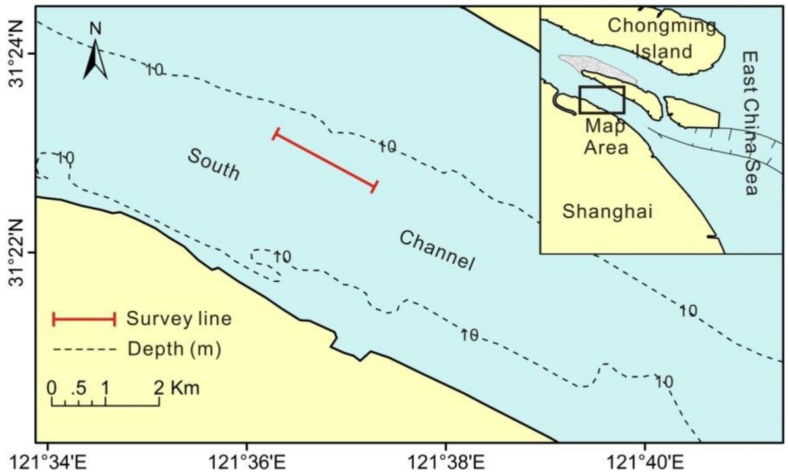

Figure 7-1. Bathymetric map of the study dune field. The inset shows the position of the dune field in the main channel of the Changjiang River, China. The red line shows the measuring line of aDcp.

7.2.2. Data collection

Field observations were made in the South Channel (Figure 7-1) and measurements on a dune field approximately 1.8 km long were taken over a semi-diurnal tidal cycle on 27th July of 2013 to see how flow and morphology changed with the tides through time (Figure 7-2). A 1200 KHz Workhorse aDcp and an Inner Space 24 kHz Thermal Depth

Recorder (449M) were deployed on a ship in order to record flow velocities and bathymetry data, respectively. Boat positions were measured by a Differential Global Positioning System (DGPS, Trimble) tied to a local navigation beacon with sub-meter accuracy.

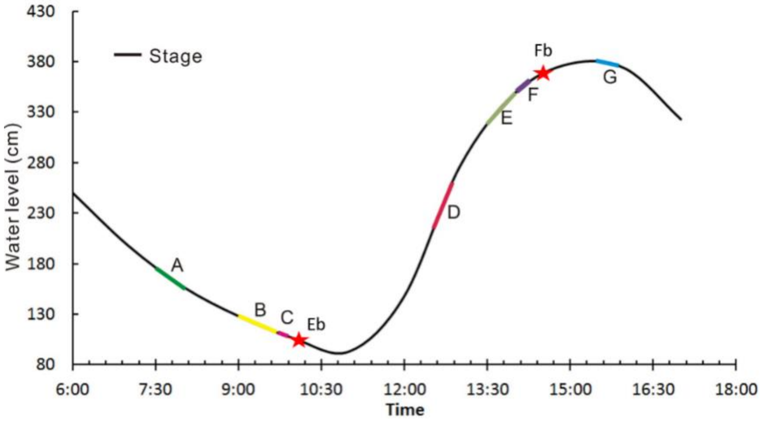

Figure 7-2. River stage at Changxing gauging station during the sampling period; survey periods are marked by letters A-G. The red stars indicate when bed surface sand samples were collected. Eb and Fb mean ebb and flood sample respectively.

Seven surveys were taken and each survey produced a continuous, overlapping streamwise transects, grouped into “Lower Falling Tide”, “Low Tide”, “Lower Rising Tide”, “Upper Rising Tide” and “High Tide” according to their location in the tidal cycle, to allow cross-cycle comparisons (Figure 7-2).

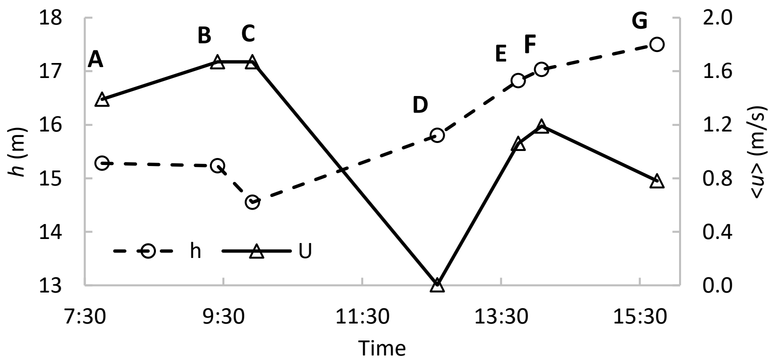

Figure 7-3. Mean water depths and transect-averaged current velocity along the transect line.

Table 7-1 summarizes spatially averaged flow velocity $<u>$ and flow depth $<h>$ along each transect (Figure 7-4). Measurements started from the Lower Falling stage (Transect A) with mean flow velocity 1.39 m/s, after then $<u>$ continued to accelerate during the falling tide (Transects B and C), both peaked at ~1.67 m/s. At the Lower Rising Tide (Transects D), $<u>$ reached the lowest value of 0.003 m/s, indicating the occurring of a slack tide. As the tide kept rising, <u> increased to 1.19 m/s at the Upper Rising stage

(Transect F). The discrepancy between tide and velocity cures suggests that variation of velocity lags behind that of the tide.

Table 7-1. Descriptive flow and suspended sediment statistics for each transect. Ebb tides were displayed by positive flow velocities. Horizontal resolution of flow data was calculated by v_{boat}/f_{aDcp}*, and* f_{aDcp} *is the sampling frequency of aDcp, ca 0.25 Hz.*

Tidal stage	Transect	v_{boat} (m/s)	<*u*> (m/s)	<*h*> (m)	Horizontal Resolution (m)
Lower Falling	A	1.07	1.39	15.3	5
Low	B	0.78	1.67	15.0	3.2
	C	2.65	1.67	14.6	12
Lower Rising	D	1.55	0.003	15.8	6
Upper Rising	E	1.21	-1.06	16.8	4
	F	2.4	-1.19	17.0	10
High	G	1.3	-0.78	17.5	5

As seven measurements were taken back and forth, some of them went against the current (e.g. A, B, E, and G) showing higher resolution which is less than 5 m in the horizontal direction. Experiment C and F were taken along with the tide show a lower resolution, higher than 10 m (Figure 7-2 and Table 7-1). TDR sampling frequency was set at 1 Hz, indicating that the horizontal resolution of bathymetry is nearly 2 m.

Besides, two bed surface samples were collected via a “cap” type sampler: one in the ebb tide and the other in flood tide (Figure 7-2). Moreover, a series (29 in total) of water samples across the water column were also taken via 600-ml glass bottles. They were further analysed in the laboratory at East China Normal University.

7.2.3. Bedform characteristics calculation

An open source MATLAB software, called bedform tracking tool proposed by *van der Mark and Blom* [2007] was employed here to assess bedform features. In this software, the subjective code has been avoided as much as possible, ensuring to be applicable to various data sets [*van der Mark et al.*, 2008]. Individual bedform height, H_i, were determined as elevation changes from troughs to downstream crests, respectively, while individual length, L_i, was calculated from the inter-crest distance. Finally, these individual values were averaged to compute the spatially averaged values (*H* and *L*).

7.2.4. Suspended sediment concentration evaluated with aDcp backscatter

During the past decade, acoustic backscatter intensity of aDcp is recognised as a surrogate approach to assessing suspended sediment concentration [*Sassi et al.*, 2012; *Latosinski et al.*, 2014]. However, this method is highly site-specific and seasonal dependence, as acoustic signal attenuation is sensitive to particle size, size distribution, shape mineralogy and concentration [*Topping et al.*, 2007; *Guerrero et al.*, 2013; *Guerrero*, 2014].

In this study, echo intensity (I_{dB}) recorded in counts, according to the calibration methodology developed by *Teledyne* [2007], was used to present the corrected results for only water absorption:

$$I_{dB} = C \cdot I_{counts} + 20log_{10}(R) + 2\alpha R - 10 \cdot log_{10}(\frac{L_{Xmit}}{cos\,\theta}) \qquad 7\text{-}1$$

where θ means beam angle (20°); L_{Xmit} is the transmit length; α indicates sound absorption coefficient; C, echo intensity scale (dB per RSSI count), equals to $127.3/(\mathrm{Te} + 273)$ where Te is the temperature (in °C). R is a function of r, L_{Xmit} and $\cos\theta$:

$$R = \frac{r + 0.5L_{Xmit}}{cos\,\theta} \qquad 7\text{-}2$$

where r presents the range from the transducer to the middle of the bin.

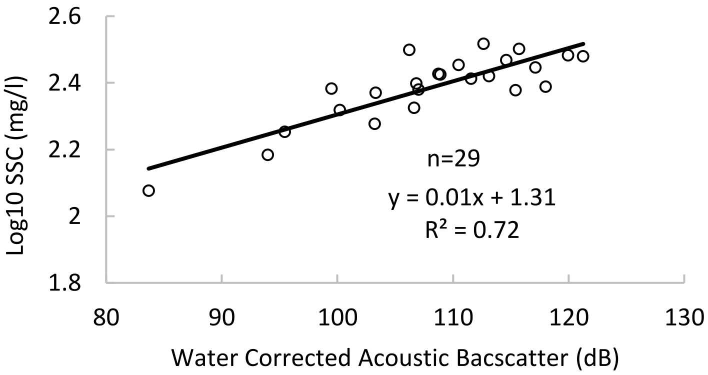

Figure 7-4. Correlation between suspended sediment concentration and water corrected acoustic backscatter.

Gartner [2004] proposed the best form of the relation between the concentrations and I_{dB} based on the equation for sound scattering from small particles:

$$log(SSC) = a + b \cdot I_{dB} \qquad 7\text{-}3$$

where a and b are regression-determined constants. Therefore, in order to convert the acoustic backscatter intensity into a concentration, measured sediment concentrations are needed. A series of bulk samples were taken through the water column and meanwhile acoustic backscatter was recorded. A total of 29 concurrent measurements of suspended sediment concentration were used to build the relationship with backscatter intensity (Figure 7-4).

7.2.5. Examination of hydro- and sediment- dynamics

Measured velocity by aDcps should be corrected by removing the boat speed (e.g. aDcp speed) referenced to the DGPS (v_{dgps}) and bottom tracking (v_{bt}), which both could be directly extracted from the software Winriver II [*Rennie*, 2002; *Muste et al.*, 2004]. In mobile bed, correcting velocity via bottom tracking may produce bias [*Rennie and Villard*, 2004], therefore, the DGPS was chosen as the reference. Afterwards, the zero net cross-stream discharge definition [*Paice*, 1990; *Lane et al.*, 2000] was adopted on Transect B to define the streamwise direction in low tide. The derived direction is about 120°, which is equal to the direction of the downstream survey line (Figure 7-1). Flow data of other transects were rotated and converted into this streamwise direction (see *Lane et al.* [2000] for a detailed explanation).

Additionally, spatially averaged streamwise velocity $\langle u \rangle$ and corrected backscatter $\langle I_{dB} \rangle$ values for entire flow fields were calculated as

$$\langle u \rangle = \frac{\sum_{x=1}^{n_x} \sum_{y=1}^{n_y} u}{n} \qquad 7\text{-}4$$

$$\langle I_{dB} \rangle = \frac{\sum_{x=1}^{n_x} \sum_{y=1}^{n_y} I_{dB}}{n} \qquad 7\text{-}5$$

where n_x is the number of horizontal planes, while n_y is the number of vertical planes; n is the total number of measurements along each transect, and u and I_{dB} are the at-a-point streamwise value. However, spatially averaged values reveal nothing about the structure over the dunes. *Bradley et al.* [2013] indicated that, as velocity generally increases logarithmically above the bed, two-dimensional plots of flow field over dunes can reveal little about the spatial flow structure, except acceleration over the stoss and deceleration over the lee (Figure 7-5), and calculating the deviation from $\langle u \rangle$ is a more effective approach to identify spatial patterns. Therefore, the deviation calculated by subtracting $\langle u \rangle$ were evaluated in this study:

$$u' = u - \langle u \rangle \qquad 7\text{-}6$$

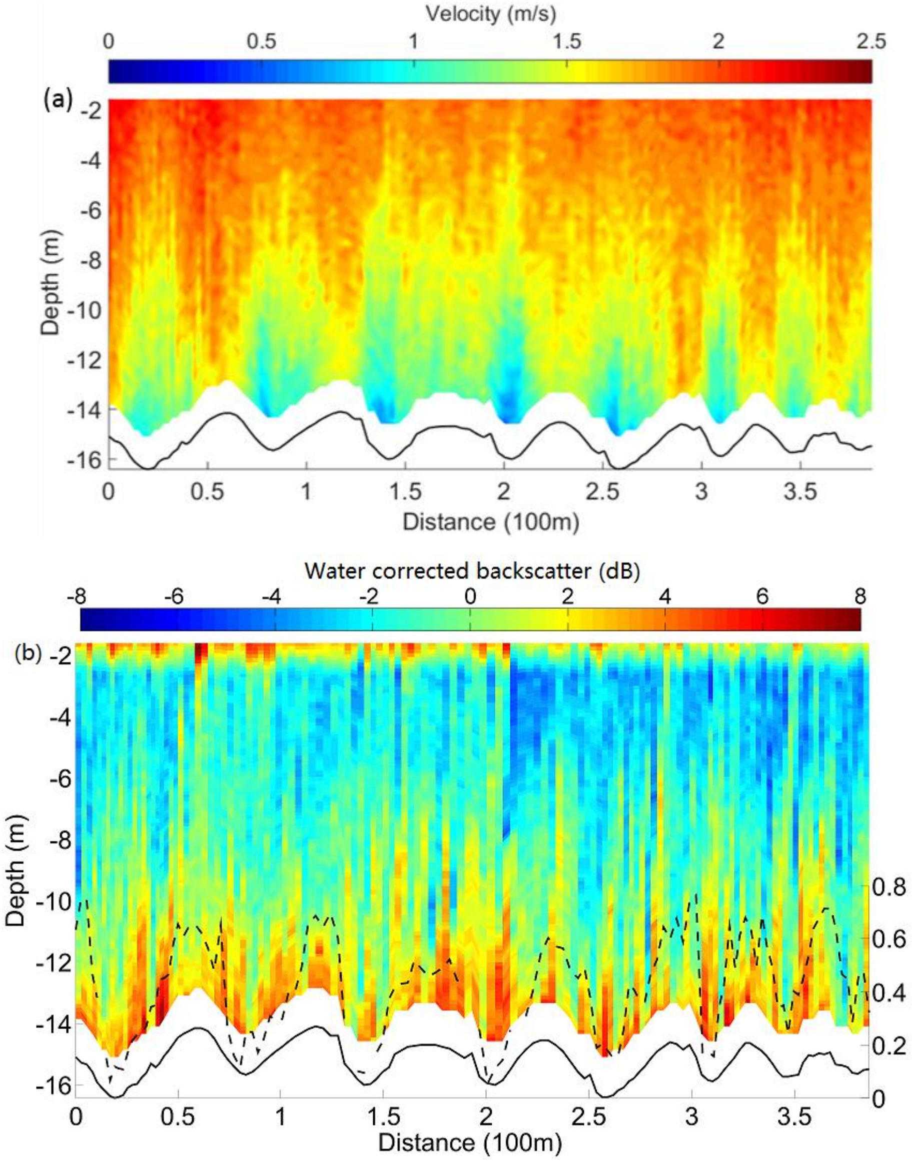

Figure 7-5. Flow (a) and deviation of water corrected backscatter distribution (b) over dunes of Survey b (the largest lee-side angle). The solid lines present the real morphology, while the dashed line in (b) indicates apparent bedload speed distribution.

7.2.6. Bedload transport speed

Rennie et al. [2002] firstly proposed that the function of aDcp, bottom track, can be used to estimate bedload transport rate in mobile bed, called apparent bed velocity (v_{bed}):

$$v_{bed} = v_{dgps} - v_{bt} \qquad 7\text{-}7$$

The accuracy of this method highly depends on the instrument itself, such as acoustic pulse length or instrument frequency, and the surrounding circumstance, such as bed material composition, but the distribution of apparent bed velocity over dunes here still could give us significant implications on near-bed sediment dynamics [*Latosinski et al.*, 2017].

7.2.7. Standardized method

Previous studies [*Best*, 1993; *Bradley et al.*, 2013] pointed out that flow structures, sediment transport and dune characteristics over dunes influence mutually in a sophisticated way. The result of Figure 7-5 verifies that the discrepancy of morphology and fluctuation near bottom between individual dunes results in assorted hydro- and sediment- dynamics patterns. In order to eliminate individual difference and obtain general flow and sediment dynamics over dunes, data (u', SSC and v_{bed}) over each individual dune was extracted, and the vertical and horizontal dimensions were normalised by water depth and dune length [*Bradley et al.*, 2013]. Afterwards, data over each dune was integrated to the same grid (50 × 50 in x and y axis) and then averaged to obtain the standardized results. Consequently, the standardized patterns were used for elaborating and analysing the mechanisms of dune evolution and migration.

7.2.8. Hydraulic roughness

In steady subcritical flow, the temporally averaged current velocity ideally displays a logarithmic profile above the bed, called the “Law of the Wall”:

$$u(z) = \frac{u_*}{\kappa} ln \frac{z}{z_0} \qquad 7\text{-}8$$

where $u(z)$ presents the time-averaged flow velocity at the height Z above the bed, and u_* is shear velocity, which can be used to calculate shear stress $\tau = \rho {u_*}^2$. κ is the von Kármán constant (0.4), and Z_0 is the roughness length (i.e. the height at which the follow velocity equals to zero).

In order to comprehend Z_0, equation (9) can be derived to the following form:

$$lnz_0 = lnz - \frac{u(z)}{u_*/\kappa} \qquad 7\text{-}9$$

However, the presence of bedforms divides the log-linear velocity profile into two parts: the lower layer, which was thought to be controlled by the friction associated with grain roughness, and the upper layer reflecting the total friction, i.e., the combined grain and bedform roughness (see figure 1 in *Lefebvre et al.* [2011b]). Moreover, when several size classes of bedforms were present (e.g., large dunes and superimposed ripples and small dunes), the presence of several log-linear segments was shown to reflect the friction induced by several scaled roughness elements [*Smith and McLean*, 1977; *Lefebvre et al.*, 2013a]. Notably, during the slack tide, the velocity profiles did not follow the log-linear principle, thus survey D was not used to test log-fits.

7.3. Results

As it is not easy to keep the survey line straight, the curve of track line may influence the accuracy of dune characteristics. In the following results and discussion section, the analysis was focused on a 280-meter long area, where the dunes are the largest ones along tracking lines and all of these seven track lines approximately overlapped each other and are relatively straight.

7.3.1. Bed material size

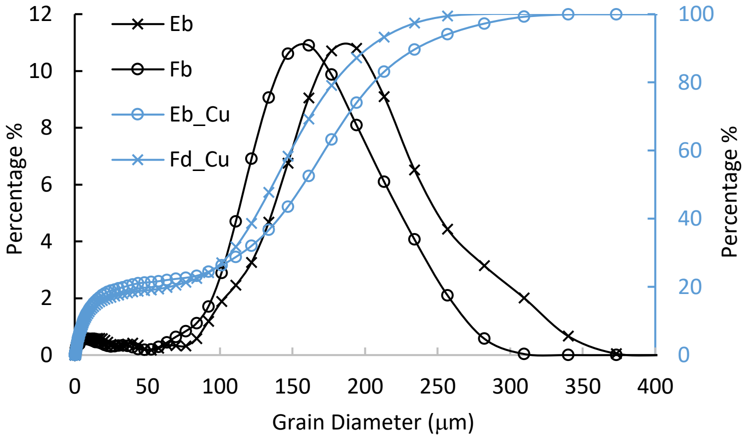

Figure 7-6. Distribution and cumulative distributions of grain size of bed materials for the Ebb tide (Eb) and Flood tide (Fd).

Distribution and cumulative curves of bed materials for both ebb and flood tide within the same tidal cycle were displayed in Figure 7-6. Bimodal patterns are observed, and the median grain size of the ebb tide is 157 μm which is 20 μm larger than that of the flood tide. Furthermore, bed mud (< 62.5 μm) and clay (< 8 μm) content does not change with the varying flow, which is ~20 and ~12% respectively. In contrast, part of the very fine sand (62.5~125 μm) and fine sand (125~250 μm) was suspended into the water column during ebb tide with high flow strength.

7.3.2. Dune Characteristics

There is no dune planform shape data in this research and few previous research on this in the Changjiang Estuary [*Shuwei et al.*, 2017]. However, for the majority part of the survey lines (except survey B and F), their lateral distance is less than 5 meters, and the computed dune lengths are relatively constant in line with previous research (e.g. [*Hendershot et al.*, 2016]). Therefore, we speculate that these bedform characteristics reasonably represent the dune geometry, except survey B and F whose results may slightly affect by the curvature of navigation line, and also variability in dune height along continuous crestlines might be considerable [*Parsons et al.*, 2005]. The results of survey B (e.g. height, lee-side, and stoss-side angle) showed a considerable discrepancy with that of survey C (Table 7-2). However, these two measurements were taken at a relatively close time, which means that the results should not have a remarkable difference. This discrepancy reflects that calculation of bedform features of survey B is most probably distorted by the curvature of the survey line.

Table 7-2. Averaged morphological characteristics of dunes along transects for each survey; the lee-side angle is calculated via the lower lee-side segment, while the stoss-side angle is calculated from trough to crest. The subscript std indicates the standard deviation for each parameter.

Survey	H (m)	H_{std}	L (m)	L_{std}	Hydraulic lee slop (°)	AL_{std}	Hydraulic stoss slope (°)	AS_{std}
A	1.5	0.22	45.2	3.8	6	1.2	3.8	0.5
B	1.5 (1~1.5)	0.3	53.9	4.5	9.9	3.2	3.3	0.6
C	1	0.25	44.3	8.5	3.1	0.3	3	0.4
D	1.3	0.32	44.5	8.2	5.4	1.2	3.9	0.57
E	1.3	0.25	46.7	3.5	2.8	1.2	4.8	0.4
F	1.3 (1.2~1.3)	0.42	60	7.7	2.6	1.1	3.2	0.6
G	1.2	0.2	44.9	4.1	2.9	1.5	4.7	0.4

Bedform length nearly kept constant (~45 m) within the tide. In contrast, bedform height decreased to the lowest (1 m) near low tide when flow velocity was the largest, and it increased to 1.3 m during the flood tide. Furthermore, the hydraulic lee-side slope was less than 10°, indicating that dunes are with low-angle (Table 7-2).

7.3.3. Flow and sediment dynamics

Although the lee-side angle of the individual dune is higher than 10° (Table 7-3), which can produce intermittent separated flow [*Paarlberg et al.*, 2009], there still no separated flow occurring during the surveys. Perhaps, the separated zone is located at the near bottom of the lee-side and trough where are limited to detect, because of the presence of blanking zone above the bottom caused by side-lobe effect. Besides, the diameter of the area that aDcp use to measure, ~11 m (water depth is nearly 15 m), is larger than the length of flow separation zone which is about 4 times of bedform height (i.e. 6 m) [*Unsworth*, 2015].

These patterns of flow (Figure 7-5) are similar to those documented in past studies of flow over angle-of-repose dunes [*Nelson et al.*, 1993; *Bennett and Best*, 1995; *McLean et al.*, 1996; *Parsons et al.*, 2005]. Therefore, although flow separation is not present in the lee side, their topographic forcing of flow (expansion flow) contributes to similar gross patterns of flow acceleration and deceleration [*Best and Kostaschuk*, 2002].

The flow data resolution (>10 m) of survey C and F, whose navigation direction is consistent with flow direction, is relatively low (Table 7-1), indicating that only 4~5 vertical profiles collected over each dune whose length is *ca* 50 m. The resolution is not high enough to support the detailed flow analysis, thus these two surveys were removed in the flowing further analysis.

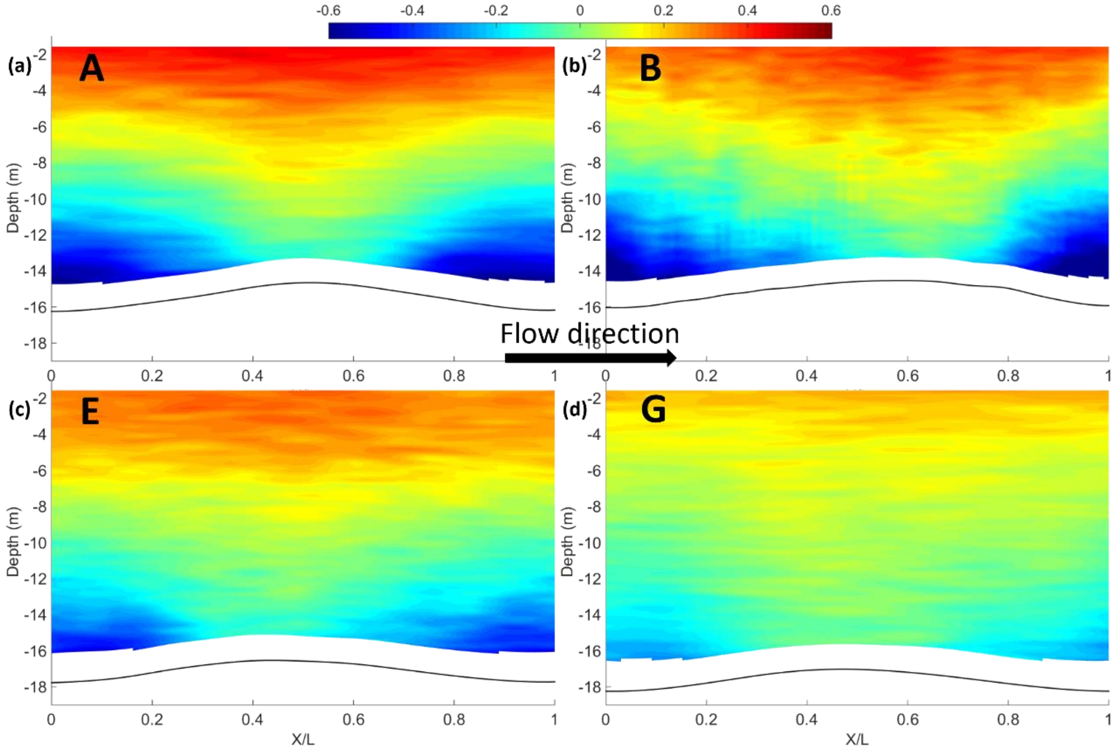

Figure 7-7. Standardized deviation of streamwise velocity from the mean velocity of the entire flow field: a) survey A, b) survey B, c) survey E and d) Survey G. Flow direction is from left to right, therefore, bedform profiles were reversed in c and d, i.e. lee-side for c and d becomes stoss-side. Unit of colour bar is m/s.

How standardized flow structure and sediment transport varied within a tidal cycle are displayed in Figure 7-7 and Figure 7-8. At lower falling tide stage, as dunes are quite symmetric, flow structure over dunes displays a relatively symmetric pattern (Figure 7-7a). In contrast, the distribution of suspended sediment concentration (especially near the bottom) and apparent bedload speed show opposite biased trends that concentration over stoss-side is relatively larger, while bedload speed over lee-side is greater (Figure 7-8). At low tide, flow velocity nearly reaches the maximum (Figure 7-3b) and the maximum near-bottom velocity inclines to downstream (Figure 7-7b). The suspended sediment is fully developed that large suspension develops to almost the whole water column over the entire bedform profile (Figure 7-8b). Moreover, high bedload speed extends to cover the whole bedform profile except the trough.

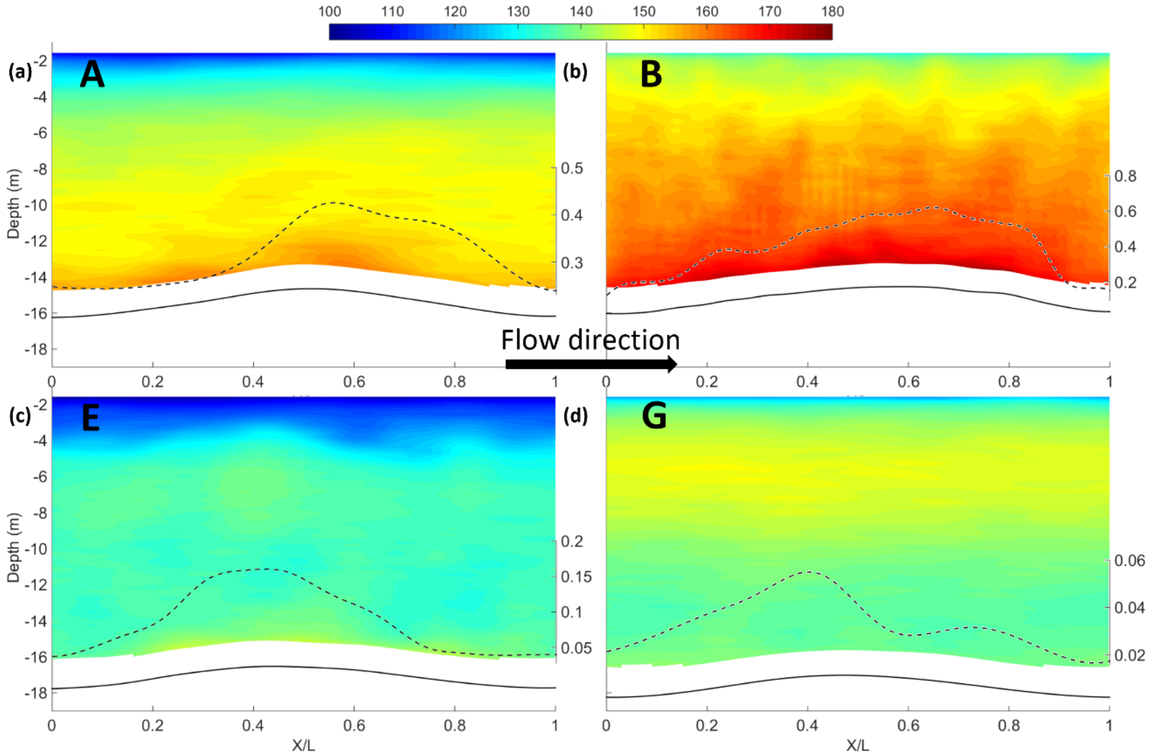

Figure 7-8. Standardized suspended sediment concentration and bedload transport speed distribution (the dashed lines): a) survey A, b) survey B, c) survey E and d) Survey G. Unit of the colour bar and the dotted line is mg/L and m/s. Note that the scale of bedload transport speed differs between subplots, in order to more clearly present their distribution over dunes.

During the upper rising stage, bedform profile is still slightly asymmetric, consistent with the bias of lower part of the flow field (Figure 7-7c) and both sediment concentration and bedload speed are much lower than those of ebb tide (Figure 7-8c). At the high tide, bedform profile evolves to become symmetric again, and lower part of flow field displays relatively small variations. Moreover, bedload speed (Figure 7-8d) drops to a very low level.

7.3.4. Spatially average velocity profile over each individual dune within every survey

According to Figure 7-5, it is obvious that there are considerable discrepancies in morphology characteristics among each individual dune, such as lee-side angle and height, especially during the ebb tide. Therefore, both of morphology characteristics of each individual dune within survey A, B, E and G (these four surveys are with higher resolution) and corresponding shear stress and roughness length were calculated via the Law of the Wall (see Table 7-3 and Table 7-4).

The roughness length calculated from the upper part of spatially averaged velocity profiles over each individual dune presents the total roughness length, i.e. the sum of skin friction, form resistance from the superimposed and primary dunes [*Villard and Kostaschuk*, 1998]. The grain roughness, derived from the lower part of the velocity profile was ignored, because it is generally more than one order smaller compared to the bedform roughness, and the lower part of velocity obtained from aDcp is not sufficiently close to the bed to estimate skin friction [*Villard and Kostaschuk*, 1998].

Table 7-3. Summary of the individual dunes during the rising stage of the ebb tide.

Ordinal	A				B			
	Lee-side angle (°)	Stoss-side angle (°)	τ (N/m^2)	Z_0 (m)	Lee-side angle (°)	Stoss-side angle (°)	τ (N/m^2)	Z_0 (m)
1	7	4.6	32.4	0.27	5.1	3.4	22.5	0.06
2	7	3.3	28.9	0.21	15	2.7	25.6	0.12
3	6.9	3.8	25.6	0.2	11.9	2.5	22.5	0.13
4	6.8	4.2	25.6	0.18	10.7	3.9	22.5	0.08
5	3.9	3.6	25.6	0.2	10.7	3.3	16.9	0.05
6	4.6	3.1	28.9	0.26	6	4.1	16.9	0.04

There is no obvious, general rule for the whole tide. But during the rising stage of ebb tide (from survey A to survey B, Table 7-3), with increasing velocity, both the shear stress τ and roughness length Z_0 display a descending trend from 0.22 to 0.08 m and from 28 to 21 N/m^2. In contrast, during the flood tide (Table 7-4), both τ and Z_0 show the same decrease trend from 0.29 to 0.19 and from 20 to 7.3 N/m^2, while velocity increases. The statistical error were on average 11% for roughness length, and 8% for shear stress with little variation [Wilkinson, 1983]. Besides, the hydraulic lee-side gets steeper with an increase in velocity and the hydraulic stoss-side slopes gentler in either ebb or flood tide.

Table 7-4. Summary of the individual dunes during flood tide; the lee-side and stoss-side are ebb lee-side and stoss-side respectively.

Ordinal	E				G			
	Lee-side angle (°)	Stoss-side angle (°)	τ (N/m^2)	Z_0 (m)	Lee-side angle (°)	Stoss-side angle (°)	τ (N/m^2)	Z_0 (m)
1	7.3	3.0	12.9	0.13	6.8	3.1	7.3	0.16
2	5.2	3.1	16.4	0.20	5.5	3.5	7.5	0.18
3	4.6	3.1	26.4	0.44	3.4	3.3	9.1	0.29
4	4.6	3.1	24.4	0.38	4.0	2.9	5.9	0.14
5	3.2	2.0	24.8	0.39	2.5	2.2	7.0	0.20
6	4.3	2.5	17.1	0.20	6.0	2.6	7.1	0.17

7.3.4.1. Velocity profile over different sections of dunes

Some research [*Kostaschuk and Villard*, 1996; *Best and Kostaschuk*, 2002; *Best et al.*, 2004] has pointed out that the velocity profile showed different patterns over different positions of dunes (e.g. lee-side, trough and crest). Therefore, in order to detail the velocity profile, a single dune is divided into 6 sections (Figure 7-9a): lower and upper flood lee-side (ebb stoss-side), crest, lower and upper ebb lee-side (flood stoss-side) and trough. The flow velocities above six successive dunes (Table 7-3 and Table 7-4) within the same survey at the six respective positions were averaged, and roughness length and shear stress of upper segments were calculated via Law of the Wall (Figure 7-9b and c). As these dunes are classified as symmetric, low-angle dunes, the delicate difference between downstream lee-side and stoss-side should result in a subtle impact on velocity pattern.

Obviously, roughness length of all of these surveys displayed a similar trend: there is a significant decrease over the upper stoss-side and that the magnitude of the decrease varies between surveys (Figure 7-9b). Over the dune lee-side, there are fewer differences between surveys. Moreover, there is also a decrease above the upper lee-side but less extent compared with that above the stoss-side. Shear stress shows less pronounced differences between the lee- and stoss-sides, and lowest shear stress occurs during survey G (Figure 7-9c). However, survey B is clearly a little different that higher roughness and shear stress were observed above the lee-side, corresponding to the flow structure bias (Figure 7-7b).

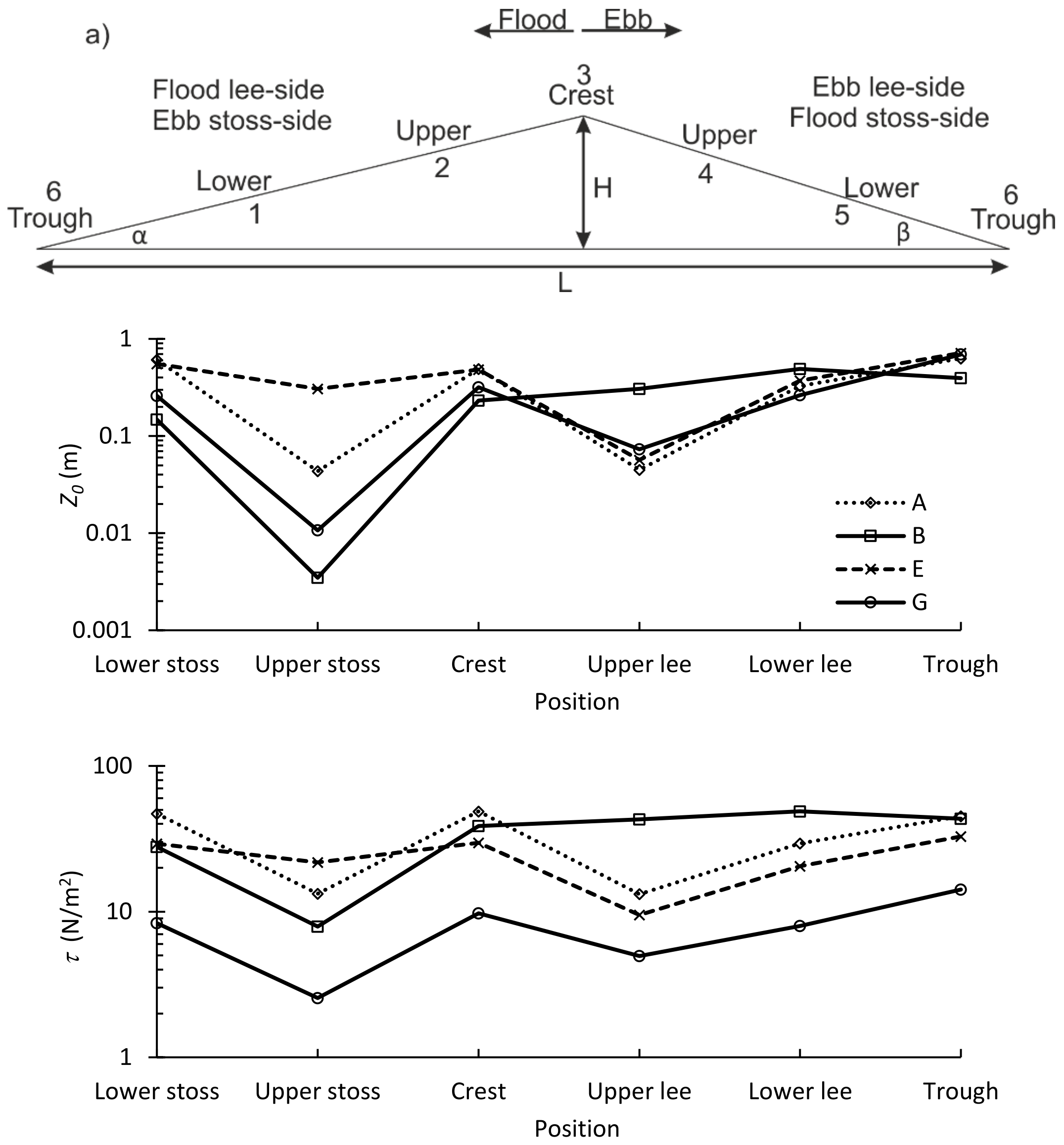

Figure 7-9. Roughness length Z_0 (b) and total shear stress τ (c) of the upper segments calculated from different positions (a) of a dune.

7.3.4.2. Measured roughness length compared with predicted results

Previous scholars have concluded several equations to calculate roughness length or shear stress related to grain size [*Morvan et al.*, 2008; *Ferguson*, 2013], bedforms [*Van Rijn*, 1984b; *Soulsby*, 1997; *Bartholdy et al.*, 2010b], vegetation [*Kadlec*, 1990; *Nepf et al.*, 2007; *Luhar et al.*, 2008]. Roughness lengths related to bedforms predicted by the equations of *Soulsby* [1997], *Van Rijn* [1984b], and *Bartholdy et al.* [2010b] (Table 7-5) were calculated via bedform dimension.

Table 7-5. Dune roughness predictors.

Authors	Equation
Soulsby [1997]	$Z_0 = H^2/\mathrm{L}$
Van Rijn [1984b]	$Z_0 = 0.04H(1 - e^{-25H/L})$, $0.01<H/L<0.2$
Bartholdy et al. [2010b]	$Z_0 = 0.0019H$

From Figure 7-10, both the variation of Van rijn and Bartholdy showed a similar trend – underpredicting roughness length. Roughness lengths predicted via Van rijn are slightly higher than those of Bartholdy, although the equation of Van rijn relates to both bedform height and length, while that of Bartholdy just includes height. The method of Soulsby seems to be the best predictor, as it shows a high positive relationship between 0 and 0.2 m. Furthermore, none of these three equations seems to be able to reasonably predict roughness length when Z_0 calculated via Law of the Wall is larger than 0.25 m.

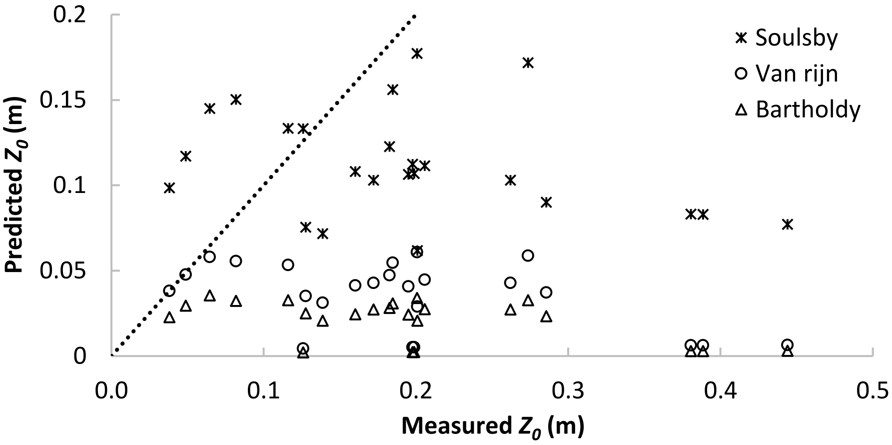

Figure 7-10. Roughness lengths (Z_0) measured from spatially averaged velocity profiles (from upper part) compared with those calculated from Soulsby [1997], Van Rijn [1984b], and Bartholdy et al. [2010b] for the primary bedforms. The dotted line presents the 1:1 line.

7.3.4.3. Shear stress estimates from quadratic stress models

The shear stress models of *Van Rijn* [1984b], and *Yalin* [2015] were used to estimate form stress and skin friction. Both of these two models rely primarily on the quadratic stress equation:

$$\tau = \rho C_D U^2 \qquad 7\text{-}10$$

where C_D is drag coefficient and U presents spatially averaged mean velocity over the entire dune. The van Rijn and Yalin models use forms of the Chezy coefficient to estimate skin friction and form stress:

$$\tau = (\tau)_f + (\tau)_\Delta = \rho U^2/{c_f}^2 + \rho U^2/{c_\Delta}^2 \qquad 7\text{-}11$$

where $c_f = U/u_* = 2.5\ln(11\,h/k_{sg})$ is pure friction of dimensionless Chezy friction factor, k_{sg} is granular roughness, c_Δ is form-drag components of dimensionless Chezy friction factor. For *Yalin* [2015], k_{sg} equals to $2D_{50}$ and $\frac{1}{{c_\Delta}^2} = \frac{1}{2}(\frac{H}{L})^2\frac{L}{h}$, while for *Van*

Rijn [1984b], $k_{sg} = 3D_{90}$ and $k_{sb} = 1.1\Delta(1 - e^{-25H/L})$.

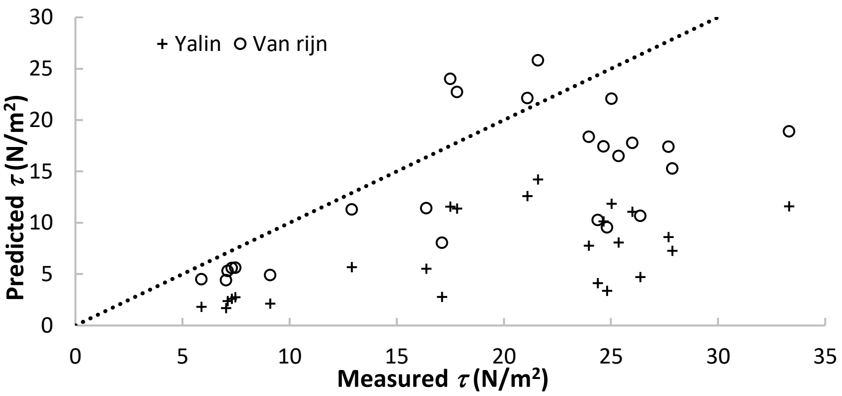

Figure 7-11. Mean Estimated and Predicted total Shear Stresses (N/m^2). The dotted line presents the 1:1 line.

From Figure 7-11, all of the values are concentrated between 5 and 35 N/m^2, which shows the same magnitude with the result of *Kostaschuk et al.* [2004]. Van rijn seems to predict better than Yalin, while Yalin shows an underestimated trend, compared with total shear stress assessed from velocity profiles.

7.4. Discussion

When significant sand transport occurs as bedload, asymmetric dunes generate, whereas symmetric, low-angle dunes develop when most sediment transport is in suspension [*Smith and McLean*, 1977; *Kostaschuk and Villard*, 1996]. Dunes in Changjiang estuary, where sediment transport is dominated by suspended sediment, confirms the latter situation. Furthermore, previous research [*Schindler et al.*, 2015; *Baas et al.*, 2016] has found that the effect of physical cohesion imparted by cohesive clay within mixed sand-mud substrates significantly influences the generation, migration, and dimension of bedforms. *Schindler et al.* [2015] established the inversely linear correlation between clay content and bedform dimensions (bedform height and aspect ratio) based on a series of controlled laboratory experiments. The aspect ratio of bedform in this study varies between 0.02~0.03, consistent with their finding that when clay content is 10~12 %, the aspect ratio is 0.03~0.02. Therefore, both high clay content and significant suspended sediment attribute to the generation of low-angle dunes in the Changjiang Estuary, and the following discussion is conducted based on low-angle dunes.

7.4.1. How does roughness length Z_0 respond to tides?

For flow over bedforms in tidally influenced areas, it is commonly recognised that, in the ebb-dominated area, Z_0 (derived from the upper segment) at a site can take two values, one pertaining to ebb, which is an order of magnitude larger than the one pertaining to flood [*Kostaschuk and Villard*, 1996; *Hoitink et al.*, 2009; *Lefebvre et al.*, 2011b]. That is because, in tidal environments, the primary bedforms usually remain oriented with the direction of dominant flow, while superimposed bedforms may reverse their direction [*Ernstsen et al.*, 2006b]. Moreover, *Lefebvre et al.* [2011b] and *Lefebvre et al.* [2013a] conjectured that the flow separation and recirculation presumably solely occurred over lee-side of dunes whose downstream slope is above 10° during the ebb, leading to the creation of form drag, while the secondary bedforms dominated the Z_0 during the flood. However, dunes in this study is with low-angle, and there were no secondary bedforms developed over primary dunes [*Shuwei et al.*, 2017]. The downstream slope of the LAD is too gentle to generate significant expansion loss during ebb or flood, thereby, hydraulic roughness associated with the bedforms will be weakened [*Hoitink et al.*, 2009; *Paarlberg et al.*, 2010; *Lefebvre et al.*, 2011b]. *Hoitink et al.* [2009] concluded that, for a given bottom topography, Z_0 is generally considered to be independent of velocity magnitude but related to the orientation of the flow. In tidal environments, flow is inevitably unsteady, resulting in persistent and concomitant alteration of bedform dimension [*Ernstsen et al.*, 2006b], thereby, Z_0 varies at different tidal stages [*Cheng et al.*, 1999]. However, the symmetry of dune geometry is highly related to different influence of ebb and flood on flows: for HADs (ebb-orientated), flow structures between ebb and flood tides are relatively different, resulting in the great differences between roughness lengths [*Lefebvre et al.*, 2013a; *Kwoll et al.*, 2016]. However, for symmetric, low-angle dunes in this study, flow structures between ebb and flood tides are very similar (Figure 7-7), resulting in little variation of Z_0 between flood and ebb tides (Table 7-3 and Table 7-4).

Furthermore, flow unsteadiness may contribute to departures from the log-linear velocity profile [*Dyer*, 1986]. For accelerating flow, the shear stress and roughness length may be subdued, while during the decelerating tide, they could be amplified [*Lefebvre et al.*, 2011b]. However, there is not enough evidence to contribute this effect to flow unsteadiness, because roughness length estimation can be also influenced by other impacts, such as suspended sediment concentration [*McLean*, 1992], and bedform evolution [*Lefebvre et al.*, 2011b; *van der Zanden et al.*, 2017].

The fine sediments (most likely the very fine sand according to Figure 7-6) are suspended by greater velocities with higher flow strength, thereby the higher suspended sediment near the bottom and deformation of bedforms alter the flow structure, i.e. shear stress and flow roughness. Moreover, the result of velocity profiles over different sections reflects that variability of individual bedform characteristics (e.g. lee-side angle) plays an important role in roughness length variations [*van der Mark et al.*, 2008].

7.4.2. What are the characteristics of τ over low-angle dunes?

It is commonly recognised that total shear stress can be accurately derived from the depth-slope product. However, it is often difficult to measure, especially in large rivers and estuaries [*Villard and Kostaschuk*, 1998], and this method is only appropriate for reach-averaged shear stress estimation. When it occurs to assess shear stress over dunes, it becomes unreliable due to the non-uniformity of flow [*Hoitink and Hoekstra*, 2005; *Sime et al.*, 2007]. Therefore, the quadratic method and velocity gradient were used to estimate total shear stress [*Schlichting et al.*, 1960; *Biron et al.*, 2004].

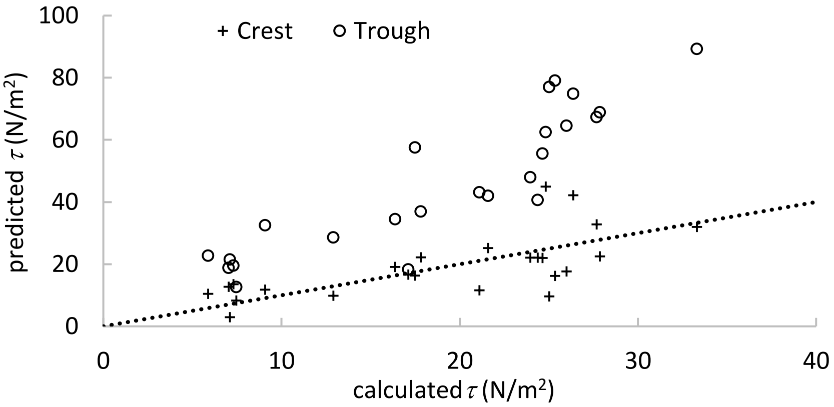

Figure 7-12. Total shear stress calculated over crest and trough compares with that predicted via spatial averages. The X-axis presents spatial averages, and the Y-axis presents crest and trough. The dotted line presents the 1:1 line.

McLean et al. [1999a] concluded that, in terms of shear stress estimation, the technique of spatial averaging is better than the method using velocity profiles, but it is still not as accurate as necessary. Estimation from local velocity profiles over the trough overpredicts total shear stress, while that from the crest fits well with the result of spatial averaging (Figure 7-12). It indicates that although the accuracy of the technique of spatial averaging is relevant to bedform characteristics (lee-side angle), flow separation and flow strength [*Lefebvre et al.*, 2016; *Lefebvre and Winter*, 2016a; *Kwoll et al.*, 2017], as for low-angle dunes, shear stress over the crest can roughly represent total stress of spatially averaged.

7.4.3. How do bedforms evolve with changing flows within a tidal cycle?

Previous research [*Allen*, 1976; *Hendershot et al.*, 2016] has concluded that dune height responds more rapidly with the variation of flow than dune length which changes very little during a tidal cycle. Herein, in this research, bedform characteristics were tracking via the Thermal Depth Recorder, therefore, the accuracy of the statistics highly depends on the accuracy of tracking lines, i.e. some of the variability is probably caused by the deviations in the positions of survey lines [*Kostaschuk and Best*, 2005]. It is hard to investigate the accurate relationship from bedform features here, but the relatively large variation of dune height and little change of wavelength are still consistent with previous findings.

Sediment deposition and erosion over the tidal cycle lead to the changes of bedform characteristics [*Hendershot et al.*, 2016], and the formation of suspension events over low-angle dunes could dominate sediment transport, reaching 70% of the total sediment carried in 50% of the flow [*Bradley et al.*, 2013]. Due to the lack of accurate result of bedform dimension, how low-angle dunes in the lower Changjiang Estuary evolve over the tidal cycle were illustrated in the following based on flow structure, sediment transport and bedform shape (Figure 7-7, Figure 7-8 and Figure 7-9).

At lower falling tide stage, according to the ratios of dimensionless shields stress to critical shear stress (τ_*/τ_{*cr}) [*Venditti et al.*, 2016] and shear velocity to settling velocity (u_*/w_s, i.e. suspension threshold) [*Bagnold*, 1966; *Ferguson and Church*, 2004], suspended sediment transport, dominates the total sediment transport, as values of τ_*/τ_{*cr} are much larger than 33, and value of u_*/w_s is always greater than 1 [*Church*, 2006; *Yalin*, 2015]. Thereby, sediment erosion on the stoss-sides and deposition on the lee-sides lead to the deformation of bedform shape (Figure 7-7a). After hours of ebb flow, at low tide, sediment on the crest was eroded, and it leads to the decrease of bedform height (Table 7-2), verifying by the relatively high bedload speed over the crest. Moreover, the suspended sediment concentration increased with flow velocity, and part of them deposited on the trough, leading to the further reduction of dune height [*Kostaschuk and Best*, 2005; *Bradley et al.*, 2013].

The discrepancy of grain size distribution between flood and ebb tide (Figure 7-6) reflects that part of fine sand was resuspended into the water at high flow strength and redeposited at low strength. Thus, some of the suspended sediment deposited over the bedform at low flows during the lower rising stage, which is not captured in this investigation. During the upper rising stage, bedload speed over flood stoss-side is larger than that over flood lee-side, indicating that the loosely structured deposits are more likely to deposit on the ebb lee-sides (flood stoss-sides) and troughs (Figure 7-8c). Moreover, they are easier to be entrained (resuspended) again into the flows [*Kostaschuk and Best*, 2005; *Hendershot et al.*, 2016], reflected by the larger shear stress over flood stoss-side (Figure 7-9c). Furthermore, the movement of these loose deposits is more likely to stay on near the bottom area, as it is not detected in Figure 7-8c. At the high tide, interactions between flow and sediment are negligible and have little effect on sediment exchange between bedload and suspended sediment, thereby bedform evolution.

However, the upper part of suspended sediment concentration in survey G displays slightly larger than concentration near the bottom (Figure 7-8d). That occurred probably due to the common dredging events in the Deep Water Channel located at the downstream of the study area (nearly 10 km). This phenomenon is particularly significant during summers. Some high-SSC water column was dumped into water surface near the dredging boats and was transported upstream during the flood tide stages, resulting in higher values of sediment concentration in the upper parts. As a result, there would also be a somewhat stochastic effect on dune evolution.

7.4.4. How does dune geometry vary with changing flow?

It is widely recognised that an anticlockwise hysteresis correlation exists between dune height (*H*), aspect ratio (*H/L*) and mean flow velocity (<*u*>) [*Gabel*, 1993; *Dalrymple and Rhodes*, 1995; *Julien et al.*, 2002; *Wilbers and Ten Brinke*, 2003; *Hendershot et al.*, 2016], while in this study, clockwise hysteresis loops are found (Figure 7-13), consistent with few studies (e.g. *Kostaschuk and Best* [2005]).

Dune length changes little during a tidal cycle, while the variation of dune height responses directly to changes in velocity [*Allen*, 1976]. Therefore, the variation of dune height dominates the direction of loops [*Kostaschuk and Best*, 2005]. Previous studies observed that mean dune geometry lags behind the changing flows in a sandy bed [*Wilbers*, 2004; *Hendershot et al.*, 2016]. Those conclusions were made under subcritical conditions when sediment transport over sandy dunes is bedload dominated [*Berg*, 1987] and dune dimension is proportional to flow strength [*Allen*, 2009]. However, in the Changjiang Estuary, especially during the flood season with relatively stronger flow strength, both transformation and migration of dunes are suspended load dominated. As a consequence, the contribution of suspended load to migrating dunes is considerable [*Naqshband et al.*, 2014c]. During the lower falling tide with high flow velocity, fine sand on the upper part of dunes (the crest and upper lee-side and stoss-side) was eroded, and smallest bedload speed leads to the deposition on the trough, resulting in the decrease of bedform height at high flow velocity. During the rising tide, the erosion of loosely structured sediment on the trough and deposition on the crest leads to the slight increase of bedform height. Thereby, the combination of suspended sediment transport and bedload transport on dune transformation and migration attributes to the clockwise hysteresis. The specific sediment composition of the riverbed, in some extent, affects the mechanism of sediment transport related to the exchange between suspended sediment and riverbed, but further investigation is needed to figure out the mechanism behind this for extended series of tides, such as spring/neap tide and tides in flooding and dry season.

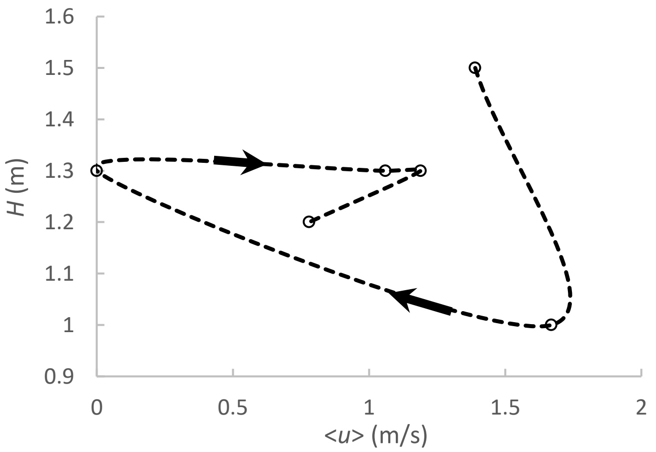

Figure 7-13. Phase diagram of mean dune height (H) with mean flow velocity (<u>).

7.5. Conclusions

The morphological changes and flow and sediment dynamics over a field *ca* 1.8 km long area during the moderate tide of flood season were examined in a tidal reach of the Changjiang Estuary, China. The dunes composed of fine sediment displayed a relatively symmetric geometry and low-angle lee-sides. Bedform development mechanisms coupled with flow and sediment transport were discussed, and the findings are summarized as follows:

1. Roughness length derived from the law of the wall changes little with the flow reversing, i.e. displaying the same level in both the ebb and flood tide, as dunes are relatively symmetric. The result of velocity profiles over different sections reflects that the variability of individual bedform features plays an important role in roughness length variation.
2. Shear stress over the crest of low-angle dunes could roughly represent total stress from spatially averaged over dunes in this study area, which has significant implications for advancing numerical models.
3. During the falling tide, as suspended sediment transport dominates the total sediment transport, the stoss-sides are eroded and sediment deposits on the lee-sides and troughs, resulting in the transformation of dunes.
4. During the rising tide, the loosely structured deposits on the flood stoss-sides are easier to be entrained/resuspended again into the flows but migrate near the bottom. Moreover, relatively higher SSC near the surface was observed, and this may attribute to frequent dredging events in the Deep Water Channel. As a consequence, there would also be a somewhat stochastic effect on dune evolution.
5. Clockwise hysteresis loops are found between dune height, aspect ratio and mean flow velocity. The combination of suspended sediment transport and bedload transport on dune transformation and migration attributes to the clockwise hysteresis. The specific sediment composition of the riverbed, in some extent, affects the mechanism of sediment transport related to the exchange between suspended sediment and riverbed, but further investigation is needed to figure out the mechanism behind this for extended series of tides, such as spring/neap tide and tides in flooding and dry season.

The results elaborate the evolution process of low-angle dunes within a tidal cycle and highlight the complex connections between flows, sediment transport and topography trough time in the tidally influenced area composed of fine sediment. This study also emphasises the need for more detailed data on accurate sediment transport and topography, in order to quantify the effect of suspended sediment on dune transformation and migration.

CHAPTER 8

8. Synthesis

This study sought to address two main research questions: *how do dunes adapt to different changing flows (floods and tides), and how does the coupled sediment transport affect dune morphology and dynamics*?

Large-scale flume experiments were conducted to simulate sand dune dynamics during carefully controlled floods with various hydrographs. The experimental research allows us to fully understand kinematics of sand dunes by imposing different flow conditions and by monitoring bed morphology, and flow- and sediment- dynamics simultaneously. Additionally, field surveys were undertaken in both the middle reach, close to the backwater zone, and within the estuary of the Changjiang (Yangtze) River whose bed contains clay, in order to examine the combined effect of the flood and tide and sticky staff on dune evolution. The combination of laboratory and field investigation gives us a whole view on dune dynamics from unidirectional fluvial rivers to bidirectional tidal areas.

8.1. Conclusions

8.1.1. Dune dynamics in unidirectional flows

The redistribution of sediment over and among dunes induced by multiple but simultaneous processes, including sediment suspension, deposition, resuspension and bypass, resulting in dune merging, splitting, bypass, etc., drives the kinematics of sand dunes [*Reesink et al.*, 2018].

Reesink et al. [2018] illustrated that water depth and flow velocity have separate effects on sediment redistribution, and further the effect of changes on morphological responses was analyzed: (1) an increase in depth and velocity more easily leads to bedform superimposition, (2) the decrease in flow depth would flatten dunes, and (3) the increase in flow velocity increases the potential for trough scour. However, in this study, sediment transport mechanism in local position is proved to be the dominated factor, which is controlling dune dynamics. Dune dynamics under bedload dominated condition (BLD), mixed-load dominated condition (MXD) and suspended sediment dominated condition (SSD) respond differently to changes in hydraulic condition.

Furthermore, systematic sediment supply is proved to be another important factor affecting dune adaptation. The change of flow discharge in a fluvial river inevitably bring net degradation or aggradation of the dune area [*Villard and Church*, 2005], as the generation and disappear of dunes are recognized to be highly related to bed erosion or deposition [*Cheng et al.*, 2001; *Cheng et al.*, 2004]. Dunes normally generate as a cluster only in a certain reach of the bed, rather than all over the riverbed. Thus, from upstream to downstream of the chain of dunes, the condition is developed from becoming adequate to generate dunes, to equilibrium condition (where flow-form feedback processes are expected to gradually dissipate), and finally to be inadequate to generate dunes (dune vanishing). It proves that dunes are not spatially homogenous, even in the same chain of dunes, under steady flows, and they are controlled by the local interaction between flow, sediment transport and bed morphology. Furthermore, if unsteady flow is added, the imposed effect of variation on flow and sediment transport along the whole dune area is different. The adaptation of dunes in downstream depends more on that in upstream, because the development of dunes in upstream would affect the sediment supply for downstream. Therefore, two separate types of the variation of sediment supply would affect dune adaptation under changing flows, which should be carefully considered in dune dynamics research: (1) the systematic sediment supply change, which leads to the net degradation or aggradation, attributes to the change of hydraulic condition and (2) the sediment supply change related to dune development in upstream.

Additionally, one of the keys to accurately predict dune adaptation is quantifying the proportion of sediment transport related to dune translation and deformation. It has been revealed, in this study, the increase of transport stage results in the increase of the fluxes attribute to both dune translation and deformation, but the deformation fraction (the ratio of the deformation flux to the total bed material flux) declines when bed condition transits from BLD to MXD, moreover, the net bed degradation/aggradation leads to the enhancement of the calculation on dune deformation (i.e. increase of deformation fraction).

Thus, in order to quickly predict sand dune adaption under changing hydraulic condition in unidirectional flows, the impact factors are recommended to consider under the following order:

1. Systemic sediment supply change.
2. Hydraulic condition change;
3. Sediment transport mechanism change;

Dune adaptation in different hydraulic condition changes was classified (Figure 8-1). Under net aggradation with hydraulic condition increasing, dunes grow via merging. In cases when the bed is always under BLD (Figure 8-1a), the larger dunes paly a dominate role on controlling dune adaptation. It is because the larger dunes with larger flow resistance obstruct sediment transport and affect sediment supply for downstream. Moreover, their development also controls the three dimensionalities of dunes. However, in cases when sediment transport mechanism changes from BLD to MXD/SSD (Figure 8-1b), as flow strength is normally larger, sediment supply from upstream is more. Sediment accumulates quickly in the upstream, leading to the quick increase of local elevation, and even a bar generates. The new generated bar, acting like a boundary, dominates the dune development in downstream and upstream.

Under net degradation with hydraulic condition increasing, dunes are more regular and two dimensional. Sediment supply is less than sediment that transports out of the dune area. When the bed is always bedload dominated (Figure 8-1c), dunes grow via merging and bed elevation slightly decreases, while in cases when sediment transport mechanism changes from BLD to MXD/SSD (Figure 8-1d), dunes grow via trough scouring with quick bed elevation declining.

Under net degradation with hydraulic condition decreasing, dune adaption significantly depends on dune length. In cases when the bed is always under bedload dominated (Figure 8-1e), dunes in the upstream decay more quickly dune size, thereby dune size decreases from the upstream to downstream. Moreover, bedform superimposition frequently occurs, especially when flow condition decreases fast. However, in cases when sediment transport mechanism changes from MXD/SSD to BLD (Figure 8-1f), dunes decay via crest flatten. It is because, the length of dunes generating under MXD/SSD is smaller, therefore, bedform length would not be the main factor affecting bedform adaptation.

The schematic diagram provides a fully summary on how dunes develop under different hydraulic condition changes, and it could help improve the accuracy of numerical modelling, especially for large scale simulations where dunes exist.

8.1.2. Low-angle dune dynamics in a tidal influenced area

Growing evidence from field observations suggests that symmetrical dunes, existing where are suspended sediment dominated, with smaller lee-side angles (i.e. low-angle dunes, generally less than 10° [Paarlberg et al., 2009]) are the prominent bedforms in tidally influenced areas, with beds consisting of fine particle size under lower flow regime conditions [Kostaschuk and Villard, 1996; Kostaschuk and Villard, 1999; Best and Kostaschuk, 2002; Best et al., 2004; Best, 2005a; Bradley et al., 2013; Venditti, 2013; Hendershot, 2014; Hendershot et al., 2016]. The effect of cohesive material (mud, clay and microorganisms, i.e. cohesive bed) on bedform geometry and dynamics is revealed to be one of the most important factors controlling dune size and shape [Malarkey et al., 2015; Schindler et al., 2015; Baas et al., 2016]. Therefore, advancing our understanding of the interactions is the key to improving our ability to accurately predict the evolution of bedform [Parsons and Best, 2013].

Surveys, herein, undertaken in Changjiang Estuary, confirm that clay content is a first-order control on bedform aspect ratio. Therefore, it could be a useful index to determine dune development. In the middle reach, close to the backwater zone, bedform superimposition were discovered in the falling limb of the hydrograph when bed is under aggradation condition. This result is consistent with superimposition occurrence in the flume experiments. Moreover, the primary dunes are the relicts of large dunes generated during the earlier freshet flows, while the secondary bedforms are spring-neap tide controlled. After the vanishing of the primary dunes by the migration of secondary dunes, the existing non-superimposed dunes are still spring-neap tide controlled. Across the channel, dunes in deeper water respond more quickly to the changing flows, as sediment transport is more significantly there, explaining the development of 3D dunes.

Previous research observed that the dimension of secondary bedform increases from the trough to crest of primary large dunes [Harbor, 1998; Wilbers, 2004; Parsons et al., 2005; Ernstsen et al., 2006a; Winter et al., 2008], and they attribute this to flow depth change with different position over the surface of primary bedforms [Jackson, 1975]. Bedforms with smaller size move faster [Best, 2005a; Venditti et al., 2005a; Venditti, 2013], resulting in bedform amalgamation (e.g. larger secondary bedforms) in the upper stoss of primary high-angle bedforms. However, the distribution of superimposed small dunes in this study displays a reverse trend (Figure 5-23). The unique distribution of the superimposed secondary dunes will result in a distinct pattern of cross-strata, which will enrich our knowledge of paleoenvironmental reconstruction in the fluvial-dominated reach of an estuary [Visser, 1980; Leclair and Bridge, 2001; Leclair and Blom, 2005].

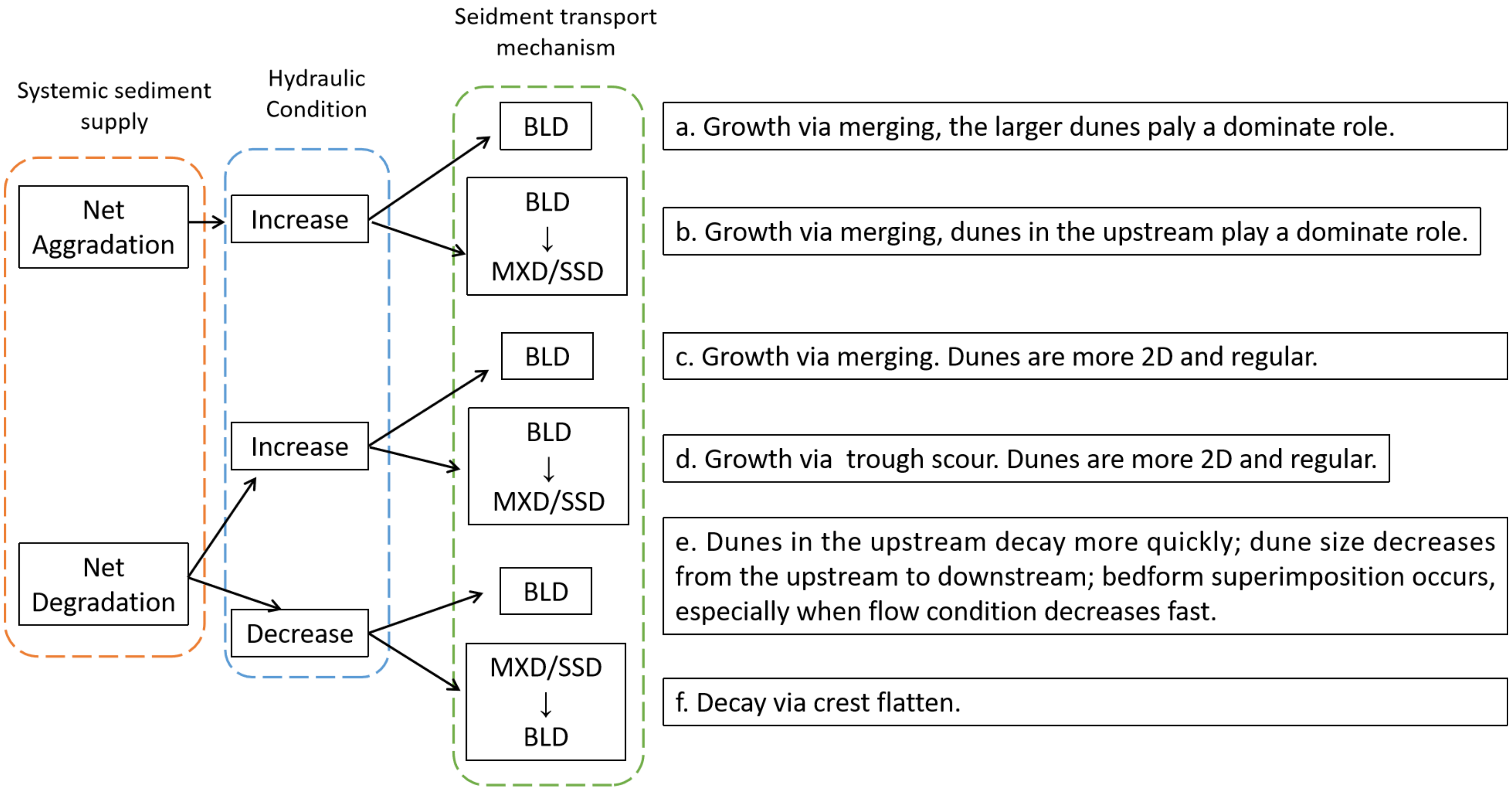

Figure 8-1 Schematic diagram of the sequence to determine dune adaptation under changing flows. Six different conditions are classified: under net degradation with hydraulic condition increase: (a) always bedload dominated and (b) from bedload dominated to mixed-load/suspended sediment dominated; under net aggradation with hydraulic condition increase: (c) always bedload dominated and (d) from bedload dominated to mixed-load/ suspended sediment dominated; under net aggradation with hydraulic condition decrease: (e) always bedload dominated and (e) from mixed-load/ suspended sediment dominated to bedload dominated.

In the place closer to the river mouth, where tides effect is stronger. Detailed sediment transport and bedform evolution within a tidal cycle is measured and analysed. Clockwise hysteresis loops are found between dune height, aspect ratio and mean flow velocity. The combination of suspended sediment transport and bedload transport on dune transformation and migration attributes to the clockwise hysteresis. The specific sediment composition of the riverbed, in some extent, affects the mechanism of sediment transport related to the exchange between suspended sediment and riverbed.

The results implicate that for investigation of dune development under tidal influence, it is necessary to investigate dune dynamics during a spring-neap tide, because dunes are controlled by the spring-neap tide, rather than the temporary current. Moreover, despite the effect of wave, secondary flows, and extreme event, single type dunes are expected to exist in the certain flow condition, if the feedback between the flow, sediment transport, and bedform morphology reaches equilibrium.

8.2. Recommendations and Further Work

The work presented in this thesis has led to a number of challenges and perspectives for further research that are summarized below. These recommendations focus on the experimental work and its advance, particularly in regard to the development of numerical models.

Previous research has long highlighted that understanding the origins and motions of flow structure over dunes is critical to quantify their contribution to flow resistance and assess the principal mechanism for sediment transport in sand bed river and estuarine systems [*Best*, 2005; *Kwoll et al.*, 2016]. Recent studies have demonstrated the impact of the dune lee slope on coherent flow structure in a controlled, fixed-bed laboratory experiment using Laser Doppler Velocimeter (LDV) or Particle Image Velocimetry [*Kwoll*, 2013; *Kwoll et al.*, 2016; *Kwoll et al.*, 2017]. Moreover, similar sediment suspension events were observed in the filed via an acoustic Doppler current profile (aDcp) [*Bradley et al.*, 2013]. However, those conclusions were drawn based on few flow conditions and the origins and motions of flow structure over non-equilibrium, regular/irregular bedforms are still poorly understood. Therefore, further research is needed on the quantification of the effect on both flow resistance and sediment transport under non-equilibrium flow conditions, in order to completely under how non-equilibrium bedforms migration and deformation.

Another important direction for future research is quantifying the contribution of each type of sediment transport on dune migration and deformation [*Kostaschuk et al.*, 2009; *Naqshband et al.*, 2014b]. With the deploying of the Acoustic Concentration and Velocity Profiler (ACVP), *Naqshband et al.* [2014b] observed that the entire bedload contributes to bedform migration, while only part of the suspended load contributes to the movement. The bypass sediment was advected to the downstream and its fraction depends on flow strength. However, this work was conducted under equilibrium condition and on angle-of-repose dunes. How bedload and suspended sediment transport attribute to bedform migration or deformation during unsteady flows is needed to be further investigated for a wider range of both flow conditions and bed topography.

Additionally, the above studies focus only on dune dynamics comprised of uniform sand, while sand mixture is widely recognised to play a significant role in sediment vertical sorting and dune irregularity in cohesionless bed [*Blom*, 2003; *Kleinhans*, 2004] and in controlling bedform size and shape, thereby flow, sediment, and bedform dynamics, in cohesive bed comprised of clay, mud or extracellular polymeric substances (EPS) [*Baas et al.*, 2013; *Malarkey et al.*, 2015; *Schindler et al.*, 2015; *Baas et al.*, 2016; *Parsons et al.*, 2016]. At present, our knowledge of how flow and bed interface, how bedforms grow, and how the sediment transport under such conditions is in its infancy. Advances, therefore, need to be made through systematically quantifying and modelling bedform dynamics in a wide range of sediment mixtures that span their biological status [*Parsons and Best*, 2013; *Parsons et al.*, 2016].

Completely understanding process-based feedbacks between sediment transport, dune morphology, and flow structure is the key challenge for modelling fluvial dynamics. An improved understanding of dune dynamics is vital in making progress.

References

Abbott, J., and J. R. D. Francis (1977), Saltation and suspension trajectories of solid grains in a water stream, *Philosophical Transactions of the Royal Society of London A: Mathematical, Physical and Engineering Sciences*, *284*(1321), 225-254.

Allen, J. (1968a), Current Ripples: Their Relation to Patterns of Water and Sedimentation Motion, edited, p. 433 pp, North-Holland, New York.

Allen, J. (1968b), The nature and origin of bed-form hierarchies, *Sedimentology*, *10*(3), 161-182.

Allen, J. (1973), Features of cross ‐ stratified units due to random and other changes in bed forms, *Sedimentology*, *20*(2), 189-202.

Allen, J. (1976), Computational models for dune time-lag: population structures and the effects of discharge pattern and coefficient of change, *Sedimentary Geology*, *16*(2), 99-130.

Allen, J. (1978), Computational models for dune time-lag: calculations using Stein's rule for dune height, *Sedimentary Geology*, *20*, 165-216.

Allen, J. (1982), *Sedimentary structures, their character and physical basis*, Elsevier.

Allen, J. (1985), Principles of Physical Sedimentology, *Allen&Unwin, London*, *272*.

Allen, J. (2009), *River bedforms: progress and problems*, Oxford: Blackwell Publishing Ltd.

Amsler, M. L., M. H. García, C. R. Neill, P. Y. Julien, and G. J. Klaassen (1997), Discussions and Closure: Sand-Dune Geometry of Large Rivers during Floods, *Journal of Hydraulic Engineering*, *123*(6), 582-585.

Amsler, M. L., and M. I. Schreider (1999), Dune height prediction at floods in the Paraná River, Argentina, *River sedimentation: Theory and applications*, 615-620.

Ashley, G. M. (1990), Classification of large-scale subaqueous bedforms: a new look at an old problem-SEPM bedforms and bedding structures, *Journal of Sedimentary Research*, *60*(1).

Ashworth, P. J., J. L. Best, J. E. Roden, C. S. Bristow, and G. J. Klaassen (2000), Morphological evolution and dynamics of a large, sand braid ‐ bar, Jamuna River, Bangladesh, *Sedimentology*, *47*(3), 533-555.

Ashworth, P. J., and J. Lewin (2012), How do big rivers come to be different?, *Earth-Science Reviews*, *114*(1), 84-107.

Baas, J. H. (1999), An empirical model for the development and equilibrium morphology of current ripples in fine sand, *Sedimentology*, *46*(1), 123-138.

Baas, J. H., J. L. Best, and J. Peakall (2016), Predicting bedforms and primary current stratification in cohesive mixtures of mud and sand, *Journal of the Geological Society*, *173*(1), 12-45.

Baas, J. H., J. L. Best, J. Peakall, and M. Wang (2009), A phase diagram for turbulent, transitional, and laminar clay suspension flows, *Journal of Sedimentary Research*, *79*(4), 162-183.

Baas, J. H., A. G. Davies, and J. Malarkey (2013), Bedform development in mixed sand-mud: The contrasting role of cohesive forces in flow and bed, *Geomorphology*, *182*, 19-32.

Baas, J. H., A. P. Oost, O. K. Sztano, P. L. Deboer, and G. Postma (1993), Time as an Independent Variable for Current Ripples Developing Towards Linguoid Equilibrium Morphology, *Terra Nova*, *5*(1), 29-35, doi:DOI 10.1111/j.1365-3121.1993.tb00223.x.

Bagnold, R. (1966), An approach to the sediment transport problem, *General Physics Geological Survey, Prof. paper*.

Bagnold, R. (1973), The nature of saltation and of 'bed-load' transport in water, paper presented at Proceedings of the Royal Society of London A: Mathematical, Physical and Engineering Sciences, The Royal Society.

Bagnold, R. (1980), An empirical correlation of bedload transport rates in flumes and natural rivers, paper presented at Proceedings of the Royal Society of London A: Mathematical, Physical and Engineering Sciences, The Royal Society.

Balachandar, R., B.-S. Hyun, and V. Patel (2007), Effect of depth on flow over a fixed dune, *Can J Civil Eng*, *34*(12), 1587-1599.

Balachandar, R., and H. P. Reddy (2011), *Bed Forms and Flow Mechanisms Associated with Dunes*, INTECH Open Access Publisher.

Bartholdy, J., V. B. Ernstsen, B. W. Flemming, C. Winter, and A. Bartholomä (2010a), A simple model of bedform migration, *Earth Surface Processes and Landforms*, *35*(10), 1211-1220.

Bartholdy, J., V. B. Ernstsen, B. W. Flemming, C. Winter, A. Bartholomä, and A. Kroon (2015), On the formation of current ripples, *Scientific reports*, *5*.

Bartholdy, J., B. W. Flemming, A. Bartholomä, and V. B. Ernstsen (2005), Flow and grain size control of depth ‐ independent simple subaqueous dunes, *Journal of Geophysical Research: Earth Surface (2003–2012)*, *110*(F4).

Bartholdy, J., B. W. Flemming, V. B. Ernstsen, and C. Winter (2010b), Hydraulic roughness over simple subaqueous dunes, *Geo-Marine Letters*, *30*(1), 63-76.

Bennett, S., and J. Best (1995), Mean flow and turbulence structure over fixed, two ‐ dimensional dunes: Implications for sediment transport and bedform stability, *Sedimentology*, *42*(3), 491-513.

Berg, J. H. (1987), Bedform migration and bed ‐ load transport in some rivers and tidal environments, *Sedimentology*, *34*(4), 681-698.

Berg, J. H., A. V. Gelder, R. Kostaschuk, and P. Villard (1998), Flow and sediment transport over large subaqueous dunes: Fraser River, Canada, *Sedimentology*, *45*(1), 217-221.

Best, J. (1993), On the interactions between turbulent flow structure, sediment transport and bedform development: some considerations from recent experimental research, *Turbulence: Perspectives on Flow and sediment transport*, 61-92.

Best, J. (1996), The fluid dynamics of small-scale alluvial bedforms, *Advances in fluvial dynamics and stratigraphy*, 67-125.

Best, J. (2005a), The fluid dynamics of river dunes: A review and some future research directions, *Journal of Geophysical Research: Earth Surface (2003–2012)*, *110*(F4).

Best, J. (2005b), Kinematics, topology and significance of dune-related macroturbulence: some observations from the laboratory and field, *Fluvial Sedimentology VII*, *35*, 41-60.

Best, J., G. Blois, J. Barros, and K. Christensen (2013), The dynamics of bedform amalgamation: new insights from a very thin flume, *VLIZ Special Publication*.

Best, J., and R. Kostaschuk (2002), An experimental study of turbulent flow over a low-angle dune, *Journal of Geophysical Research: Oceans*, *107*(C9), 18-11-18-19, doi:10.1029/2000JC000294.

Best, J., R. Kostaschuk, and R. Hardy (2004), The fluid dynamics of low-angle river dunes: results from integrated field monitoring, laboratory experimentation and numerical modelling, *Marine Sandwave and River Dune Dynamics II, University of Twente, Enschede, Netherlands*, 17-23.

Bhaganagar, K., and T.-J. Hsu (2009), Direct numerical simulations of flow over two-dimensional and three-dimensional ripples and implication to sediment transport: Steady flow, *Coastal Engineering*, *56*(3), 320-331.

Biron, P. M., C. Robson, M. F. Lapointe, and S. J. Gaskin (2004), Comparing different methods of bed shear stress estimates in simple and complex flow fields, *Earth Surface Processes and Landforms*, *29*(11), 1403-1415.

Blom, A. (2003), A vertical sorting model for rivers with non-uniform sediment and dunes, *PROEFSCHRIFT ter verkrijging van de graad van doctor aan de Universiteit Twente, op gezag van de rector magnificus, prof. dr. FA van Vught, volgens besluit van het College voor Promoties in het openbaar te verdedigen op donderdag 6 maart 2003 om 15: 00 uur*.

Bolle, A., M. Mathys, and P. Haerens (2013), How the Belgian wind farm business made us discover the challenging environment of marine sand dunes, paper presented at Proceedings of 4th International Conference on Marine and River Dune Dynamics.

Bradley, R. W., J. Venditti, R. Kostaschuk, M. Church, M. Hendershot, and M. Allison (2013), Flow and sediment suspension events over low-angle dunes: Fraser Estuary, Canada, *Journal of Geophysical Research: Earth Surface*, *118*(3), 1693-1709.

Bradley, R. W., and J. G. Venditti (2016), Reevaluating dune scaling relations, *Earth-Science*

Reviews.

Bridge, J. S. (2009), *Rivers and floodplains: forms, processes, and sedimentary record*, John Wiley & Sons.

Bridge, J. S., and R. S. Tye (2000), Interpreting the dimensions of ancient fluvial channel bars, channels, and channel belts from wireline-logs and cores, *AAPG bulletin*, *84*(8), 1205-1228.

Carling, P., E. Golz, H. Orr, and A. Radecki-Pawlik (2000a), The morphodynamics of fluvial sand dunes in the River Rhine, near Mainz, Germany. I. Sedimentology and morphology, *Sedimentology*, *47*(1), 227-252.

Carling, P., K. Richardson, and H. Ikeda (2005), A flume experiment on the development of subaqueous fine‐gravel dunes from a lower‐stage plane bed, *Journal of Geophysical Research: Earth Surface (2003–2012)*, *110*(F4).

Carling, P., J. Williams, E. Golz, and A. Kelsey (2000b), The morphodynamics of fluvial sand dunes in the River Rhine, near Mainz, Germany. II. Hydrodynamics and sediment transport, *Sedimentology*, *47*(1), 253.

Cellino, M., and W. Graf (2000), Experiments on suspension flow in open channels with bed forms, *Journal of Hydraulic Research*, *38*(4), 289-298.

Cheel, R. (2005), Introduction to clastic sedimentology, *ERSC 2P10 Course Notes. Brock University, Ontario*.

Chen, J., Z. Wang, M. Li, T. Wei, and Z. Chen (2012), Bedform characteristics during falling flood stage and morphodynamic interpretation of the middle-lower Changjiang (Yangtze) River channel, China, *Geomorphology*, *147*, 18-26.

Chen, Z., K. Xu, and M. Watanabe (2008), Dynamic hydrology and geomorphology of the Yangtze River, *Large Rivers: Geomorphology and Management*, 457.

Cheng, H., R. Kostaschuk, and Z. Shi (2004), Tidal currents, bed sediments, and bedforms at the South Branch and the South Channel of the Changjiang (Yangtze) estuary, China: Implications for the ripple-dune transition, *Estuaries*, *27*(5), 861-866.

Cheng, H., M. Li, Y. Xue, T. Zhou, and B. Song (2001), High resolution survey on microtopography movement in Yangtze Estuary, *Progress in Natural Science*, *11*(10), 1085-1091.

Cheng, N.-S. (2002), Exponential formula for bedload transport, *Journal of Hydraulic Engineering*, *128*(10), 942-946.

Cheng, N.-S., and A. Emadzadeh (2014), Average velocity of solitary coarse grain in flows over smooth and rough beds, *Journal of Hydraulic Engineering*, *140*(6), 04014015.

Cheng, R. T., C. H. Ling, J. W. Gartner, and P. Wang (1999), Estimates of bottom roughness length and bottom shear stress in South San Francisco Bay, California, *Journal of Geophysical Research: Oceans*, *104*(C4), 7715-7728.

Chezy, A. (1768), On the origin of the Chezy formula by C. Herschel, *J Assoc Eng Soc*, *18*, 363-368.

Chriss, T., and D. R. Caldwell (1987), Evidence for the influence of form drag on bottom boundary layer flow.

Church, M. (2006), Bed material transport and the morphology of alluvial river channels, *Annu. Rev. Earth Planet. Sci.*, *34*, 325-354.

Clifford, N., A. Robert, and K. Richards (1992), Estimation of flow resistance in gravel‐bedded rivers: A physical explanation of the multiplier of roughness length, *Earth Surface Processes and Landforms*, *17*(2), 111-126.

Coleman, S., and V. Nikora (2011), Fluvial dunes: initiation, characterization, flow structure, *Earth Surface processes and landforms*, *36*(1), 39-57.

Coleman, S. E., and B. Eling (2000), Sand wavelets in laminar open-channel flows, *Journal of Hydraulic Research*, *38*(5), 331-338.

Coleman, S. E., and B. W. Melville (1996), Initiation of bed forms on a flat sand bed, *Journal of Hydraulic Engineering*, *122*(6), 301-310.

Coleman, S. E., M. H. Zhang, and T. Clunie (2005), Sediment-wave development in subcritical water flow, *Journal of Hydraulic Engineering*, *131*(2), 106-111.

Costello, W. R., and J. B. Southard (1981), Flume experiments on lower-flow-regime bed forms in coarse sand, *Journal of Sedimentary Research*, *51*(3).

Crawford, A. M., and A. E. Hay (2001), Linear transition ripple migration and wave orbital velocity skewness: Observations, *Journal of Geophysical Research: Oceans*, *106*(C7), 14113-14128.

CWRC (2011), *Changjiang Sediment Bulletin*, (available at:) http://www.cjh.com.cn/pages/nsgb.html (in Chinese).

CWRC, C. W. R. C. (2014), Changjiang Sediment Bulletin, edited, http://www.cjh.com.cn (in Chinese).

Dade, W. (2000), Grain size, sediment transport and alluvial channel pattern, *Geomorphology*, *35*(1), 119-126.

Dai, Z., J. T. Liu, W. Wei, and J. Chen (2014), Detection of the Three Gorges Dam influence on the Changjiang (Yangtze River) submerged delta, *Scientific reports*, *4*, 6600.

Dalrymple, R. W., and R. N. Rhodes (1995), Estuarine dunes and bars, *Developments in sedimentology*, *53*, 359-422.

Darby, S. E., H. Q. Trieu, P. A. Carling, J. Sarkkula, J. Koponen, M. Kummu, I. Conlan, and J. Leyland (2010), A physically based model to predict hydraulic erosion of fine‐grained riverbanks: The role of form roughness in limiting erosion, *Journal of Geophysical Research: Earth Surface (2003–2012)*, *115*(F4).

Davies, A., and P. Robins (2017), Residual flow, bedforms and sediment transport in a tidal channel modelled with variable bed roughness, *Geomorphology*.

Davis, J. C., and R. J. Sampson (1986), *Statistics and data analysis in geology*, Wiley New York et al.

de Almeida, R. P., C. P. Galeazzi, B. T. Freitas, L. Janikian, M. Ianniruberto, and A. Marconato (2016), Large barchanoid dunes in the Amazon River and the rock record: Implications for interpreting large river systems, *Earth and Planetary Science Letters*, *454*, 92-102.

Dietrich, W. E., and P. Whiting (1989), Boundary shear stress and sediment transport in river meanders of sand and gravel, *River meandering*, 1-50.

Dreano, J., A. Valance, D. Lague, and C. Cassar (2010), Experimental study on transient and steady‐state dynamics of bedforms in supply limited configuration, *Earth Surface Processes and Landforms*, *35*(14), 1730-1743.

Duin, O. J. M. (2015), Sediment transport processes in dune morphology and the transition to upper-stage plane bed, University of Twente.

Duin, O. J. M., S. J. Hulscher, J. S. Ribberink, and C. M. Dohmen-Janssen (2016), Modeling of spatial lag in bed-load transport processes and its effect on dune morphology, *Journal of hydraulic engineering*, *143*(2), 04016084.

Dyer, K. (1971), Current velocity profiles in a tidal channel, *Geophysical Journal International*, *22*(2), 153-161.

Dyer, K. (1986), Coastal and estuarine sediment dynamics, *Chichester: Wiley*.

Edmonds, D. A., and R. L. Slingerland (2010), Significant effect of sediment cohesion on delta morphology, *Nature Geoscience*, *3*(2), 105-109.

Einstein, H. A. (1942), Formulas for the transportation of bed load, *Trans. ASCE Paper*, *2140*, 561-597.

Einstein, H. A. (1950), *The bed-load function for sediment transportation in open channel flows*, US Department of Agriculture Washington DC.

Elbelrhiti, H., P. Claudin, and B. Andreotti (2005), Field evidence for surface-wave-induced instability of sand dunes, *Nature*, *437*(7059), 720.

Engelund, F., and J. Fredsøe (1976), A sediment transport model for straight alluvial channels, *Hydrology Research*, *7*(5), 293-306.

Engelund, F., and J. Fredsoe (1982), Sediment ripples and dunes, *Annual Review of Fluid Mechanics*, *14*(1), 13-37.

Ernstsen, V. B., M. Becker, C. Winter, A. Bartholomä, B. W. Flemming, and J. Bartholdy (2007), Bedload transport in an inlet channel during a tidal cycle, *River, Coastal and Estuarine Morphodynamics: RCEM 2007*, 351-358.

Ernstsen, V. B., R. Noormets, D. Hebbeln, A. Bartholomä, and B. W. Flemming (2006a), Precision of high-resolution multibeam echo sounding coupled with high-accuracy positioning in a shallow water coastal environment, *Geo-marine letters*, *26*(3), 141-149.

Ernstsen, V. B., R. Noormets, C. Winter, D. Hebbeln, A. Bartholomä, B. W. Flemming, and J.

Bartholdy (2005), Development of subaqueous barchanoid ‐ shaped dunes due to lateral grain size variability in a tidal inlet channel of the Danish Wadden Sea, *Journal of Geophysical Research: Earth Surface*, *110*(F4).

Ernstsen, V. B., R. Noormets, C. Winter, D. Hebbeln, A. Bartholomä, B. W. Flemming, and J. Bartholdy (2006b), Quantification of dune dynamics during a tidal cycle in an inlet channel of the Danish Wadden Sea, *Geo-Marine Letters*, *26*(3), 151-163.

Ernstsen, V. B., C. Winter, M. Becker, and J. Bartholdy (2009), Tide-controlled variations of primary-and secondary-bedform height: Innenjade tidal channel (Jade Bay, German Bight), in *River, coastal and estuarine morphodynamics: RCEM*, edited, pp. 779-786.

Fan, D., and C. Li (2002), Rhythmic deposition on mudflats in the mesotidal Changjiang Estuary, China, *Journal of Sedimentary Research*, *72*(4), 543-551.

Ferguson, R. (2013), Reach-Scale Flow Resistance in River Channels, *Treatise on Geomorphology*, *9*, 50-68.

Ferguson, R., and M. Church (2004), A simple universal equation for grain settling velocity, *Journal of sedimentary Research*, *74*(6), 933-937.

Fernandez Luque, R., and R. Van Beek (1976), Erosion and transport of bed-load sediment, *Journal of hydraulic research*, *14*(2), 127-144.

Fernandez, R., J. Best, and F. Lόpez (2006), Mean flow, turbulence structure, and bed form superimposition across the ripple ‐ dune transition, *Water Resources Research*, *42*(5).

Field, M. E., C. H. Nelson, D. A. Cacchione, and D. E. Drake (1981), Sand waves on an epicontinental shelf: Northern Bering Sea, *Marine Geology*, *42*(1), 233-258.

Flemming, B. (2000), The role of grain size, water depth and flow velocity as scaling factors controlling the size of subaqueous dunes, paper presented at Marine Sandwave Dynamics, International Workshop.

Flemming, B. W., and R. A. Davis, Jr. (1992), Dimensional adjustment of subaqueous dunes in the course of a spring-neap semicycle in a mesotidal backbarrier channel environment (German Wadden Sea, southern North Sea), *Tidal Clastics*, *92*, 28-30.

Fredsøe, J. (1981), Unsteady flow in straight alluvial streams, *Part*, *2*, 431-453.

Fredsøe, J. (2005), Calculation of dune morphology, *JOURNAL OF GEOPHYSICAL RESEARCH-EARTH SURFACE*, *110*(F4).

Friedrich, H. (2010), Evaluation of statistical analysis techniques for developing bedforms recorded in 3D, ResearchSpace@ Auckland.

Friedrich, H., B. Melville, S. Coleman, T. Clunie, V. Nikora, and D. Goring (2006), Three-dimensional properties of laboratory sand waves obtained from two-dimensional autocorrelation analysis, paper presented at Int. Conf. on Fluvial Hydraulics, River Flow 2006, Lisbon, Portugal, 6-8 September 2006.

Gabel, S. L. (1993), Geometry and kinematics of dunes during steady and unsteady flows in the Calamus River, Nebraska, USA, *Sedimentology*, *40*(2), 237-269.

Ganju, N. K., and C. R. Sherwood (2010), Effect of roughness formulation on the performance of a coupled wave, hydrodynamic, and sediment transport model, *Ocean Modelling*, *33*(3), 299-313.

Ganti, V., C. Paola, and E. Foufoula ‐ Georgiou (2013), Kinematic controls on the geometry of the preserved cross sets, *Journal of Geophysical Research: Earth Surface*, *118*(3), 1296-1307.

Garcia, M. (2008), Sedimentation engineering: processes, measurements, modeling, and practice, American Society of Civil Engineers.

Gartner, J. W. (2004), Estimating suspended solids concentrations from backscatter intensity measured by acoustic Doppler current profiler in San Francisco Bay, California, *Marine Geology*, *211*(3), 169-187.

Goff, J. A., L. A. Mayer, P. Traykovski, I. Buynevich, R. Wilkens, R. Raymond, G. Glang, R. L. Evans, H. Olson, and C. Jenkins (2005), Detailed investigation of sorted bedforms, or “rippled scour depressions,” within the Martha's Vineyard Coastal Observatory, Massachusetts, *Continental Shelf Research*, *25*(4), 461-484, doi:http://dx.doi.org/10.1016/j.csr.2004.09.019.

Gomez, B. (1991), Bedload transport, *Earth-Science Reviews*, *31*(2), 89-132.

Gomez, B., and M. Church (1989), An assessment of bed load sediment transport formulae for gravel bed rivers, *Water Resources Research*, *25*(6), 1161-1186.

Goncharov, V. N. (1962), *Basic River Dynamic*, Hydro-Meteorological Press, Leningrad.

Goring, D., V. Nikora, and I. McEwan (1999), Analysis of the texture of gravel beds using 2-D structure functions, paper presented at River, Coastal, and Estuarine Morphodynamics: Proceedings of the IAHR Symposium.

Grant, W. D., and O. S. Madsen (1982), Movable bed roughness in unsteady oscillatory flow, *Journal of Geophysical Research: Oceans (1978–2012)*, *87*(C1), 469-481.

Guerrero, M. (2014), The investigation of sediment processes in rivers by means of the Acoustic Doppler Profiler, *Proceedings of Evolving Water Resources Systems: Understanding, Predicting and Managing Water–Society Interactions, Bologna, Italy: IAHS*, 364.

Guerrero, M., and A. Lamberti (2013), Bed-roughness investigation for a 2-D model calibration: the San Martìn case study at Lower Paranà, *International Journal of Sediment Research*, *28*(4), 458-469.

Guerrero, M., R. N. Szupiany, and F. Latosinski (2013), Multi-frequency acoustics for suspended sediment studies: an application in the Parana River, *Journal of Hydraulic Research*, *51*(6), 696-707.

Gutierrez, R. R. (2016), Bedforms Analysis Tool for Multiscale Modeling (Bedforms-ATM v1.1)*Rep.*

Gutierrez, R. R., J. D. Abad, D. R. Parsons, and J. L. Best (2013), Discrimination of bed form scales using robust spline filters and wavelet transforms: Methods and application to synthetic signals and bed forms of the Río Paraná, Argentina, *Journal of Geophysical Research: Earth Surface*, *118*(3), 1400-1418.

Guy, H. P., D. B. Simons, and E. V. Richardson (1966), Summary of alluvial channel data from flume experiments, 1956-61*Rep. 2330-7102*.

Gyr, A., and W. Kinzelbach (2004), Bed forms in turbulent channel flow, *Applied Mechanics Reviews*, *57*(1), 77-93.

Hanes, D. (1986), Grain flows and bed-load sediment transport: review and extension, *Acta Mechanica*, *63*(1-4), 131-142.

Harbor, D. J. (1998), Dynamics of bedforms in the lower Mississippi River, *Journal of Sedimentary Research*, *68*(5).

Hardy, R., T. Marjoribanks, D. Parsons, A. Reesink, B. Murphy, P. Ashworth, and J. Best (2014), Modelling time dependent flow fields over three dimensional dunes.

Hendershot, M. (2014), Low angle dune response to variable flow, dune translation, and crestline dynamics in Fraser Estuary, British Columbia, Canada, Environment: Department of Geography.

Hendershot, M. L., J. G. Venditti, R. W. Bradley, R. A. Kostaschuk, M. Church, and M. A. Allison (2016), Response of low ‐ angle dunes to variable flow, *Sedimentology*, *63*(3), 743-760.

Hervouet, J.-M. (2007), *Hydrodynamics of free surface flows: modelling with the finite element method*, John Wiley & Sons.

Hey, R. D. (1979), Flow resistance in gravel-bed rivers, *Journal of the Hydraulics Division*, *105*(4), 365-379.

Hoekstra, P., P. Bell, P. van Santen, N. Roode, F. Levoy, and R. Whitehouse (2004), Bedform migration and bedload transport on an intertidal shoal, *Continental Shelf Research*, *24*(11), 1249-1269.

Hoitink, A., F. Buschman, and B. Vermeulen (2009), Continuous measurements of discharge from a horizontal acoustic Doppler current profiler in a tidal river, *Water resources research*, *45*(11).

Hoitink, A., and P. Hoekstra (2005), Observations of suspended sediment from ADCP and OBS measurements in a mud-dominated environment, *Coastal Engineering*, *52*(2), 103-118.

Holmes, J. R. R., and M. H. Garcia (2008), Flow over bedforms in a large sand-bed river: A field investigation, *Journal of Hydraulic Research*, *46*(3), 322-333.

Hong, J.-H., Y.-M. Chiew, P.-H. Yeh, and H.-C. Chan (2016), Evolution of Local Pier-Scour Depth with Dune Migration in Subcritical Flow Conditions, *Journal of Hydraulic Engineering*, *143*(4), 04016098.

Huybrechts, N., G. V. Luong, Y. Zhang, C. Villaret, and M. Verbanck (2011), Dynamic Routing of Flow Resistance and Alluvial Bed-Form Changes from the Lower to the Upper Regime, *Journal of hydraulic engineering*, *137*(9), 932-944.

Jackson, R. G. (1975), Hierarchical attributes and a unifying model of bed forms composed of cohesionless material and produced by shearing flow, *Geological Society of America Bulletin*, *86*(11), 1523-1533.

Jerolmack, D. J., and D. Mohrig (2005), A unified model for subaqueous bed form dynamics, *Water Resources Research*, *41*(12).

Jiang, X., P. J. Scott, D. J. Whitehouse, and L. Blunt (2007), Paradigm shifts in surface metrology. Part II. The current shift, paper presented at Proceedings of the Royal Society of London A: Mathematical, Physical and Engineering Sciences, The Royal Society.

Johns, B., T. Chesher, and R. Soulsby (1990), The modelling of sandwave evolution resulting from suspended and bed load transport of sediment, *Journal of Hydraulic Research*, *28*(3), 355-374.

Jordan, P. R. (1965), *Fluvial sediment of the mississippi river at St. Louis, Missouri*, US Government Printing Office.

Julien, P. Y. (2010), *Erosion and sedimentation*, Cambridge University Press.

Julien, P. Y., and G. J. Klaassen (1995), Sand-dune geometry of large rivers during floods, *Journal of Hydraulic Engineering*, *121*(9), 657-663.

Julien, P. Y., G. J. Klaassen, W. B. M. Ten Brinke, and A. W. E. Wilbers (2002), Case study: Bed resistance of Rhine River during 1998 flood, *Journal of Hydraulic Engineering*, *128*(12), 1042-1050.

Kadlec, R. H. (1990), Overland flow in wetlands: vegetation resistance, *Journal of Hydraulic Engineering*, *116*(5), 691-706.

Kamphuis, J. (1974), Determination of sand roughness for fixed beds, *Journal of Hydraulic Research*, *12*(2), 193-203.

Karim, F. (1995), Bed configuration and hydraulic resistance in alluvial-channel flows, *Journal of Hydraulic Engineering*, *121*(1), 15-25.

Karim, F. (1999), Bed-form geometry in sand-bed flows, *Journal of Hydraulic Engineering*, *125*(12), 1253-1261.

Kean, J. W., and J. D. Smith (2006), Form drag in rivers due to small‐scale natural topographic features: 1. Regular sequences, *Journal of Geophysical Research: Earth Surface (2003–2012)*, *111*(F4).

Kleinhans, M. (2004), Sorting in grain flows at the lee side of dunes, *Earth-Science Reviews*, *65*(1), 75-102.

Kleinhans, M. (2005a), Phase diagrams of bed states in steady, unsteady, oscillatory and mixed flows.

Kleinhans, M. (2005b), Upstream sediment input effects on experimental dune trough scour in sediment mixtures, *Journal of Geophysical Research: Earth Surface*, *110*(F4).

Kleinhans, M., A. Wilbers, A. De Swaaf, and J. Van Den Berg (2002), Sediment supply-limited bedforms in sand-gravel bed rivers, *Journal of sedimentary research*, *72*(5), 629-640.

Kocurek, G., R. C. Ewing, and D. Mohrig (2010), How do bedform patterns arise? New views on the role of bedform interactions within a set of boundary conditions, *Earth Surface Processes and Landforms*, *35*(1), 51-63.

Kornman, B. (1995), The effect of changes in the lee shape of dunes on the flow field, turbulence, and hydraulic roughness, *Rep. Meas. R 95*, *1*.

Kostaschuk, R. (2006), Sediment transport mechanics and subaqueous dune morphology, *River, Coastal and Estuarine Morphodynamics: London, Taylor & Francis Group*, 795-801.

Kostaschuk, R., J. Best, P. Villard, J. Peakall, and M. Franklin (2005), Measuring flow velocity and sediment transport with an acoustic Doppler current profiler, *Geomorphology*, *68*(1), 25-37.

Kostaschuk, R., and M. Church (1993), Macroturbulence generated by dunes: Fraser River, Canada, *Sedimentary Geology*, *85*(1), 25-37.

Kostaschuk, R., D. Shugar, J. Best, D. Parsons, S. Lane, R. Hardy, and O. Orfeo (2008), Suspended sediment transport over a dune, *Marine Sand-wave and River Dune Dynamics III. University of Leeds, UK*, 197-201.

Kostaschuk, R., D. Shugar, J. Best, D. Parsons, S. Lane, R. Hardy, and O. Orfeo (2009), Suspended sediment transport and deposition over a dune: Río Paraná, Argentina, *Earth Surface Processes and Landforms*, *34*(12), 1605.

Kostaschuk, R., and P. Villard (1999), Turbulent sand suspension over dunes, paper presented at Proceedings of the 6th International Conference on Fluvial Sedimentology, edited by ND Smith, and J. Rogers.

Kostaschuk, R. A. (2000), A field study of turbulence and sediment dynamics over subaqueous dunes with flow separation, *Sedimentology*, *47*(3), 519-531.

Kostaschuk, R. A., and J. Best (2005), Response of sand dunes to variations in tidal flow: Fraser Estuary, Canada, *Journal of Geophysical Research: Earth Surface (2003–2012)*, *110*(F4).

Kostaschuk, R. A., and P. Villard (1996), Flow and sediment transport over large subaqueous dunes: Fraser River, Canada, *Sedimentology*, *43*(5), 849-863.

Kostaschuk, R. A., P. Villard, and J. Best (2004), Measuring velocity and shear stress over dunes with acoustic Doppler profiler, *Journal of hydraulic engineering*, *130*(9), 932-936.

Kuru, W. C., D. T. Leighton, and M. J. McCready (1995), Formation of waves on a horizontal erodible bed of particles, *International Journal of Multiphase Flow*, *21*(6), 1123-1140, doi:https://doi.org/10.1016/0301-9322(95)00035-V.

Kwoll, E. (2013), Bedforms, macroturbulence, and sediment transport at the fluid-bed interface, Staats-und Universitätsbibliothek Bremen.

Kwoll, E., M. Becker, and C. Winter (2014), With or against the tide: The influence of bed form asymmetry on the formation of macroturbulence and suspended sediment patterns, *Water Resources Research*, *50*(10), 7800-7815.

Kwoll, E., J. Venditti, R. Bradley, and C. Winter (2016), Flow structure and resistance over subaquaeous high‐and low‐angle dunes, *Journal of Geophysical Research: Earth Surface*, *121*(3), 545-564.

Kwoll, E., J. G. Venditti, R. W. Bradley, and C. Winter (2017), Observations of Coherent flow structures over Sub-aqueous high- and low-angle Dunes, *Journal of Geophysical Research: Earth Surface*, n/a-n/a, doi:10.1002/2017JF004356.

Lajeunesse, E., L. Malverti, and F. Charru (2010), Bed load transport in turbulent flow at the grain scale: Experiments and modeling, *Journal of Geophysical Research: Earth Surface*, *115*(F4).

Lane, S., K. Bradbrook, K. Richards, P. Biron, and A. Roy (1999), The application of computational fluid dynamics to natural river channels: three-dimensional versus two-dimensional approaches, *Geomorphology*, *29*(1), 1-20.

Lane, S., K. Bradbrook, K. Richards, P. Biron, and A. Roy (2000), Secondary circulation cells in river channel confluences: measurement artefacts or coherent flow structures?, *Hydrological Processes*, *14*(11‐12), 2047-2071.

Lane, S., R. Hardy, L. Elliott, and D. Ingham (2004), Numerical modeling of flow processes over gravelly surfaces using structured grids and a numerical porosity treatment, *Water Resources Research*, *40*(1).

Latosinski, F. G., R. N. Szupiany, C. M. García, M. Guerrero, and M. L. Amsler (2014), Estimation of concentration and load of suspended bed sediment in a large river by means of acoustic Doppler technology, *Journal of Hydraulic Engineering*, *140*(7), 04014023.

Latosinski, F. G., R. N. Szupiany, M. Guerrero, M. L. Amsler, and C. Vionnet (2017), The ADCP's bottom track capability for bedload prediction: evidence on method reliability from sandy river applications, *Flow Measurement and Instrumentation*.

Leclair, S. F. (2002), Preservation of cross‐strata due to the migration of subaqueous dunes: an experimental investigation, *Sedimentology*, *49*(6), 1157-1180.

Leclair, S. F., and A. Blom (2005), A qualitative analysis of the distribution of bed-surface elevation and the characteristics of associated deposits for subaqueous dunes, *Spec. Publ. Int. Assoc. Sedimentol*, *35*, 121-134.

Leclair, S. F., and J. S. Bridge (2001), Quantitative interpretation of sedimentary structures formed by river dunes, *Journal of Sedimentary Research*, *71*(5), 713-716.

Leeder, M. (2009), On the interactions between turbulent flow, sediment transport and bedform mechanics in channelized flows, *Modern and Ancient Fluvial Systems*, 3-18.

Lefebvre, A., V. B. Ernstsen, and C. Winter (2011a), Bedform characterization through 2D spectral analysis, *Journal of Coastal Research*, 781-785.

Lefebvre, A., V. B. Ernstsen, and C. Winter (2011b), Influence of compound bedforms on hydraulic roughness in a tidal environment, *Ocean Dynamics*, *61*(12), 2201-2210.

Lefebvre, A., V. B. Ernstsen, and C. Winter (2013a), Estimation of roughness lengths and flow separation over compound bedforms in a natural-tidal inlet, *Continental Shelf Research*, *61*, 98-111.

Lefebvre, A., Y. Ferret, A. Paarlberg, V. B. Ernstsen, and C. Winter (2013b), Variation of flow separation over large bedforms during a tidal cycle, *Marine and river dune dynamics MARID IV, Bruges, Belgium*, *15*, 169-175.

Lefebvre, A., A. Paarlberg, V. B. Ernstsen, and C. Winter (2014a), Flow separation and roughness lengths over large bedforms in a tidal environment: A numerical investigation, *Continental Shelf Research*, *91*, 57-69.

Lefebvre, A., A. J. Paarlberg, and C. Winter (2014b), Flow separation and shear stress over angle-of-repose bed forms: A numerical investigation, *Water Resources Research*, *50*(2), 986-1005.

Lefebvre, A., A. J. Paarlberg, and C. Winter (2016), Characterising natural bedform morphology and its influence on flow, *Geo-Marine Letters*, *36*(5), 379-393.

Lefebvre, A., and C. Winter (2016a), The influence of bed form lee angle to hydraulic roughness, *Geo Marine Letters, on Jan*, *17*, 2016.

Lefebvre, A., and C. Winter (2016b), Predicting bed form roughness: the influence of lee side angle, *Geo-Marine Letters*, *36*(2), 121-133.

Levy, E. E. (1956), *River Mechanics*, National Energy Press, Moscow.

Li, J., X. Chen, X. Wan, Y. Xue, and J. Gu (2003), Field observation on bed sediments and sandwaves in dry season in Changjiang Estuary, *Geographical Research*, *22*(4), 513-519.

Li, P., S. Yang, J. Milliman, K. Xu, W. Qin, C. Wu, Y. Chen, and B. Shi (2012), Spatial, temporal, and human-induced variations in suspended sediment concentration in the surface waters of the Yangtze Estuary and adjacent coastal areas, *Estuaries and Coasts*, *35*(5), 1316-1327.

Lin, C. Y. M., and J. G. Venditti (2013), An empirical model of subcritical bedform migration, *Sedimentology*, *60*(7), 1786-1799.

Lisle, T. E., Y. Cui, G. Parker, J. E. Pizzuto, and A. M. Dodd (2001), The dominance of dispersion in the evolution of bed material waves in gravel ‐ bed rivers, *Earth Surface Processes and Landforms*, *26*(13), 1409-1420.

Luan, H. L., P. X. Ding, Z. B. Wang, J. Z. Ge, and S. L. Yang (2016), Decadal morphological evolution of the Yangtze Estuary in response to river input changes and estuarine engineering projects, *Geomorphology*, *265*, 12-23.

Luhar, M., J. Rominger, and H. Nepf (2008), Interaction between flow, transport and vegetation spatial structure, *Environmental Fluid Mechanics*, *8*(5-6), 423-439.

Lyn, D. (1993), Turbulence measurements in open-channel flows over artificial bed forms, *Journal of Hydraulic Engineering*, *119*(3), 306-326.

Müller, A., and A. Gyr (1986), On the vortex formation in the mixing layer behind dunes, *Journal of Hydraulic Research*, *24*(5), 359-375.

Maddux, T., S. McLean, and J. Nelson (2003a), Turbulent flow over three ‐ dimensional dunes: 2. Fluid and bed stresses, *Journal of Geophysical Research: Earth Surface (2003–2012)*, *108*(F1).

Maddux, T., J. Nelson, and S. McLean (2003b), Turbulent flow over three ‐ dimensional dunes: 1. Free surface and flow response, *Journal of Geophysical Research: Earth Surface (2003 –2012)*, *108*(F1).

Madsen, O. S. (1991), Mechanics of cohesionless sediment transport in coastal waters, paper presented at Coastal sediments, ASCE.

Malarkey, J., et al. (2015), The pervasive role of biological cohesion in bedform development, *Nature Communications*, *6*.

Manning, R., J. P. Griffith, T. Pigot, and L. F. Vernon-Harcourt (1890), *On the flow of water in open channels and pipes*.

Martin, R. L., and D. J. Jerolmack (2013), Origin of hysteresis in bed form response to unsteady flows, *Water Resources Research*, *49*(3), 1314-1333.

Masselink, G., M. Austin, T. O'Hare, and P. Russell (2007), Geometry and dynamics of wave ripples in the nearshore zone of a coarse sandy beach, *Journal of Geophysical Research: Oceans*, *112*(C10).

McCann, D. L., A. G. Davies, and J. D. Bennell (2011), Bed roughness feedback in TELEMAC-2D and SISYPHE, *Proceedings of the XVIII Telemac and Mascaret User Club*, 99-104.

McElroy, B., and D. Mohrig (2007), Correlation decay and dynamic equilibrium in sandy transport systems, paper presented at Conference proceedings: River, Coastal, and Estuarine Morphodynamics 2007.

McElroy, B. J. (2009), Expressions and implications of sediment transport variability in sandy rivers.

McElroy, B. J., and D. Mohrig (2009), Nature of deformation of sandy bed forms, *Journal of Geophysical Research: Earth Surface*, *114*(F3).

McLean, S. (1992), On the calculation of suspended load for noncohesive sediments, *Journal of Geophysical Research: Oceans (1978–2012)*, *97*(C4), 5759-5770.

McLean, S., J. Nelson, and S. Wolfe (1994), Turbulence structure over two ‐ dimensional bed forms: Implications for sediment transport, *Journal of Geophysical Research: Oceans (1978 – 2012)*, *99*(C6), 12729-12747.

McLean, S., and J. D. Smith (1979), Turbulence measurements in the boundary layer over a sand wave field, *Journal of Geophysical Research: Oceans (1978–2012)*, *84*(C12), 7791-7808.

McLean, S., S. Wolfe, and J. Nelson (1999a), Predicting boundary shear stress and sediment transport over bed forms, *Journal of Hydraulic Engineering*, *125*(7), 725-736.

McLean, S., S. Wolfe, and J. Nelson (1999b), Spatially averaged flow over a wavy boundary revisited, *Journal of Geophysical Research: Oceans (1978–2012)*, *104*(C7), 15743-15753.

McLean, S. R., J. Nelson, and R. Shreve (1996), Flow-sediment interactions in separating flows over bedforms, *Coherent flow structures in open channels*, 203-226.

Mendoza, C., and H. Wen Shen (1990), Investigation of turbulent flow over dunes, *Journal of Hydraulic Engineering*, *116*(4), 459-477.

Meyer-Peter, E., and R. Müller (1948), Formulas for bed-load transport, paper presented at IAHSR 2nd meeting, Stockholm, appendix 2, IAHR.

Middleton, G. V., and J. B. Southard (1984), Mechanics of sediment movement, edited, SEPM.

Miles, J., A. Thorpe, P. Russell, and G. Masselink (2014), Observations of bedforms on a dissipative macrotidal beach, *Ocean Dynamics*, *64*(2), 225-239.

Millar, R. G. (1999), Grain and form resistance in gravel-bed rivers Résistances de grain et de forme dans les rivières à graviers, *Journal of Hydraulic Research*, *37*(3), 303-312.

Morvan, H., D. Knight, N. Wright, X. Tang, and A. Crossley (2008), The concept of roughness in fluvial hydraulics and its formulation in 1D, 2D and 3D numerical simulation models, *Journal of Hydraulic Research*, *46*(2), 191-208.

Muste, M., K. Yu, and M. Spasojevic (2004), Practical aspects of ADCP data use for quantification of mean river flow characteristics; Part I: moving-vessel measurements, *Flow measurement and instrumentation*, *15*(1), 1-16.

Németh, A., S. Hulscher, and R. Van Damme (2006), Simulating offshore sand waves, *Coastal Engineering*, *53*(2), 265-275.

Nabi, M., I. Kimura, and Y. Shimizu (2013a), The Effect of Discharge Variability on River Bedform, *Journal of Japan Society of Civil Engineers, Ser. A2 (Applied Mechanics (AM))*, *69*(2), I_553-I_562.

Nabi, M., d. H. Vriend, E. Mosselman, C. Sloff, and Y. Shimizu (2013b), Detailed simulation of morphodynamics: 2. Sediment pickup, transport, and deposition, *Water resources research*, *49*(8), 4775-4791.

Nabi, M., H. Vriend, E. Mosselman, C. Sloff, and Y. Shimizu (2012), Detailed simulation of morphodynamics: 1. Hydrodynamic model, *Water Resources Research*, *48*(12).

Nabi, M., H. Vriend, E. Mosselman, C. Sloff, and Y. Shimizu (2013c), Detailed simulation of morphodynamics: 3. Ripples and dunes, *Water resources research*, *49*(9), 5930-5943.

Nakagawa, H. (1980), Sand bed instability due to bed load motion, paper presented at Proc. ASCE.

Naqshband, S. (2014), Morphodynamics of river dunes: suspended sediment transport along mobile dunes and dune development towards upper stage plane bed, University of Twente.

Naqshband, S., O. J. Duin, J. S. Ribberink, and S. J. Hulscher (2016), Modeling river dune development and dune transition to upper stage plane bed, *Earth Surface Processes and Landforms*, *41*(3), 323-335.

Naqshband, S., A. Hoitink, B. McElroy, D. Hurther, and S. J. Hulscher (2017), A sharp view on river dune transition to upper stage plane bed, *Geophysical research letters*.

Naqshband, S., J. S. Ribberink, and S. J. Hulscher (2014a), Using both free surface effect and sediment transport mode parameters in defining the morphology of river dunes and their evolution to upper stage plane beds, *Journal of Hydraulic Engineering*, *140*(6), 06014010.

Naqshband, S., J. S. Ribberink, D. Hurther, P.-A. Barraud, and S. J. Hulscher (2014b), Experimental evidence for turbulent sediment flux constituting a large portion of the total sediment flux along migrating sand dunes, *Geophysical research letters*, *41*(24), 8870-8878.

Naqshband, S., J. S. Ribberink, D. Hurther, and S. J. Hulscher (2014c), Bed load and suspended load contributions to migrating sand dunes in equilibrium, *Journal of Geophysical Research: Earth Surface*, *119*(5), 1043-1063.

Nelson, J., R. L. Shreve, S. R. McLean, and T. G. Drake (1995), Role of near‐bed turbulence structure in bed load transport and bed form mechanics, *Water Resources Research*, *31*(8), 2071-2086.

Nelson, J., and J. D. Smith (1989), Mechanics of flow over ripples and dunes, *Journal of Geophysical Research: Oceans (1978–2012)*, *94*(C6), 8146-8162.

Nelson, J. M., B. L. Logan, P. J. Kinzel, Y. Shimizu, S. Giri, R. L. Shreve, and S. R. McLean (2011), Bedform response to flow variability, *Earth Surface Processes and Landforms*, *36*(14), 1938-1947.

Nelson, J. M., S. R. McLean, and S. R. Wolfe (1993), Mean flow and turbulence fields over two-dimensional bed forms, *Water Resour. Res*, *29*(12), 3935-3953.

Nelson, J. M., Y. Shimizu, S. Giri, and R. McDonald (2010), Computational modeling of bedform evolution in rivers with implications for predictions of flood stage and bed evolution, paper presented at Proceedings of the 2nd Joint Federal Interagency Conference, June.

Nepf, H., M. Ghisalberti, B. White, and E. Murphy (2007), Retention time and dispersion associated with submerged aquatic canopies, *Water Resources Research*, *43*(4).

Nezu, I. (1993), Turbulence in open-channel flows.

Niño, Y., and M. García (1998), Using Lagrangian particle saltation observations for bedload sediment transport modelling, *Hydrological Processes*, *12*(8), 1197-1218.

Nielsen, P. (1992), *Coastal bottom boundary layers and sediment transport*, World Scientific Publishing Co Inc.

Nikora, V. I., A. N. Sukhodolov, and P. M. Rowinski (1997), Statistical sand wave dynamics in one-directional water flows, *Journal of Fluid Mechanics*, *351*, 17-39.

Nikuradse, J. (1950), *Laws of flow in rough pipes*, National Advisory Committee for Aeronautics Washington.

Nittrouer, J. A., M. A. Allison, and R. Campanella (2008), Bedform transport rates for the lowermost Mississippi River, *Journal of Geophysical Research: Earth Surface*, *113*(F3).

Nordin, C. F. (1971), *Statistical properties of dune profiles*, US Government Printing Office.

Ohata, K., H. Naruse, M. Yokokawa, and E. Viparelli (2017), New bedform phase diagrams and discriminant functions for formative conditions of bedforms in open‐channel flows, *Journal of Geophysical Research: Earth Surface*.

Paarlberg, A., C. Dohmen-Janssen, S. Hulscher, R. Schielen, and A. Termes (2008), Modelling dynamic roughness in rivers during floods, paper presented at Marine and River Dune Dynamics 3, Third International Workshop, April 1-3 2008, Leeds (United Kingdom).

Paarlberg, A. J. (2008), Modelling dune evolution and dynamic roughness in rivers, University of Twente.

Paarlberg, A. J., C. M. Dohmen‐Janssen, S. J. Hulscher, and P. Termes (2007), A parameterization of flow separation over subaqueous dunes, *Water Resources Research*, *43*(12).

Paarlberg, A. J., C. M. Dohmen‐Janssen, S. J. Hulscher, and P. Termes (2009), Modeling river dune evolution using a parameterization of flow separation, *Journal of Geophysical Research: Earth Surface (2003–2012)*, *114*(F1).

Paarlberg, A. J., C. M. Dohmen‐Janssen, S. J. Hulscher, P. Termes, and R. Schielen (2010), Modelling the effect of time‐dependent river dune evolution on bed roughness and stage, *Earth surface processes and landforms*, *35*(15), 1854-1866.

Paice, C. (1990), Hydraulic control of river bank erosion: an environmental approach, University of East Anglia.

Parker, G., and P. R. Wilcock (1993), Sediment feed and recirculating flumes: Fundamental difference, *Journal of Hydraulic Engineering*, *119*(11), 1192-1204.

Parsons, D., J. Best, S. Lane, R. Hardy, R. Kostaschuk, D. Shugar, and O. Orfeo (2006), Morphology, flow and sediment transport over a natural 3D dune field: Rio Paraná, Argentina, paper presented at River Flow.

Parsons, D., J. Best, O. Orfeo, R. Hardy, R. Kostaschuk, and S. Lane (2005), Morphology and flow fields of three - dimensional dunes, Rio Paranά, Argentina: Results from simultaneous multibeam echo sounding and acoustic Doppler current profiling, *Journal of Geophysical Research: Earth Surface (2003–2012)*, *110*(F4).

Parsons, D., J. L. Best, S. N. Lane, O. Orfeo, R. J. Hardy, and R. Kostaschuk (2007), Form roughness and the absence of secondary flow in a large confluence-diffluence, Rio Parana, Argentina, *Earth Surface Processes and Landforms*, *32*(1), 155-162.

Parsons, D., P. Jackson, J. Czuba, F. Engel, B. Rhoads, K. Oberg, J. Best, D. Mueller, K. Johnson, and J. Riley (2013), Velocity Mapping Toolbox (VMT): a processing and visualization suite for moving - vessel ADCP measurements, *Earth Surface Processes and Landforms*, *38*(11), 1244-1260.

Parsons, D. R., and J. Best (2013), Bedforms: views and new perspectives from the third international workshop on Marine and River Dune Dynamics (MARID3), *Earth Surface Processes and Landforms*, *38*(3), 319-329.

Parsons, D. R., R. J. Schindler, J. A. Hope, J. Malarkey, J. H. Baas, J. Peakall, A. J. Manning, L. Ye, S. Simmons, and D. M. Paterson (2016), The role of biophysical cohesion on subaqueous bed form size, *Geophysical research letters*, *43*(4), 1566-1573.

Penko, A., J. Calantoni, S. Rodriguez - Abudo, D. Foster, and D. Slinn (2013), Three - dimensional mixture simulations of flow over dynamic rippled beds, *Journal of Geophysical Research: Oceans*, *118*(3), 1543-1555.

Perumal, M., K. B. Shrestha, and U. Chaube (2004), Reproduction of hysteresis in rating curves, *Journal of Hydraulic Engineering*, *130*(9), 870-878.

Petit, F. (1989), The evaluation of grain shear stress from experiments in a pebble - bedded flume, *Earth Surface Processes and Landforms*, *14*(6), 499-508.

Pope, N., J. Widdows, and M. Brinsley (2006), Estimation of bed shear stress using the turbulent kinetic energy approach—a comparison of annular flume and field data, *Continental Shelf Research*, *26*(8), 959-970.

Ramirez, M. T., and M. A. Allison (2013), Suspension of bed material over sand bars in the Lower Mississippi River and its implications for Mississippi delta environmental restoration, *Journal of Geophysical Research: Earth Surface*, *118*(2), 1085-1104.

Raudkivi, A. (1966), Bed forms in alluvial channels, *Journal of Fluid Mechanics*, *26*(03), 507-514.

Raudkivi, A. (1988), The roughness height under waves, *Journal of Hydraulic Research*, *26*(5), 569-584.

Raudkivi, A., and H. Witte (1990), Development of bed features, *Journal of Hydraulic Engineering*, *116*(9), 1063-1079.

Rauen, W. B., B. Lin, and R. A. Falconer (2009), Modelling dynamic bed roughness associated with bed form development, in *Advances in Water Resources and Hydraulic Engineering*, edited, pp. 865-870, Springer.

RD, I. (2011), Principles of Operation A Practical Primer, *Available from RDInstruments. com*.

Reesink, A., and J. Bridge (2007), Influence of superimposed bedforms and flow unsteadiness on formation of cross strata in dunes and unit bars, *Sedimentary Geology*, *202*(1), 281-296.

Reesink, A., D. Parsons, P. Ashworth, J. Best, S. Darby, and R. Hardy (2016), Visualizing bed deformation and sediment dispersal across dune fields, paper presented at Marine and River Dunes conference.

Reesink, A., D. Parsons, P. Ashworth, R. Hardy, J. Best, C. Unsworth, S. McLelland, and B. Murphy (2013), The response and hysteresis of alluvial dunes under transient flow conditions, *Presented at: Marine and River Dune Dynamics-MARIDIV*, *15*, 17.

Reesink, A. J. H., and J. Bridge (2009), Influence of bedform superimposition and flow unsteadiness on the formation of cross strata in dunes and unit bars—Part 2, further experiments, *Sedimentary Geology*, *222*(3), 274-300.

Reesink, A. J. H., and J. S. Bridge (2011), Evidence of Bedform Superimposition and Flow Unsteadiness in Unit-Bar Deposits, South Saskatchewan River, Canada, *Journal of Sedimentary Research*, *81*(11-12), 814-840.

Reesink, A. J. H., D. R. Parsons, P. J. Ashworth, J. L. Best, R. J. Hardy, B. Murphy, S. J. McLelland, and C. Unsworth (2017), The adaptation of dunes to changes in river flow, *Earth-science reviews*, *Under review*.

Reesink, A. J. H., J. Van den Berg, D. Parsons, M. Amsler, J. Best, R. Hardy, O. Orfeo, and R. Szupiany (2015), Extremes in dune preservation: Controls on the completeness of fluvial deposits, *Earth-Science Reviews*, *150*, 652-665.

Rennie, C. D. (2002), Non-invasive measurement of fluvial bedload transport velocity, University of British Columbia.

Rennie, C. D., R. G. Millar, and M. A. Church (2002), Measurement of bed load velocity using an acoustic Doppler current profiler, *Journal of Hydraulic Engineering*, *128*(5), 473-483.

Rennie, C. D., and F. Rainville (2006), Case study of precision of GPS differential correction strategies: Influence on aDcp velocity and discharge estimates, *Journal of hydraulic engineering*.

Rennie, C. D., and P. V. Villard (2004), Site specificity of bed load measurement using an acoustic Doppler current profiler, *Journal of Geophysical Research: Earth Surface (2003–2012)*, *109*(F3).

RESON, I. (2007), SeaBat 7125 Operator Manual, v5. Goleta, CA: RESON Inc.*Rep.*

RL, A. J. (1982), *Sedimentary structures, their character and physical basis*, Elsevier.

Roden, J. (1998), The sedimentology and dynamics of mega-dunes, Jamuna River, Bangladesh, University of Leeds.

Rodrigues, S., E. Mosselman, N. Claude, C. L. Wintenberger, and P. Juge (2015), Alternate bars in a sandy gravel bed river: generation, migration and interactions with superimposed dunes, *Earth Surface Processes and Landforms*, *40*(5), 610-628.

Rubin, D., and D. McCulloch (1980), Single and superimposed bedforms: a synthesis of San Francisco Bay and flume observations, *Sedimentary Geology*, *26*(1), 207-231.

Rubin, D. M. (2012), A unifying model for planform straightness of ripples and dunes in air and water, *Earth-Science Reviews*, *113*(3), 176-185.

Saleh, A. (1993), Soil roughness measurement: chain method, *Journal of Soil and Water Conservation*, *48*(6), 527-529.

Sandbach, S., S. Lane, R. Hardy, M. Amsler, P. Ashworth, J. Best, A. Nicholas, O. Orfeo, D. Parsons, and A. Reesink (2012), Application of a roughness ‐ length representation to parameterize energy loss in 3 ‐ D numerical simulations of large rivers, *Water Resources Research*, *48*(12).

Sassi, M., A. Hoitink, and B. Vermeulen (2012), Impact of sound attenuation by suspended sediment on ADCP backscatter calibrations, *Water Resources Research*, *48*(9).

Schields, A. (1936), Application of Similarity Mechanics and Turbulence Research for Bed-load Transport, *Mitt. der Preussischen Versuchsanstalt für Wasserbau und Schiffbau, Berlin*.

Schindler, R. J., D. R. Parsons, L. Ye, J. A. Hope, J. H. Baas, J. Peakall, A. J. Manning, R. J. Aspden, J. Malarkey, and S. Simmons (2015), Sticky stuff: Redefining bedform prediction in modern and ancient environments, *Geology*, *43*(5), 399-402.

Schlichting, H., K. Gersten, E. Krause, H. Oertel, and K. Mayes (1960), *Boundary-layer theory*, Springer.

Schmeeckle, M. (2015), The role of velocity, pressure, and bed stress fluctuations in bed load transport over bed forms: numerical simulation downstream of a backward-facing step, *Earth Surface Dynamics*, *3*(1), 105-112.

Sekine, M., and H. Kikkawa (1992), Mechanics of saltating grains. II, *Journal of Hydraulic Engineering*, *118*(4), 536-558.

Shamov, G. E. (1952), Formulas for Determining Near-Bed Velocity and Bed Load Discharge, *Proc. Soviet National Hydrology Institute*, *36*.

Shimizu, Y., S. Giri, S. Yamaguchi, and J. Nelson (2009), Numerical simulation of dune–flat bed transition and stage ‐ discharge relationship with hysteresis effect, *Water Resources Research*, *45*(4).

Shimizu, Y., and M. W. Schmeeckle (2001), Direct numerical simulation of turbulence over two-dimensional dunes using CIP method, *Journal of hydroscience and hydraulic engineering*, *19*(2), 85-92.

Shinohara, K., and T. Tsubaki (1959), *On the characteristics of sand waves formed upon the beds of the open channels and rivers*, Research Institute for Applied Mechanics, Kyushu University.

Shun-ichiro, H., T. OHMOTO, and K. TAKIKAWA (2003), Direct numerical simulation of coherent vortex structures in an open-channel flow over dune type wavy bed, *Journal of hydroscience and hydraulic engineering*, *21*(1), 1-10.

Shuwei, Z., C. Heqin, W. Shuaihu, S. Shengyu, X. Wei, Z. Quanping, and J. Yuehua (2017), Morphology and mechanism of the very large dunes in the tidal reach of the Yangtze River, China, *Continental Shelf Research*, *139*, 54-61.

Sime, L. C., R. I. Ferguson, and M. Church (2007), Estimating shear stress from moving boat acoustic Doppler velocity measurements in a large gravel bed river, *Water Resources Research*, *43*(3).

Simoes, F. J. (2010), Flow resistance in open channels with fixed and movable bed, paper presented at Proc., 2nd Joint Federal Interagency Conference on Sedimentation and Hydrologic Modeling, Reston, VA.

Simons, D. B., and E. V. Richardson (1961), Forms of Bed Roughness in Alluvial Channel, *Journal of the Hydraulics Division*, *87*(3), 87-105.

Simons, D. B., E. V. Richardson, and C. Nordin Jr (1965), Bedload equation for ripples and dunes*Rep. 2330-7102*.

Smith, G. A., A. V. Babanin, P. Riedel, I. Young, S. Oliver, and G. Hubbert (2011), Introduction of a new friction routine into the SWAN model that evaluates roughness due to bedform and sediment size changes, *Coastal Engineering*, *58*(4), 317-326.

Smith, J. D., and S. R. McLean (1977), Spatially averaged flow over a wavy surface, *Journal of Geophysical research*, *82*(12), 1735-1746.

Smith, M. (2014), Roughness in the earth sciences, *Earth-Science Reviews*, *136*, 202-225.

Song, D., X. H. Wang, Z. Cao, and W. Guan (2013), Suspended sediment transport in the Deepwater Navigation Channel, Yangtze River Estuary, China, in the dry season 2009: 1. Observations over spring and neap tidal cycles, *Journal of Geophysical Research: Oceans*, *118*(10), 5555-5567.

Song, L. L. (2002), Research on the location of tidal current limit of Yangtze River, *Hydrology*, *5*, 25-27.

Soulsby, R. (1997), *Dynamics of marine sands: a manual for practical applications*, Thomas Telford.

Soulsby, R., and R. Whitehouse (1997), Threshold of sediment motion in coastal environments, paper presented at Pacific Coasts and Ports' 97: Proceedings of the 13th Australasian Coastal and Ocean Engineering Conference and the 6th Australasian Port and Harbour Conference; Volume 1, Centre for Advanced Engineering, University of Canterbury.

Southard, J. B. (1991), Experimental determination of bed-form stability, *Annual Review of Earth and Planetary Sciences*, *19*(1), 423-455.

Southard, J. B., and L. A. Boguchwal (1990), Bed configurations in steady unidirectional water flows. Part 2. Synthesis of flume data, *Journal of Sedimentary Research*, *60*(5).

Southard, J. B., and J. C. Harms (1972), Sequence of Bedform and Stratification in Silts, Based on Flume Experiments, *Am Assoc Petr Geol B*, *56*(3), 654-&.

Stacey, M. T., S. G. Monismith, and J. R. Burau (1999), Observations of turbulence in a partially stratified estuary, *Journal of Physical Oceanography*, *29*(8), 1950-1970.

Swanson, T., D. Mohrig, G. Kocurek, M. Perillo, and J. Venditti (2017), Bedform spurs: a result of a trailing helical vortex wake, *Sedimentology*, doi:10.1111/sed.12383.

Teledyne, R. (2007), WinRiver II user's guide.*Rep.*, N 957-6231-00.

Termes, A. (2004), Herziening Qh-relaties Venlo en Megen en afleiding Qh-relaties Belfeld-beneden en Lith-boven*Rep.*, Technical Report PR902 (in Dutch), HKV Consultants, Lelystad, Netherlands.

Terwindt, J. H. (1971), Sand waves in the Southern Bight of the North Sea, *Marine Geology*, *10*(1), 51-67.

Thorne, P. D., and D. M. Hanes (2002), A review of acoustic measurement of small-scale sediment processes, *Continental shelf research*, *22*(4), 603-632.

Topping, D., S. Wright, T. Melis, and D. Rubin (2007), High-resolution measurements of suspended-sediment concentration and grain size in the Colorado River in Grand Canyon using a multi-frequency acoustic system, paper presented at Proceedings of the 10th International Symposium on River Sedimentation.

Torrence, C., and G. P. Compo (1998), A practical guide to wavelet analysis, *Bulletin of the American Meteorological society*, *79*(1), 61-78.

Traykovski, P. (2007), Observations of wave orbital scale ripples and a nonequilibrium time - dependent model, *Journal of Geophysical Research: Oceans*, *112*(C6).

Tuijnder, A., and J. Ribberink (2008), Bedform dimensions under supply limited conditions.

Tuijnder, A., and J. Ribberink (2009), Prediction of bedform dimensions, bed roughness and sediment transport under supply-limited conditions in rivers*Rep.*, Tech. rep., Faculty of Engineering Technology, University of Twente, The Netherlands.

Tuijnder, A. P., J. S. Ribberink, and S. J. Hulscher (2009), An experimental study into the geometry of supply - limited dunes, *Sedimentology*, *56*(6), 1713-1727.

Turowski, J. M. (2010), Probability distributions of bed load transport rates: A new derivation and comparison with field data, *water resources research*, *46*(8).

Unsworth, C. A. (2015), River Dunes in Unsteady Conditions, PhD thesis, University of Hull.

Van Balen, W., W. S. Uijttewaal, and K. Blanckaert (2010), Large-eddy simulation of a curved open-channel flow over topography, *Phys Fluids*, *22*(7), 075108.

Van Den Berg, J. H., and A. Van Gelder (2009), A new bedform stability diagram, with emphasis on the transition of ripples to plane bed in flows over fine sand and silt, *Alluvial Sedimentation (Special Publication 17 of the IAS)*, *66*, 11.

van der Mark, C., and A. Blom (2007), A new & widely applicable bedform tracking tool*Rep.*, Tech. rep.

van der Mark, C. F., A. Blom, and S. J. M. H. Hulscher (2008), Quantification of variability in bedform geometry, *Journal of Geophysical Research-Earth Surface*, *113*(F3).

van der Zanden, J., D. Hurther, I. Cáceres, T. O'Donoghue, and J. S. Ribberink (2017), Suspended sediment transport around a large-scale laboratory breaker bar, *Coastal engineering*, *125*, 51-69.

Van Rijn, L. C. (1982), Equivalent roughness of alluvial bed, *Journal of Hydraulic Engineering*, *108*(10), 1215-1218.

Van Rijn, L. C. (1984a), Sediment transport, part I: bed load transport, *Journal of hydraulic engineering*, *110*(10), 1431-1456.

Van Rijn, L. C. (1984b), Sediment transport, part III: bed forms and alluvial roughness, *Journal of hydraulic engineering*, *110*(12), 1733-1754.

Van Rijn, L. C. (1993), *Principles of sediment transport in rivers, estuaries and coastal seas*, Aqua publications Amsterdam.

Van Rijn, L. C. (2007), Unified view of sediment transport by currents and waves. I: Initiation of motion, bed roughness, and bed-load transport, *Journal of hydraulic engineering*, *133*(6), 649-667.

Venditti, J. G. (2003), Initiation and development of sand dunes in river channels, University of British Columbia.

Venditti, J. G. (2007), Turbulent flow and drag over fixed two - and three - dimensional dunes, *Journal of Geophysical Research: Earth Surface (2003 - 2012)*, *112*(F4).

Venditti, J. G. (2013), Bedforms in sand-bedded rivers, *Treatise on Geomorphology*, 137-162.

Venditti, J. G., and S. J. Bennett (2000), Spectral analysis of turbulent flow and suspended sediment transport over fixed dunes, *Journal of Geophysical Research: Oceans (1978–2012)*, *105*(C9), 22035-22047.

Venditti, J. G., M. Church, and S. J. Bennett (2005a), Morphodynamics of small-scale superimposed sand waves over migrating dune bed forms, *Water resources research*, *41*(10).

Venditti, J. G., M. Church, and S. J. Bennett (2005b), On the transition between 2D and 3D dunes, *Sedimentology*, *52*(6), 1343-1359.

Venditti, J. G., M. A. Church, and S. J. Bennett (2005c), Bed form initiation from a flat sand bed, *Journal of Geophysical Research: Earth Surface (2003–2012)*, *110*(F1).

Venditti, J. G., C. Y. M. Lin, and M. Kazemi (2016), Variability in bedform morphology and kinematics with transport stage, *Sedimentology*, *63*(4), 1017-1039.

Villard, P., and M. Church (2005), Bar and dune development during a freshet: Fraser river estuary, British Columbia, Canada, *Sedimentology*, *52*(4), 737-756.

Villard, P., and R. Kostaschuk (1998), The relation between shear velocity and suspended sediment concentration over dunes: Fraser Estuary, Canada, *Marine Geology*, *148*(1), 71-81.

Villaret, C., N. Huybrechts, A. Davies, and O. Way (2011), Effect of bed roughness prediction on morphodynamic modelling: Application to the Dee estuary (UK) and to the Gironde estuary (France), paper presented at Proceedings of the 34th World Congress of the International Association for Hydro-Environment Research and Engineering: 33rd Hydrology and Water Resources Symposium and 10th Conference on Hydraulics in Water Engineering, Engineers Australia.

Visser, M. J. (1980), Neap-Spring Cycles Reflected in Holocene Subtidal Large-Scale Bedform Deposits - a Preliminary Note, *Geology*, *8*(11), 543-546.

Wang, Y. W., Q. Yu, J. Jiao, P. K. Tonnon, Z. B. Wang, and S. Gao (2016), Coupling bedform roughness and sediment grain-size sorting in modelling of tidal inlet incision, *Marine Geology*, *381*, 128-141.

Warmink, J., M. Booij, H. Van der Klis, and S. Hulscher (2013), Quantification of uncertainty in design water levels due to uncertain bed form roughness in the Dutch river Waal, *Hydrological processes*, *27*(11), 1646-1663.

Warmink, J. J. (2014), Dune dynamics and roughness under gradually varying flood waves, comparing flume and field observations, *Advances in geosciences*, *39*, 115-121.

Warmink, J. J., C. M. Dohmen ‐ Janssen, J. Lansink, S. Naqshband, O. J. Duin, A. J. Paarlberg, P. Termes, and S. J. Hulscher (2014), Understanding river dune splitting through flume experiments and analysis of a dune evolution model, *Earth surface processes and landforms*, *39*(9), 1208-1220.

Weisbach, J. (1845), Lehrbuch der Ingenieur-und Maschinen, *Mechanik*, *1*, 434.

Whatmore, S. J., and C. Landström (2010), Manning's n: Putting Roughness to Work, in *How well do facts travel?: The dissemination of reliable knowledge*, edited by P. Howlett and M. S. Morgan, p. 111, Cambridge University Press.

Wiberg, P. L., and J. M. Nelson (1992), Unidirectional flow over asymmetric and symmetric ripples, *Journal of Geophysical Research: Oceans*, *97*(C8), 12745-12761.

Wiberg, P. L., and J. D. Smith (1985), A theoretical model for saltating grains in water, *Journal of Geophysical Research: Oceans*, *90*(C4), 7341-7354.

Wijbenga, J., and G. Klaassent (2009), Changes in bedform dimensions under unsteady flow conditions in a straight flurne, *Modern and Ancient Fluvial Systems (Special Publication 6th of the IAS)*, 35.

Wijbenga, J., and A. Van Nes (1986), Flow resistance and bedform dimensions for varying flow conditions; results of flume experiments with flood waves, *TOW rivers R*.

Wilbers, A. (2004), The development and hydraulic roughness of subaqueous dunes, Utrecht University.

Wilbers, A., and W. Ten Brinke (2003), The response of subaqueous dunes to floods in sand and gravel bed reaches of the Dutch Rhine, *Sedimentology*, *50*(6), 1013-1034.

Wilcock, P. R. (1996), Estimating local bed shear stress from velocity observations, *Water Resources Research*, *32*(11), 3361-3366.

Wilkinson, R. (1983), A method for evaluating statistical errors associated with logarithmic velocity profiles, *Geo-marine letters*, *3*(1), 49-52.

Williams, G. P. (1970), *Flume width and water depth effects in sediment-transport experiments*, Citeseer.

Williams, J. J. (1995), Drag and sediment dispersion over sand waves, *Estuarine, Coastal and Shelf Science*, *41*(6), 659-687.

Wilson, K. C. (1966), Bed-load transport at high shear stress, *Journal of the hydraulics division*, *92*(6), 49-59.

Winter, C., G. Vittori, V. B. Ernstsen, and J. Bartholdy (2008), On the superimposition of bedforms in a tidal channel, *Marine and River Dune Dynamics*, 337-344.

Wren, D., R. Kuhnle, and C. Wilson (2007), Measurements of the relationship between turbulence and sediment in suspension over mobile sand dunes in a laboratory flume, *Journal of Geophysical Research: Earth Surface (2003–2012)*, *112*(F3).

Wu, J., Y. Wang, and H. Cheng (2009), Bedforms and bed material transport pathways in the Changjiang (Yangtze) Estuary, *Geomorphology*, *104*(3), 175-184.

Yalin, M. S. (1963), An expression for bed-load transportation, *Journal of the Hydraulics Division*, *89*(3), 221-250.

Yalin, M. S. (1972), *Mechanics of sediment transport*, Pergamon press.

Yalin, M. S. (2015), *River mechanics*, Elsevier.

Yamaguchi, S., and N. Izumi (2002), Weakly nonlinear stability analysis of dune formation, paper presented at Proceedings of the International Conference on Fluvial Hydraulics.

Yamaguchi, S., and N. Izumi (2003), Weakly nonlinear analysis of dunes including suspended load, paper presented at Proceedings of the 3rd IAHR Symposium on River, Coastal and Estuarine Morphodynamics.

Yang, S.-l., Q.-y. Zhao, and I. M. Belkin (2002), Temporal variation in the sediment load of the Yangtze River and the influences of human activities, *Journal of Hydrology*, *263*(1), 56-71.

Yang, S., Z. Liu, S. Dai, Z. Gao, J. Zhang, H. Wang, X. Luo, C. Wu, and Z. Zhang (2010), Temporal variations in water resources in the Yangtze River (Changjiang) over the Industrial Period based on reconstruction of missing monthly discharges, *Water Resources Research*, *46*(10).

Yang, S., J. Milliman, K. Xu, B. Deng, X. Zhang, and X. Luo (2014), Downstream sedimentary and geomorphic impacts of the Three Gorges Dam on the Yangtze River, *Earth-Science Reviews*, *138*, 469-486.

Yang, S., S. Tan, and S. Lim (2005), Flow resistance and bed form geometry in a wide alluvial channel, *Water resources research*, *41*(9).

Yang, S., J. Zhang, S. Dai, M. Li, and X. Xu (2007), Effect of deposition and erosion within the main river channel and large lakes on sediment delivery to the estuary of the Yangtze River, *Journal of Geophysical Research: Earth Surface*, *112*(F2).

Yang, S., Z. Zhang, W. Xie, and S. He (1999), A Study of Sandwaves in the South Channel of the Yangtze Estuary, *The Ocean Engineering*, *17*(2), 88-94.

Yen, C., and K. T. Lee (1995), Bed topography and sediment sorting in channel bend with unsteady flow, *Journal of Hydraulic Engineering*, *121*(8), 591-599.

You, Z. (2005), Estimation of bed roughness from mean velocities measured at two levels near the seabed, *Continental Shelf Research*, *25*(9), 1043-1051.

Yuen, K. (1989), A study of boundary shear stress, flow resistance and momentum transfer in open channels with simple and compound trapezoidal cross sections, University of Birmingham.

Yun, C. X. (2004), Recent Evolution of the Yangtze Estuary and Its Mechanisms, *China Ocean Press, Beijing, China (in Chinese)*.

Zhang, R., J. Xie, and M. Wang (1989), *River sediment dynamics*, Water Resources and Electric Power Press, Beijing.

Zhou, C. (1993), On sand-waves in Yawosha channel of the Yangtze Estuary, paper presented at Proceedings on the Second International Symposium of River Sedimentation. Water Resources and Electric Power Press.

Appendix A

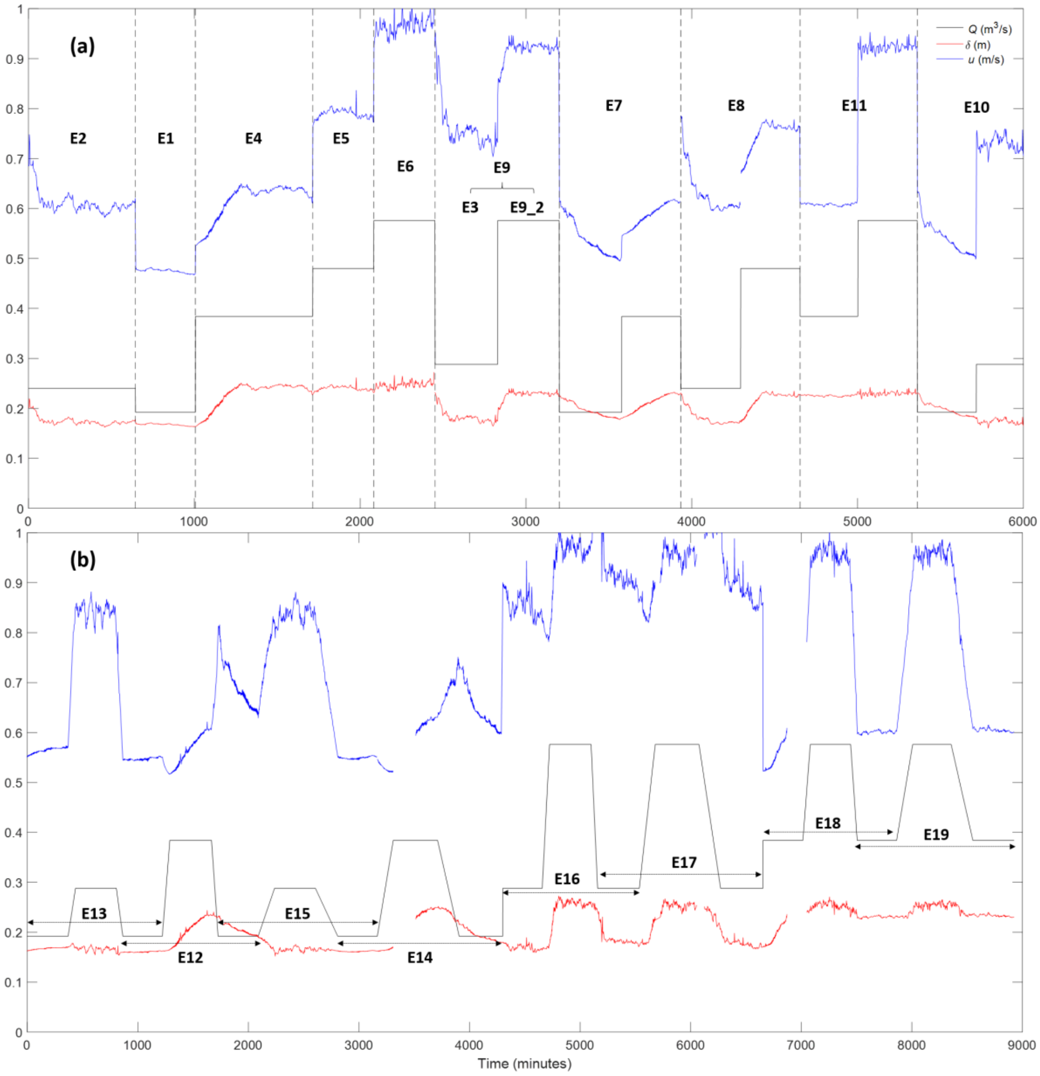

Variation of imposed flow discharge (solid black lines), and measured depth-averaged flow velocity (solid blue lines) and bed elevation (solid red lines): (a) for sudden change and (b) gradual change. Dashed black lines indicate where channel bed was re-levelled to flatbed. Details for each experiment could be found in the following table.

Overview of the flow conditions for 19 individual experiment. Flow depth d, flow velocity, and Q are all designed values. Q was strictly imposed trough all experiments, but the designed flow depth and velocity slightly affected via the variation of bed elevation.

Name	S1			S2			S3			Change rate
	d	*u*	Q	*d*	*u*	Q	*d*	*u*	Q	
E1	0.2	0.6	0.192							
E2	0.2	0.75	0.24							
E3	0.2	0.9	0.288							
E4	0.4	0.6	0.384							
E5	0.4	0.75	0.48							
E6	0.4	0.9	0.576							
E7	0.2	0.6	0.192	0.4	0.6	0.384				Sudden
E8	0.2	0.75	0.24	0.4	0.75	0.48				Sudden
E9	0.2	0.9	0.288	0.4	0.9	0.576				Sudden
E10	0.2	0.6	0.192	0.2	0.9	0.288				Sudden
E11	0.4	0.6	0.384	0.4	0.9	0.576				Sudden
E12	0.2	0.6	0.192	0.4	0.6	0.384	0.2	0.6	0.192	Fast
E13	0.2	0.6	0.192	0.2	0.9	0.288	0.2	0.6	0.192	Fast
E14	0.2	0.6	0.192	0.4	0.6	0.384	0.2	0.6	0.192	Slow
E15	0.2	0.6	0.192	0.2	0.9	0.288	0.2	0.6	0.192	Slow
E16	0.2	0.9	0.288	0.4	0.9	0.576	0.2	0.9	0.288	Fast
E17	0.2	0.9	0.288	0.4	0.9	0.576	0.2	0.9	0.288	Slow
E18	0.4	0.6	0.384	0.4	0.9	0.576	0.4	0.6	0.384	Fast
E19	0.4	0.6	0.384	0.4	0.9	0.576	0.4	0.6	0.384	Slow

Appendix B

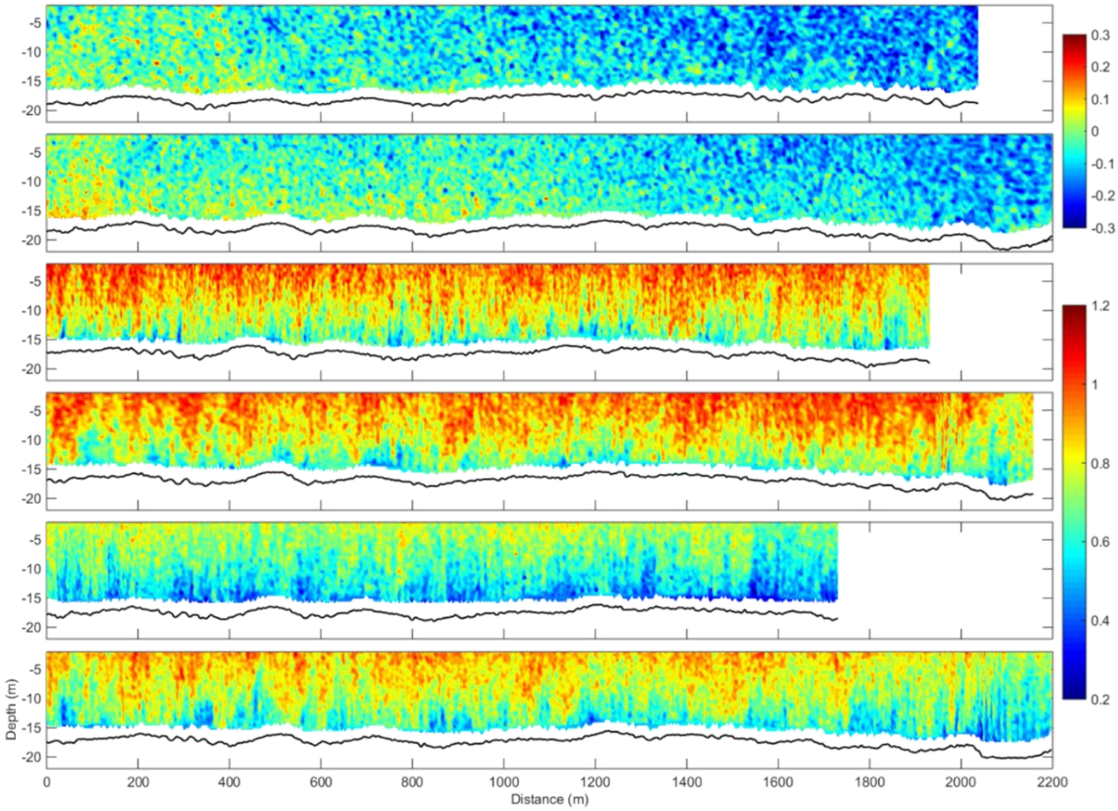

Distribution of Downstream velocity over bed profiles. Figure from the top to the bottom presents flow field for T1, T4, T2, T3, T5, and T6. The solid lines present the real bed profiles.

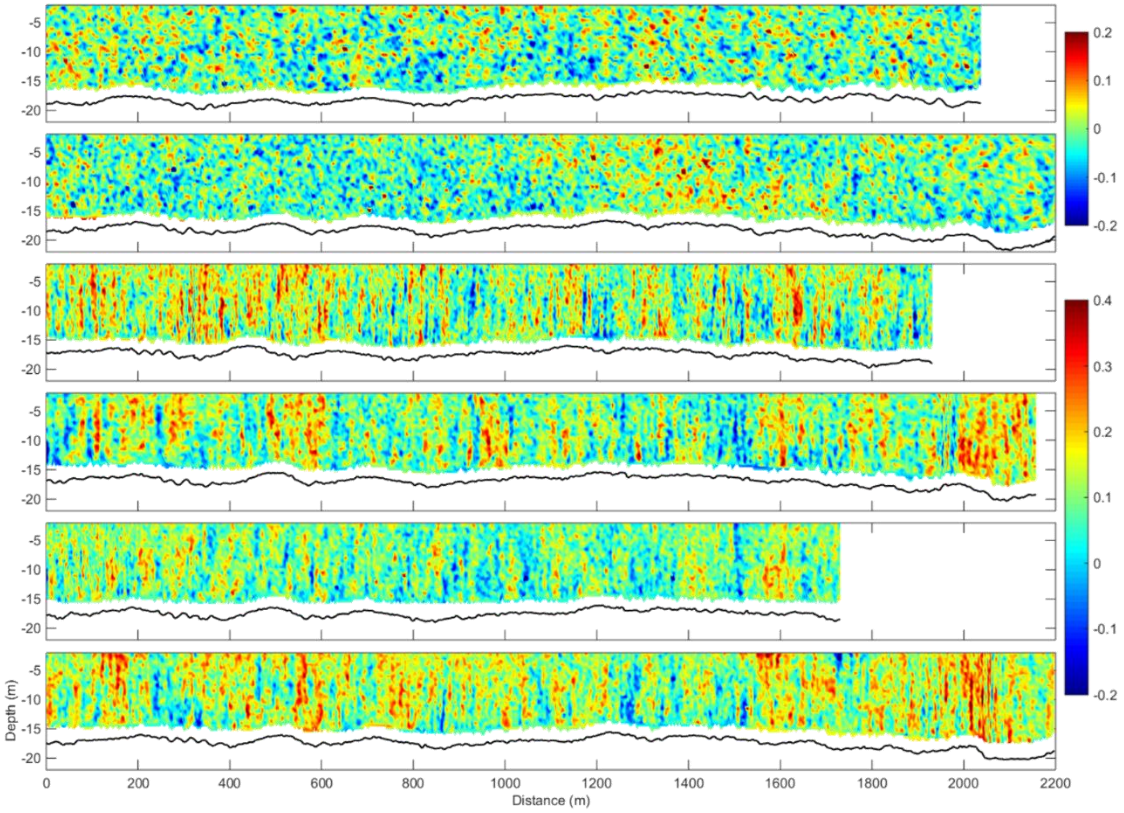

Distribution of Cross-stream velocity over bed profiles. Figure from the top to the bottom presents flow field for T1, T4, T2, T3, T5, and T6. The solid lines present the real bed profiles.

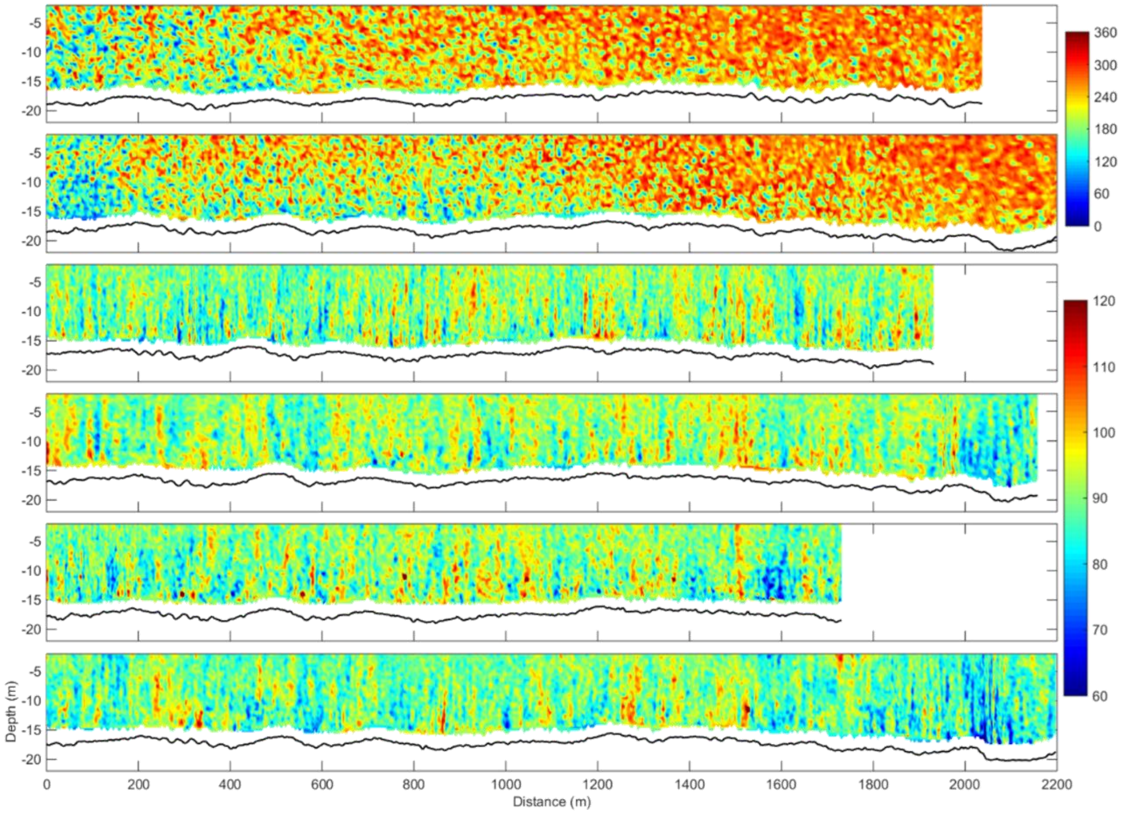

Distribution of velocity direction over bed profiles. Figure from the top to the bottom presents flow field for T1, T4, T2, T3, T5, and T6. The solid lines present the real bed profiles.

Appendix C

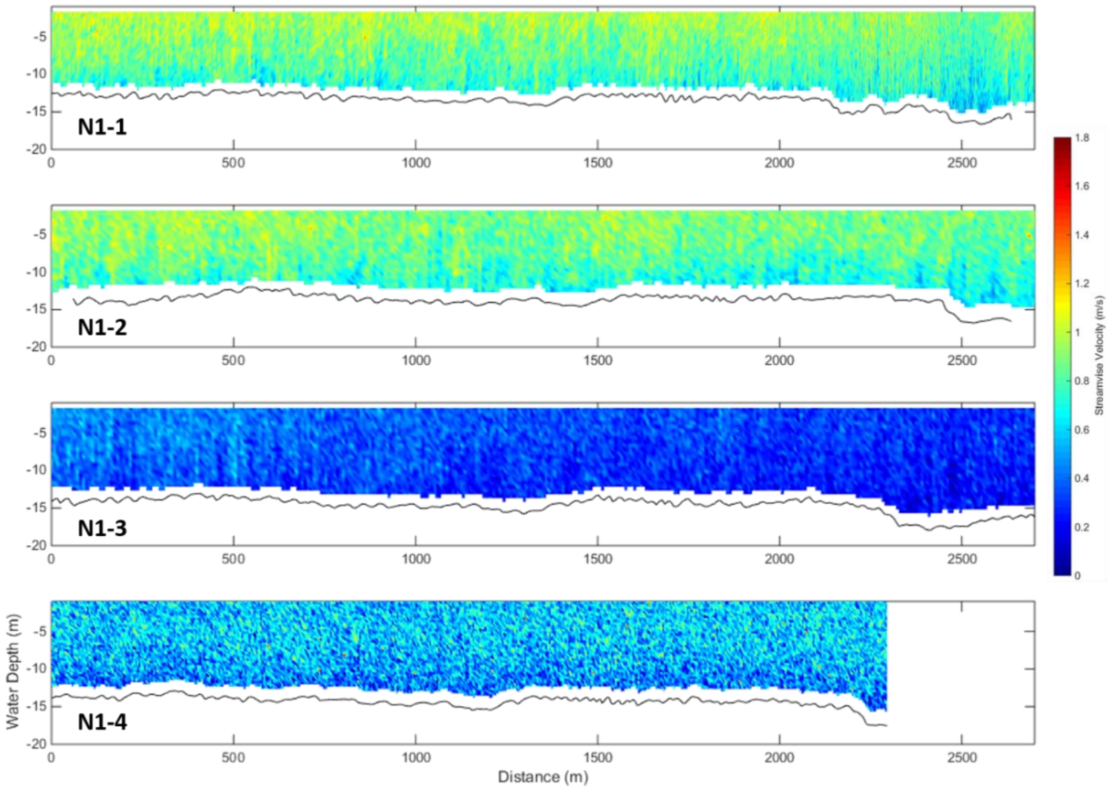

Distribution of streamwise velocity over bed profiles for N1-1 to N1-4. The solid lines present the real bed profiles.

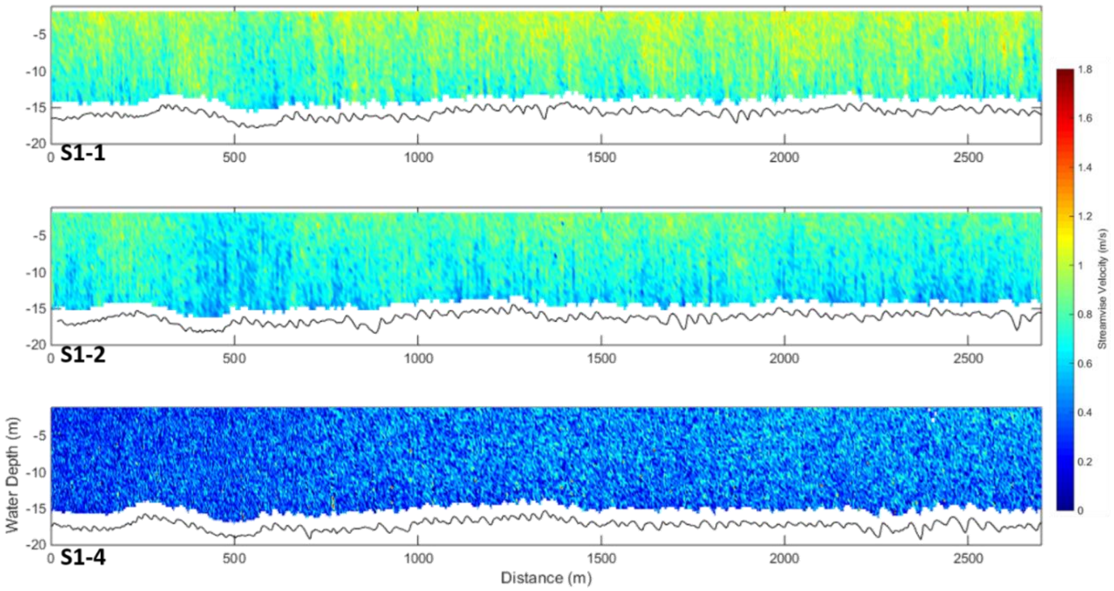

Distribution of streamwise velocity over bed profiles for S1-1 to S1-4. The solid lines present the real bed profiles.

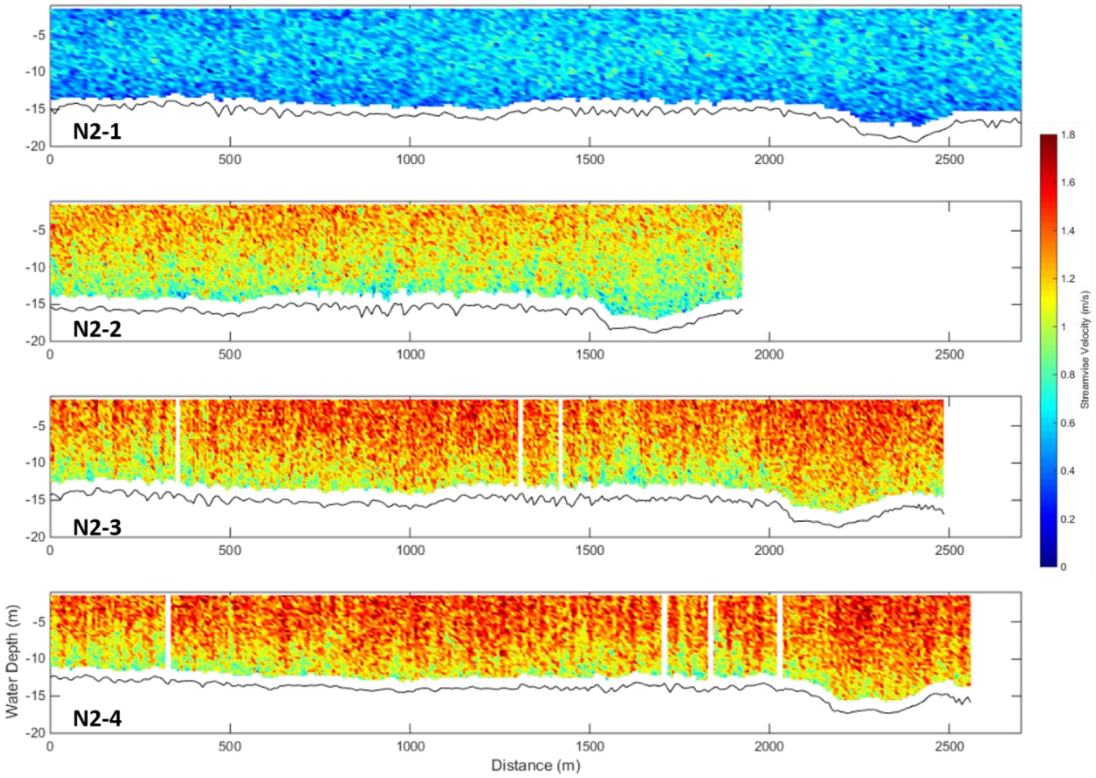

Distribution of streamwise velocity over bed profiles for N2-1 to N2-4. The solid lines present the real bed profiles.

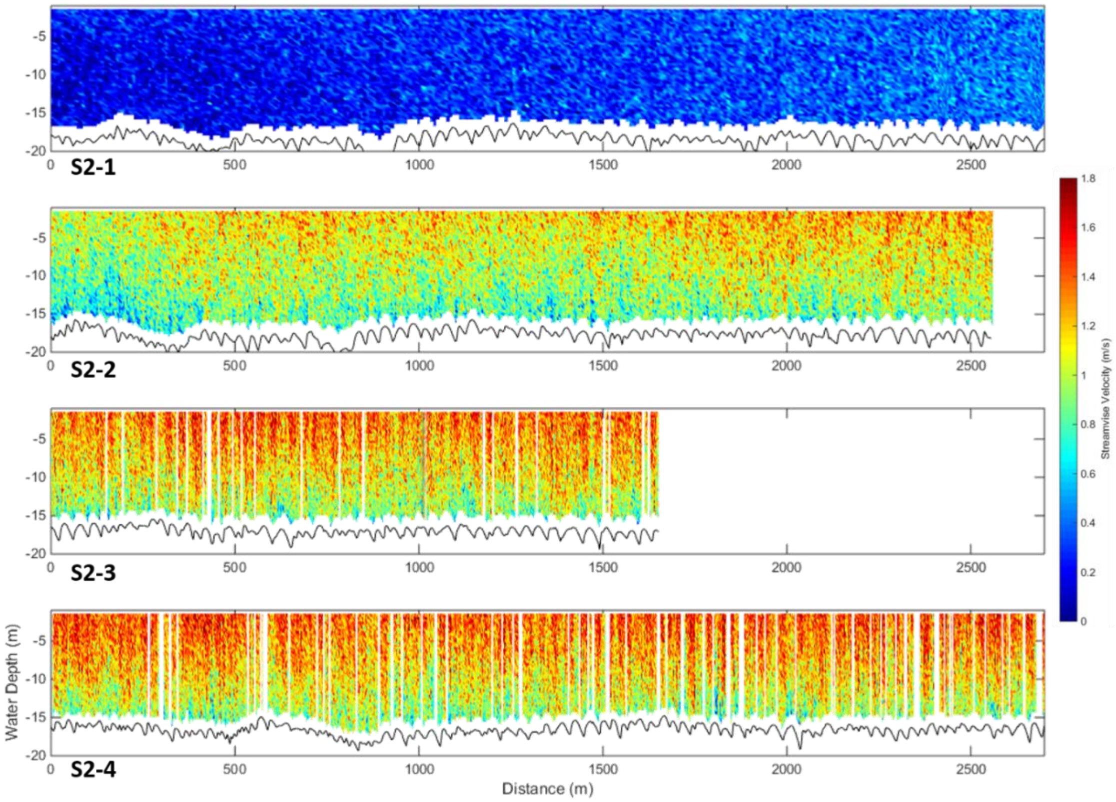

Distribution of streamwise velocity over bed profiles for S2-1 to S2-4. The solid lines present the real bed profiles.